Dissertation
submitted to the
Combined Faculties for the Natural Sciences and for Mathematics
of the Ruperto-Carola University of Heidelberg, Germany
for the degree of
Doctor of Natural Sciences

put forward by
Dipl.-Phys. Sebastian Thomas Ohlmann
born in St. Wendel

Date of oral exam: 06.07.2016

Hydrodynamics of the Common Envelope Phase in Binary Stellar Evolution

Zusammenfassung

Die Phase einer gemeinsamen Hülle (GH) ist wichtig für das Entstehen enger Binärsternsysteme mit mindestens einem kompakten Stern. In dieser Phase umgibt ein Riesenstern seinen Begleiter, der daraufhin spiralförmig in die Hülle des Riesen fällt. Die Hülle wird ausgestoßen und ein enges Binärsternsystem entsteht. Der Ausstoßmechanismus ist allerdings unbekannt und es ist ein seit Langem bestehendes Problem der Binärsternentwicklung, den Endzustand solcher Systeme vorherzusagen.

Diese Arbeit etabliert AREPO, einen Hydrodynamikcode auf einem bewegten Gitter, als neuen Ansatz zur Modellierung der GH-Phase und geht damit über den aktuellen Stand vergleichbarer Simulationen hinaus. Zunächst werden Hüllen von Riesensternen als Anfangsbedingungen stabilisiert. Dann zeigt die erste GH-Simulation auf einem bewegten Gitter, dass dynamische Instabilitäten auftreten. Die Gitterverfeinerung des AREPO-Codes erlaubt eine hohe Auflösung um die Punktmassen, die den Kern des Riesen und den Begleiter modellieren – eine wichtige Voraussetzung für Konvergenz.

Die ersten magnetohydrodynamischen GH-Simulationen ergeben hohe Feldverstärkungen, die auf die Magnetorotations-Instabilität als Ursache hinweisen. Eine Analyse des Drehimpuls- und Energietransports ergibt jedoch keinen wesentlichen Beitrag der Magnetfelder; Hauptursachen sind Drehmomente durch Gravitation und Stoßwellen. Wird der Ionisationszustand des Gases behandelt, erhöht sich die ungebundene Masse durch die Freisetzung von Rekombinationsenergie, die Hülle kann jedoch auch dadurch nicht vollständig ausgestoßen werden.

Abstract

The common envelope (CE) phase is critical for the formation of close binary stars with at least one compact star. During this phase, a giant star engulfs its companion, which spirals into the giant's envelope. The envelope is ejected and a close binary system results. The ejection mechanism is unknown and predicting the final state of the system is a long-standing problem in binary stellar evolution.

This work establishes the moving-mesh hydrodynamics code AREPO as a new approach to model CE phases, going beyond the current state of the art. Envelopes of giants are stabilized as initial conditions. Then, the first CE simulation on a moving mesh demonstrates the occurence of dynamical instabilities. AREPO's refinement capabilities allow high resolution around the point masses representing the core of the giant and the companion; this is essential for convergence.

The first magnetohydrodynamic CE simulations show strong field amplifications possibly due to the magnetorotational instability. Analyzing the transport of angular momentum and energy yields no significant contribution by magnetic fields; main drivers are gravitational torques and shocks. Including the ionization state of the gas increases the unbound mass by releasing recombination energy, but still fails to completely eject the envelope during the simulation.

Contents

Contents

Chapter 1

Prelude

A binary star system consists of two orbiting stars held together by their mutual gravitational interaction. The idea that stars move in a binary system could only be perceived after Aristotle's cosmology of an immutable sphere of stars[1] was overcome by the observations of Tycho Brahe. He observed that the supernova in 1572 – a very bright, transient event – did not show a parallax and thus must have been located near the sphere of stars (Brahe, 1573). Moreover, he was the first to determine the proper motions of stars by comparing his measurements to ancient observations made by Timocharis, Hipparchos, and Ptolemy (Brahe, 1610, p. 233-247, 253-256).[2] Thus, stars were no longer seen as immutable and could be imagined to move on the sky.

With the invention of the telescope, observations steadily improved and stars with close separations, double stars, were observed. Michell was the first to argue that it was very unlikely that such close separations were by chance only. He remarkably stated, "We may [...] conclude [...] that the stars are really collected together in clusters in some places, where they form a kind of systems, whilst in others there are either few or none of them, to whatever cause this may be owing, whether to their mutual gravitation, or to some other law or appointment of the Creator." (Michell, 1767) The systematic study of double stars began with the catalogue of about 100 objects compiled by Mayer (1779) in Mannheim, although there was still a dispute at that time about the nature of these systems (see Mayer, 1778). William Herschel later enlarged this to a few hundred double stars (Herschel, 1782, 1785).

Nowadays, it is known that binary stars are very common, with about half the stars in the solar neighbourhood being binary stars (Duquennoy & Mayor, 1991). Due to detection limits regarding long periods and small companion masses, this can only be an upper bound, and Eggleton (2011, Chapter 1) argues that about 30% of all systems are single, about 60% binary, and the rest multiple. If the separation of both components of a binary is larger than the largest radius that either of the stars assumes during its life, they will not interact significantly and the system will be effectively single.[3] At smaller separations, however, gravitational interaction between the components can lead to mass transfer. This changes the stellar evolution of both stars with a wide variety of outcomes. Single stars burn their nuclear fuel faster and evolve on shorter timescales when they are more massive (see, e.g., Kippenhahn et al., 2012). A classic example for the impact of mass

---

[1]As described in *On the Heavens* (Περὶ οὐρανοῦ, 4th century BCE): the Earth rests as a sphere in the center of the Universe with the Sun, and the planets, surrounded by the immutable sphere of stars, revolving around the Earth. This view of the world dominated Western astronomy for almost two millennia.

[2]Tycho determined the proper motions of stars on top of the precession of the equinoxes that was already known to Hipparchos in the 2nd century BCE as later described and confirmed by Ptolemy in his *Almagest* (2nd century CE, originally called Μαθηματικὴ Σύνταξις, see book 7). See also the overview of this history and the German translation of the *Almagest* by Bode (1795).

[3]Although there might be still an interaction through a wind at somewhat larger radii.

transfer in a binary system is the Algol binary[4]: the paradox that the more evolved star is less massive than its companion could only be explained by mass transfer in this system that changes the usual evolution (see the overviews by Batten, 1989; Pustylnik, 1998).

1.1 White Dwarfs in Close Binary Systems: a Riddle

White dwarfs (WDs) are compact stars stabilized against gravity by the degeneracy pressure of electrons. In single star systems, they are born as cores of evolved stars that were unable to ignite He or C in their center. Hence, WDs consist of He or a mixture of C and O, respectively. Their evolved progenitor stars are giants with radii up to several hundred solar radii. However, WDs are observed in binary systems with much smaller separations, down to a few solar radii in cataclysmic variable stars (CVs) where the separation is so small that the companion star transfers mass to the primary WD (see, e.g., King, 1988 and the catalogue by Ritter & Kolb, 2003). For a long time, it was unclear how WDs can form in such close binary systems that show much smaller separations compared to the radius that the progenitor giant must have once had. As a solution to this riddle, Paczynski (1976) proposed that the giant star may engulf the secondary star during its expansion, a common envelope forms around the giant core and the companion, and the secondary spirals in due to frictional drag in the envelope. The decrease in orbital separation releases gravitational binding energy of the binary via drag and may thus lead to an ejection of the envelope. This can explain the loss of energy and angular momentum necessary to form such a close binary system. A similar idea was proposed by Sparks & Stecher (1974) in connection with supernovae.

After the first ideas were set out, it became clear that this common envelope (CE) phase plays an important role in binary stellar evolution in order to explain compact stars in close binary systems, such as, e.g., close WD and main sequence (MS) binaries (Schreiber & Gänsicke, 2003; Zorotovic et al., 2010), CVs (King, 1988; Ritter, 2012), double white dwarfs (Iben & Tutukov, 1985; Han et al., 1995; Nelemans et al., 2001b), low-mass X-ray binaries (Lewin et al., 1997), subdwarf B binaries (Han et al., 2002, 2003; Heber, 2009), binary central stars of planetary nebulae (PNe, De Marco, 2009), and the progenitor systems of Type Ia supernovae (Iben & Tutukov, 1984; Belczynski et al., 2005). Since the in-spiralling star may also merge with the core of the primary, the origin of some peculiar single stars was linked to the CE phase; examples include FK Comae stars (Bopp & Stencel, 1981) and Thorne–Żytkow objects (Thorne & Żytkow, 1977).

A CE event can be subdivided in different phases (see, e.g., Ivanova et al., 2013b), but the ejection mechanism and the transitions between different phases are still unknown. The CE phase can be sketched as follows: it can be initiated for low-mass companions by a tidal instability driving the companion into the giant envelope or by mass transfer that accelerates to the dynamical timescale due to the reaction of the deep convective envelope. This is followed by the dynamical spiral-in that is caused by gravitational drag and that features complex, multi-dimensional flows. At the end of the dynamical spiral-in, the evolution can slow down to proceed on a thermal timescale where the envelope structure adapts to the input of gravitational drag luminosity. At some point, the envelope is ejected and a close binary or a merger of the giant core and the companion can result. After the ejection, there may be still interaction with parts of the envelope. Finally, a wind of the hot central star can lead to the formation of a planetary nebula with a binary nucleus.

For an overview of existing simulations and observations regarding the CE phase, the reviews by Iben & Livio (1993), Taam & Sandquist (2000), and Ivanova et al. (2013b) can be recommended.

---

[4]Algol was identified as an eclipsing binary system by Pickering (1880).

1.2 Previous Work on the Common Envelope Phase

After the idea of CE evolution had been proposed by Paczynski (1976), first simulations of this interaction were conducted in one dimension in spherical symmetry using stellar evolution codes (Taam et al., 1978; Meyer & Meyer-Hofmeister, 1979; Delgado, 1980; Livio & Soker, 1984a,b; Soker et al., 1984). In these models, gravitational drag is included by injecting the luminosity as calculated using the Bondi–Hoyle accretion theory (Bondi & Hoyle, 1944) and by changing the position of the companion accordingly. In these simulations, no significant amount of mass is ejected because the frictional energy is transported efficiently to the surface and radiated away. This is due to the injection of the frictional energy in a spherical shell instead of a local injection owing to the spherical symmetry of the modeling approach. Meyer & Meyer-Hofmeister (1979) determined the duration of the CE phase to $\lesssim 1000$ yr, much smaller than typical evolutionary timescales of stars.

The gravitational drag exerted on the companion during its passage through the envelope leads to a conversion of gravitational binding energy of the binary system to internal and kinetic energy of the envelope finally ejecting the envelope. This led Webbink (1984) to introduce an approximation for the final separation of the system by equating the differences in orbital energy to the binding energy of the envelope (for more details, see Sec. 2.5). An efficiency factor α is introduced that accounts for the fact that not the whole orbital energy can be used for ejecting the envelope. This treatment is still in use today for binary evolution calculations and binary population synthesis studies.

The assumption of spherical symmetry was lifted in multi-dimensional simulations (2D: Bodenheimer & Taam, 1984; Taam & Bodenheimer, 1989; Livio et al., 1990; Taam & Bodenheimer, 1991; Yorke et al., 1995; Taam et al., 1994, 3D: de Kool, 1987; Livio & Soker, 1988; Terman et al., 1994, 1995; Terman & Taam, 1996; Rasio & Livio, 1996; Sandquist et al., 1998, 2000; De Marco et al., 2003a,b; Ricker & Taam, 2008, 2012; Passy et al., 2012; Nandez et al., 2014, 2015; Staff et al., 2016a,b; Iaconi et al., 2016; Ohlmann et al., 2016). These simulations show that mass ejection is possible and occurs primarily near the orbital plane. This is caused by the local injection[5] of gravitational drag luminosity opposed to the spherical treatment in one dimension. Although the envelope is not ejected during these simulations, its ejection seems possible and the efficiency of converting the orbital energy is estimated to be quite low (0.15 to 0.6, see, e.g., Taam & Sandquist, 2000). The CE interaction seems to result in a merger for a primary that is not very evolved (i.e., still in the Hertzsprung gap) or for a very low-mass companion (Iben & Livio, 1993). The first case is due to the giant structure: the core is not compact enough, thus, the density gradients around the core are not steep enough to halt the spiral-in which is the case for more evolved giants. For the second case, a low-mass companion, the orbital energy of the system can be to little to unbind the envelope.

Moreover, multi-dimensional simulations established the presence of spiral shocks caused by both the companion and the core of the giant (depending on the mass ratio, Sandquist et al., 1998, 2000; Ricker & Taam, 2012) that lead to non-local transport of energy and angular momentum. Some mass is ejected during the first orbit in a spiral stream (Sandquist et al., 1998, 2000; Ohlmann et al., 2016). Ejecting the rest of the envelope takes much longer and is not completed on the simulated dynamical timescales. As assumed in the one-dimensional simulations, gravitational drag is much larger than hydrodynamical drag, although the Bondi–Hoyle formula overestimates the drag force (Ricker & Taam, 2008, 2012). Energy from recombination of H and He has long been

---

[5]The injection is parametrized in two-dimensional simulations and occurs in tori for axisymmetric simulations. For the three-dimensional simulations, the gravitational interaction between the point mass and the gas injects this energy locally.

discussed to be important for the ejection of the envelope (e.g., Livio, 1989). Recent simulations claim to reach envelope ejection when including this energy (Nandez et al., 2015), but this is still to be confirmed by a detailed analysis and using different numerical methods.

Up to now, multi-dimensional simulations have been unable to cover the whole CE phase including the ejection of the envelope. Hence, it is difficult to constrain properties such as the ejection efficiency. Another way to approach the problem of estimating this efficiency is simulating large populations of binary stars using approximate stellar evolution tracks, a technique called binary population synthesis.[6] By following the binary interactions and the evolution of the single stars using approximate prescriptions, numbers and properties of different classes of binary systems can be obtained and compared to observations. A major source of uncertainty in this modeling approach, however, is the treatment of the CE phase: depending on the parametrization, the delay times and rates of Type Ia supernovae differ significantly (e.g., Ruiter et al., 2011).

The evolutionary history of Type Ia supernovae – thermonuclear explosions of WDs – is very complex, involving several mass transfer phases (Iben & Tutukov, 1984). To constrain properties of the CE phase, systems are well suited that undergo only one CE phase. A good example for such systems are post-CE binaries (PCEBs) consisting of a WD and a MS star in a close orbit. These systems are progenitors of CVs (Ritter, 1986) and observed samples exist (Schreiber & Gänsicke, 2003; Zorotovic et al., 2011). Binary population synthesis studies of these systems (e.g., Davis et al., 2010; Toonen & Nelemans, 2013) point to low values of the ejection efficiency. Another promising approach tries to reconstruct the evolutionary history of single systems in a sample to estimate the pre-CE properties of the original system (Zorotovic et al., 2010; De Marco et al., 2011; Davis et al., 2012). These studies find that global values for α of about 0.2-0.3 can reproduce the reconstructed parameters of the observed PCEB systems.

The situation is, however, less clear and more complex for the case of double white dwarf binaries. Nelemans et al. (2000) could only explain the formation of double helium white dwarfs if they assume that in the first mass-transfer episode the envelope is lost without spiral-in, leading to a system with larger orbital energy. They introduce a parametrization based on conservation of angular momentum rather than energy to compute the final separation after the first mass transfer episode between low-mass binaries of similar mass. With this parametrization, subsequent population synthesis studies (Nelemans et al., 2001b,a; Nelemans & Tout, 2005) improved in reproducing observed sample properties of double white dwarfs. There is, however, no underlying physical model of this parametrization and Webbink (2008) suspected that the first episode of mass transfer in these double white dwarfs proceeds rather slowly on a thermal or nuclear timescale. Thus, the evolutionary model for these systems still lacks a physical description.

1.3 What Can Still Be Learned?

Despite more than three decades of modeling, a sound physical understanding of the mechanism of envelope ejection during a CE phase has not been reached. The reason is that modeling this phase is difficult because of the wide range in temporal and spatial scales that are involved and because of the necessity of a three-dimensional treatment. To reduce the range in scales, the giant core and

---

[6]See, e.g., the description in Nelemans (2010); different codes have been developed to tackle the problem (Kornilov & Lipunov, 1983; Dewey & Cordes, 1987; Lipunov & Postnov, 1988; de Kool, 1990; Yungelson & Tutukov, 1991; Kolb, 1993; Pols & Marinus, 1994; Portegies Zwart & Verbunt, 1996; Vanbeveren et al., 1997; Fryer et al., 1998; Nelemans et al., 2001b; Hurley et al., 2002; Han et al., 2003; Belczynski et al., 2008). Four different binary population synthesis codes are compared by Toonen et al. (2014) for similar physics assumptions.

the companion are usually approximated as point masses that interact only gravitationally. The influence of the numerical method on the evolution, especially modeling the interaction of these point masses with the envelope gas, is still poorly understood; only recently, different resolutions were studied and different methods compared (Passy et al., 2012). It is also still unclear on which scales transport and conversion processes in the envelope and surrounding the cores operate and how these can be resolved properly.

Furthermore, the question remains still open whether energy reservoirs other than the orbital energy of the binary can be tapped to enhance the ejection of the envelope. First simulations indicate that recombination of H and He may help ejecting the envelope (Nandez et al., 2015), but a more detailed analysis is necessary to understand the ejection mechanism. Nuclear energy may be tapped by influencing the H burning shell around the core, but modeling this fails currently at the discrepancy in spatial scales. Magnetic fields have been proposed to be amplified in a dynamo process during a CE phase (e.g., Regős & Tout, 1995) with implications for magnetic fields in WDs and CVs (Tout et al., 2008), but the dynamical evolution during the spiral-in has not been considered so far.

Because simulations have not been able to provide a physical model so far, parametrizations of the CE phase have been mainly constrained by analyzing observed systems and by comparing population synthesis models to samples of binary stars. Making better predictions using these methods would, however, require a parametrization that is calibrated using simulations – which is the long-term goal of this work.

1.4 Goals of This Work

Much of the common envelope phase still remains in the dark. The main goal of this thesis is to model this long-standing problem of binary stellar evolution to shed some light on the CE phase. Specifically, we aim at answering the following questions:

1. Current methods for simulating the CE phase have limitations regarding resolution and convergence. The new moving-mesh code AREPO combines advantages of different modeling approaches: for example, it shows only small numerical diffusion, conserves angular momentum well, and its mesh can be refined on arbitrary criteria. How can we apply this new method to the CE phase to benefit from its improved modeling capabilities? How can we generate stable models of giant envelopes that are needed as initial conditions for simulating the CE phase?

2. Due to the wide range in temporal and spatial scales, approximations are mandatory. What is the nature of the errors these approximations introduce? How can convergence be achieved? How sensitive is the method to changes of the initial conditions, such as mass ratio, rotational state, or initial separation?

3. During the spiral-in, energy and angular momentum are transferred from the binary system of the giant core and the companion to the gas of the envelope. Which processes are responsible for the transfer of energy and angular momentum and its redistribution in the envelope? Are we able to resolve the corresponding spatial scales?

4. Magnetic fields are discussed to be potentially important during CE phases, but up to now, they have been neglected in detailed simulations. How do magnetic fields evolve during the dynamical part of the CE phase?

5. Energy from recombination has been long discussed to possibly help ejecting the envelope. How does the ionization state of the gas influence the evolution of the CE phase? Can recombination energy be released in order to drive the envelope ejection?

6. The most important physics during the CE phase is the combination of hydrodynamics and gravity. How can we further improve the modeling of gravitational flows using a better coupling of gravity to hydrodynamics?

1.5 Outline

The outline of this dissertation is as follows: first, the theoretical foundations of physical processes important during the CE phase are introduced in Chapter 2, and the numerical methods for solving the corresponding equations are described in Chapter 3. After this, we describe the new method that allows us to go beyond the state of the art of modeling the dynamical part of CE phases. The problem of creating initial conditions for the CE phases is tackled in Chapter 4; approximations to giant atmospheres are introduced and it is shown how stable representations in hydrodynamics simulations can be obtained. Then, in Chapter 5, we present the first CE simulation on a moving mesh. To better understand the numerical modeling, different initial conditions are explored in Chapter 6, including convergence studies.

After having established the method, we extend it to test the relevance of other physical processes, such as magnetic fields or recombination. The results of the first magnetohydrodynamic simulations of the CE phase are presented in Chapter 7. Transport processes of energy and angular momentum are examined in Chapter 8, including the impact of magnetic fields. Next, we include a description of the ionization state to study the impact of releasing recombination energy on the CE evolution in Chapter 9. To further improve the modeling of gravitational flows, as needed in CE simulations, a new scheme for solving hydrodynamics with gravity is proposed and first steps towards its implementation are shown in Chapter 10. We end with conclusions in Chapter 11.

Chapter 2

Theoretical Foundations

In this chapter, a brief overview of the physics is given that is important for the processes during a common envelope event. The flow of stellar plasma during a CE phase can be described macroscopically using the theory of hydrodynamics combined with gravity and potentially with magnetic fields (Sec. 2.1). Thermodynamic relations are important to understand the behaviour of stellar plasma in different regimes, including a treatment of the ionization state of the plasma (Sec. 2.2). Radiation (Sec. 2.3) plays an important role when trying to link the simulations of a CE phase to an optical display. A short account of single star evolution is given in Sec. 2.4, up to evolved giant stages that precede CE phases. A brief overview of the impact of introducing a companion star on the evolution of binary systems is given in Sec. 2.5. The CE phase is described as a special interaction in binary systems in Sec. 2.6.

2.1 Hydrodynamics

The theory of hydrodynamics describes the macroscopic motion of fluids. Since fluids consist of atoms or – in a plasma – of ions and electrons, the treatment of these particles as a macroscopic fluid is justified when the following two conditions are fulfilled (Müller, 1998): first, the microscopic behaviour of the particles must be negligible, i.e., their mean free path must be much smaller then a characteristic length scale of the system. In this case, a fluid element can be defined as a small part of the fluid volume where the fluid is in local thermodynamic equilibrium and where the thermodynamic quantities are averaged over this element. Second, only short range forces are admitted between the particles, otherwise they have to be taken into account additionally as an external force to include also collective effects. Such long range forces include gravity and electromagnetism, although electromagnetic interactions are screened in electrically neutral systems and possess short range character there.

These conditions are fulfilled for the stellar plasma of giant envelopes that are modeled during a CE phase: the mean free path of photons is of the order of centimeters, and the collisional mean free path of the plasma particle is several orders of magnitude smaller (Kippenhahn et al., 2012). This is clearly much smaller than the length scale of the stars (10^{12} cm to 10^{13} cm) and also much smaller than the fluid volumes on the discretized grid. Thus, thermodynamic equilibrium is well fulfilled in these fluid elements. Gravity is included as an external long range force by adding the corresponding terms as source terms to the hydrodynamic equations.

2.1.1 The equations of hydrodynamics

As the conditions mentioned above are met under the conditions we are interested in, the state of the fluid can be described by the thermodynamic quantities and the velocities that depend on

space and time. The evolution of these quantities in time is governed by balance equations for mass, momentum, and energy, the *Navier–Stokes equations* (see textbooks on hydrodynamics, e.g, Batchelor, 2000; Landau & Lifshitz, 1987),

$$
\frac{\partial \rho}{\partial t} + \nabla(\rho \boldsymbol{v}) = 0,
$$
$$
\frac{\partial \rho \boldsymbol{v}}{\partial t} + \nabla(\rho \boldsymbol{v} \otimes \boldsymbol{v} + p\mathbf{I}) = \rho f + \nabla \boldsymbol{\sigma}, \tag{2.1}
$$
$$
\frac{\partial \rho e_{\text{tot}}}{\partial t} + \nabla(\boldsymbol{v}(\rho e_{\text{tot}} + p)) = \rho \boldsymbol{v} f + \rho Q + \nabla(\boldsymbol{v}\boldsymbol{\sigma}),
$$

where ρ denotes the density of the fluid, $\boldsymbol{v}$ the velocity, p the pressure, $e_{\text{tot}} = \epsilon/\rho + \boldsymbol{v}^2/2$ the total specific energy (ϵ: internal energy density), f an external force (e.g., gravity, cf. Sec. 2.1.2), Q an additional energy source (e.g., nuclear reactions) and $\boldsymbol{\sigma}$ the stress tensor due to viscosity:

$$
\sigma_{ij} = \kappa \nabla \boldsymbol{v} \delta_{ij} + \mu \left(\frac{\partial v_i}{\partial x_j} + \frac{\partial v_j}{\partial x_i} - \frac{2}{3} \nabla \boldsymbol{v} \delta_{ij} \right). \tag{2.2}
$$

Here, δ_{ij} is the Kronecker delta, κ the bulk viscosity, and μ the shear viscosity. As these equations show, mass is always conserved; momentum is only conserved if the force is conservative and can be written as the gradient of a potential. Stress due to viscosity leads only to a transport of momentum, not to dissipation. The total energy is also only conserved if the force is conservative and if $Q = 0$. The viscous term leads to a redistribution of energy and does not dissipate energy.

The Navier–Stokes equations (2.1) can be non-dimensionalized by dividing all quantities by combinations of a characteristic length scale L and a characteristic velocity V. This leads to the occurence of the dimensionless *Reynolds number*,

$$
\text{Re} = \frac{\rho L V}{\mu}, \tag{2.3}
$$

which is a measure for the ratio of inertial to viscous forces. Different hydrodynamical flows with similar Reynolds number show similar dynamical behaviour: for small Reynolds numbers, viscous forces dominate, resulting in laminar flows. For large Reynolds numbers, however, inertial forces dominate and non-linear behaviour and turbulent motions can result.

For many astrophysical systems, the dynamical viscosity μ/ρ of the material is similar to materials on Earth, but the length and velocity scales are orders of magnitude larger than usual values on Earth. This leads to very large Reynolds numbers for many astrophysical systems, including the stellar plasma in CE simulations, and viscous forces are small compared to inertial forces. Thus, when modeling hydrodynamic flows in astrophysical systems, the viscous shear tensor is usually neglected ($\mu, \kappa \to 0$). Taking this limit yields the *Euler equations*,

$$
\frac{\partial \rho}{\partial t} + \nabla(\rho \boldsymbol{v}) = 0,
$$
$$
\frac{\partial \rho \boldsymbol{v}}{\partial t} + \nabla(\rho \boldsymbol{v} \otimes \boldsymbol{v} + p\mathbf{I}) = \rho f, \tag{2.4}
$$
$$
\frac{\partial \rho e_{\text{tot}}}{\partial t} + \nabla(\boldsymbol{v}(\rho e_{\text{tot}} + p)) = \rho \boldsymbol{v} f + \rho Q,
$$

that are usually solved in the context of astrophysical fluid dynamics instead of the full Navier–Stokes equations (2.1). Hence, the numerical methods as described in Chapter 3 discretize this

system of equations. The Euler equations are a system of hyperbolic partial differential equations, in contrast to the Navier–Stokes equations that possess a parabolic part due to the viscous terms. Thus, they have different mathematical properties and have to be discretized in a different way than the hyperbolic Euler equations.

The sets of equations (2.1) and (2.4) consist of five equations for the six quantities ρ, $\boldsymbol{v}$ (three components), e_{tot}, and p. Thus, an additional equation is needed in order to close the system: the equation of state relating the thermodynamic quantities as some equation $f(\rho, e_{\text{tot}}, p) = 0$ (see also Sec. 2.2.2). The other quantities f, Q, κ, and μ depend on the material and are given functions of the thermodynamic quantities.

2.1.2 Gravity

One important force that has to be included as a source term in the Euler equations for simulations of the CE phase is gravity. The most general theory of gravity is general relativity that explains gravitational forces as a result of distortions in spacetime. In the stars we are interested in, however, the gravitational fields are weak enough such that the Newtonian description – which is a limiting case of the Einstein equations of general relativity – is completely adequate. When treating stars as macroscopic fluids (see also Sec. 2.1 and 2.2), the mass density ρ causes a gravitational field Φ that can be computed using the Poisson equation

$$\Delta\Phi = 4\pi G\rho, \tag{2.5}$$

where G is the gravitational constant. The gravitational acceleration is then given by $\boldsymbol{g} = \nabla\Phi$.

The elliptic partial differential equation (2.5) can be solved using the Greens function of the Laplace operator,

$$\Phi(\boldsymbol{r}) = G \int \mathrm{d}^3 r' \frac{\rho(\boldsymbol{r}')}{|\boldsymbol{r} - \boldsymbol{r}'|}, \tag{2.6}$$

with the boundary condition that the potential vanishes at infinity.

2.1.3 Magnetic fields

Throughout the Universe, magnetic fields are common and many astrophysical objects can only be explained by the presence of magnetic fields. Examples range from Sun spots to jets in active galaxies to pulsars. For CE simulations, magnetic fields have been discussed to be important (see Sec. 7.1), but no hydrodynamics simulations exist that include magnetic fields. In order to include magnetic fields in the hydrodynamical treatment of the astrophysical plasma, the mean free path of the particles must be small compared to the Debye length that is a measure of the length scale of electrostatic effects (Shore, 2007). This means that the plasma is electrically neutral without internal electrical fields, and the current can be determined by the magnetic field only. This is usually well fulfilled for the hot and dense plasma of stellar gas. In this limit, the Navier–Stokes equations (2.1) can be combined with the Maxwell equations, leading to the equations of *magnetohydrodynamics*

(MHD, e.g., LeVeque, 1998),

$$\frac{\partial \rho}{\partial t} + \nabla(\rho \boldsymbol{v}) = 0,$$

$$\frac{\partial \rho \boldsymbol{v}}{\partial t} + \nabla(\rho \boldsymbol{v} \otimes \boldsymbol{v} + (p + \frac{1}{2}\boldsymbol{b}^2)\mathbf{I} - \boldsymbol{b} \otimes \boldsymbol{b}) = \rho \boldsymbol{f} + \nabla \boldsymbol{\sigma},$$

$$\frac{\partial \rho \tilde{e}_{\text{tot}}}{\partial t} + \nabla(\boldsymbol{v}(\rho \tilde{e}_{\text{tot}} + p + \frac{1}{2}\boldsymbol{b}^2 - \boldsymbol{b} \otimes \boldsymbol{b})) = \rho \boldsymbol{v} \boldsymbol{f} + \rho Q + \nabla(\boldsymbol{v} \boldsymbol{\sigma}), \tag{2.7}$$

$$\frac{\partial \boldsymbol{b}}{\partial t} + \nabla(\boldsymbol{v} \otimes \boldsymbol{b} - \boldsymbol{b} \otimes \boldsymbol{v}) = \eta \nabla^2 \boldsymbol{b},$$

$$\nabla \boldsymbol{b} = 0,$$

where $\boldsymbol{b} = \boldsymbol{B}/\sqrt{4\pi}$ denotes the rescaled magnetic field $\boldsymbol{B}$, $\tilde{e}_{\text{tot}} = e_{\text{tot}} + \boldsymbol{b}^2/(2\rho)$ the total energy including the magnetic energy, and η the resistivity of the medium. The resistivity η leads to a decay of the magnetic field due to Ohmic dissipation.

The number of equations increases by three for the three components of the magnetic field, that have to fulfill in addition the divergence constraint $\nabla \boldsymbol{b} = 0$. The magnetic field enters the momentum and energy equations in form of an additional isotropic pressure $\boldsymbol{b}^2/2$ and a shear tensor $\boldsymbol{b} \otimes \boldsymbol{b}$. Similar to the Reynolds number including viscosity (cf. Eq. 2.3), the *magnetic Reynolds number* can be defined as a dimensionless quantity,

$$\text{Re}_{\text{m}} = \frac{LV}{\eta}, \tag{2.8}$$

where L and V give characteristic length and velocity scales. This number is large for astrophysical objects because of their huge dimensions; consequently, the dissipation term is often neglected. If the viscous terms are also neglected, this yields the equations of *ideal magnetohydrodynamics* that are often used for modeling astrophysical plasmas. Because of these reasons, we solve the ideal MHD equations to treat the effect of magnetic fields in CE phases. The corresponding numerical methods are described in Sec. 3.2.2, and the MHD simulations are presented in Chapter 7.

2.2 Thermodynamics

Thermodynamics describes equilibrium states of macroscopic systems of matter and is based on the observation that stable configurations of matter exist in Nature (for a textbook on thermodynamics, see, e.g., Reichl, 2009, or in general Joos, 1945). One part of thermodynamics is a phenomenological theory based on four principles: thermodynamic equilibrium is transitive; energy is conserved; entropy can only increase; the entropy of a fluid or solid is zero at zero temperature. With only these principles, a plethora of macroscopic phenomena can be explained. The microscopic part of thermodynamics uses statistical physics which has its roots in the quantum nature of single particles in order to understand these laws from a deeper point of view.

2.2.1 Thermodynamic relations

The first law of thermodynamics, the conservation of energy, may be stated in differential form as

$$dU = \delta Q - p dV + \sum_i \mu_i dN_i, \tag{2.9}$$

where dU is the change of internal energy of the corresponding system, δQ the change in heat[1], p the pressure of the system and V the volume. μ_i gives the chemical potential of species i, dN_i the change in number of species i. The term pdV describes the mechanical work.

The second law of thermodynamics, the increase of entropy, is given as

$$dS = \frac{\delta Q}{T} \geq 0, \tag{2.10}$$

where dS denotes the change in entropy and where the equal sign stands for reversible processes. Combining this with the first law gives

$$dU = TdS - pdV + \sum_i \mu_i dN_i. \tag{2.11}$$

The state of the system is fixed by two thermodynamic quantities when the composition is known. If the energy U is known as a function of entropy S, volume V, and numbers N_i, we can derive from Eq. (2.11) (cf. Reichl, 2009, Sec. 3.4) the thermal equation of state,

$$T = \left.\frac{\partial U}{\partial S}\right|_{V, N_i}, \tag{2.12}$$

the mechanical equation of state,

$$p = -\left.\frac{\partial U}{\partial V}\right|_{S, N_i}, \tag{2.13}$$

and the chemical equation of state,

$$\mu_i = \left.\frac{\partial U}{\partial N_i}\right|_{S, V, N_{j, j \neq i}}. \tag{2.14}$$

In stellar astrophysics, the use of mass density ρ is more convenient than the use of volume; moreover, the extensive quantities (e.g., U, S) are usually given as specific quantities, i.e., per unit mass. The specific heat for a system at constant volume, c_V, or constant pressure c_p, is given by

$$c_V = \left.\frac{\delta Q}{dT}\right|_V, \quad \text{or} \quad c_p = \left.\frac{\delta Q}{dT}\right|_p. \tag{2.15}$$

They are related by (eg. Weiss et al., 2004, Eq. 9.86)

$$c_p - c_V = \frac{p}{\rho T} \frac{\chi_T^2}{\chi_\rho}, \tag{2.16}$$

where $\chi_T = (\partial \ln P / \partial \ln T)_\rho$ and $\chi_\rho = (\partial \ln P / \partial \ln \rho)_T$. The ratio of specific heats is $\gamma = c_p / c_V$.

For adiabatic changes, i.e., $\delta Q = 0$ (these are also isentropic $dS = 0$ and reversible), one can define the adiabatic exponents (Weiss et al., 2004, Eq. 9.88)

$$\Gamma_1 = \left.\frac{d \ln p}{d \ln \rho}\right|_{ad}, \quad \frac{\Gamma_2}{\Gamma_2 - 1} = \left.\frac{d \ln p}{d \ln T}\right|_{ad}, \quad \Gamma_3 - 1 = \left.\frac{d \ln T}{d \ln \rho}\right|_{ad}. \tag{2.17}$$

These quantities are interesting for processes in stellar interiors: Γ_1 is related to dynamical instabilities and the propagation of sound waves. Γ_2 is important for convective instability in stars (especially important for the giant envelopes in CE phases, see also Sec. 2.4.3), Γ_3 is related to pulsational instabilities.

---

[1]Since the differential of the heat function is not a total differential, the symbol δQ is used.

2.2.2 Equation of state

For an ideal gas, the mechanical equation of state is given by

$$p = \frac{R}{\mu}\rho T, \tag{2.18}$$

where $R = 8.31 \times 10^7 \, \mathrm{erg\,K^{-1}\,g^{-1}}$ is the universal gas constant and μ the dimensionless molecular weight. For a completely ionized gas consisting of mass fractions X_i of different nuclei of type i (Z_i: charge number, μ_i: atomic weight), the contributions of electrons and nuclei add up to a total pressure as in Eq. (2.18) with mean molecular weight μ given by

$$\frac{1}{\mu} = \sum_i \frac{X_i(1 + Z_i)}{\mu_i}. \tag{2.19}$$

The thermal equation of state for a monatomic gas is given by

$$u = \frac{3}{2}\frac{R}{\mu}T, \tag{2.20}$$

where u denotes the specific internal energy. In this case, the gamma coefficients defined in the previous section are all equal: $\gamma = \Gamma_1 = \Gamma_2 = \Gamma_3 = 5/3$.

Usually, in addition to the plasma in a star, radiation is present. If the radiation is assumed to be in equilibrium with the plasma at the same temperature T, the black body law integrated over all frequencies gives an additional component to pressure and internal energy (cf. Eq. (2.34)), resulting in

$$p = \frac{R}{\mu}\rho T + \frac{a}{3}T^4,$$
$$u = \frac{3}{2}\frac{R}{\mu}T + a\frac{T^4}{\rho}, \tag{2.21}$$

with the radiation constant

$$a = \frac{8\pi^5 k^4}{15c^3 h^3} \tag{2.22}$$

(k: Boltzmann constant, c: speed of light, h: Planck constant). The ratio of gas pressure to total pressure is called $\beta = p_\mathrm{g}/p$ and its departure from one shows the importance of radiation pressure. For main sequence stars, one can show that this starts to play a role only for stars with masses larger than two to three solar masses (see Weiss et al., 2004, Table 11.1). In cool stars, such as the red giants comprising the initial state in CE phases, radiation pressure is only important in the interior, where the temperature is larger.

Other effects altering the ideal gas behaviour include electrostatic corrections due to shielding in the plasma. Furthermore, for higher densities and temperatures, the electrons in the plasma form a degenerate gas, thus altering the equation of state. Another influence is due to the ionization state of the plasma that may change from being completely ionized especially for lower temperatures and densities to partial ionization (see Sec. 2.2.3), which can be important during CE evolution (see Chapter 9).

All these effects can be taken into account using complicated calculations; for stellar evolution calculations or hydrodynamic simulations one usually uses pre-computed tables. For the hydrodynamic simulations of CE phases in this work, either an ideal gas equation of state or the OPAL equation of state (Rogers et al., 1996; Rogers & Nayfonov, 2002) is used. It is based on an expansion of the grand canonical partition function and includes ionization effects.

2.2.3 Ionization

In a gas of atoms of a certain chemical element, some of the atoms may be in different ionization and excitation states. The treatment in this section follows Kippenhahn et al. (2012, Sec. 14). The number density of atoms in an excited state s having a degeneracy factor g_s depends on the energy difference ψ_s to the ground state and is given by the Boltzmann factor

$$\frac{n_s}{n_0} = \frac{g_s}{g_0} e^{-\frac{\psi_s}{kT}}, \tag{2.23}$$

where the quantities with index 0 stand for the ground state. If one considers the ionization of an r-fold ionized atom to an $(r + 1)$-fold ionized atom, one has to integrate over all possible continuum states of the released electron. In addition, all excited states of each ionization state have to be taken into account. This yields the *Saha equation* for element i (cf. Kippenhahn et al., 2012, Eq. 14.17),

$$\frac{n_{r+1}^{(i)}}{n_r^{(i)}} \frac{E}{E + 1} = \frac{u_{r+1}^{(i)}}{u_r^{(i)}} \frac{2}{p_g} \frac{(2\pi m_e)^{3/2} (kT)^{5/2}}{h^3} e^{-\frac{\chi_r^{(i)}}{kT}} \equiv K_r^{(i)}, \tag{2.24}$$

where $E = n_e/n$ denotes the electron number fraction, u_r the partition function of the ionization state r, p_g the gas pressure, m_e the electron mass, and $\chi_r^{(i)}$ the energy difference between the ionization states r and $r + 1$ of element i. Since E depends on the ionization states of all elements considered, the equations for all elements i are coupled.

For the envelopes of red giants or AGB stars with low to intermediate masses (that are the initial models for CE evolution), the most important elements that undergo partial ionization are hydrogen and helium. This system consists of five species (H, H^+, He, He^+, He^{2+}) and the electron fraction E. The three Saha equations for the three ionization stages are given by

$$\frac{x_1^H}{x_0^H} \frac{E}{E + 1} = K_0^H, \quad \frac{x_1^{He}}{x_0^H} \frac{E}{E + 1} = K_0^{He}, \quad \frac{x_2^{He}}{x_1^H} \frac{E}{E + 1} = K_1^{He}, \tag{2.25}$$

with the number fractions x_r. The electron fraction is

$$E = (X x_1^H + \frac{Y}{4}(x_1^{He} + 2 x_2^{He}))\mu_0 \tag{2.26}$$

where the chemical composition in mass fractions is X and Y for hydrogen and helium, and $\mu_0 = 1/(X + Y/4) = \mu(1 + E)$ is the average particle mass per nucleus. These four equations are complemented by equations for the conservation of particle numbers,

$$x_0^H + x_1^H = 1, \quad x_0^{He} + x_1^{He} + x_2^{He} = 1. \tag{2.27}$$

These equations can now be solved for the ionization state of the plasma.

The contribution to the specific internal energy, the ionization energy, is (Kippenhahn et al., 2012, Eq. 14.42)

$$u_{\text{ion}} = \sum_i \frac{X_i}{\mu_i m_u} \sum_{r=0}^{Z_i} x_r^{(i)} \sum_{s=0}^{r-1} \chi_s^{(i)}, \tag{2.28}$$

where X_i is the mass fraction of element i and m_u the atomic mass number. The last sum is necessary as the χ values are defined only as the energy difference between neighbouring ionization states. For the hydrogen-helium mixture, this yields (Kippenhahn et al., 2012, Eq. 14.33)

$$u_{\text{ion}} = \frac{1}{m_u} \left\{ X x_1^H \chi_0^H + \frac{Y}{4} \left[x_1^{He} \chi_0^{He} + x_2^{He}(\chi_0^{He} + \chi_1^{He}) \right] \right\}. \tag{2.29}$$

The impact of partial ionization on various thermodynamics quantities can be computed from this (cf. Weiss et al., 2004, Sec. 9.18). The different gammas from Eq. 2.17 have similar values, they are smaller for partial ionization compared to the value of 5/3 for a monoatomic ideal gas that is completely ionized or completely neutral, ranging down to ~ 1.1 for a pure hydrogen gas (Weiss et al., 2004). This also means that the adiabatic gradient $\nabla_{\mathrm{ad}} = (\Gamma_2 - 1)/\Gamma_2$ decreases and thus changes the stability properties of stratifications (cf. Sec. 2.4.3): convection ensues also for smaller temperature gradients. Moreover, the specific heat increases up to a factor for 20–30 for hydrogen ionization (Weiss et al., 2004). This means that work that is done on the system (e.g., in the form of adiabatic compression) or heat that is fed into the system goes primarily into the ionization of the gas and not into thermal or kinetic energy.

2.3 Radiation

Electromagnetic radiation that is emitted from a star determines its observational properties. To link CE simulations to an optical display of the event that can possibly be observed, the radiation emitted from the plasma has to be modeled. Moreover, radiation plays an important role in transporting energy in stars.

The radiation field depends on space, time, a direction, and frequency. The information in this section is mainly taken from the book by Mihalas & Mihalas (1984). The specific intensity I of radiation is defined as the amount of energy dE that propagates in direction $\boldsymbol{n}$ through a surface dS in solid angle $d\Omega$ around $\boldsymbol{n}$ for a frequency range $d\nu$ during a time interval dt (Mihalas & Mihalas, 1984, Eq. 63.1),

$$dE = I(\boldsymbol{x}, t, \boldsymbol{n}, \nu)\boldsymbol{n} \cdot dS d\Omega d\nu dt. \tag{2.30}$$

Thus, the function I depends on seven parameters. The corresponding radiative energy is obtained by integrating over the solid angle,

$$E_\nu = E(\boldsymbol{x}, t, \nu) = \frac{1}{c} \int d\Omega I(\boldsymbol{x}, t, \boldsymbol{n}, \nu),$$
$$E(\boldsymbol{x}, t) = \int_0^\infty d\nu E(\boldsymbol{x}, t, \nu), \tag{2.31}$$

and the radiative flux by integrating over the first moment,

$$\boldsymbol{F}_\nu = \boldsymbol{F}(\boldsymbol{x}, t, \nu) = \int d\Omega \boldsymbol{n} I(\boldsymbol{x}, t, \boldsymbol{n}, \nu),$$
$$\boldsymbol{F}(\boldsymbol{x}, t) = \int_0^\infty d\nu \boldsymbol{F}(\boldsymbol{x}, t, \nu). \tag{2.32}$$

For radiation in thermal equilibrium, one can show that the specific intensity is given by Planck's law,

$$B_\nu(T) = \frac{2h\nu^3}{c^2} \frac{1}{e^{h\nu/(kT)} - 1}, \tag{2.33}$$

using methods of statistical physics for a Bose-Einstein gas of photons. This isotropic radiation leads to the well-known expressions for radiation energy and flux,

$$E(T) = aT^4, \quad F(T) = \frac{ac}{4\pi^2}T^4, \tag{2.34}$$

where the radiation constant is given by Eq. (2.22).

When interacting with matter, the intensity of radiation can change through absorption and emission processes (Mihalas & Mihalas, 1984, Sec. 6.3). Absorption is characterized by the extinction coefficient or opacity $\chi(\boldsymbol{x}, t, \boldsymbol{n}, \nu) = \rho \kappa(\boldsymbol{x}, t, \boldsymbol{n}, \nu)$ (κ: specific opacity), and the absorbed energy is proportional to χ and I. The mean free path of photons is given by $\chi^{-1} = (\kappa\rho)^{-1}$. The emission coefficient or emissivity is denoted $\eta(\boldsymbol{x}, t, \boldsymbol{n}, \nu) = \rho j(\boldsymbol{x}, t, \boldsymbol{n}, \nu)$ (j: specific emissivity), and the emitted energy is proportional to the emissivity. Both functions include effects due to scattering of light that may change its wavelength as well as "true" absorption and emission processes of the material (e.g., connected to atomic lines). The radiative transfer equation is now given by (Mihalas & Mihalas, 1984, Eq. 76.3)

$$\left(\frac{1}{c}\frac{\partial}{\partial t} + \frac{\partial}{\partial s}\right) I(\boldsymbol{x}, t, \boldsymbol{n}, \nu) = \eta(\boldsymbol{x}, t, \boldsymbol{n}, \nu) - \chi(\boldsymbol{x}, t, \boldsymbol{n}, \nu) I(\boldsymbol{x}, t, \boldsymbol{n}, \nu), \tag{2.35}$$

where the derivative with respect to s is taken along the ray path.

The optical depth τ between two points $\boldsymbol{x}$ and $\boldsymbol{x}'$ is obtained by integrating along the straight line between them (Mihalas & Mihalas, 1984, Eq. 77.1),

$$\tau_\nu(\boldsymbol{x}, \boldsymbol{x}') = \int_0^l \mathrm{d}s\, \chi(\boldsymbol{x} + s\boldsymbol{n}, \boldsymbol{n}, \nu), \tag{2.36}$$

where l denotes the distance between $\boldsymbol{x}$ and $\boldsymbol{x}'$. Since χ^{-1} gives the mean free path of the photons, τ_ν measures how many mean free paths correspond to the distance l.

For large optical depths – as, e.g, in the interior of stars –, the radiative transfer equation (2.35) may be approximated by a diffusion process. The effective radiative flux is given by

$$\boldsymbol{F} = -\frac{4ca}{3\chi_{\mathrm{R}}} T^3 \nabla T, \tag{2.37}$$

where χ_{R} is given by the Rosseland mean opacity (Mihalas & Mihalas, 1984, Eq. 80.9),

$$\frac{1}{\chi_{\mathrm{R}}} = \frac{\int_0^\infty \mathrm{d}\nu \frac{1}{\chi_\nu} \frac{\partial B_\nu}{\partial T}}{\int_0^\infty \mathrm{d}\nu \frac{\partial B_\nu}{\partial T}}. \tag{2.38}$$

The Rosseland mean opacity is a harmonic mean and thus dominated by the parts in the spectrum where $1/\chi_\nu$ is largest, i.e., by the most transparent parts. It ensures the correct energy transport and momentum balance in the diffusion limit. Thus, it is widely used for modeling stellar interiors. It will also be utilized to estimate the location of the photosphere in CE simulations as a first step towards connecting CE simulations to observations (Sec. 9.5).

Since the computation of opacities involves atomic structures and hence also requires atomic data, these are usually pre-computed as tables that can be used to interpolate to the desired values of density and temperature. For our computations, tables from the OPAL project (Iglesias & Rogers, 1996) and for lower temperatures the tables by Ferguson et al. (2005) are used (see Sec. 9.5).

2.4 Stellar Evolution

At the point where the CE phase commences, the primary star has evolved already from the beginning of nuclear burning in its interior to the giant stage. To compute the structure and

evolution of stars, they may be treated as self-gravitating, spherical, non-rotating balls of gas without magnetic fields to a first approximation. Ingredients that are important for describing stars include hydrostatic equilibrium, energy transport by radiation or convection, and energy conversion by nuclear reactions, neutrinos, and contraction or expansion.

2.4.1 Equations of Stellar Evolution

The content and notation in this section follows Kippenhahn et al. (2012) and the equations are given in the Eulerian frame using the radius as independent variable. In a stationary spherical configuration, the mass profile of the star is given by

$$\frac{\partial m(r, t)}{\partial r} = 4\pi r^2 \rho(r, t), \tag{2.39}$$

which is simply a consequence of the geometry. The spherical radius inside the star is denoted by r, ρ the density, and m the mass. The boundary condition is $m(0) = 0$. For the hydrostatic equilibrium, we need the gravitational acceleration that is given by $g = Gm(r)/r^2$ ($G = 6.673 \times 10^{-8}$ dyn cm^2 g^{-2}: gravitational constant) for a spherical mass distribution m. In hydrostatic equilibrium, this self-gravity balances the force resulting from the pressure gradient,

$$\frac{\partial p(r, t)}{\partial r} = -\frac{Gm(r, t)}{r^2} \rho(r, t), \tag{2.40}$$

with p denoting the pressure. Here, the boundary condition at the surface radius R is usually taken as $p(R) = 0$, but can be replaced by a more sophisticated treatment. These two equations, (2.39) and (2.40), describe the mechanical equilibrium of the star. These are two ordinary differential equations for the three quantities ρ, p, and m. To solve this system of equations, an additional relation has to be supplied: the equation of state, in general given as $\rho(p, T)$. For special cases of the equation of state, Eqs. (2.39) and (2.40) may be integrated analytically. An example class of analytical solutions are polytropes as solutions of the Lane–Emden equation (see, e.g., Kippenhahn et al., 2012) for a polytropic equation of state. Since the equation of state depends in general also on the temperature, the internal structure may not be determined by only considering the mechanical equilibrium, but also the thermal equilibrium that depends on energy sources or sinks and energy transport.

Let $l(r, t)$ be the net energy flux through a sphere of radius r, then energy conservation demands

$$\frac{\partial l(r, t)}{\partial r} = 4\pi r^2 \rho(r, t) \left(\varepsilon_n - \varepsilon_\nu + \varepsilon_g \right), \tag{2.41}$$

where the right hand side includes the energy change rates for nuclear reactions (ε_n), neutrino losses (ε_ν), and mechanical work due to contraction or expansion (ε_g). At the center of the star $l(0) = 0$, whereas at the surface $l(R) = L$ yields the total luminosity of the star. The shape of l depends on the distribution of energy sources and sinks throughout the star. The distribution of the temperature, however, depends on the way energy is transported in the star – either by radiation or by convection – and may be written as

$$\frac{\partial T(r, t)}{\partial r} = -\frac{Gm(r, t)}{r^2} \frac{T(r, t)}{p(r, t)} \nabla, \tag{2.42}$$

where $\nabla = \mathrm{d}\ln T / \mathrm{d}\ln p$ denotes the temperature gradient that depends on the energy transport mechanism. If energy transport by radiation dominates, a diffusion approximation leads to

$$\nabla_{\text{rad}} = \frac{3}{16\pi acG} \frac{\kappa lp}{mT^4},\tag{2.43}$$

where a denotes the radiation constant, c the speed of light, and κ the opacity (cf. Sec. 2.3). If, however, convection is the dominant energy transport mechanism, ∇ has to be supplied by a theory of convection, which is usually the mixing-length theory; in the deep interior it is usually near the adiabatic value ∇_{ad}.

The chemical composition is given by the mass fractions $X_i(r, t)$ for species i. These change due to nuclear reactions and due to mixing in convective regions,

$$\frac{\mathrm{d}X_i(r, t)}{\mathrm{d}t} = \frac{m_i}{\rho}\left(\sum_j r_{ji} - \sum_k r_{ik}\right),\tag{2.44}$$

where the derivative is taken in the Lagrangian frame to take into account mixing processes. Here, m_i denotes the mass of nucleus i, and r_{ij} the reaction rate from nucleus i to nucleus j. Moreover, the composition is assumed to be homogeneous in convective regions.

These equations govern the evolution of the star and are usually solved in the Lagrangian frame. They have to be closed by the equation of state giving the thermodynamic quantities, by the opacity, by the nuclear reaction rates and by the energy losses or gains due to neutrinos. These functions depend on pressure, temperature and composition of the material.

2.4.2 Timescales

During the evolution of a star, mainly three timescales are important (e.g., Kippenhahn et al., 2012). Usually the shortest timescale, the *hydrostatic timescale* gives a typical timescale for the propagation of perturbations of the hydrostatic equilibrium of the star. It can be approximated by the free fall time of the gas, yielding

$$t_{\text{hyd}} = \left(\frac{R^3}{GM}\right)^{1/2}.\tag{2.45}$$

On timescales longer than the hydrostatic timescale, the star is in mechanical equilibrium.

Another important timescale is the thermal or *Kelvin–Helmholtz timescale* that gives an estimate for the timescale of contraction or cooling. Assuming that the total luminosity of the star is only supplied by the gravitational energy of the gas yields

$$t_{\text{KH}} = \frac{|E_{\text{g}}|}{L} \approx \frac{GM^2}{2R}.\tag{2.46}$$

When the star evolves on a timescale longer than the Kelvin–Helmholtz timescale, it is in thermal equilibrium.

In most parts of stellar evolution the longest timescale is the *nuclear timescale* describing the change due to nuclear reactions,

$$t_{\text{n}} = \frac{E_{\text{n}}}{L},\tag{2.47}$$

where E_n denotes the total nuclear energy that may be released by the nuclear reactions in the corresponding phase.

For the longest part in a stellar life, namely during core H and He burning,

$$t_n \gg t_{KH} \gg t_{hyd}. \tag{2.48}$$

Thus, the evolution proceeds on the nuclear timescales and the star is in mechanical and thermal equilibrium.

These timescales are also important to estimate the timescale of mass transfer in binary systems (see Sec. 2.5); the mass transfer has to proceed on a hydrostatic or dynamical timescale for the initiation of a CE phase.

2.4.3 Stability of Stratifications

The stratification in parts of the star may be subject to hydrodynamical instabilities; most important is the convective instability that is caused by buoyancy (see textbooks, e.g., Weiss et al., 2004 or Kippenhahn et al., 2012). Suppose a fluid element embedded in a stellar profile rises adiabatically (i.e., with constant entropy). If at the new radius the buoyancy force is larger compared to the surroundings, the fluid element will rise further; thus, the stratification is unstable. The buoyancy force per unit volume is given by

$$\boldsymbol{F} = \boldsymbol{g} \cdot ((\nabla \rho)_e - (\nabla \rho)_s) \Delta r \hat{\boldsymbol{r}}, \tag{2.49}$$

where $\boldsymbol{g}$ denotes the gravitational acceleration, the indices denote the quantities in the element (e) and surrounding (s), Δr denotes the radial shift, and $\hat{\boldsymbol{r}}$ the unit vector in radial direction. Since the gravity is antiparallel to the density gradient, the difference of the density gradients has to be larger than zero for the right-hand side to be negative; this means that the buoyancy force points downwards, the fluid element is pulled back, and the stratification is stable.

This can also be formulated as an equation of motion for the fluid element with the gradient transformed to an entropy gradient,

$$\frac{\partial^2 (\Delta r)}{\partial t^2} = -\frac{\boldsymbol{g} \nabla s}{c_p} \Delta r, \tag{2.50}$$

where the entropy gradient of the element vanishes because of the adiabatic motion. Here, c_p denotes the specific heat capacity at constant pressure, and s the specific entropy. This differential equation leads to an oscillatory motion with the *Brunt–Väisälä frequency*

$$N^2 = -\frac{\boldsymbol{g} \nabla s}{c_p} = -\frac{g \delta}{H_p} \left(\nabla_{ad} - \nabla + \frac{\phi}{\delta} \nabla_\mu \right), \tag{2.51}$$

if $N^2 > 0$. For $N^2 < 0$, the solution grows exponentially and convective motions set in. In this equation, $\delta = -\partial \ln \rho / \partial \ln T$, $\phi = \partial \ln \rho / \partial \ln \mu$, $H_p = -dr/d\ln p$ is the pressure scale height,

$$\nabla_{ad} = \left(\frac{d \ln T}{d \ln p} \right)_{ad}, \quad \nabla = \left(\frac{d \ln T}{d \ln p} \right)_s, \quad \nabla_\mu = \left(\frac{d \ln \mu}{d \ln p} \right)_s, \tag{2.52}$$

denote the adiabatic temperature gradient of the element, the temperature gradient of the surrounding and the chemical gradient of the surrounding. The adiabatic gradient can also be written as $\nabla_{ad} = (\Gamma_2 - 1)/\Gamma_2$ and the value for an ideal monoatomic gas is 0.4.

Thus, for a layer in a star to be convectively stable, the radial entropy gradient must be negative. For a radiation layer with $\nabla = \nabla_{\mathrm{rad}}$, Eq. (2.51) leads to the *Ledoux criterion*,

$$\nabla_{\mathrm{rad}} < \nabla_{\mathrm{ad}} + \frac{\phi}{\delta}\nabla_{\mu}, \tag{2.53}$$

which reduces for a uniform composition with $\nabla_{\mu} = 0$ to the *Schwarzschild criterion* $\nabla_{\mathrm{rad}} < \nabla_{\mathrm{ad}}$.

The giant models entering CE evolution usually possess deep, convectively unstable envelopes. Moreover, dynamical instabilities can trigger convection during a CE phase (see Chapter 5).

2.4.4 Overview of Low- to Intermediate-Mass Stellar Evolution

Since this work is mainly about low- to intermediate mass stars, this section shall give a brief overview of their evolution (for a textbook, see Kippenhahn et al., 2012). The main parameter determining the evolution of a star is its initial mass. The contraction due to self-gravity drives the evolution and is counteracted by the energy release from nuclear reactions at different stages during its life. The strength of the contraction depends on the initial mass and determines which nuclear burning stages will be reached.

A star is born when a molecular cloud collapses under its own self-gravity to form a self-gravitating sphere. If its mass is larger than $0.08 M_{\odot}$, the temperatures are large enough to ignite hydrogen burning in the core of the star. This point where hydrogen burning starts marks the begin of the life of the star and is called zero-age main sequence (ZAMS). The main sequence denotes hydrogen burning models in complete equilibrium.

After the hydrogen is exhausted, burning may continue in a shell around the helium core. The further evolution depends on the initial mass. If the mass is below $\sim 0.5 M_{\odot}$, helium is not ignited and the star ends as a helium white dwarf.

For stars with masses above $\sim 2.5 M_{\odot}$, the core contracts and the envelope expands on a thermal timescale and the star becomes a red giant (RG) with a hydrogen burning shell. In the Hertzsprung–Russell diagram, the star moves across the Hertzsprung gap to the red giant branch. After this, the core heats up due to contraction and core helium burning sets in, at a core mass of roughly $0.5 M_{\odot}$; and the star moves to the horizontal branch. When the helium is exhausted in the core, shell helium burning may continue and the star can be found on the asymptotic giant branch (ABG) in the Hertzsprung–Russell diagram. For masses above $\sim 8 M_{\odot}$, carbon is ignited in the core, leading to a neon-oxygen-magnesium core. For masses above $\sim 10 M_{\odot}$, all further burning stages are also ignited resulting in an iron core that leads to a core-collapse supernova. The star finally transforms to a neutron star or black hole. For stars with a mass lower than $\sim 8 M_{\odot}$, the outer envelope is ejected and the final stage is a white dwarf consisting mainly of degenerate carbon and oxygen matter with possibly some helium and/or hydrogen on top.

If the initial stellar mass is between $\sim 0.5 M_{\odot}$ and $\sim 2.5 M_{\odot}$, the evolution through helium burning is different. Because these stars have almost no or small convective cores, the transition from core burning to shell burning is smooth. The larger initial densities lead to the formation of a degenerate helium core that grows through shell burning. When the core mass reaches about $\sim 0.5 M_{\odot}$, helium is ignited under degenerate conditions leading to a thermonuclear runaway, also called helium flash. When the temperature has grown large enough, the degeneracy is lifted and the core evolves to stable helium burning in the core. From here on, the evolution is similar to the higher-mass case.

2.5 Evolution of Binary Stars

The life of a star was described in the previous section. This evolution, however, may change drastically when the star is not single but comes in a binary or multiple stellar system because of the gravity of the companion(s) that can result in mass transfer. The number of stars in binary systems is large and depends on the mass of the more massive star. For G dwarfs, e.g., Duquennoy & Mayor (1991) find that 43% of all systems are binary or multiple systems; this corresponds to 62% of all stars being members of a binary or multiple system. Moreover, the multiplicity may be even larger due to restrictions of the observation method. Thus, binary stars are common and understanding the influence of companions on the stellar evolution is important for modeling the populations of stars we see. One classic example is the *Algol paradox*: the less massive component of Algol is more evolved than the more massive component that is still on the main sequence. This can only be explained by mass transfer between the two stars (see the overviews by Batten, 1989; Pustylnik, 1998).

The description of binary interactions follows Eggleton (2011), which gives a good and detailed account of binary stellar evolution. The presence of a companion will only influence the evolution of a star when they interact at some point during their life. Since the radius of a single star may increase by up to a factor of ~ 1000 during its evolution, binaries with periods larger than 10 000 d do not interact gravitationally[2], although a interaction with a stellar wind may still take place at somewhat larger radii.

2.5.1 Impact on Structure and Orbit

The structure of a binary stellar system can be analysed approximately in terms of the Roche potential. This potential treats both stars as point masses and includes an additional term for the centrifugal force due to the rotation of the system. The shape of the potential depends on the mass ratio q of the stars and possesses five points with vanishing gradients that are called Lagrange points. The isosurfaces of the Roche potential play the role of isobars in this model since the effective force is orthogonal to those isosurfaces. They are nearly spherical near the center of mass of each star and become more distorted when going outwards. The isosurface for which the encompassed volumes around each point mass touch each other is called the Roche lobe, and they touch exactly at the first Lagrange point. When a star expands further than its Roche lobe, parts of the material are not bound to this star anymore and will flow through the first Lagrange point to the companion star: mass transfer sets in.

Several effects can influence the evolution of the orbit of the system (Eggleton, 2011, Sec. 3.2.7). The shape of the star approaching the Roche lobe differs from spherical symmetry, introducing a quadrupole moment of gravity and also changing circulation patterns in the star. The quadrupole moment of the star disturbs the Keplerian orbit of the system, leading to an apsidal motion. If the rotation axis of the star differs from the rotation axis of the system, precession of the stellar spin ensues. Another effect leading to apsidal motion is the inclusion of terms from general relativity. Moreover, the emission of gravitational waves may shrink the orbit; this is important only for close compact binaries. An important effect leading to circularization and synchronization of the orbit is friction due to tides. The presence of a third body may have a strong influence on the orbital motion of the binary by, e.g., inducing Kozai cycles. Mass loss through stellar winds and mass

---

[2]The third law of Kepler gives the period as $P = 2\pi \sqrt{a^3/(GM)}$ (a: semi-major axis of orbit, M: total mass). For $M = 1 M_\odot$ and $a = 1000 R_\odot$, this gives 3.6×10^3 d.

transfer by Roche lobe overflow can lead to expansion or contraction of the orbit. Mass transfer furthermore changes the mass of both stars and thus also their single star evolution.

2.5.2 Mass Transfer Modes

During mass transfer in a binary system, some mass may be lost from the system. In this case, the mass transfer is called non-conservative, otherwise it is called conservative (mass and angular momentum of the system are conserved). Depending on the timescale of the mass transfer, three modes can be distinguished (Eggleton, 2011, Sec. 3.3.2): mode 1 on a nuclear timescale, mode 2 on a thermal timescale, and mode 3 on a hydrodynamical timescale. This timescale depends on the sensitivity of the radius of the star overflowing its Roche lobe to mass loss compared to the sensitivity of the Roche lobe.

This sensitivity can be quantified by logarithmic derivatives of the radius with respect to mass: let $R'_L = d \log R_L / d \log M$ be the change of the Roche lobe that depends on the mass ratio. Let R'_{TE} be the corresponding change of the stellar radius in thermal equilibrium, i.e., for mass loss on time scales between the Kelvin–Helmholtz and the nuclear timescale, and R'_{TD} the corresponding change for mass loss in thermal disequilibrium, i.e., on roughly the Kelvin–Helmholtz timescale. These two values depend on the stellar structure and are usually negative for radiative envelopes and positive for convective envelopes. This means that stars with radiative envelopes usually shrink in response to mass loss whereas stars with convective envelopes usually expand.

If now $R'_L < R'_{TE}$, the star does not expand stronger than the Roche lobe and the mass transfer is stable on a nuclear timescale: this is mode 1. For $R'_{TE} < R'_L < R_{TD}$, the star responds to the mass loss with an expansion that is weaker than the Roche lobe expansion only for the thermal timescale, thus this is mode 2 mass transfer. For $R'_{TD} < R'_L$, the mass transfer is unstable and will evolve on a hydrodynamical timescale: mode 3.

Another historical distinction was made in cases A, B, C (first defined in Kippenhahn & Weigert, 1967, see also Eggleton, 2011). For case A mass transfer, the primary star is still on the main sequence; for case B, the primary is before He ignition; for case C, the primary has ignited He. Case A mass transfer usually corresponds to conservative Roche lobe overflow as mode 1 mass transfer on a nuclear timescale. For early case B (the primary is in the Hertzsprung gap) and early case C (core He burning), the primary has a radiative envelope, resulting in mode 2 transfer. For late case B (red giant branch) and late case C (asymptotic giant branch/supergiants), the envelope of the primary is convective, leading to fast mode 3 transfer on hydrodynamic time scales. This corresponds to the transition to a CE phase with a RG (late case B) or AGB (late case C) primary star. Most simulations conducted in this work take a RG with a He core as a primary star and are thus examples of late case B mass transfer.

2.6 Common Envelope Phase

For an overview of the common envelope phase, the reviews by Iben & Livio (1993), Taam & Sandquist (2000), and Ivanova et al. (2013b) can be recommended.

When mass transfer in the binary system becomes unstable on thermal timescales and proceeds on a hydrodynamical timescale, the transferred mass cannot be accreted by the companion and a common envelope around both stars forms. This may happen for mode 3 mass transfer when the mass of the donor star is at least ~ 0.66 of the mass of the gaining star.

Another route to the common envelope phase is the Darwin instability. A binary system is subject to this instability, when the spin angular momentum of the primary is more than one third of the orbital angular momentum. In this case, the star expands and tidal forces try to synchronize the rotation, thereby transferring angular momentum from the orbit to the spin of the star. Thus, the orbit shrinks, the period decreases, and the star has to be spun up even more. This leads to a decay of the orbit until the secondary plunges into the envelope of the primary. The Darwin instability occurs only for large mass ratios, about 5 for red giant primaries and about 18 to 30 for main sequence primaries (Eggleton, 2011).

Once the secondary star is engulfed by the common envelope, drag due to friction will lead to a decay of the orbit and the companion will spiral into the envelope. This force can be approximated using Bondi–Hoyle accretion theory (Bondi & Hoyle, 1944, see also Ostriker, 1999). The outcome may either be a merger of the companion and the core of the primary star or a close binary system with the envelope being ejected. The final radius of the resulting binary may be estimated by equating the change in gravitational binding energy of the orbit to the binding energy of the envelope (Webbink, 1984),

$$\alpha_{CE}\left(\frac{GM_cM_2}{2a_f} - \frac{GM_1M_2}{2a_i}\right) = \frac{GM_1M_e}{\lambda R_1},\tag{2.54}$$

where a_i, a_f are the initial and final separation, M_c, M_e, M_1, M_2 the mass of the core and the envelope of the primary, the mass of the primary and secondary, and R_1 the radius of the primary. α_{CE} parametrizes the uncertainties about the efficiency of the mass ejection and λ characterizes the binding energy of the envelope that depends strongly on the definition of the core-boundary interface (Dewi & Tauris, 2000). Most binary population synthesis codes use constant values for the combination $\alpha_{CE}\lambda$ to compute the final outcome of common envelope phases. For most giants, $\lambda = 0.5$ seems to be a reasonable approximation (Dewi & Tauris, 2000).

This parametrization has been successfully used to describe post-common envelope binaries (PCEBs, Schreiber & Gänsicke, 2003; Zorotovic et al., 2011) that consist of a WD and a MS star (Zorotovic et al., 2010; Davis et al., 2010; De Marco et al., 2011; Davis et al., 2012; Toonen & Nelemans, 2013). Comparisons to observed systems constrain the efficiency α to a range of 0.2 to 0.3.

However, Nelemans et al. (2000) found that this prescription fails when reconstructing the evolution of double helium white dwarfs: negative values for α are necessary to describe the first mass transfer episode, since the orbit seems to have widened. Since the underlying physics is unclear, they introduce an alternative description based on the conservation of angular momentum,

$$\frac{\Delta J}{J} = \gamma\frac{\Delta M}{M},\tag{2.55}$$

where J denotes the angular momentum, M denotes the mass and ΔJ, ΔM the changes in angular momentum and mass. The parameter γ was found to lie in the range between 1.4 and 1.7 for the analyzed systems. In subsequent population synthesis studies (Nelemans et al., 2001b,a; Nelemans & Tout, 2005), the properties of observed samples could be reproduced when assuming this prescription with $\gamma \approx 1.75$ for the first mass transfer episode. Webbink (2008) attributes the increase in the orbital separation and energy during this first mass-transfer episode to a slower process on a thermal or nuclear timescale rather than to a CE event. In order to settle this issue, a better knowledge of the reaction of the corresponding giant envelopes to mass loss is needed to see if mass transfer results on a dynamical timescale or not.

An overview of previous work on CE phases is also given in the introduction (Sec. 1.2). One-dimensional studies utilized stellar evolution codes that inject a parametrized frictional energy at the location of the spiralling-in companion (Taam et al., 1978; Meyer & Meyer-Hofmeister, 1979; Delgado, 1980; Livio & Soker, 1984a,b; Soker et al., 1984). Those models did not find significant mass ejection because the energy could be transported to the surface and radiated away. The assumption of spherical symmetry was abandoned in multi-dimensional simulations: two-dimensional simulations in axisymmetric geometry (Bodenheimer & Taam, 1984; Taam & Bodenheimer, 1989; Livio et al., 1990; Taam & Bodenheimer, 1991; Yorke et al., 1995) and in the orbital plane (Taam et al., 1994). Fully three-dimensional simulations were conducted using smoothed particle hydrodynamics (SPH, de Kool, 1987; Livio & Soker, 1988; Terman et al., 1994, 1995; Terman & Taam, 1996; Rasio & Livio, 1996; Passy et al., 2012; Nandez et al., 2014, 2015; Iaconi et al., 2016), using finite differences on a nested grid (Sandquist et al., 1998, 2000; De Marco et al., 2003a,b), and using a finite volume method with adaptive mesh refinement (AMR, Ricker & Taam, 2008, 2012; Iaconi et al., 2016), on a uniform grid (Passy et al., 2012; Staff et al., 2016a,b), and on a moving mesh (Ohlmann et al., 2016, and this work). These multi-dimensional simulations established that the local injection of gravitational drag luminosity is important to accelerate the gas. However, these simulations show only partial ejection of the envelope, with most of the material being ejected during the first orbit. Thus, the ejection mechanism is still unclear and predicting the final state of the system is still out of reach of current simulations.

The long term goal of the work begun in this thesis is to improve the parametrizations by simulating the common envelope phase using three-dimensional hydrodynamic simulations. By relating the final separations to the initial separations in the simulations, the parametrizations can be calibrated – or new ones may be devised.

Chapter 3

Numerical Methods

The dynamics of the stellar plasma during the common envelope phase is governed by the Euler equations (2.4). The finite volume scheme is a popular method to discretize these partial differential equations on a grid (Sec. 3.1). A finite volume scheme is also the cornerstone of the AREPO code that is used in this work and that is described in Sec. 3.2.

3.1 Finite Volume Schemes

In order to model fluid flows using computer simulations, the Euler equations of hydrodynamics, Eqs. (2.4), have to be discretized. A variety of methods exists for solving these hyperbolic conservation laws; one class of methods that are popular in modeling astrophysical fluid flows are finite volume methods. In the following, a brief introduction to finite volume methods is given since they are the basis of our simulations of the common envelope phase. For a more general overview and further references, see LeVeque (1998).

3.1.1 Properties of Conservation Laws

A simple example for a hyperbolic equation is a one-dimensional conservation law for some density q,

$$(q(x,t))_t + (f(q(x,t)))_x = 0, \tag{3.1}$$

where $f(q)$ denotes the flux function. This differential form may be cast in an integral form that makes the conservation character of the equation manifest (LeVeque, 1998, Eq. 2.18),

$$\int_{x_1}^{x_2} q(x,t_2)\mathrm{d}x = \int_{x_1}^{x_2} q(x,t_1)\mathrm{d}x + \int_{t_1}^{t_2} f(q(x_1,t))\mathrm{d}t - \int_{t_1}^{t_2} f(q(x_2,t))\mathrm{d}t. \tag{3.2}$$

Here, x_1 and x_2 define an interval in space and t_1 and t_2 an interval in time. Eq. (3.2) shows that the integral of q over space changes only in time due to fluxes over the left or right border of the interval. The structure of the solution (cf. LeVeque, 1998, Sec. 3) can be seen more easily in the quasilinear form of Eq. (3.1),

$$q_t + f'(q)q_x = 0, \tag{3.3}$$

which has – locally – the form of an advection equation with a propagation speed of $f'(q)$. If the flux, however, is not constant, but depends on q, the solutions may develop discontinuities although the initial conditions are smooth. One example is Burgers' inviscid equation with $f'(q) = q$: the propagation speed is proportional to the quantity q itself. For a larger value in negative x direction than in positive x direction, the quantity q will be transported faster in the left part and at some point, the slope will become infinite: a shock builds up. If q is smaller in negative x direction than

in positive x direction, the region in between will be rarefied. In this case, however, the solution is not unique. To obtain a unique solution, an additional entropy constraint has to be introduced that yields the same solution as the vanishing viscosity approach[1]. The same phenomena can also be observed for more complicated systems such as, e.g., the Euler equations.

Eqs. (3.1) and (3.3) can be extended to systems of conservation laws by interpreting q and $f(q)$ as m-dimensional vectors (cf. LeVeque, 1998, Secs. 3.2, 3.3). In this case, $f'(q) \equiv A$ is the Jacobian matrix of the flux. The system of equations is called hyperbolic if A is diagonalizable with real eigenvalues for all q. Then, the Jacobian can be written as $A = R\Lambda R^{-1}$, where $\Lambda = \mathrm{diag}(\lambda_1, \ldots, \lambda_m)$ contains the eigenvalues and R the eigenvectors of A. With this, the equations can be transformed to characteristic variables, $v = R^{-1}q$, leading to

$$v_t + \Lambda v_x = 0. \tag{3.4}$$

If A is constant, this is a system of m decoupled scalar equations. The solution of this consists of advection waves in the characteristic variables that propagate with speed λ_p, i.e., given by the eigenvalues of A. If A depends on q, as is the case for the Euler equations, the situation is more complex and the solution can only be constructed locally along the characteristics (for more details, see LeVeque, 1998, Sec. 3.3).

An important problem highlighting the structure of the solution of the equations is the Riemann problem that consists of discontinuous initial conditions (cf. LeVeque, 1998, Sec. 3.2.2, 3.4),

$$q(x, 0) = \begin{cases} q_l, & x < 0 \\ q_r, & x > 0. \end{cases} \tag{3.5}$$

The left and right states can be decomposed into the basis of eigenvectors of A; this can be evolved along the characteristics. The solution to the Riemann problem is self-similar, i.e., $q(x, t) = w(x/t)$.

3.1.2 Discretization

A discretization of a partial differential equation (PDE) in space and time is should converge to the true solution of the PDE. In order to reach this convergence, a necessary condition is that the discretization is consistent and stable (cf. the discussion in LeVeque, 1998, Sec. 4.1). Consistency means that the local truncation error of the method should vanish for vanishing Δx and Δt. Stability means for hyperbolic PDEs that the numerical domain of dependence must include the true domain of dependence; this leads to the CFL (due to Courant, Friedrichs, Lewy; see Courant et al., 1928, part II) condition. For non-linear conservation laws, more conditions are needed to show convergence via the Lax-Wendroff theorem (for more details, see LeVeque, 1992, Sec. 12.4).

In order to discretize conservation laws, different strategies exists. One can use finite differences to compute the derivatives in Eq. (3.1). Using this approach can easily violate the conservation law character, and especially near discontinuities, the approximation of the derivatives with finite differences introduces large errors.

The finite volume approach discretizes the integral form of the conservation law, Eq. (3.2) and thus retains the character of a conservation law also on the discrete level (cf. LeVeque, 1998, Sec. 4.2). For a finite volume approach, the average of q over a cell $C_i = [x_i, x_{i+1}]$ at time t^n is defined as

$$Q_i^n = \frac{1}{\Delta x} \int_{C_i} q(x, t^n)\mathrm{d}x. \tag{3.6}$$

---

[1]Here, a small viscosity term ϵu_{xx} is added to the right hand side and then the limit $\epsilon \to 0$ is taken.

The numerical flux between two cells may be written as

$$F_i^n = \frac{1}{\Delta t} \int_{t^n}^{t^{n+1}} f(q(x_i, t)) \mathrm{d}t \approx F(Q_{i-1}^n, Q_i^n),$$ (3.7)

where the last expression stands for some approximation of the numerical flux that now only depends on the values of Q in the adjacent cells. Using these formulae leads to the scheme

$$Q_i^{n+1} = Q_i^n - \frac{\Delta t}{\Delta x} \left[F(Q_i^n, Q_{i+1}^n) - F(Q_{i-1}^n, Q_i^n) \right],$$ (3.8)

where the expression for F still has to be given. Using this scheme, the value of Q at the new timestep can be computed.

In Godunov's method (LeVeque, 1998, Sec. 4.5), the average values Q_i^n are interpreted to define a piecewise constant function $\tilde{q}^n$. Then the solution of the problem reduces to solving Riemann problems at the discontinuities of the cell interfaces and can be written as

$$\tilde{q}^n(x_i, t) = q^*(Q_{i-1}^n, Q_i^n),$$ (3.9)

where q^* gives the solution of the Riemann problem at the position of the interface. It can be shown that this solution is self-similar, thus, it is constant in time at the interface and the flux can be written as

$$F_i^n = f(q^*(Q_{i-1}^n, Q_i^n)),$$ (3.10)

and this can be plugged into the scheme of Eq. (3.8). The Riemann solution is constant only if there are no interactions with neighbouring Riemann problems, i.e., no waves of these are allowed to propagate from the neighbouring interface through the cell during a timestep. This leads to the CFL condition

$$\Delta t \leq \frac{\Delta x}{\max_p |\lambda_p|},$$ (3.11)

where λ_p is the speed of the p-th wave, i.e., an eigenvalue of the Jacobian matrix of the flux (cf. Eq. 3.3). This condition also ensures that the numerical domain of dependence always includes the true domain of dependence that can be found using the maximum wave speed.

The Riemann problem for the Euler equations can be solved exactly yielding the function q^* for computing the numerical fluxes. This involves, however, the solution of nonlinear equations that is done iteratively and thus computationally expensive. Since the solution to the Euler equations is approximate anyway, one can also employ approximate Riemann solvers that facilitate the solution of the intermediate states (LeVeque, 1998, Sec. 4.6). One example is the HLLC solver (Toro et al., 1994): it introduces two intermediate states that can be computed explicitly. The outer wave speeds have to be slightly larger than the true wave speeds to ensure stability. The middle wave was introduced in order to be able to resolve contact discontinuities. Another popular example is the Roe solver (Roe, 1981) that employs a specific linearization of the Jacobian matrix at the interface. A different approach is employed by relaxation schemes that are discussed in Sec. 10.1.

Up to now, the finite volume scheme Eq. (3.8) converges only to first order in space and time. For constructing higher-order schemes, the reconstruct-solve-average algorithm can be used (LeVeque, 1998, Sec. 4.7.1). First, a function $\tilde{q}^n$ is reconstructed using the cell average values Q_i^n as a piecewise constant, linear, or parabolic function. To ensure the conservation of the quantities, the reconstruction must not change the average value. In the next step, the equations are solved in

time by, e.g., using a Riemann solver. Then, this solution at time t^{n+1} is averaged over the cells to yield the new values Q_i^{n+1} for the cell averages.

The higher order reconstruction leads to a higher order convergence in regions where the flow is smooth. Near discontinuities, however, the reconstruction can cause spurious oscillations. This can be avoided by using slope limiters that effectively reduce the slope near discontinuities and thus also reduce the order of the scheme near discontinuities to first order. This ensures that no spurious extrema are generated and that the total variation of the solution does not increase. Examples of limiters are the minmod or superbee limiters (for more limiters and a detailed discussion, see LeVeque, 1998, Sec. 4.7).

To benefit from a higher order spatial convergence, also the temporal discretization has to be improved to converge to a higher order. For this, the scheme is formulated in a semi-discrete way where only the spatial derivatives are discretized using the finite volume method (LeVeque, 1998, Sec. 4.8.1),

$$Q_i'(t) = -\frac{1}{\Delta x} \left(F_{i+1}^n - F_i^n \right), \tag{3.12}$$

where F_i^n gives the numerical flux at the interface between cell $i-1$ and cell i at time t^n. Then, the time integration can be discretized separately, for example by using higher-order Runge-Kutta methods, instead of the first-order forward Euler integration as employed in Eq. (3.8).

If now in addition to the Euler equations source terms have to be included (e.g., gravity), one can treat this using operator splitting: the time integration is done alternating the hydrodynamics and the source terms. Since the operations usually do not commute, this method introduces a splitting error that – depending on the method – can be reduced to be of second order (see discussion in LeVeque, 1998, Sec. 5.3). This method can also be used for dimensional splitting, where one-dimensional sweeps are computed for each direction. In this way, a one-dimensional method can be easily extended to two or three dimensions.

3.2 The Scheme of AREPO

For the hydrodynamics simulations in this work, the AREPO code was used. It was written by V. Springel and is described in Springel (2010a). It solves the Euler equations with a finite volume method on an unstructured mesh. Its distinct feature is an arbitrary motion of the mesh that may be used to ensure a nearly Lagrangian behaviour of the method without the need for remapping strategies of the grid. In this way, the method combines the advantages of the two main approaches of modeling astrophysical fluid flows: smoothed particle hydrodynamics (e.g., Springel, 2010b) and static grid codes (e.g., LeVeque, 1998).

3.2.1 Hydrodynamics and Gravity

The unstructured grid that AREPO uses is a Voronoi tessellation of space for a given set of mesh-generating points (Springel, 2010a, Sec. 2). The Voronoi cell around each mesh-generating point consists of all points in space that are nearest to this point and defines the volume for the hydrodynamics cell. The mesh is generated in each timestep by first creating a Delaunay tessellation that is defined as a tessellation into simplices for which every circumsphere does not contain another mesh-generating point. Then, the Voronoi tessellation can be obtained as the topological dual of the Delaunay tessellation. Complications arise especially in the three-dimensional version due to the necessary accuracy and the treatment of degenerate cases (for more details, see Springel, 2010a,
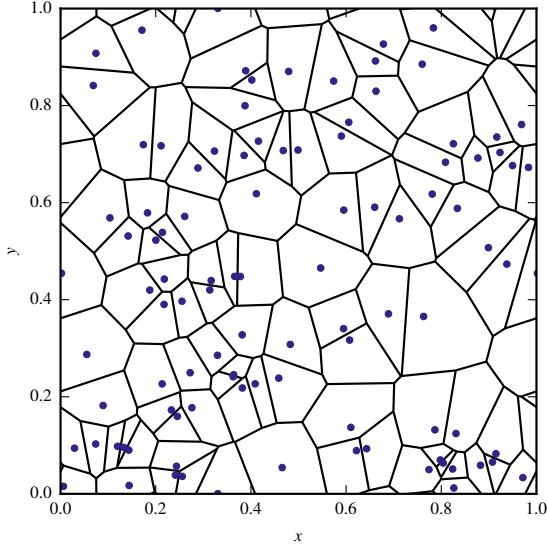
Figure 3.1 | Voronoi mesh in 2D generated for 100 randomly chosen points in the unit square with periodic boundaries. The mesh-generating points are shown as blue dots.

Sec. 2). An example of a Voronoi mesh is shown in Fig. 3.1 for 100 randomly chosen mesh-generating points.

On this Voronoi mesh, a finite volume method is constructed as follows (Springel, 2010a, Sec. 3): the mesh is allowed to move with a velocity w. Then, the change of the integral quantities Q_i (mass, momentum and total energy) in cell i is given by (Springel, 2010a, Eq. 10)

$$\frac{\mathrm{d}Q_i}{\mathrm{d}t} = -\int_{\partial V_i} (F(U) - U \otimes w) \, \mathrm{d}n, \tag{3.13}$$

where the integral is a surface integral over the surface ∂V_i of cell i. U is the vector of conserved quantities, i.e., density, momentum density, and total energy density. The second term in the integral accounts for advection across the cell boundary due to the mesh motion. For each of the Voronoi cells, the integral in Eq. (3.13) can be converted into a sum over all interfaces to neighbouring cells (Springel, 2010a, Eq. 12). The integral over each interface is then approximated by a one-point evaluation at the center of the surface. The numerical fluxes are computed in the restframe of the interface using the HLLC Riemann solver (Toro et al., 1994) with the normal vector pointing in the x direction. After computing the numerical fluxes, these are turned back into the lab frame and the mesh velocity is accounted for by an advection term (Springel, 2010a, Sec. 3). In this way, the scheme is Galilean invariant, which means that the solution of a problem does not depend on the background velocity at the same resolution (Springel, 2010a, Sec. 3.4). It is an unsplit method and the time integration of this semi-discrete formulation can be discretized separately.

The time integration and spatial reconstruction have been improved recently (Pakmor et al., 2016). Using these improvements, AREPO was numerically shown to converge to second order for general moving meshes (cf. Pakmor et al., 2016, Fig.4). For computing the fluxes, the values at the interface are computed using linear reconstruction. For this, gradients are calculated using a least squares technique (Pakmor et al., 2016, Sec. 4). The equations are integrated in time using Heun's method, a second order Runge-Kutta method, in combination with a prediction in time where the temporal derivatives are replaced by spatial derivatives, similar to a MUSCL-Hancock scheme (Pakmor et al., 2016, Sec. 3). The time integration employs a hierarchy of individual timesteps, improving computational efficiency (Springel, 2010a, Sec. 7).

The mesh motion is coupled to the fluid velocity to obtain a Lagrangian scheme. In order to avoid grid irregularities, a regularization component is added that corresponds to a small velocity of the mesh-generating point in direction of the center of mass of the cell (Springel, 2010a, Sec. 4). This ensures that the mesh stays near a centroidal configuration with roundish cells with only small distances between the mesh-generating point of a cell and its center of mass. In addition to the motion, the mesh can be refined and derefined on arbitrary criteria (Springel, 2010a, Sec.6). For refinement, an additional mesh-generating point is added near the one that is being refined; for derefinement, the mesh-generating point is deleted (see Springel, 2010a, Fig. 16). The conserved quantities in each participating cell are updated according to the new volumes of the cells. The usual refinement criterion ensures nearly constant cell masses within a factor of two larger and smaller than a reference value.

The self-gravity of the gas is computed using a tree algorithm that was adopted from the GADGET-2 code (Springel, 2005). The gravitational force between cells is softened on a length scale comparable to the cell radius using a spline function. This avoids unphysically large forces and clumping between adjacent cells.

3.2.2 Magnetohydrodynamics

Magnetic fields can be treated in AREPO by solving the equations of ideal magnetohydrodynamics (2.7). The implementation is described by Pakmor et al. (2011) and updated by Pakmor & Springel (2013). The problem in solving the ideal MHD equation is the divergence constraint $\nabla \cdot \boldsymbol{B} = 0$. Different numerical methods exist to tackle this problem, and Pakmor et al. (2011) implemented the approach of Dedner et al. (2002): an additional equation is added to the system that leads to an advection and damping of $\nabla \cdot \boldsymbol{B}$. For computing the numerical fluxes, a fallback strategy is employed: first, the HLLD solver (Miyoshi & Kusano, 2005) is used. If this yields a negative density or pressure, the solution of the HLL solver (Harten et al., 1983) is computed. If this fails, the Rusanov flux (Rusanov, 1961) yields a stable alternative. In this way, a stable solution is established.

Pakmor & Springel (2013) present an update of the algorithm: instead of the Dedner scheme, the approach by Powell et al. (1999) is used that includes source terms leading to a passive advection of $\nabla \cdot \boldsymbol{B}$. A comparison of both methods shows that the divergence error is small enough also for the Powell scheme, and that it does not put any constraints on the timestep. Thus, Pakmor & Springel (2013) recommend using the Powell scheme for MHD calculations with AREPO. This is also what we use in the first MHD simulations of the CE phase (Chapter 7).

Chapter 4

Creating Initial Models

Solving hyperbolic equations, such as the Euler equations, requires initial conditions, and the solution is determined by these initial conditions. For simulations of the CE phase, we need initial conditions for the binary system consisting of a giant as well as a companion star. To cope with the large range in scales in giants, approximations to their structure are necessary (Sec. 4.1). Since their envelopes are very dilute and only loosely bound, a careful method is needed to obtain stable models (Sec. 4.2). Once the primary star is available, a binary system can be set up including the companion (Sec. 4.3).

4.1 Stellar Structures

To simulate the CE phase, we first need to obtain models of single stars that can be used as initial conditions for the evolution of the binary system. In this section, we address the problem of creating different stellar atmospheres of full stars, especially giants, that are stable when evolved using the hydrodynamics code AREPO. This means that the models should retain their structure on the unstructured three-dimensional grid for several dynamical time scales to ensure that the evolution of the binary system is not influenced by numerical artifacts caused by the hydrodynamics code.

In the evolutionary stages we are interested in, stars are in mechanical equilibrium and their mechanical structure is governed by hydrostatic equilibrium. Taking a model from a one-dimensional stellar evolution code and mapping it to the multi-dimensional grid of a hydrodynamics code introduces discretization errors in the hydrostatic equilibrium. First, the stellar evolution code usually operates in spherical geometry in mass coordinates and can afford a high radial resolution, whereas this is not possible in the hydrodynamics code, especially for regions with steep gradients. Second, in the hydrodynamics code itself, the gradient of the pressure and the gravitational force are discretized in different ways thus not exactly canceling out. This can lead to spurious velocities and special care is needed to obtain models that are stable in the hydrodynamics simulation, especially because convective motions are expected in some envelopes.

To construct stellar models in different evolutionary stages ranging from the main sequence (MS) to the asymptotic giant branch (AGB) for different masses, we use the stellar evolution code MESA (Paxton et al., 2011, 2013, 2015) in version 6208. We impose a metallicity of $Z = 0.02$ and use the standard settings otherwise, i.e., the Reimers prescription with $\eta = 0.5$ for red giant (RG) winds (Reimers, 1975) and the Blöcker prescription with $\eta = 0.1$ for AGB winds (Blöecker, 1995). These values are the same as in Paxton et al. (2013, see there for further information and references).

First, we introduce the hydrostatic equilibrium (Sec. 4.1.1), and compare stellar profiles at different evolutionary stages in Sec. 4.1.2. This shows that giant profiles cover a large range in temporal and spatial scales that is too large to tackle with a hydrodynamics code. Thus, approximations are necessary: the core is replaced by a point mass (Sec. 4.1.3). To obtain suitable profiles near the core

that can be fitted to the envelope, we introduce a modified Lane–Emden equation in Sec. 4.1.4. In Sec. 4.1.5, we reconstruct models from stellar evolution calculations for use in AREPO, including the approximations from the previous sections for giant atmospheres. Moreover, we show that using a different equation of state for the reconstruction leads to a different convective behaviour in the model.

4.1.1 Hydrostatic Equilibrium Equations

A hydrostatic equilibrium for a gas follows from the Euler equations (2.4) for vanishing velocities and requires the pressure gradient (∇p) to be balanced by the gravitational force ($\boldsymbol{g}$),

$$\nabla p = \rho \boldsymbol{g} = -\rho \nabla \Phi, \tag{4.1}$$

where Φ denotes the gravitational potential. A star can be treated as a spherically symmetric aggregation of gas held together by its own gravity – to a first approximation. In this case, Eq. (4.1) reduces to a one-dimensional equation in radius, and only the mass up to some radius r contributes to the gravitational acceleration:

$$\frac{\mathrm{d}p(r)}{\mathrm{d}r} = -G\frac{m(r)\rho(r)}{r^2}, \tag{4.2}$$

where G, ρ, and m denote gravitational constant, density, and integrated mass, respectively. Mass balance on spherical shells yields

$$\frac{\mathrm{d}m(r)}{\mathrm{d}r} = 4\pi r^2 \rho(r). \tag{4.3}$$

These equations are complemented by boundary conditions at the center $m(0) = 0$ and $\mathrm{d}\rho/\mathrm{d}r(0) = 0$. As the behavior of the solution at the center is important for the stability of the atmosphere, we expand the solution into a series in radius about $r = 0$. To lowest order in the density,

$$\rho(r) = \rho_0 + O(r), \tag{4.4}$$

where $\rho_0 = \rho(0)$. This yields

$$m(r) = \frac{4\pi}{3}\rho_0 r^3 + O(r^4),$$
$$\frac{\mathrm{d}p(r)}{\mathrm{d}r} = -\frac{4\pi}{3}G\rho_0^2 r + O(r^2), \tag{4.5}$$
$$p(r) = p_0 - \frac{2\pi}{3}G\rho_0^2 r^2 + O(r^3),$$

where $p_0 = p(0)$. It is important for the stability of the atmosphere in a hydrodynamics simulation that it is resolved down to the scale in radius on which this expansion is valid. The reason is that in a three-dimensional geometry, the gradients will be flat at the center on radii comparable to the local resolution simply because of the continuous distribution of the variables. If the gradients are too large at the center, a cusp in density or pressure is present in the initial model and will excite sound waves, thereby smoothing out the cusp but introducing unwanted velocities.
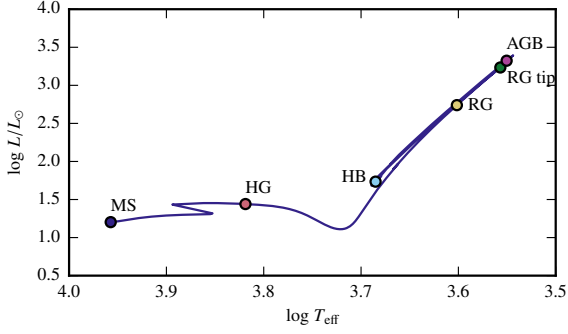
Figure 4.1 | Hertzsprung–Russell diagram for the evolution of a $2M_\odot$ star using MESA. Different evolutionary phases are marked for which the profiles are shown in Figs. 4.2 and 4.3.
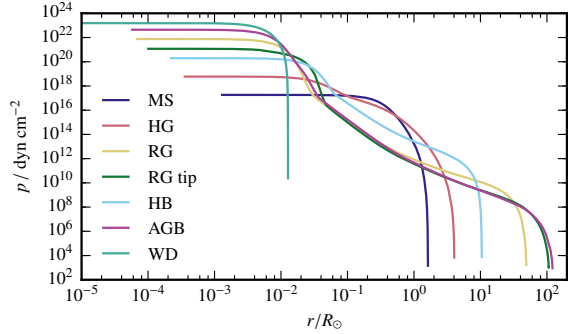

Figure 4.2 | Pressure profiles at different evolutionary stages for a $2M_\odot$ star and for a cold isothermal WD of $0.6M_\odot$.

4.1.2 Spatial Structure at Different Evolutionary Stages

To compare stellar profiles at different evolutionary stages, we choose a stellar model with a zero-age main sequence (ZAMS) mass of $2M_\odot$, which is evolved until the first thermal pulse on the AGB with MESA. The evolution of the model is shown in a Hertzsprung–Russell diagram in Fig. 4.1,
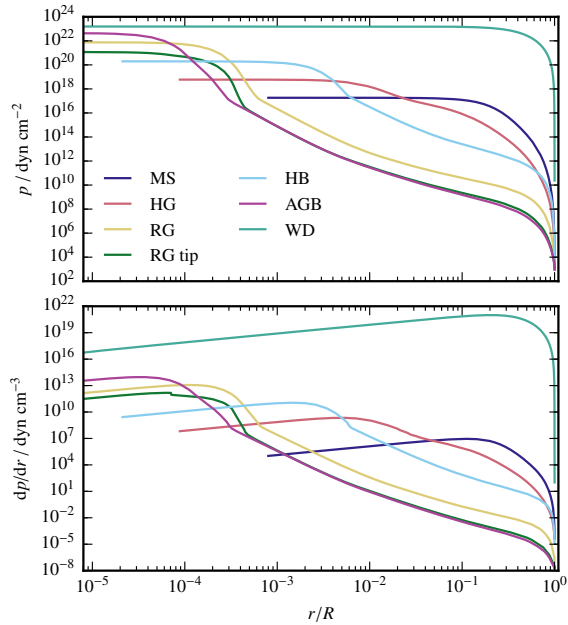
Figure 4.3 | Profiles of pressure p and pressure derivative dp/dr plotted over the relative radius r/R, where R is the stellar radius of the corresponding profile. Shown are different evolutionary states for a ZAMS of $2M_\odot$ and a cold isothermal WD of $0.6M_\odot$.
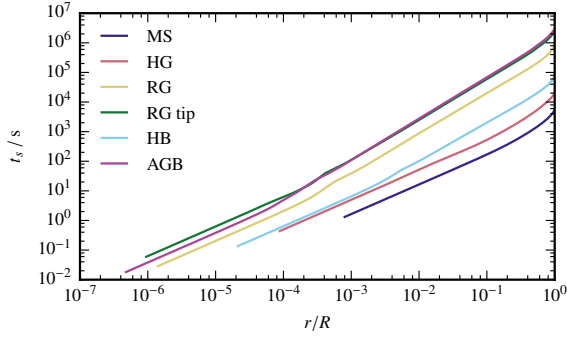
Figure 4.4 | Sound crossing time. Plotted is the sound crossing time t_s according to Eq. (4.7) for different stellar models over the relative radius r/R, where R is the stellar radius of the corresponding profile. Shown are different evolutionary states for a ZAMS of $2M_\odot$.

where different evolutionary points are marked for which the pressure profiles are given in Figs. 4.2 and 4.3. For comparison, a profile of a cold, isothermal $0.6M_\odot$ WD with $T = 5 \times 10^5$ K is shown. This model was set up by integrating the hydrostatic equilibrium equations with the Helmholtz equation of state (Timmes & Swesty, 2000) starting from a central density of 3.2×10^6 g cm^{-3}. The composition was set to equal parts of carbon and oxygen by mass.

Fig. 4.2 shows the expected behaviour: the core of the star contracts while its envelope expands when it evolves away from the MS. During core He burning on the horizontal branch (HB), the core expands and the envelope contracts slightly. On the AGB, the envelope expands even further than on the first red giant branch (RGB) and the maximum pressure in the core rises. The RGB and AGB pressure profiles are very similar, especially in the outer parts.

In Fig. 4.3, the profiles of the pressure and its spatial derivative are compared as functions of the relative radius r/R, where R is the stellar radius of the corresponding model. The pressure profiles (upper panel) show that the range in scales of radius and pressure increases drastically during the evolution. In the relative radius, it increases from roughly one to two decades for the MS model to five decades for the AGB model. The pressure derivative (Fig. 4.3, lower panel) shows the expected linear behaviour for $r \to 0$ (see Eq. 4.5). To obtain stable models, the profile has to be resolved down to this scale, which is not feasible for more evolved models with current numerical techniques.

In addition to the wide range of spatial scales, giant profiles span several orders of magnitude in temporal scales. When removing the pressure support of a star, it collapses under its own gravitation on the free-fall time scale

$$t_{\text{ff}}(r) = \sqrt{\frac{2r^3}{Gm(r)}}. \tag{4.6}$$

The free-fall time can also be interpreted as the time scale on which disturbances of the hydrostatic equilibrium propagate in the star from the center to the respective radius r. This timescale, however, is better characterized by the sound crossing time t_s,

$$t_s(r) = \int_0^r \frac{\mathrm{d}r'}{c_s(r')}, \tag{4.7}$$

where c_s denotes the sound speed in the stellar model. Profiles of the sound crossing time for different evolutionary states are plotted in Fig. 4.4. The more compact profiles of the MS and WD stars show only a small variation in sound crossing times on the spatial scales where the pressure changes (see Fig. 4.3). Thus, a hydrodynamics simulation of these profiles shows rather
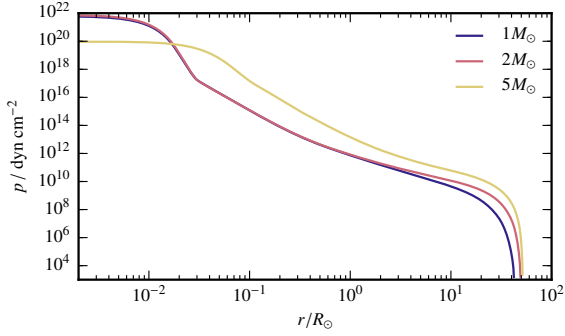
Figure 4.5 | Pressure profiles for different masses. Shown are RG models with ZAMS masses of $1M_\odot$, $2M_\odot$, and $5M_\odot$.

uniform time step constraints and disturbances can be damped uniformly over the whole star on a comparatively short time. In contrast, giant profiles show larger ranges in time scales the farther they evolve. For the AGB model, e.g., the time scales span almost six orders of magnitude. In a multi-dimensional hydrodynamics code, this cannot be easily accommodated since the inner part would require time steps that are a factor of about 10^6 smaller than in the outer part. This would be computationally costly and it would introduce large time integration errors.

Thus, we need approximations for giant profiles in order to construct stable hydrostatic atmospheres in a hydrodynamics simulation – as opposed to MS and WD atmospheres. These can be mapped stably without special approximations to a hydrodynamics simulation due to the smaller range in scales.

A comparison of pressure profiles for RG models of different mass (Fig. 4.5) shows similarities, especially for $1M_\odot$ and $2M_\odot$ due to the similar size of the degenerate core. Thus, we expect similar approximations to hold for giant profiles of different masses.

### 4.1.3 Approximations of Giant Atmospheres

To approximate giant profiles, we crop the profiles at a certain radius and continue them in a stable way to the center. The core of the star is represented by a point mass which interacts only gravitationally with the gaseous envelope. Using the combined gravitational force, the hydrostatic equilibrium can be integrated to obtain the new stellar profile.

A similar approach is taken in most hydrodynamics simulations of common envelope phases in grid codes so far (e.g. Sandquist et al., 1998; Passy et al., 2012; Staff et al., 2016a,b; Iaconi et al., 2016, for recent simulations). For the simulations using an Eulerian grid code, the core of the RG is represented by a particle which interacts only gravitationally. Another approach in the same context is the cloud-in-cell method, where the core of the giant is replaced by a cloud of particles, for which the density is mapped to the hydrodynamics grid (Ricker & Taam, 2008, 2012).

We represent the core by a particle that interacts only gravitationally; this is already implemented in AREPO for modeling dark matter (Springel, 2010a). The gravitational acceleration is given by a spline function (Springel, 2010a)

$$g_c(r) = -Gm_c \frac{r}{h^3} \begin{cases} -\frac{32}{3} + u^2\left(\frac{192}{5} - 32u\right), & 0 \le u < \frac{1}{2}, \\ \frac{1}{15u^3} - \frac{64}{3} + 48u \\ \quad -\frac{192}{5}u^2 + \frac{32}{3}u^3, & \frac{1}{2} \le u < 1, \\ -\frac{1}{u^3}, & u \ge 1, \end{cases} \tag{4.8}$$
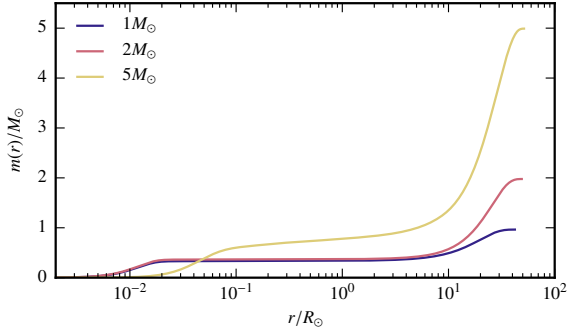
Figure 4.6 | Mass profiles of RG models for $1M_\odot$, $2M_\odot$, and $5M_\odot$. Shown is the mass in solar masses over the radius in solar radii.

where $u = r/h$, h is the softening length of the interaction, and m_c is the mass of the particle representing the core.

We then modify the hydrostatic equilibrium equations (4.2) and (4.3) to account for the presence of the core particle. The mass function now encompasses only the gas mass without the core. The pressure balance equation (4.2) is modified to

$$\frac{\mathrm{d}p(r)}{\mathrm{d}r} = -G\frac{m(r)\rho(r)}{r^2} - \rho(r)g_c(r), \tag{4.9}$$

where g_c is given in Eq. (4.8). Expanding this modified equation into a series in radius about $r = 0$ yields

$$\frac{\mathrm{d}p(r)}{\mathrm{d}r} = -G\frac{4\pi}{3}\rho_0^2\left(1 + \frac{8}{\pi}\frac{m_c}{h^3\rho_0}\right)r + O(r^2), \tag{4.10}$$

which shows the same scaling as in the original equation (4.5), although with a different pre-factor that depends on the ratio of the mean density of the core particle to the central density of the gas.

The mass profile of a $2M_\odot$ RG model is shown in Fig. 4.6 along with the mass profiles for $1M_\odot$ and $5M_\odot$ RG models. It is constant for large scales in relative radii, from about 5×10^{-4} to 0.1 (for the $5M_\odot$ model, this range is a bit smaller). This means that the core is very compact compared to the dilute envelope. Thus, the approximation of the core as a rigidly moving body should be justified when cutting the profile off in the region where the mass profile is flat.

In order to create a stellar profile from the center of the star to the surface, a continuation of the profile from the cut inwards has to be found. The requirements for this continuation are that it should be smooth, lead to a similar profile when mapped into the hydrodynamics code and thus should be aware of the presence of the gravitational force of the core and adhere to the scaling relations as given in Eqs. (4.5). A simple approach taking a solution of the Lane–Emden equation does not take into account the gravitational force of the core; hence, this leads to the generation of spurious velocities when mapped into the hydrodynamics code. To obtain continuations that fulfill these requirements, we introduce a modified Lane–Emden equation that can be derived by combining the mass equation (4.3) with the modified pressure equation (4.9). Integrating this ODE enables us to fit the resulting functions and their derivatives smoothly to the stellar profile outside the cut.

4.1.4 A Modified Lane–Emden Equation

The modified pressure equation (4.9) can be combined with the mass equation (4.5) to yield

$$\frac{1}{r^2}\frac{\mathrm{d}}{\mathrm{d}r}\left(\frac{r^2}{4\pi G\rho}\frac{\mathrm{d}p}{\mathrm{d}r} + \frac{r^2 g_c(r)}{4\pi G}\right) + \rho = 0,\tag{4.11}$$

where g_c is the gravitational force of the core given by Eq. (4.8). One can now introduce a polytropic relation $p = K\rho^{1+\frac{1}{n}}$ (K: polytropic constant, n: polytropic index), and $\rho = \rho_c\theta^n$ with the polytropic temperature θ, and a scaled radius $\xi = r/\alpha$ with

$$\alpha^2 = \frac{K(n+1)\rho_c^{\frac{1}{n}-1}}{4\pi G}.\tag{4.12}$$

Inserting these relations in Eq. (4.11) yields the well-known Lane–Emden equation (cf., e.g., Kippenhahn et al., 2012), but including an additional term that accounts for the core,

$$\frac{1}{\xi}\frac{\mathrm{d}}{\mathrm{d}\xi}\left(\xi^2\frac{\mathrm{d}\theta}{\mathrm{d}\xi} + \xi^2\frac{g_c(\alpha\xi)}{4\pi G\rho_c\alpha}\right) + \theta^n = 0.\tag{4.13}$$

By introducing a new function χ,

$$\chi\left(\frac{\xi}{\xi_h}\right) = \frac{h^3}{Gm_c\alpha\xi}g_c(\alpha\xi),\tag{4.14}$$

where $\xi_h = h/\alpha$ is the non-dimensional cut radius, Eq. (4.13) can be written as

$$\frac{1}{\xi^2}\frac{\mathrm{d}}{\mathrm{d}\xi}\left(\xi^2\frac{\mathrm{d}\theta}{\mathrm{d}\xi}\right) + \frac{\overline{\rho}}{\rho_c}\left(\chi(\xi/\xi_h) + \frac{\xi}{3\xi_h}\chi'(\xi/\xi_h)\right) + \theta^n = 0,\tag{4.15}$$

where $\overline{\rho} = m_c/(4\pi h^3/3)$ denotes the mean density of the core. The function $u\chi(u)$ can be seen as a dimensionless form of the gravitational acceleration in Eq. (4.8) and is compared in Fig. 4.7 (left panel) to the unsoftened Newtonian acceleration $1/u^2$. The interesting point is that the gravitational force of the core appears as an additional density term that depends on the ratio of the mean density of the core to the central density of the polytropic solution. This can be seen even more clearly when converting Eq. (4.15) into two first-order ODEs that can be used for integrating,

$$\begin{aligned}\frac{\mathrm{d}\theta}{\mathrm{d}\xi} &= -\frac{\eta}{\xi^2},\\[6pt]\frac{\mathrm{d}\eta}{\mathrm{d}\xi} &= \xi^2\left(\theta^n + \frac{\overline{\rho}}{\rho_c}\left(\chi(\xi/\xi_h) + \frac{\xi}{3\xi_h}\chi'(\xi/\xi_h)\right)\right),\end{aligned}\tag{4.16}$$

where η is the non-dimensional mass and where the initial conditions are given by $\eta(0) = 0$, $\theta(0) = 1$. The original Lane–Emden equation does not feature the second term in brackets in the lower equation of Eq. (4.16). Hence, it can be clearly seen that this additional term in the mass integration corresponds to an additional density source corresponding to the core particle. Thus, assuming a smoothed gravitational force for the core as given in Eq. (4.8) corresponds to smearing out the mass of the core inside a sphere of radius h with a density profile given in Eq. (4.16). This density profile is shown in Fig. 4.7 (right panel).
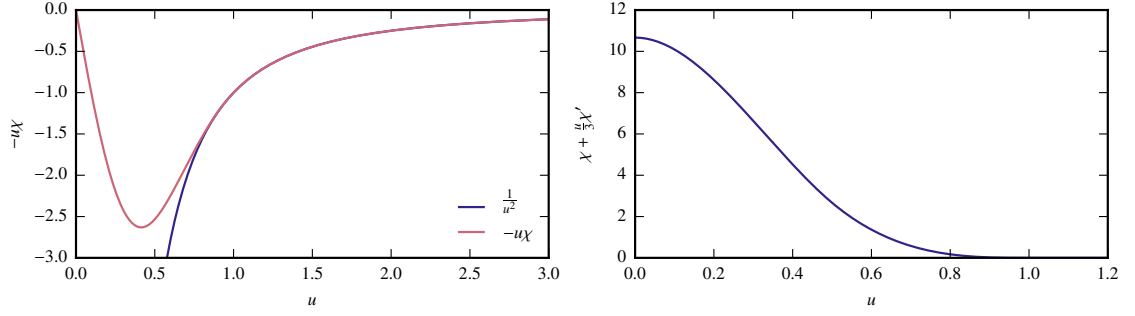
Figure 4.7 | Approximate gravitational acceleration (left) and corresponding density for the modified Lane–Emden equation (right). The left panel shows $-u\chi(u)$ (χ from Eq. 4.8) compared to a $1/u^2$ acceleration of a point mass. Above $u = 1$, both functions coincide by construction. The right panel shows $\chi(u) + \frac{u}{3}\chi'(u)$, the dimensionless density distribution from Eq. (4.16) associated with a softened gravitational acceleration as shown in the left panel.

The solution of this modified Lane–Emden equation now depends not only on the polytropic index n, but also now on the parameters $\overline{\rho}/\rho_c$, ξ_h, and on the form of the function χ. For χ given by Eq. (4.14) the corresponding term in Eq.(4.15) reduces to zero for $\xi > \xi_h$, i.e., in the outer part. Thus, the modified Lane–Emden equation is reduced to the usual Lane–Emden equation in this region. The behaviour of the solution in the inner part ($\xi < \xi_h$) depends on the ratio $\overline{\rho}/\rho_c$. For $\overline{\rho} \ll \rho_c$, the impact of the modification is small since the density resulting from smearing out the point mass is small compared to the gas density and the solution is similar to the solution of the Lane–Emden equation. In the other case, $\overline{\rho} \gg \rho_c$, the contribution of the gas density is negligible in the inner part for integrating the solution, and hence the gas mass in the interior part is negligible compared to the mass of the core.

The solutions of the modified Lane–Emden equation show the same behaviour for convective stability as the solutions of the Lane–Emden equation. For the entropy $s(\xi)$ given by

$$\frac{s(\xi)}{c_p} = \ln\left(\frac{p(\xi)}{\rho(\xi)^\gamma}\right) + \text{const} = (n(1 - \gamma) + 1)\ln(\theta(\xi)) + \text{const}, \tag{4.17}$$

the Schwarzschild criterion, $\mathrm{d}s/\mathrm{d}\xi > 0$, yields convective stability for

$$n > \frac{1}{\gamma - 1}, \tag{4.18}$$

since θ decreases monotonically. The heat capacity at constant pressure is denoted by c_p. For an adiabatic index $\gamma = 5/3$ corresponding to an ideal monoatomic gas, this yields $n > 3/2$ for convectively stable stratifications.

In order to obtain a smooth transition to a stellar profile at a certain radius, the solution of the modified Lane–Emden equation can be fitted to yield the corresponding density and its derivative. As the integration of Eq. (4.16) yields the function $\theta(\xi; n, h, \overline{\rho}; \alpha, \rho_c)$, where the parameters n, h, and $\overline{\rho}$ are known, the density given by

$$\rho(r; n, h, \overline{\rho}; \alpha, \rho_c) = \rho_c \theta^n(\alpha r; n, h, \overline{\rho}; \alpha, \rho_c) \tag{4.19}$$

can be used to fit the parameters α and ρ_c to give the density and its derivative at the transition radius. This has been implemented using a non-linear root finder.
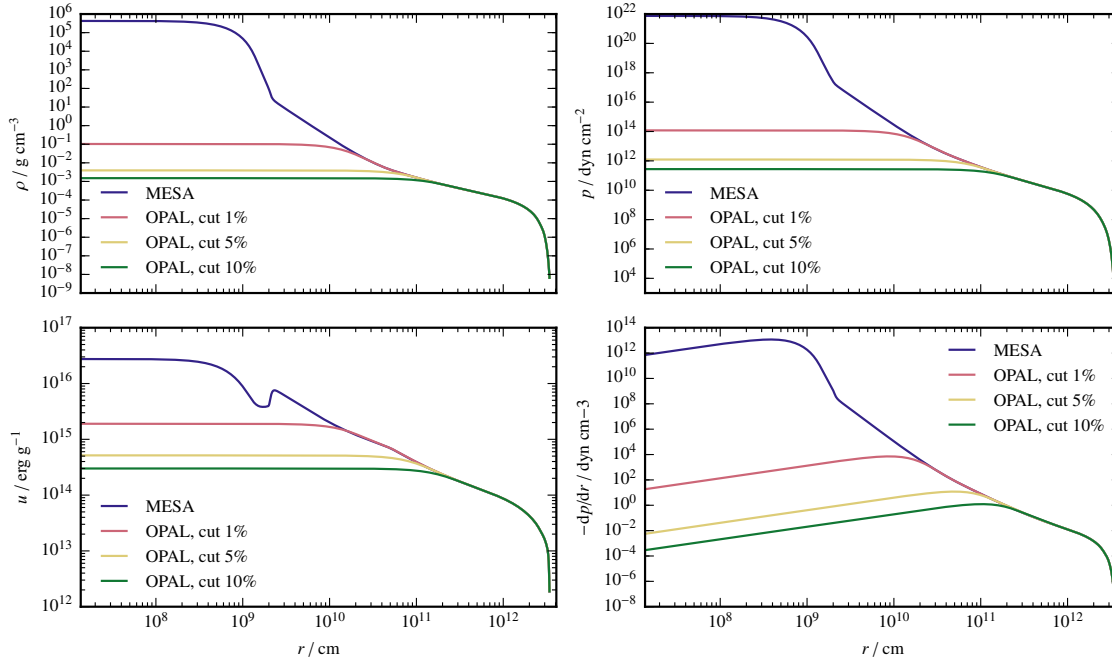
Figure 4.8 | Comparison of density (upper left), pressure (upper right), internal energy (lower left) and derivative of pressure (lower right) for a $2M_\odot$ RG with a $\sim 0.4M_\odot$ He core. Shown is the original profile from the MESA stellar evolution code as well as approximate profiles for cut radii of 1%, 5%, and 10% of the total radius. The approximate profiles were computed using a polytropic index of $n = 3$ for the interior part.

A few examples for such approximate stellar profiles are shown in Fig. 4.8 for a $2M_\odot$ RG with a $\sim 0.4M_\odot$ He core (the RG model in Fig. 4.1) for different core cutoff radii where the profile was cut. For this example, a polytropic index of $n = 3$ was used for the modified Lane–Emden solution in the interior part that was fitted to the profile. For the subsequent integration of the hydrostatic equilibrium of the profile, the OPAL equation of state (Rogers et al., 1996; Rogers & Nayfonov, 2002) was used that is the same as used by MESA in this ρ-T regime. The plots show that the stellar profile is reproduced very well in the outer part for radii larger than the cut radius for the important thermodynamic quantities. The connection to the inner part of the modified Lane–Emden solutions is smooth, as expected. Moreover, the derivative of the pressure (Fig. 4.8, lower right) shows the right behaviour for $r \rightarrow 0$ as required by Eq. (4.5), which is very important for the hydrostatic equilibrium at the center of the star.

4.1.5 Reconstructing Stellar Profiles

In order to use a stellar profile from a stellar evolution code in a hydrodynamics code, the stellar structure equations (4.2) and (4.3) have to be integrated when using a different equation of state or when using an approximate profile such as described in the previous section. Especially when using a different equation of state, some of the thermodynamic quantities will differ. In this case, the question is which quantities are most important to be recovered in the hydrodynamics simulation and how the stellar structure equations have to be integrated to ensure this.

The usual procedure is taking the density from the stellar profile for integrating the stellar structure equations: given $\rho(r)$ as function of the radius, one can easily integrate

$$\frac{\mathrm{d}m(r)}{\mathrm{d}r} = 4\pi r^2 \rho(r),$$
$$\frac{\mathrm{d}p(r)}{\mathrm{d}r} = -\frac{Gm(r)\rho(r)}{r^2}. \tag{4.20}$$

This ensures that the density, mass, and pressure profiles equal the values from the stellar evolution code. However, the values of the internal energy, entropy, sound speed, temperature gradients and other quantities may differ compared to the stellar evolution code. Thus, regions of convective stability or instability may differ.

As a second approach, the temperature profile of the star can be taken from the stellar evolution code as a function $T(r)$ to integrate the equations

$$\frac{\mathrm{d}m(r)}{\mathrm{d}r} = 4\pi r^2 \rho(p(r), T(r)),$$
$$\frac{\mathrm{d}p(r)}{\mathrm{d}r} = -\frac{Gm(r)\rho(p(r), T(r))}{r^2}, \tag{4.21}$$

simultaneously. For this approach, the equation of state has to be available as a function of pressure and temperature. Although the temperature of the original stellar profile is recovered using this approach, the convective stability of the profile may change since this depends on the temperature gradient compared to the adiabatic gradient. This method is used to integrate profiles of isothermal WDs (see, e.g., Fig. 4.2.

To conserve the convective stability or instability of the profile in different regions, the difference $\nabla - \nabla_{\mathrm{ad}}$ between the temperature gradient and the adiabatic gradient can be integrated in a third way.[1] In order to achieve this, a third equation for the temperature has to be added that is integrated along with the other equations,

$$\frac{\mathrm{d}m(r)}{\mathrm{d}r} = 4\pi r^2 \rho(p(r), T(r)),$$
$$\frac{\mathrm{d}p(r)}{\mathrm{d}r} = -\frac{Gm(r)\rho(p(r), T(r))}{r^2}, \tag{4.22}$$
$$\frac{\mathrm{d}T(r)}{\mathrm{d}r} = \frac{\mathrm{d}p(r)}{\mathrm{d}r}\frac{T(r)}{p(r)}\nabla(r),$$

where the temperature gradient is given by

$$\nabla(r) = (\nabla - \nabla_{\mathrm{ad}})(r) + \nabla_{\mathrm{ad}}(p(r), T(r)), \tag{4.23}$$

and ∇_{ad} is the adiabatic gradient given by the equation of state. This method ensures that the difference $\nabla - \nabla_{\mathrm{ad}}$ remains the same with respect to the corresponding equation of state. Hence, the criterion for convective stability will be fulfilled in the same regions of the stellar profile. This method, however, may change the mass profile of the star and thus also its radius and total mass. Hence, the quantities that one wants to preserve when mapping to a hydrodynamics code decide which method one should use.

---

[1]A similar procedure to the one followed here was originally proposed by Edelmann et al. (2016, in prep.), although with fixed gravity.
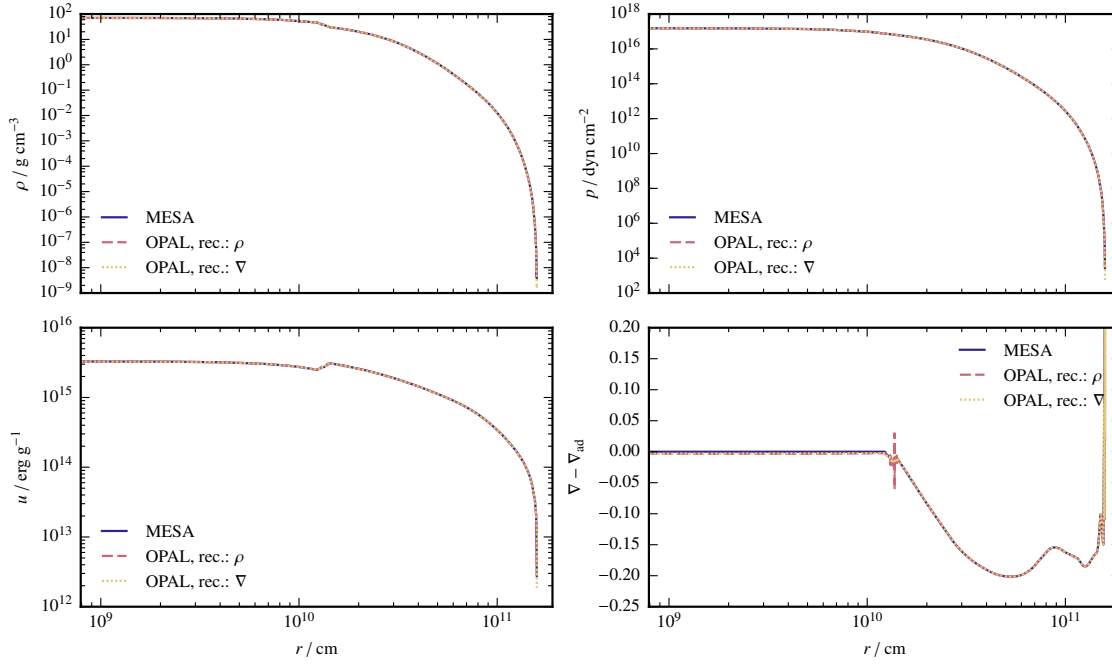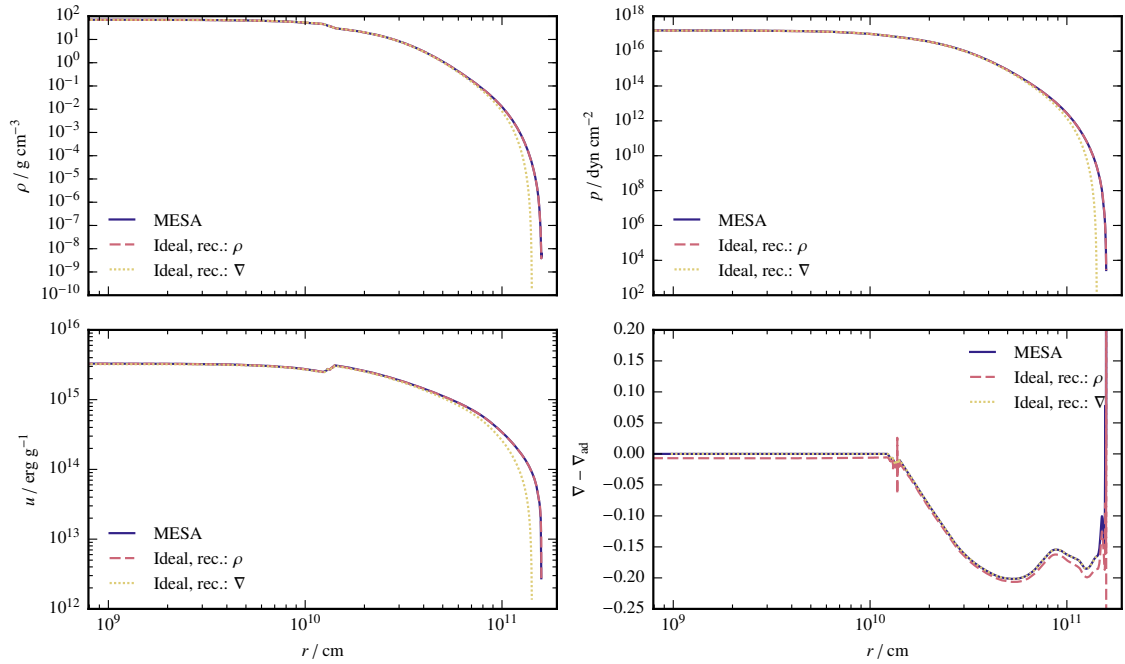
Figure 4.9 | Comparison of different integration methods for a $2M_\odot$ star at the end of the MS using the OPAL equation of state. Shown are the density ρ (upper left), the pressure p (upper right), the internal energy u (lower left), and the difference between the gradient ∇ and the adiabatic gradient ∇_{ad} (lower right).

When using the same equation of state in the stellar evolution code and in the hydrodynamics code, both integration methods yield the same result. This is demonstrated in Fig. 4.9 for a $2M_\odot$ star at the terminal main sequence (TMS). The figure shows the density ρ, the pressure p, the internal energy u, and the difference between the gradient ∇ and the adiabatic gradient ∇_{ad} for the profile from MESA and reconstructed profiles using ρ or $\nabla - \nabla_{ad}$ as given quantities. As one can see, the different methods yield almost the same result with the exception of the very interior, where a small difference in $\nabla - \nabla_{ad}$ is visible. This is probably due to the chemical gradient that is neglected in the reconstruction, but taken into account in MESA. The difference is larger when using an ideal gas equation of state, as shown in Fig. 4.10 for the same stellar model. The density and pressure are reproduced accurately; also the difference in the internal energy is not visible. Nevertheless, $\nabla - \nabla_{ad}$ deviates from the original model; it is smaller in most parts of the envelope. Especially in the convective core, it is smaller than zero (although only by a small amount), thus indicating convective stability in this region. Overall, the differences are not very pronounced leading to the conclusion that the departure from ideal gas behaviour is not large in the star. The profile of the difference $\nabla - \nabla_{ad}$ can be reproduced by using the corresponding reconstruction given in Eq. (4.22) (yellow profile in Fig. 4.9). Since this makes the temperature profile steeper, the new profile is smaller in radius (11%) and in mass (3%). Nonetheless, it reproduces the convective instability of the core and the convective stability of the envelope.

Since the difference between the ideal gas equation of state and the OPAL equation of state is larger for lower densities and temperatures, where recombination plays an important role, the

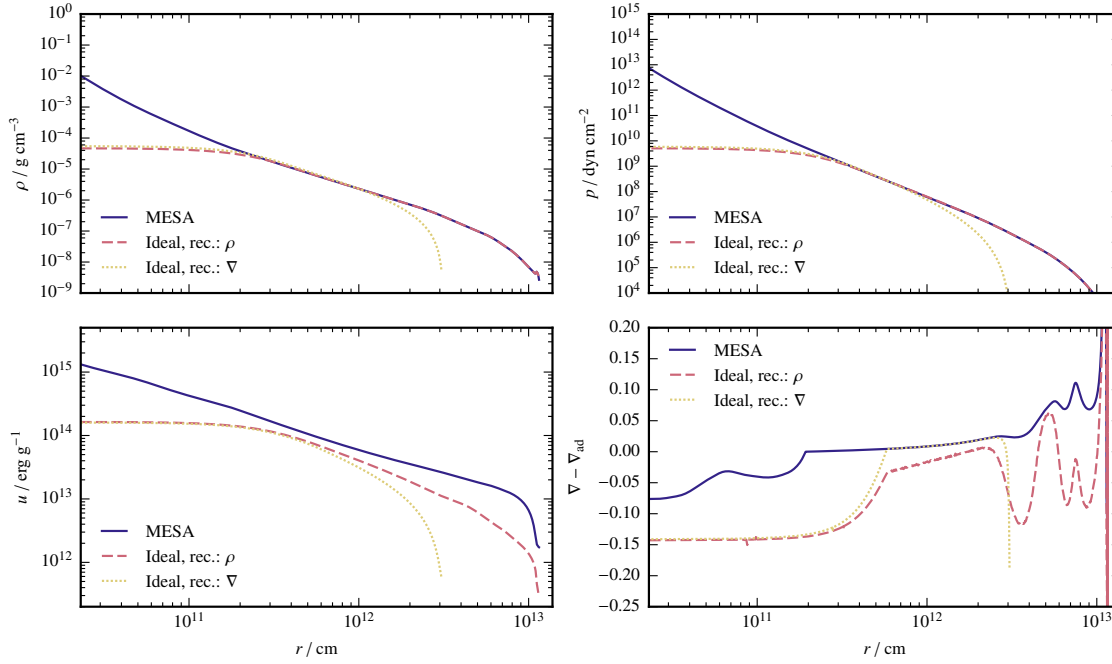**Figure 4.10 |** Comparison of different integration methods for a $2M_\odot$ star at the end of the MS using an ideal equation of state. The panels show the same quantities as in Fig. 4.9.
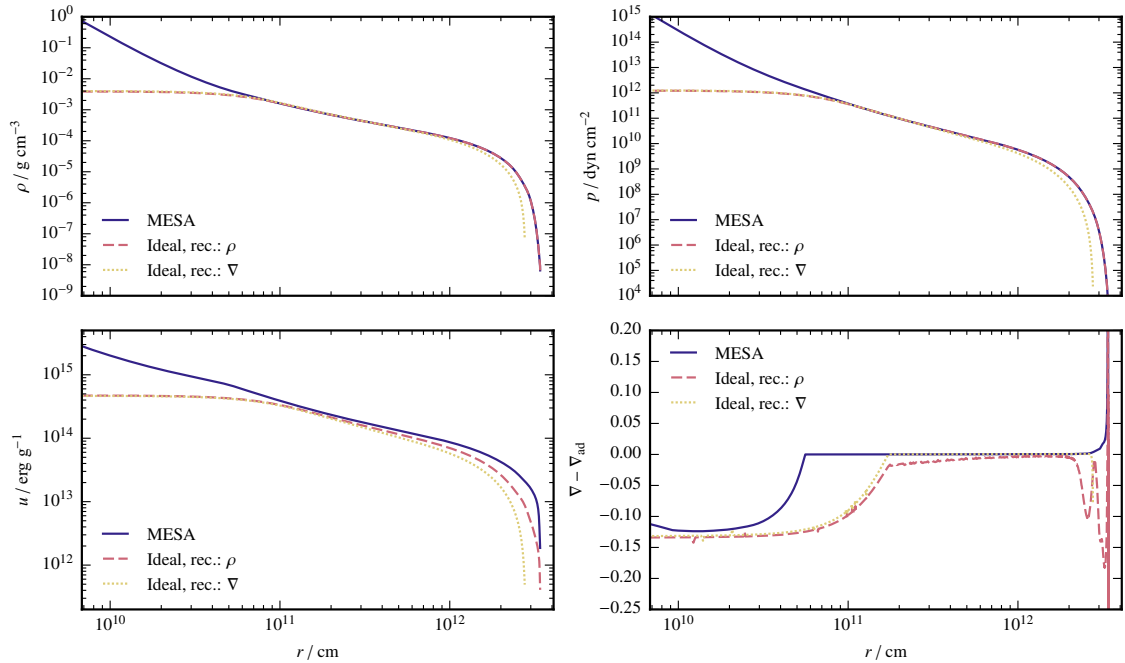
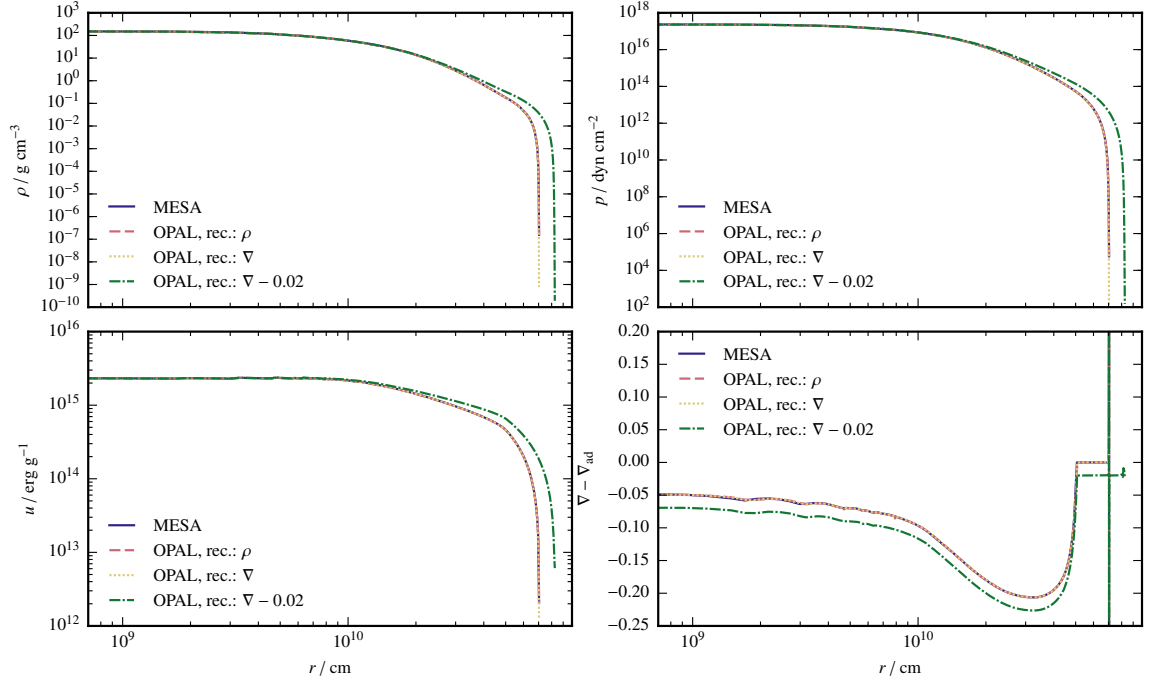
Figure 4.11 | Comparison of different integration methods for a $2M_\odot$ RG using an ideal equation of state. The profile was cut at 5% of the stellar radius. The panels show the same quantities as in Fig. 4.9.

Figure 4.12 | Comparison of different integration methods for a $0.67 M_\odot$ AGB star using an ideal equation of state. The profile was cut at 5% of the stellar radius. The panels show the same quantities as in Fig. 4.9.

difference in the resulting stellar profiles is larger for extended giant profiles that range to lower densities and temperatures when using the ideal gas equation of state. For a $2M_\odot$ RG that was cut at 5% of the stellar radius, this is shown in Fig. 4.11 (this is the same model as in Fig. 4.8). When reconstructing using the density (red line in Fig. 4.11), the profiles of density and pressure are recovered accurately, while the internal energy is smaller for the outer parts of the envelope. Moreover, $\nabla - \nabla_{ad} < 0$ for most parts of the envelope which means that the envelope is convectively stable when using this profile for mapping to the hydrodynamics code in contradiction to the original profile. The largest deviation can be seen in the outer part, where the two dips correspond to the ionization of He and H that is not treated in the ideal gas equation of state. This model can also be reconstructed using $\nabla - \nabla_{ad}$ (Fig. 4.11, yellow line) which reproduces the convectively unstable behaviour of the envelope for radii larger than the cut radius. Similarly to the TMS case, the profile constructed in this way is smaller in radius (18%) and in gas mass (27%, without core). This behaviour is even more pronounced for the more extended profile of a $0.67 M_\odot$ AGB star (ZAMS mass: $1 M_\odot$) that is shown in Fig. 4.12. Due to the even lower densities and temperatures, recombination plays a larger role in the outer part of the envelope and hence, the difference to the integration using an ideal equation of state is even larger. Similar to the RG profile in Fig. 4.11, the profile reconstructed using ρ (Fig. 4.12, red line) is convectively stable in most parts of the envelope because $\nabla - \nabla_{ad} < 0$, except for a small layer at about $60 R_\odot$. Also here, the dips can be attributed to the recombination of He (twice) and H. When one wants to reproduce a convective envelope using the ideal gas equation of state by reconstructing $\nabla - \nabla_{ad}$, the profile changes substantially and shrinks by 73% in radius and 79% in mass.
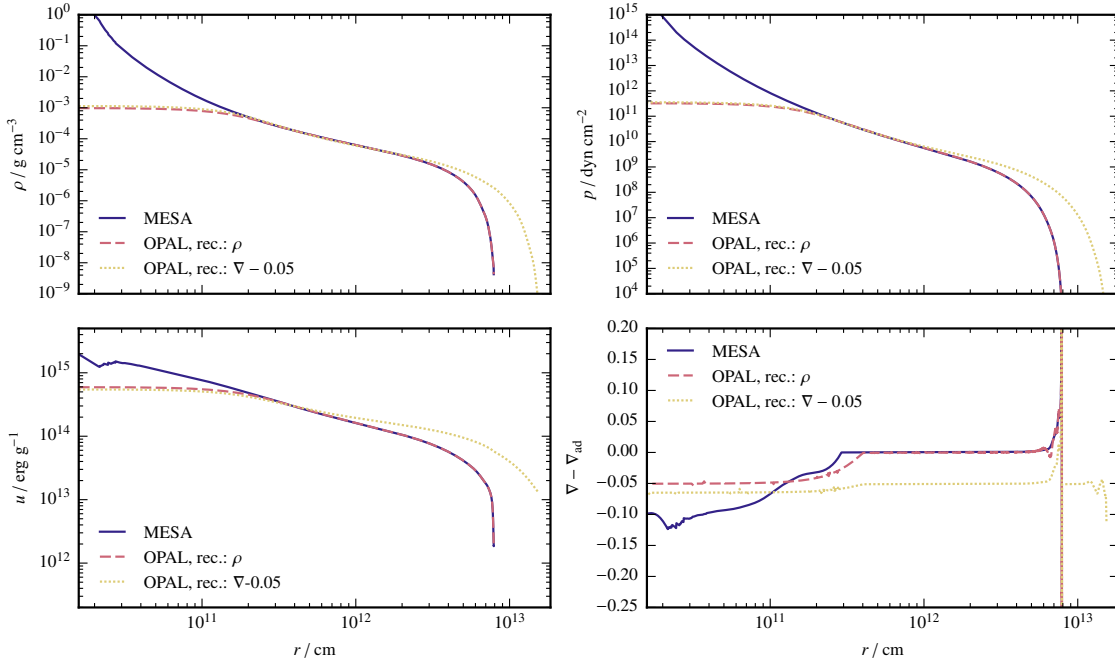
Figure 4.13 | Comparison of different integration methods for a $1M_\odot$ star at the terminal MS using the OPAL equation of state. The panels show the same quantities as in Fig. 4.9.

Apart from reproducing stellar models for a different equation of state, the reconstruction method for $\nabla - \nabla_{\mathrm{ad}}$ also allows the generation of stellar profiles for use in the hydrodynamics code that can artificially be made convectively unstable or stable by adding or subtracting a constant in Eq. (4.23). A convective envelope, e.g., has a nearly adiabatic stratification over large parts of the envelope. Changing ∇ by a small amount (0.01-0.05, i.e., about 2.5% to 12.5% of the ideal gas adiabatic gradient of 0.4) leads to a convectively stable stratification. Since the temperature gradient is now shallower than in the original profile, the envelope will be larger in radius and mass. This depends on the point where the integration is started: if the integration is started too far out in the envelope, negative values for $m(r)$ may result in the interior. For red giant atmospheres that are treated in the approximate manner outlined in Sec. 4.1.3, this can be circumvented by starting the integration at the boundary to the core and cutting the core out afterwards.

As a first example, Fig. 4.13 shows a $1M_\odot$ TMS star that has a convective surface layer. The reconstruction using the OPAL equation of state reproduces the original profile well. Decreasing ∇ by 0.05 (green line in Fig. 4.13) and starting the integration from the center yields a slightly larger model (17% in radius, 12% in mass) that shows a convectively stable stratification also in the surface layer and thus should not develop any convective motions when mapped to a hydrodynamics code. In Fig. 4.14, the same reconstruction method with a reduced ∇ is applied to a $2M_\odot$ RG that was cut at 5% of the radius using the approximation from Sec. 4.1.3. This results in a model with a convectively stable envelope. However, the mass profile here deviates quite strongly from the original profile: it is 61% larger in radius and 88% larger in mass. This effect is even larger for more extended profiles as can be seen for a $5M_\odot$ AGB star that is shown in Fig. 4.15. Also here, this reconstruction method yields a convectively stable model, but the radius increases by 95%
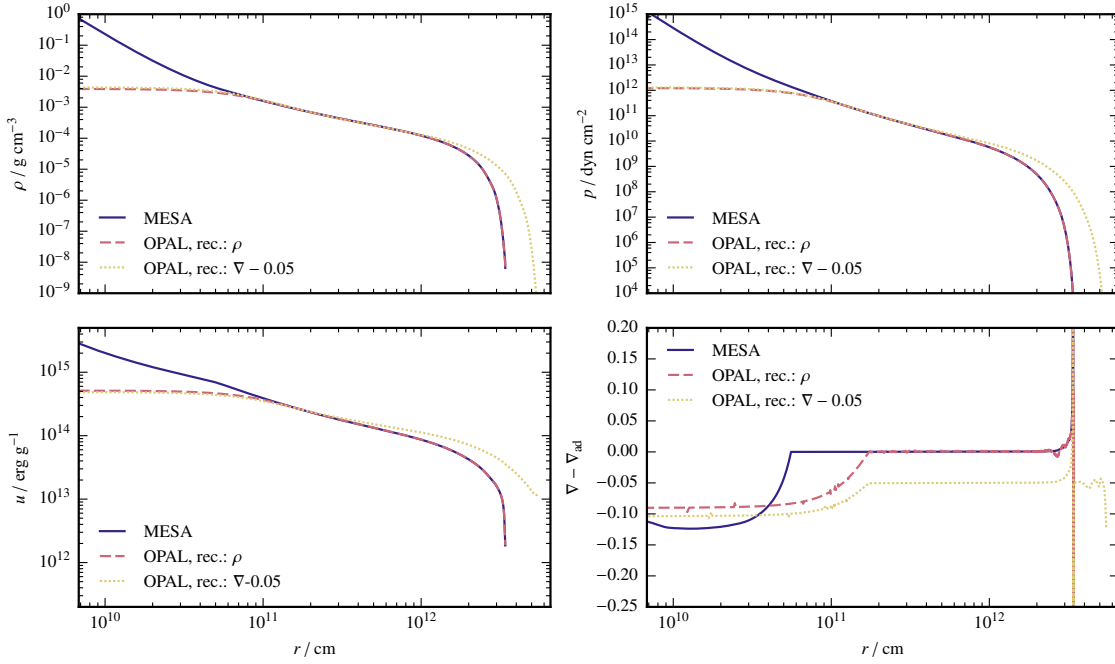
Figure 4.14 | Comparison of different integration methods for a $2M_\odot$ RG using the OPAL equation of state. The profile was cut at 5% of the stellar radius. The panels show the same quantities as in Fig. 4.9.

Figure 4.15 | Comparison of different integration methods for a $5M_\odot$ AGB star using the OPAL equation of state. The profile was cut at 5% of the stellar radius. The panels show the same quantities as in Fig. 4.9.

and the mass by 160%. Although the mass profile changes using this reconstruction method, these models can be used for testing the numerical stability in the hydrodynamics simulation (because convective motions should be absent) while still having density and pressure profiles with similar shapes in similar ranges.

4.2 Initial Single Star Models

In this section, we use the approximation and reconstruction methods as described in the previous section to create stable models of giant atmospheres that can be used as suitable initial conditions for CE simulations. We discuss the numerical stability of models in Sec. 4.2.1 and explain additional numerical methods in Sec. 4.2.2. Results from hydrodynamics simulations are shown in Sec. 4.2.3 for RG stars and Sec. 4.2.4 for AGB stars, where we examine the stability of stellar models for different resolutions, different grids and different parameters of the integration method. Since most giant envelopes are convectively unstable, we also study the numerical stability in convectively stable models to discriminate velocities that are physical from those that are numerical artifacts. We conclude in Sec. 4.2.5.

4.2.1 Stable Numerical Representations

After creating the initial radial profiles – either by taking the stellar evolution data or by applying some approximations – they are mapped to a grid and used for three-dimensional hydrodynamics simulations. Numerical schemes for hydrodynamics are complex and there are several sources for discretization errors which may lead to unstable representations of atmospheres. In this case, instabilities may emerge with large, potentially also non-symmetric, spurious velocities resulting in expanded profiles or pulsating envelopes.

The objective is thus to arrive at stable representations of these atmospheres in hydrodynamics simulations. It is, however, difficult to define stringent criteria on the stability since inherent, convective motions are present in convectively unstable envelopes, and hence the hydrostatic equilibrium cannot be fulfilled exactly. For Mach numbers that are not too large ($\lesssim 0.1$), a stationary state should result with only small deviations from the hydrostatic equilibrium.

We require that after several dynamical time scales the following approximate conditions are met in the hydrodynamics simulations:

1. The deviations from the initial pressure and density distributions should be small.

2. The difference of both sides of the hydrostatic equilibrium equation (4.1), i.e. $|\nabla p + \rho \nabla \Phi|$, should be small.

3. For convectively stable atmospheres, the Mach numbers in the atmosphere should be very small compared to the Mach numbers expected in the problem.

4. For convectively unstable models, a stationary state should be reached.

5. To exclude the presence of pulsations, the potential energy of the system should be constant.

To allow the hydrodynamics code to relax the initial profile to a stable representation, sufficient numerical resolution is required and damping has to be applied which smoothes out unphysical velocity fluctuations caused by different discretizations of pressure and gravitational acceleration (see Sec. 4.2.2).

4.2.2 Numerical Methods

For the hydrodynamics simulations, we employ the finite volume code AREPO (Springel, 2010a) as described in Sec. 3.2. As equation of state, we will use either an ideal equation of state with $\gamma = 5/3$ as appropriate for a monatomic gas or the OPAL equation of state (Rogers et al., 1996; Rogers & Nayfonov, 2002) which is the same equation of state in the density-temperature region of interest as used in the MESA stellar evolution code with which the initial stellar models are computed.

Resolution Requirement

The mapping of stellar models to hydrodynamics grids introduces various errors in the discrete hydrostatic equilibrium that may vary for different numerical methods. The stellar model grid with high resolution in radial direction is mapped to a multi-dimensional grid with lower radial resolution, thus introducing interpolation errors. Apart from this, velocity fluctuations in hydrostatic atmospheres arise in a hydrodynamics simulation mainly due to the different discretization of the Euler equations and gravity. In the finite volume scheme of AREPO, the pressure is computed from the equation of state using the conserved quantities that are updated by calculating their fluxes over the interface between neighboring cells. The pressure gradient is computed by a least square fit using data from neighboring cells. The gravitational source term, in contrast, is computed at the center of mass of each cell using a tree solver in an independent step. This introduces a mismatch between the pressure gradient and the gravitational force thus violating the hydrostatic equilibrium.

The magnitude of the velocity fluctuations caused by this mismatch can be estimated for a simple one-dimensional example of an isothermal atmosphere with pressure scale height H. For this atmosphere, the update of the momentum can be computed according to the finite volume scheme. The discrete pressure can be expanded into a Taylor series in the grid spacing δ, where the first order term cancels the gravitational source term. The higher order terms depend on the numerical flux function, i.e., on the Riemann solver and on the reconstruction. For the AREPO scheme, these terms lead to spurious velocities that can be expressed in terms of the Mach number[2] as (for details of the computation, see Appendix B)

$$M = \frac{C_{\mathrm{CFL}}}{12\gamma} \left(\frac{\delta}{H}\right)^3 + O\left(\left(\frac{\delta}{H}\right)^4\right), \tag{4.24}$$

where γ is the adiabatic index and C_{CFL} the Courant-Friedrichs-Levy constant from the stability constraint for the time step $\Delta t = C_{\mathrm{CFL}}\delta/c_s$.

This result depends on the Riemann solver and on the reconstruction employed in the numerical scheme and will differ for other solvers or reconstructions. Moreover, it is strictly only valid in the one-dimensional case. It should, nevertheless, give a lower limit for the resolution that is needed also in multi-dimensional simulations to reduce velocity fluctuations due to the spatial discretization.

Thus, to stabilize a hydrostatic atmosphere down to Mach numbers of 0.01 (0.001), one pressure scale height has to be resolved with at least 3.2 (6.8) cells (assuming $\gamma = 5/3$ and $C_{\mathrm{CFL}} = 0.4$). This is of course only a necessary but not a sufficient condition for stable hydrostatic equilibria. We ensure that all our initial models fulfill this criterion and have sufficient resolution per pressure scale height.

---

[2]The Mach number is defined as fluid velocity divided by sound speed.

Relaxation

Even if the resolution requirement is met, other sources of numerical error (e.g., interpolation error, errors from the gravity solver) still introduce spurious velocity fluctuations. Thus, an appropriate relaxation procedure is necessary when mapping 1D stellar models to grids: spurious velocity fluctuations have to be damped. Damping can be reached by adding a term in the momentum equation corresponding to

$$\dot{\boldsymbol{v}} = -\frac{1}{\tau}\boldsymbol{v}, \tag{4.25}$$

that has on the PDE level the solution

$$\boldsymbol{v}(t) = \boldsymbol{v}_0 \exp\left(-\frac{t}{\tau}\right), \tag{4.26}$$

which tends to zero on the damping time scale τ. The time discretization is the same as for the rest of the scheme, and Eq. (4.25) is simply added as an additional source term.

The value of the damping timescale is essential for reaching stable models, especially for dilute giant envelopes that encompass many timescales. The following scheme, based on Pakmor et al. (2012) and Rosswog et al. (2004), proved to produce stable models (for the simulations, see Sec. 4.2.3): the physical time of the whole relaxation run is chosen to be $10t_{\mathrm{dyn}}$ where the dynamical timescale t_{dyn} can either be the sound crossing time or the free-fall timescale (which are usually of similar order); we use the sound crossing time of the stellar models (cf. Fig. 4.4 for $2M_\odot$ models). For the value of the damping timescale, we use a small value $\tau_1 = t_{\mathrm{dyn}}/10$ in the beginning that is subsequently reduced to $\tau_2 = t_{\mathrm{dyn}}$ according to

$$\tau(t) = \begin{cases} \tau_1, & t < 2t_{\mathrm{dyn}} \\ \tau_1 \left(\frac{\tau_2}{\tau_1}\right)^{\frac{t-2t_{\mathrm{dyn}}}{3t_{\mathrm{dyn}}}}, & t < 5t_{\mathrm{dyn}} \\ \infty, & t > 5t_{\mathrm{dyn}} \end{cases} \tag{4.27}$$

The exponential form ensures that the temporal change of the damping timescale is proportional to the damping timescale itself. This means that damping on longer timescales (i.e., a larger value of τ) is also applied for a longer time. Taking τ_2 of the order of the dynamical timescale is necessary to suppress pulsations that typically occur on this timescale. After $5t_{\mathrm{dyn}}$, the damping is shut off and the system is evolved for further $5t_{\mathrm{dyn}}$ to ensure that the stellar model is stable in the hydrodynamics simulation without damping being applied.

This damping procedure can also be seen as enforcing the algebraic equation $\boldsymbol{v} = 0$ as part of the hydrostatic equilibrium which is easier than trying to enforce the differential equation $\nabla p = -\rho\nabla\Phi$. This does, however, not guarantee that the intended hydrostatic equilibrium profile is recovered. But, as stated above, we check that the final atmosphere follows the initial pressure and density distributions closely.

Computational Grids

Because AREPO uses an unstructured grid, one has to define the locations of the mesh-generating points alongside the quantities needed by the code (mass, internal energy) in the corresponding cells to define the initial conditions. Different computational grid types are presented in Appendix A. The main grid type used in the following is the HEALPix grid that consists of spherical shells following the mass distribution inside the star with cell positions in the shells according to the HEALPix distribution (Górski et al., 2005).

Table 4.1 | Overview of Relaxation Runs. The table shows data for 14 different simulations for the initial $2M_\odot$ RG model. The columns display a model letter, a model name (first letter: EOS, O – OPAL, I – Ideal; second: reconstruction method: d – density, g – temperature gradient, additional number: shift of temperature gradient in per cent; then two letters for the grid: HP – HEALPix, CU – cubic, CA – cubic adaptive, CN – cubic nested; then rxx specifying the core cutoff radius in xx%; finally nxey denoting the number of cells as $x \times 10^y$), the equation of state, the reconstruction method (cf. Sec. 4.1.5), the grid type (HP – HEALPix, CU – cubic, CA – cubic adaptive, CN – cubic nested; cf. Sec. 4.2.2), the core cutoff radius r_c as a fraction of the initial model radius (cf. the approximation in Sec. 4.1.3), the number of cells N, the radius and gas mass of the reconstructed profile in solar units, the mean Mach number at the end of the relaxation run and the mean relative difference in the hydrostatic equilibrium. The mean values are computed using the cell mass as weight. The core mass in all simulations is $0.38M_\odot$.

|	Model	EOS	Recon.	Grid	r_c/R	N	$\frac{R}{R_\odot}$	$\frac{M_{env}}{M_\odot}$	$\overline{\mathcal{M}}$	$\frac{|\rho\boldsymbol{g}-\nabla p|}{\max(|\rho\boldsymbol{g}|,|\nabla p|)}$
A	OdHPr05n2e6	OPAL	ρ	HP	0.05	2×10^6	49	1.6	1.2×10^{-1}	2.7×10^{-2}
B	OdHPr05n5e5	OPAL	ρ	HP	0.05	5×10^5	49	1.6	1.2×10^{-1}	2.7×10^{-2}
C	OdHPr05n1e5	OPAL	ρ	HP	0.05	1×10^5	49	1.6	7.5×10^{-2}	2.6×10^{-2}
D	OdHPr02n5e5	OPAL	ρ	HP	0.02	5×10^5	49	1.6	1.3×10^{-1}	3.0×10^{-2}
E	OdHPr10n5e5	OPAL	ρ	HP	0.10	5×10^5	49	1.6	8.6×10^{-2}	2.3×10^{-2}
F	Og02HPr02n5e5	OPAL	$\nabla - 0.02$	HP	0.02	5×10^5	62	2.8	1.9×10^{-2}	1.4×10^{-2}
G	Og02HPr05n5e5	OPAL	$\nabla - 0.02$	HP	0.05	5×10^5	59	2.1	9.6×10^{-3}	1.3×10^{-2}
H	Og02HPr05n2e6	OPAL	$\nabla - 0.02$	HP	0.05	2×10^6	59	2.1	9.1×10^{-3}	8.2×10^{-3}
I	Og05HPr05n5e5	OPAL	$\nabla - 0.05$	HP	0.05	5×10^5	79	3.0	5.3×10^{-3}	1.2×10^{-2}
J	IdHPr05n5e5	Ideal	ρ	HP	0.05	5×10^5	49	1.6	6.0×10^{-3}	1.3×10^{-2}
K	Ig00HPr05n5e5	Ideal	∇	HP	0.05	5×10^5	40	1.2	4.5×10^{-2}	1.6×10^{-2}
L	OdCUr05n5e5	OPAL	ρ	CU	0.05	5×10^5	49	1.6	1.2×10^{-1}	2.6×10^{-2}
M	OdCAr05n5e5	OPAL	ρ	CA	0.05	5×10^5	49	1.6	1.1×10^{-1}	2.6×10^{-2}
N	OdCNr05n5e5	OPAL	ρ	CN	0.05	5×10^5	49	1.6	1.1×10^{-1}	2.7×10^{-2}

4.2.3 Relaxation Simulations: RG Models

The numerical methods as outlined in the previous sections can now be tested to examine if stable stars in hydrodynamics simulations can be obtained. Since the parameter space of stellar models as well as numerical parameters is huge, only a subset can be tested. To this end, we ran a suite of 14 simulations for an initial model of a $2M_\odot$ RG in the middle of the giant branch (RG model in Fig. 4.1). A summary of these models is presented in Tab. 4.1. In the following, we study how well the initial model is reproduced in terms of the mechanical structure (i.e., density and pressure distributions) but also regarding convectively stable or unstable layers.

Convectively Stable Atmospheres

The envelope of the $2M_\odot$ RG is convectively unstable and should thus show convective motions. At this evolutionary stage, the magnitude of these velocities is quite substantial: the Mach number according to mixing-length theory as computed by MESA ranges up to 0.5 in the outermost layers. When setting up such an initial model, it is thus difficult to judge if velocities are due to convective motions or if they are numerical artifacts caused by the code. Hence, the magnitude of spurious velocities introduced by the numerical method is best studied for convectively stable stars. We created a set of four artificial, convectively stable models (Og02HPr02n5e5 [F], Og02HPr05n5e5 [G], Og02HPr05n2e6 [H], Og05HPr05n5e5 [I]; see Tab. 4.1) by reconstructing the $2M_\odot$ stellar profile using a temperature gradient shifted by a small amount for convective stability (cf. Sec. 4.1.5) and
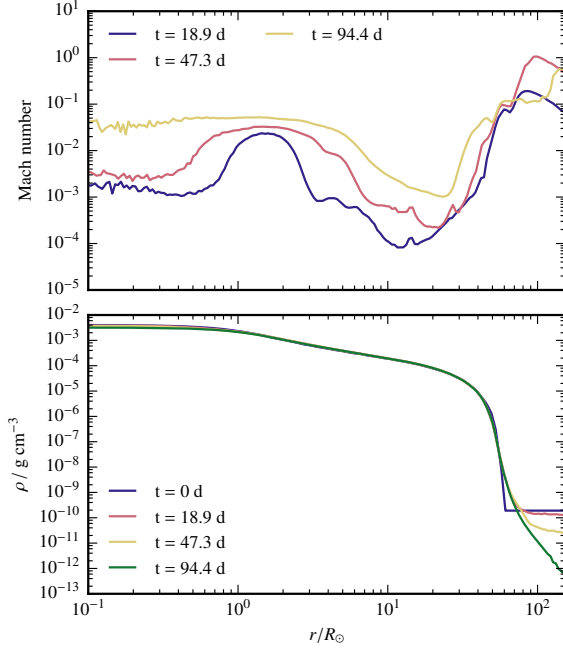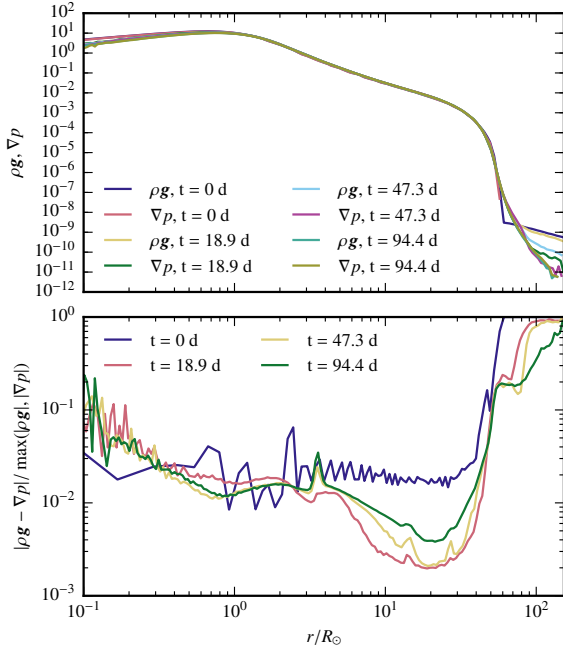
Figure 4.16 | Mach number and density profile for Og02HPr05n2e6 [H]. The top panel show the Mach number at different times during the relaxation run, the bottom panel shows the density at the same times. Both quantities were radially binned and averaged in shells. This model should be convectively stable.

using the OPAL EOS, the same as in the stellar evolution code (in this ρ-T regime). In this way, models are created for which the density and pressure structure resembles the initial stellar profile (see Fig. 4.14). The shift of 0.02 (0.05) corresponds to 5% (12.5%) of the adiabatic gradient for a value of 0.4 in the deeper interior. The flatter temperature gradient, however, leads to larger atmospheres with more mass (Tab. 4.1 and Fig. 4.14).

For the convectively stable model Og02HPr05n2e6 [H], the Mach number and density distributions are shown in Fig. 4.16, and the hydrostatic equilibrium in Fig. 4.17. As required for a stable atmosphere, the density profile follows the initial profile closely (Fig. 4.16, lower panel). In the central part, it decreases by about 10%, and at the surface, the very steep initial gradient cannot be resolved in the hydrodynamics code, hence, a slight expansion occurs. After the damping is switched off at 47.3 d, the profile does not expand further but remains at the same radius. The Mach numbers are very small initially and increase during the relaxation run (Fig. 4.16, upper panel). The atmosphere stays very subsonic with Mach numbers up to 0.05 in the inner part and less than 0.01 in most parts of the envelope. Near the surface, the Mach numbers increase again up to 0.1. In the background regions outside of the star, large spurious fluctuations occur. Nevertheless, the mean Mach number over the whole grid is 9×10^{-3}. An interesting fact during the evolution is that the Mach numbers during the damping phase (at 18.9 d) are largest near the surface and at the radius where the core is connected to the envelope, i.e., at the softening length of its gravitational interaction. From these points, the fluctuations disperse slowly into other regions of the envelope (compare red and yellow lines in Fig. 4.16, upper panel; five dynamical timescales lie in between those profiles).

The hydrostatic equilibrium for model Og02HPr05n2e6 [H] is shown in Fig. 4.17. Both sides of the hydrostatic equilibrium equation are very similar and constant over time (Fig. 4.17, upper panel); small changes can be seen in the center (correlated to the decrease in density there) and near the surface due to the expansion. The error in the hydrostatic equilibrium is shown in Fig. 4.17 (lower panel). Initially, the error is roughly 2% throughout the atmosphere, but decreases during the

Figure 4.17 | Hydrostatic equilibrium for Og02HPr05n2e6 [H]. The top panel shows the two sides of the hydrostatic equilibrium, ∇p and ρg at different times during the relaxation run. The bottom panel shows the relative error in the hydrostatic equilibrium. All quantities were radially binned and averaged in shells. This model should be convectively stable.

relaxation run as the code converges to a hydrostatic equilibrium that is stable in the hydrodynamics simulation. The decrease is largest between $3R_\odot$ and $40R_\odot$ where most of the mass of the envelope is located. The mean error of the hydrostatic equilibrium over the whole grid computed for this model is 8×10^{-3} and hence, the final model fulfills the hydrostatic equilibrium to better than a per cent on average.

The facts that the density profile is constant after disabling the damping and that the Mach number is small indicate that no pulsation is present. This is confirmed by the potential energy showing very small fluctuations < 1% after the initial expansion. Pulsations would cause regular changes in the potential energy with a period of the dynamical timescale (about 9 d for this model). The initial expansion causes a small decrease of the potential energy by 2% to 3% (for all models). After this, the relative difference stays below 1% for all models in Tab. 4.1. Moreover, the error in the total energy is roughly 1% for all models except model OdHPr05n1e5 [C] (about 3%) due to the lower resolution. Thus, none of the models show significant pulsations.

Combining all these facts, we conclude that we are able to generate a model that is in good hydrostatic equilibrium for a convectively stable atmosphere using the methods as described in Sec. 4.2.2. For model Og02HPr05n5e5 [G] with a lower resolution, the results are very similar, only the mean error in the hydrostatic equilibrium is slightly larger with 1.3%. For the model with a smaller core cutoff radius, Og02HPr02n5e5 [F], the error in the hydrostatic equilibrium is similar (1.4%), but the resulting mean Mach number is larger: 0.02 instead of 0.01. Since the generation of the spurious velocities starts at the boundary of the core, this indicates that higher resolutions are needed to stabilize models with smaller core cutoff radii. The model that is farther away from the threshold to convective instability, Og05HPr05n5e5 [I], shows a similar hydrostatic equilibrium error and even lower Mach numbers with a mean of 0.005. Thus, spurious motions are even smaller for this model.

In summary, convectively stable atmospheres that resemble RG envelopes can be reproduced to a good accuracy in AREPO with the methods proposed here.
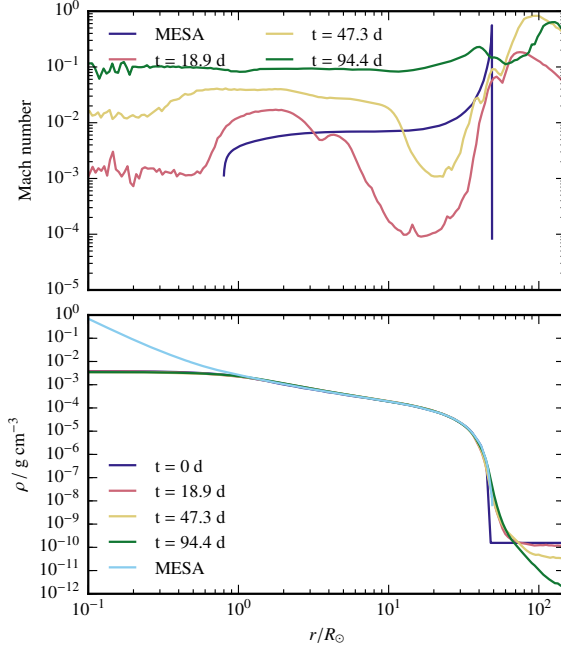
Figure 4.18 | Mach number and density profile for OdHPr05n2e6 [A]. The top panel show the Mach number at different times during the relaxation run, the bottom panel shows the density at the same times. Both quantities were radially binned and averaged in shells. Moreover, the profile from the MESA model is plotted. This model should be convectively unstable.
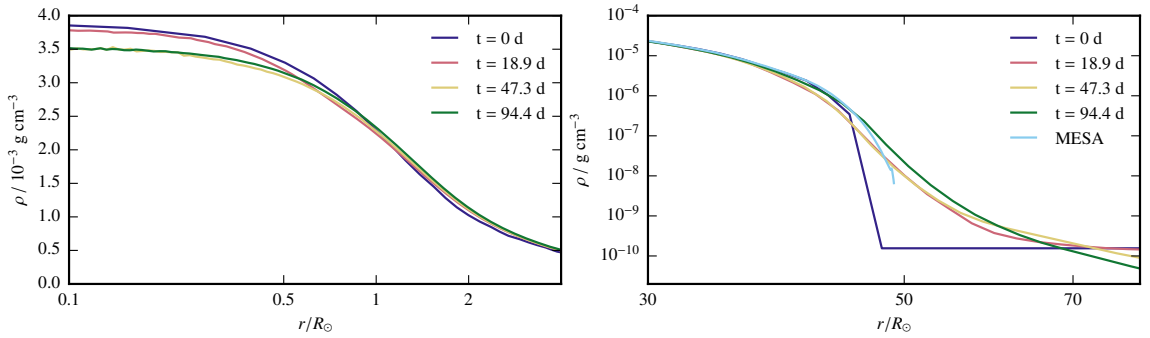
Figure 4.19 | Details of the density profile for OdHPr05n2e6 [A]. The left panel shows the central density distribution at different times. In the right panel, the density profile near the surface is plotted. The density profiles are radially binned and averaged over shells. For comparison, the initial MESA model is also shown in the right panel.

Convectively Unstable Atmospheres

Since our method is able to reproduce convectively stable atmospheres with only small Mach number fluctuations, we now model convectively unstable atmospheres with convective motions in addition. If the Mach number of the convective motions is larger than the Mach number fluctuations (0.01 to 0.02), they should not be influenced by these spurious fluctuations.

As an example of a convectively unstable model, we study OdHPr05n2e6 [A] that is similar to model Og02HPr05n2e6 [H] studied in the previous section, but is reconstructed using the density profile with the same equation of state (OPAL) and thus reproduces the convective behaviour of the original $2M_\odot$ model from MESA.
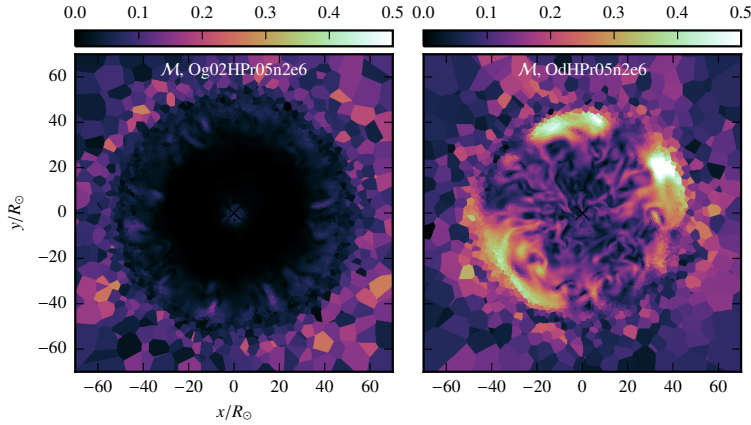
Figure 4.20 | Comparison of Mach number distributions for Og02HPr05n2e6 [H] (left panel) and OdHPr05n2e6 [A] (right panel). Og02HPr05n2e6 [H] should be convectively stable, OdHPr05n2e6 [A] convectively unstable. The low-density region outside the stars (large cells) shows spurious Mach number fluctuations.

The Mach number and density profiles are plotted in Fig. 4.18 together with the original MESA model. The density profile (lower panel) reproduces the original profile quite well throughout the envelope and differs only in the inner part, where it was cut off, and near the surface, where it expands slightly. This can be seen in more detail in Fig. 4.19: in the central part (left panel), the density profile flattens and the central density decreases by about 10%. Near the surface (right panel), the star slightly expands since the density gradient is too steep to be resolved. The difference becomes significant only below $10^{-7}\,\mathrm{g\,cm^{-3}}$ and as the transition to the ambient medium is gradual, the definition of a new radius would be ambiguous. Although convective motions are present, the density profile changes only slightly near the surface after the damping is disabled (i.e., between 47.3 d and 94.4 d, see Fig. 4.19) and is nearly stationary in the rest of the envelope.

The Mach number (Fig. 4.18, upper panel) evolves from a state similar to the non-convective model in the beginning (cf. Fig. 4.16, upper panel) to a state with a Mach number between 0.1 and 0.2 throughout the envelope. The mean Mach number in this model is 0.12. This indicates that convective motions develop and dominate the flow in the envelope. Outside of the star, spurious Mach number fluctuations can be seen similar to the non-convective model. Compared to the Mach number of convective motions according to the mixing-length theory as computed by MESA, the Mach numbers in the hydrodynamics model are much larger in most parts of the envelope. The increase of the Mach number near the surface, however, is similar in both the MESA model and our hydrodynamics model and is due to the decrease in sound speed in the outer layers. The kinetic energy due to the convective motions in this model is 1% of the total energy. This value is similar for the other convective models in Tab. 4.1 whereas for the non-convective model the kinetic energy only amounts to 0.01% to 0.1% of the total energy.

The Mach number distribution in the x-y plane is compared in Fig. 4.20 for the non-convective model Og02HPr05n2e6 [H] (left panel) and for the convective model OdHPr05n2e6 [A] (right panel). For both simulations, one can see spurious fluctuations in the outer region that is discretized in coarse cells.[3] The non-convective model (left panel) shows higher Mach numbers oup to 0.05 only near the center and near the surface, as also seen in the radial profile (Fig. 4.16, upper panel). For the convective model (Fig. 4.20, right panel), a complicated flow pattern is seen that emerged after the damping was turned off. It shows large plumes near the surface where the Mach number

---

[3]This is because the outer region has a low density and because the refinement criterion ensures similar cell masses; thus low-density cells have large volumes.
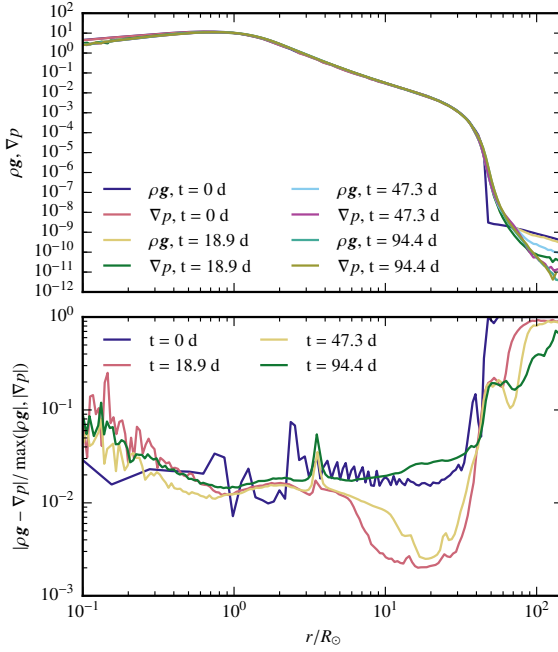
Figure 4.21 | Hydrostatic equilibrium for OdHPr05n2e6 [A]. panel shows the two sides of the hydrostatic equilibrium, ∇p and $\rho \boldsymbol{g}$ at different times during the relaxation run. The bottom panel shows the relative error in the hydrostatic equilibrium. All quantities were radially binned and averaged in shells. This model should be convectively unstable.

can reach values up to 0.5 and features updrafts and downdrafts during its evolution. Thus, the convectively unstable model OdHPr05n2e6 [A] develops convection that can be followed in the hydrodynamics code.

After checking the density profile and the Mach number distribution, we need to examine how well the hydrostatic equilibrium is fulfilled, although a perfect agreement is not expected due to the convective motions. In Fig. 4.21 (upper panel), both sides of the hydrostatic equilibrium equation are compared; in Fig. 4.21 (lower panel), the relative difference is plotted. The general agreement of the pressure gradient and the gravitational acceleration is good (upper panel) and changes in time only slightly in the center (due to the decrease in density there) and near the surface (due to the expansion). The relative difference (lower panel) is about 2% in the beginning, similar to the non-convective model. During the relaxation with damping applied, the profile adapts to even smaller differences, especially between $6R_\odot$ and $30R_\odot$, also similar to the non-convective case. After the convective motions are established, however, the relative difference increases again: the hydrostatic equilibrium is fulfilled slightly worse. The mean error here is 2.7% and thus a factor of 3 larger than in the non-convective case, but still on the per cent level. This indicates that the dynamic motions induced by convection lead to changes in ρ and decrease the quality of the hydrostatic equilibrium.

We can hence conclude that with our method we are able to reproduce a convective envelope of a RG model for which a stationary density structure results that follows the original model. Furthermore, it still approximately fulfills the hydrostatic equilibrium at the per cent level and shows convective motions as expected in the envelope.

Equation of State

All hydrodynamics simulations of CE phases published so far (including most simulations presented in this work) use an ideal gas EOS for the hydrodynamics – except for the SPH simulations by

Nandez et al. (2015). Since stellar evolution codes usually employ an equation of state that accounts for the ionization state of the plasma, the stellar profile has different thermodynamic properties when using an ideal gas EOS. As shown in Sec. 4.1.5 (cf. Fig. 4.11 and Fig. 4.12), this leads to a different behaviour regarding convective stability: stellar models reconstructed with an ideal gas EOS using the density profile from the stellar evolution code are convectively stable in most parts of the envelope. This is because of the different temperature structure and different values for the adiabatic gradient. The thermodynamic structure and the behaviour regarding convection can only be reproduced using the same (or a very similar) EOS.

Model IdHPr05n5e5 [J] of our simulation suite was set up by reconstructing the stellar profile of the $2M_\odot$ RG using the density profile and an ideal gas EOS with $\gamma = 5/3$. According to the stellar evolution code (that uses the OPAL EOS), this model has a deep convective envelope. However, the reconstruction with the ideal gas EOS leads to a convectively stable stratification (cf. Fig. 4.11). This is reproduced by model IdHPr05n5e5 [J]; it does not develop convective motions: the mean Mach number remains as low as 6×10^{-3} and the mean error in the hydrostatic equilibrium is 1.3% (see Tab. 4.1). In this respect, the model is very similar to the artificially stabilized model Og02HPr05n5e5 [G] at the same resolution. Thus, mapping the density and pressure profile from the stellar evolution code to the hydrodynamics code and using an ideal EOS results in a suppression of convective motions that should be present in the convective envelope.

In Sec. 4.1.5, it was shown that the envelope structure can be modified by reconstructing $\nabla - \nabla_{\rm ad}$, i.e., the difference to the adiabatic gradient. Setting this to zero for the reconstruction yields an adiabatic stratification that is convectively unstable. Since this leads to a smaller temperature gradient, a smaller envelope results with less mass (see Fig. 4.11 and model Ig00HPr05n5e5 [K] in Tab. 4.1). The relaxation run for model Ig00HPr05n5e5 [K] shows convective motions, as expected for a convectively unstable model: the mean Mach number is 0.045 and the mean hydrostatic equilibrium error 1.6%. The mean Mach number is smaller than for the models reconstructed using the OPAL EOS which have a mean Mach number of about 0.12 (models OdHPr05n2e6 [A] and OdHPr05n5e5 [B], see Tab. 4.1). This is possibly due to the different stratification.

Hence, we can conclude that with our method we are able to reproduce the expected behaviour of initial stellar profiles also using an ideal EOS. The expected behaviour using this EOS, however, differs from the expected behaviour using the EOS from the stellar evolution code: the convective envelope of the giant is now expected to be convectively stable. Using a different reconstruction method, we showed that stellar profiles that are expected to be convectively unstable using an ideal EOS are reproduced as such in our simulation. Thus, to generate stellar models for the hydrodynamics simulations that show the correct convective behaviour, the same equation of state has to be used as in the stellar evolution code.

Numerical Parameters

The construction of the initial models is influenced by the choice of the parameters resolution, core cutoff radius, and grid type.

To study the convergence behaviour of the simulations, the model reconstructed using the density profile and the OPAL EOS was run in three resolutions (see Tab. 4.1): with 10^5 cells (model OdHPr05n1e5 [C]), with 5×10^5 cells (model OdHPr05n5e5 [B]), and with 2×10^6 cells (model OdHPr05n2e6 [A]). At the lowest resolution, the mean Mach number (0.075) was smaller than for the other resolutions (0.12 for both); the errors in the hydrostatic equilibrium are similar and probably dominated by the presence of convective motions. Since the two highest resolutions show

Table 4.2 | Overview of AGB Relaxation Runs. The table shows data for 2 different simulations for the initial $0.67M_\odot$ AGB model. The columns display a model letter, a model name, the equation of state, the radius and gas mass of the reconstructed profile in solar units, the mean Mach number at the end of the relaxation run and the mean relative difference in the hydrostatic equilibrium. The mean values are computed using the cell mass as weight. Both simulations are reconstructed using the density and mapped on a HEALPix grid with a resolution of 5×10^5 cells. The core mass in both simulations is $0.54M_\odot$, the total mass $0.68M_\odot$ ($0.67M_\odot$ in the MESA model).

|	Model	EOS	$\frac{R}{R_\odot}$	$\frac{M_{\text{env}}}{M_\odot}$	$\overline{\mathcal{M}}$	$\frac{|\rho\boldsymbol{g}-\nabla p|}{\max(|\rho\boldsymbol{g}|,|\nabla p|)}$
O	AGB-OPAL	OPAL	166	0.137	2.1×10^{-1}	8.2×10^{-2}
P	AGB-Ideal	Ideal	166	0.137	1.8×10^{-2}	1.7×10^{-2}

very similar properties, we conclude that the resolution of the convective motions is converged when using more than 5×10^5 cells. The convectively stable atmosphere created by reconstructing the profile of ∇ with a shift of 0.02 was run in two resolutions: with 5×10^5 cells (model Og02HPr05n5e5 [G]) and with 2×10^6 cells (model Og02HPr05n2e6 [H]). For these models, the mean Mach number fluctuations are similar (9.6×10^{-3} vs. 9.1×10^{-3}). The mean error in the hydrostatic equilibrium decreases by a factor of 1.6 which corresponds to the increase in resolution by a factor of 4 in number of cells which roughly means a factor of $4^{1/3} \approx 1.6$; hence, the error decreases to first order with the mean linear cell size.

The properties of simulations using different core cutoff radii are quite similar (compare models OdHPr05n5e5 [B], OdHPr02n5e5 [D], OdHPr10n5e5 [E]), although for a large radius (10%, OdHPr10n5e5 [E]), the mean Mach number is slightly smaller. Decreasing the core cutoff radius is a goal for CE simulations because in this way, a larger fraction of the envelope can be reproduced on the grid. For convectively stable models, the model with a smaller core cutoff radius (model Og02HPr02n5e5 [F], 2% of radius) shows a larger value of the mean Mach number as the model Og02HPr05n5e5 [G] (core is 5% of radius). Here, probably a larger resolution is needed to resolve the hydrostatic equilibrium better where the largest pressure gradients occur, namely at the boundary between core and envelope.

All simulations presented so far used as initial grid configuration spherical shells with cells distributed on these shells according to the HEALPix distribution (cf. Sec. 4.2.2). Simulations similar to model OdHPr05n5e5 [B] have been also carried out for different initial grids: model OdCUr05n5e5 [L] using a cubic grid, model OdCAr05n5e5 [M] using a cubic adaptive grid, and model OdCNr05n5e5 [N] using a cubic nested grid (see Tab. 4.1). However, since we employ a moving mesh with an adaptive refinement to ensure similar cell masses, the difference between these simulations is small and the influence of the initial grid is negligible when using a moving mesh with a refinement on the cell mass. This is, however, not true for static meshes: tests on static meshes show that the mass-adaptive grids show much better equilibria since they are adapted to the symmetry and allow for high spatial resolution in the center. When using a moving mesh with adaptive refinement, the grid will adapt very fast to a similar, mass-adaptive configuration, thus the difference between simulations using different initial grids is negligible. For further simulations, we will use initial models based on the HEALPix grid.
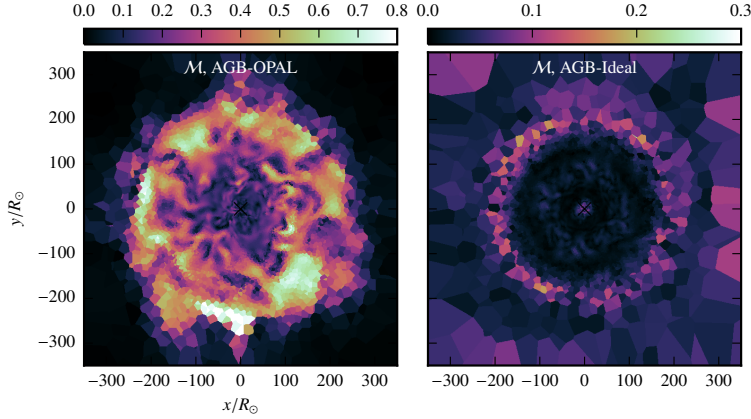
Figure 4.22 | Comparison of Mach number distributions for AGB-OPAL [O] (left panel) and AGB-Ideal [P] (right panel). AGB-OPAL [O] should be convectively unstable, AGB-Ideal [P] convectively stable.
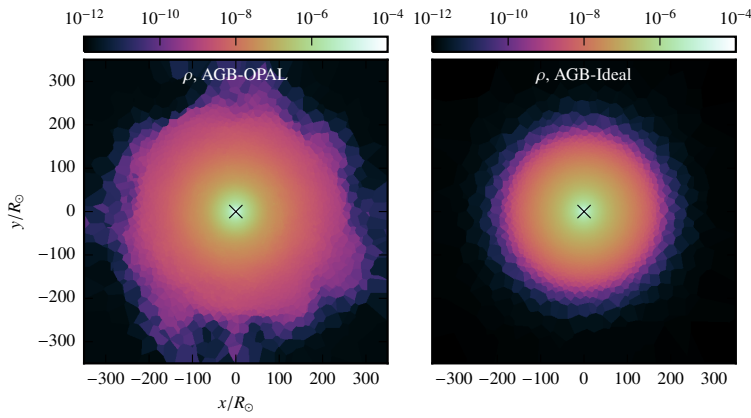
Figure 4.23 | Comparison of density distributions for AGB-OPAL [O] (left panel) and AGB-Ideal [P] (right panel). AGB-OPAL [O] should be convectively unstable, AGB-Ideal [P] convectively stable.

4.2.4 Relaxation Simulations: AGB Models

In addition to the $2M_\odot$ RG model presented in the previous section, a $0.68M_\odot$ AGB star (from a ZAMS model with $1M_\odot$) was set up using the OPAL EOS and the ideal EOS (Tab. 4.2). Both models were reconstructed using the density and mapped to a HEALPix grid with 5×10^5 cells. As shown in Sec. 4.1.5, the model using the ideal EOS is expected to be convectively stable in most parts of the envelope (except near the surface and in a zone at a radius of about $80R_\odot$), whereas the model using the OPAL EOS should be convectively unstable throughout the envelope (Fig. 4.12).

This behaviour is indeed reproduced by our simulations: the mean Mach number in the convectively unstable model AGB-OPAL [O] is 0.2, whereas it is about 0.02 for the convectively stable model AGB-Ideal [P]. Moreover, the distribution of the Mach number in the x-y plane (Fig. 4.22) shows convective motions and large plumes with Mach numbers up to 0.8 for model AGB-OPAL [O] (left panel). Model AGB-Ideal [P] (right panel) shows only small Mach numbers in the envelope that are located in the central region, near the surface, and in a shell at approximately the radius that is expected to be convectively unstable (about $80R_\odot$, see Fig. 4.12).

Model AGB-Ideal [P] also shows a spherical density distribution following the original MESA model (Fig. 4.23, right panel) and the mean error of the hydrostatic equilibrium is about 2%. Hence, this model is still in a good hydrostatic equilibrium. Model AGB-OPAL [O], however, shows a

very dynamic behaviour: the convective cells are comparable to the size of the star and lead to non-spherical density distribution that is also more extended compared to the original model (Fig. 4.23, left panel). This violent behaviour with large convective cells is similar to what is seen in the radiation hydrodynamics simulations by Freytag & Höfner (2008) and Freytag et al. (2012). They use a Cartesian grid, fixed gravitational field, non-local radiative transport and insert energy in the interior corresponding to the core luminosity to drive convection. They find a complex dynamical behaviour with large convective cells and shocks in the atmosphere. Although we do not include radiative transport, the convective motions in the atmosphere look qualitatively similar in our models.

4.2.5 Conclusions

Creating stable models of giant stars in hydrodynamics simulations is paramount for modeling the CE phase, but poses a tough problem because of the large range in temporal and spatial scales. As an approximation, the core of the giant can be replaced by a point mass. Taking the softened gravitational acceleration of the core into account, approximate stellar profiles of the envelope can be created. A correct continuation of the density profile to the center of the star is important for the stability of the profiles. These profiles can be mapped to different unstructured grids and a specific damping is applied to relax the models to a hydrostatic equilibrium in hydrodynamics simulations. The damping is only applied in the first half of the relaxation run and switched off for the second half to ensure that no unphysical processes occur on several dynamical timescales. These methods are applied to the profile of a $2M_\odot$ RG in the middle of the RGB and to a $0.68M_\odot$ AGB star, both calculated using the stellar evolution code MESA (Paxton et al., 2011, 2013, 2015). The simulations demonstrate that stable models of these convective envelopes can be created in hydrodynamics simulations using the AREPO code.

To asses the numerical stability of the models, we also study envelopes that are reconstructed to be convectively stable for the $2M_\odot$ RG model. Convective stability is reproduced in the hydrodynamics simulations with mean Mach numbers at the end of the relaxation runs being below 0.02. The convectively unstable models develop convective motions with mean Mach numbers of 0.12 that are much larger as expected from the velocities given by mixing-length theory. The simulations seem to be converged in resolving the convective motions already using 5×10^5 cells. Other numerical parameters, such as the core cutoff radius or the grid type play only minor roles. If the hydrodynamics simulations use an ideal gas EOS and not the same EOS as the stellar evolution code, the resulting profile is convectively stable. This behaviour is consistently reproduced in our simulations. This means that simply mapping the density and pressure of a stellar model taken from a stellar evolution code (that usually accounts for ionization in its EOS) to a hydrodynamics code using an ideal EOS fails to reproduce the convective behaviour of the envelope. It is, however, possible that the injection of kinetic energy through spurious velocity fluctuations can activate convective behaviour since the envelope is near the border to convective instability.

The simulation of an AGB star using the same EOS as in the stellar evolution code shows a very dynamic behaviour with convective cells reaching the size of the star and Mach numbers up to 0.8. This behaviour is similar to the radiation hydrodynamics simulations by Freytag & Höfner (2008) and Freytag et al. (2012).

Hence, we conclude that our relaxation procedure allows to create initial single-star models for giants that are in a stable hydrostatic equilibrium in hydrodynamics simulations. These models are suitable for being used as initial conditions for binary systems.

4.3 Initial Binary System Models

After having created stable models of giant atmospheres, these can be used for generating initial conditions for simulations of binary systems, i.e., for simulations of the CE phase. In this section, we will first describe how to setup a binary in different rotation states without doing an additional relaxation step in Sec. 4.3.1. Then, a method for relaxing the system in the corotating binary frame is presented in Sec. 4.3.2.

4.3.1 Setup of Binary Systems

In order to create initial conditions for hydrodynamics simulations of CE phases, a relaxed model of a single RG star obtained as described in Sec. 4.2.3 is used as a primary star. A companion star may be added as a resolved star or as a point mass[4] that is treated in the same way as the RG core. The companion is placed at a distance a from the RG core in positive x direction. For first simulations, this distance is chosen as the radius of the RG such that the companion starts at the surface of the RG. Both stars are placed on a Kepler orbit with a frequency of

$$\omega = \sqrt{\frac{G(m_{\mathrm{RG}} + m_{\mathrm{comp}})}{a^3}}, \tag{4.28}$$

where G is the gravitational constant and m_{RG} and m_{comp} the mass of the RG and the companion, respectively.

Instead of a synchronous rotation with the frequency given in Eq. (4.28), a general degree of corotation χ (0: no corotation; 1: synchronous rotation) is enforced by adding

$$-(1 - \chi)\boldsymbol{\omega} \times (\boldsymbol{r} - \boldsymbol{r}_{\mathrm{core,RG}}) \tag{4.29}$$

to the velocity of the RG envelope, where $\boldsymbol{r}_{\mathrm{core,RG}}$ is the position of the RG core and $\boldsymbol{\omega}$ points in the z direction. Using this approach, different rotational states of the envelope can be compared in simulations.

This approach, however, yields only approximate initial conditions, because the RG model was not relaxed taking into account the gravitational field of the companion and the rotation of the system. Moreover, the companion is placed at the surface of the RG envelope, although mass transfer sets in already at the Roche lobe radius. Thus, the timescale of spiral-in is expected to be shorter compared to initial conditions with a companion placed at the Roche lobe. Nevertheless, these conditions provide an approximate starting point that enables us to study the hydrodynamic interaction of a CE phase during the spiral-in; also it allows comparison to other recent studies with similar initial conditions (e.g., Passy et al., 2012). Moreover, the timescale of orbital decay at the Roche lobe distance is still so large that it is computationally not feasible to start the simulations from there.

4.3.2 Relaxation in the Corotating Binary Frame

The initial conditions given in the previous section neglect the presence of the companion as well as the rotation of the system during the relaxation procedure. This can be improved using an

---

[4]This depends on the nature of the companion star: for compact companions, such as white dwarfs or neutron stars, the difference in temporal and spatial scales are too large. MS companions may perhaps be resolved, since the difference in scales is not as large. In the simulations presented in this work, the companion is always treated as point mass.

additional relaxation step in a corotating frame that includes the companion star. Dan et al. (2011) found in their mass transfer simulations in double white dwarf binaries that carefully constructed initial conditions lead to a more stable mass transfer and increase the time until the system merges. For simulations of the CE phase, creating initial conditions in a better equilibrium should be especially important when one tries to connect the simulation to the progenitor binary prior to the onset of mass transfer. It is, however, still unclear how this can be reached in a computationally feasible way.

The first step in this relaxation procedure consists of placing the model obtained from the single star relaxation run and the companion on the grid at a distance of 110% of the Roche lobe radius as given by the Eggleton (1983) approximation,

$$R_{\mathrm{RLOF}} = \frac{0.49 q^{2/3}}{0.6 q^{2/3} + \ln(1 + q^{1/3})}, \tag{4.30}$$

which is better than 1% over the whole range $0 < q < \infty$ (q: mass ratio).

In the next step, additional accelerations are added to each cell during the relaxation run that correspond to the centrifugal force and a damping term, similar to the procedure outlined by Dan et al. (2011). The centrifugal acceleration is given by

$$\boldsymbol{a}_{i,\mathrm{cent}} = -\boldsymbol{\omega} \times \left[\boldsymbol{\omega} \times (\boldsymbol{r}_i - \boldsymbol{r}_{\mathrm{cm}}) \right], \tag{4.31}$$

where $\boldsymbol{\omega} = \omega \hat{\boldsymbol{e}}_z$ points in the z direction with the orbital frequency given by the Kepler law,

$$\omega = \sqrt{\frac{G(M_1 + M_2)}{a^3}}, \tag{4.32}$$

that is computed every time the system is propagated on the largest timestep. Here, $\boldsymbol{r}_{\mathrm{cm}}$ denotes the center of mass of the system, $\boldsymbol{r}_i$ the position of cell i, M_1 the mass of the first star, M_2 the mass of the second star, and a the distance between their centers of mass. Additionally, a damping term is added,

$$\boldsymbol{a}_{i,\mathrm{damp}} = -\frac{\boldsymbol{v}_i}{\tau}, \tag{4.33}$$

that includes a damping timescale τ that is set to a tenth of the dynamical timescale of the primary red giant. One (or both) of the stars can be enforced to a certain degree χ of corotation by adding the corresponding velocity from Eq. (4.29) to the damping term (cf. Dan et al., 2011)

$$\boldsymbol{a}_{i,\mathrm{damp}} = -\frac{\boldsymbol{v}_i + (1 - \chi)\boldsymbol{\omega} \times (\boldsymbol{r}_i - \boldsymbol{r}_{\mathrm{core,RG}})}{\tau}, \tag{4.34}$$

where $\chi = 0$ corresponds to stars at rest and $\chi = 1$ to a synchronized state, and where $\boldsymbol{r}_{\mathrm{core,RG}}$ denotes the position of the core of the RG or in a more general case, the center of mass of the corresponding star (primary or secondary). Moreover, an additional acceleration accounting for the Coriolis force,

$$\boldsymbol{a}_{i,\mathrm{cor}} = -2\boldsymbol{\omega} \times \boldsymbol{v}_i, \tag{4.35}$$

can be included, although this should not be necessary for finding initial conditions that are in perfect hydrostatic equilibrium. If the primary RG, however, possesses a convectively unstable envelope, convective motions are present. In this case, the Coriolis force is needed and, moreover, the damping should be reduced after some initial relaxation time.
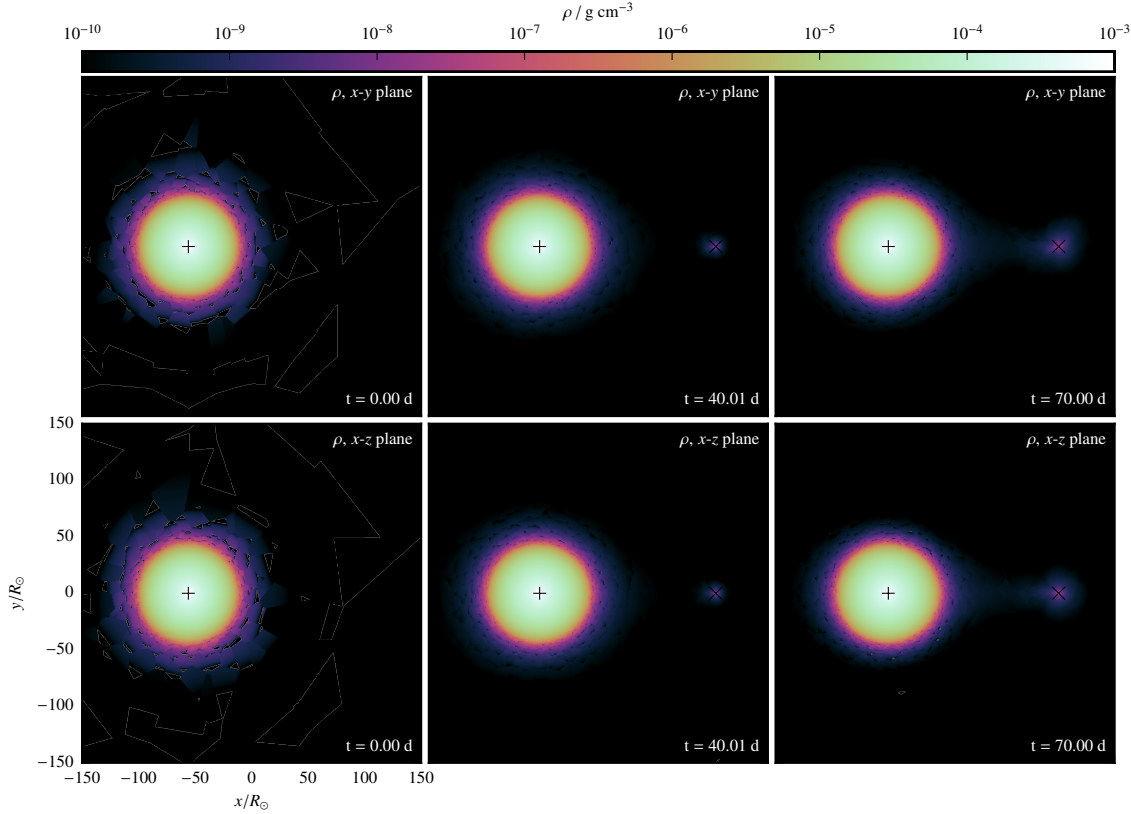
Figure 4.24 | Relaxation in corotating frame. Shown is the density in the orbital x-y plane (top row) and in the perpendicular x-z plane (bottom row) for different times during the binary relaxation run. The initial configuration with a distance of $1.1 R_{\mathrm{RLOF}} = 168 R_\odot$ is shown in the left column. The middle column shows the system after applying damping for 40 d, now at $156 R_\odot$. In the right column, the system has been shrunk to the Roche lobe distance of $R_{\mathrm{RLOF}} = 151 R_\odot$ after 70 d (i.e., ten dynamical timescales). The white lines in the left columns are rendering artifacts caused by very large cells.

During the relaxation run, the system is evolved for ten dynamical timescales in total. During the first two dynamical timescales, the distance between the two components remains constant. After this, the secondary is moved towards the primary with a velocity

$$\boldsymbol{v} = -\frac{a - R_{\mathrm{RLOF}}}{5\tau}\hat{\boldsymbol{e}}_x. \tag{4.36}$$

This means that the remaining distance to the Roche lobe overflow point is bridged in approximately five dynamical timescales. After eight dynamical timescales, this additional velocity is switched off. Moreover, between 7τ and 8τ, the damping timescale is increased exponentially by a factor of 10; after 8τ, the damping is deactivated.

The course of such a relaxation run is shown in Fig. 4.24 for a corotating system ($\chi = 1$), including all of the forces mentioned above. The primary giant is the $2M_\odot$ RG as introduced in Sec. 4.2.3 with a $1M_\odot$ companion ($q = 0.5$). Its radius is $49R_\odot$, thus the Roche lobe radius is $R_{\mathrm{RLOF}} = 152 R_\odot$ for $q = 0.5$ according to Eq. (4.30). The initial distance is chosen 10% larger as $1.1 R_{\mathrm{RLOF}} = 168 R_\odot$. The upper row shows slices of the density in the x–y plane, the lower row the same in the x–z plane.

The leftmost column shows the state at the start of the simulation, the middle column after applying damping for 40 d and reducing the distance between the components to $156R_\odot$. The rightmost column shows the system after 70 d, after it reached the Roche lobe distance and was evolved without damping for two dynamical time scales. One can see that the initial relaxation phase leads to a deformation of the RG envelope that adapts now to the gravitational field of the secondary and to the centrifugal force. After reaching the Roche lobe distance, the primary overflows its Roche lobe slightly and some small mass transfer to the secondary sets in. This is probably due to the relaxed initial model being slightly larger than the stellar evolution model, thus the Roche lobe distance is slightly larger and mass transfer proceeds at the original Roche lobe distance of the stellar evolution model.

A snapshot of this simulation may now be transferred to the laboratory system by adding the rotational velocities to study the further evolution of the mass transfer. This method has the advantage that after the mapping, less oscillations of the star are introduced since the envelope structure has already adapted to the combined gravitational field of the primary and the companion. These improvements to the initial conditions will be studied in future work.

Chapter 5

A First Common Envelope Simulation on a Moving Mesh

This chapter has been published as:

In this chapter, we present a new hydrodynamic simulation of the dynamical spiral-in forming a CE system. We apply the moving-mesh code AREPO to follow the interaction of a $1M_\odot$ compact companion with a $2M_\odot$ RG possessing a $0.4M_\odot$ core. This code solves the Euler equations on a moving computational grid with adaptive resolution, thus combining the advantages of traditional SPH and AMR codes, e.g., conservation of angular momentum and total energy and resolution of low-mass flows and small-scale flow features. Here, we show that the AREPO code, developed originally for cosmological simulations (e.g., Vogelsberger et al., 2014b; Marinacci et al., 2014), allows us to resolve the hydrodynamical structure of the CE phase in unprecedented detail. Our simulations reproduce the initial transfer of energy and angular momentum from the binary core to the envelope by spiral shocks seen in previous studies, but after about 20 orbits a new phenomenon is observed. Large-scale flow instabilities are triggered by shear flows between adjacent shock layers. These indicate the onset of turbulent convection in the common envelope, thus altering the transport of energy on longer time scales. At the end of our simulation, only 8% of the envelope mass is ejected. The failure to unbind the envelope completely may be caused by processes on thermal time scales or unresolved microphysics. Details of the initial setup are presented in Sec. 5.1. We show the results of the simulation in Sec. 5.2 and conclude in Sec. 5.3.

5.1 Setup

We simulate the dynamical spiral-in of the CE phase with the finite volume hydrodynamics code AREPO (Springel, 2010a, see also Sec. 3.2). AREPO solves the Euler equations on a moving, unstructured Voronoi mesh using an HLLC-type approximate Riemann solver. Self-gravity is included with a tree-based algorithm. We employ an improved gradient estimate and time integration scheme (Pakmor et al., 2016) yielding second order convergence also for general mesh motions. Individual and adaptive time stepping is used, which boosts the computational efficiency due to the multi-scale nature of the system: not all cells are evolved on the shortest time step, but only the cells requiring the smallest time steps. Periodic boundary conditions were chosen for the hydrodynamics solver

with the box size large enough (3.3×10^{14} cm), such that no mass flows over the boundary for a sufficiently long time. The simulation was stopped when the first outflow reaches the boundary.

The binary system was set up by placing a red giant (RG) model on the grid with the core replaced by a gravitation-only particle and then adding another gravitation-only particle to model a non-resolved, compact companion star, e.g., a main sequence star or a white dwarf. Thus, the simulation consists of cells representing the gas of the envelope and the background ("gas cells") and gravitation-only particles representing the RG core and the companion ("core cells").

For preparing the single-star initial conditions, we followed the procedure outlined in Chapter 4. The RG model was created using the stellar evolution code MESA (Paxton et al., 2011, 2013) with a zero-age main sequence mass of $2M_\odot$. To limit the range in time scales, we replaced the core of the RG by a particle interacting only gravitationally. We mapped the resulting model to a grid with mass-adaptive radial shells using a HEALPix distribution (Górski et al., 2005) on each shell. The gravitational force of the particle was smoothed at a length of $h = 7.3 \times 10^{10}$ cm ($\sim 1.0R_\odot$)[1] according to the spline function given in Springel (2010a). This enables us to reach a stable configuration around the particle since the pressure gradients can be resolved sufficiently to counteract the gravitational force of the particle. We treat the gas as an ideal gas with an adiabatic index of 5/3 which is different from the MESA equation of state. However, since we are interested in the envelope where the departure from ideal gas behaviour is small, this approach still allows for a reasonable representation of the star calculated with MESA in AREPO. The mechanical structure of the star is well reproduced in the envelope (differences in density, pressure, and sound speed are less than 5%). Only in the internal energy we observe larger deviations, because we neglect the ionization state of the gas as a first approximation (but see the simulations in Chapter 9. The RG atmosphere was then relaxed by employing an additional damping term to reduce spurious velocities for several dynamical time scales (for details, see Sec. 4.2.2). This resulted in a stable profile with a core mass of $0.38M_\odot$ and an envelope mass of $1.60M_\odot$ (total: $1.98M_\odot$). The Mach numbers in the envelope reach up to 0.1 after the relaxation procedure, similar to what would be expected from the initial MESA model, although we are not able to properly resolve the convection in the envelope. The density and pressure profiles are stable for several dynamical time scales after relaxation without applying any damping. The total number of cells was about 1.8×10^6 with a mean cell mass of $8.7 \times 10^{-7} M_\odot$ at the beginning and 2.7×10^6 with $5.8 \times 10^{-7} M_\odot$ at the end of the simulation due to mesh refinement. The refinement criterion was set to a target cell mass of $8.4 \times 10^{-7} M_\odot$. Additionally, in a sphere of five softening lengths of the gravitation-only particle, the maximum cell radius was bound to a tenth of the softening length. The smallest cells near the RG core have a radius of about 4.6×10^9 cm ($0.07R_\odot$) at the beginning and about 8×10^8 cm ($0.01R_\odot$) at the end of the simulation. This allows us to study small-scale flow features in detail. In the direct vicinity of the RG core, the hydrodynamical flow is only resolved outside of a sphere of radius of the softening length. Nevertheless, we find that a resolution of about 10 cells per softening length is required to ensure energy conservation during the in-spiral. The spatial resolution in recent hydrodynamics simulations of CE phases was lower: the AMR simulations of Ricker & Taam (2008, 2012) have $0.3R_\odot$ cells for a $32R_\odot$ RG, the SPH simulations of Passy et al. (2012) have $0.1R_\odot$ smoothing lengths, and the grid simulations of Passy et al. (2012) $1.7R_\odot$ and $3.4R_\odot$ cells for a $83R_\odot$ RG.

---

[1]This value gives the equivalent Plummer sphere length such that the resulting value of the potential at $r = 0$ is the same as for the Plummer softening. The value where the real softening is applied is $2.8h = 2.9R_\odot$. The reduction of the softening length during the evolution (see later in text) is also applied to this value of $2.8h$.
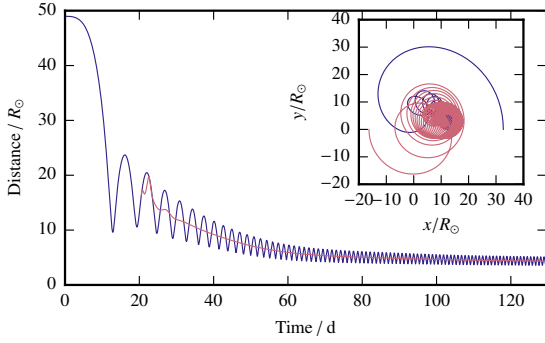
Figure 5.1 | Orbital evolution. Distance of RG core and companion (blue) and major semi-axis (red) in solar radii over time in days. The inset shows the positions of the RG core (red) and companion (blue) in the x-y plane up to 80 d.

The companion was placed on the surface of the RG at the same y and z coordinates as the RG core and at a distance of $49R_\odot$ in the x direction. The mass of the secondary was chosen to be $0.99M_\odot$, half of the primary mass. The velocities were initialized to a rigid rotation around the center of mass with the Keplerian rotation period of 23 d. Moreover, the envelope was assumed to be in 95% co-rotation, similar to the simulations of Ricker & Taam (2008, 2012). More realistic initial conditions would start at the point of Roche lobe overflow to take into account the transfer of energy and angular momentum from the orbit to the envelope. Moreover, the hydrostatic equilibrium in the outer layers is less distorted compared to placing the companion at the surface. However, since the time scales of orbital decay are very long when the first mass transfer starts, it is at the moment computationally infeasible for us to start the simulation at the Roche lobe distance.

The RG atmosphere and the companion were placed in a large box with a side length of 3.3×10^{14} cm and a low background density[2] of 10^{-16} g cm^{-3}. To resolve the gravitational interaction between the cores, the softening lengths of the cores are required to be at most a fifth of the distance between the cores. The simulation was stopped after about 120 d, when the first low-density tidal arm reached the boundary. Since the box was chosen very large, no mass is lost during the simulation. Angular momentum was conserved to high accuracy during the run with an error below 1%.

5.2 Results and Discussion

The simulation starts with tidal deformation of the envelope and mass accretion on the secondary. When the accretion stream hits itself, shocks emerge and the orbit shrinks rapidly by a factor of five during the first revolution (Fig. 5.1). This fast spiral-in slows down after a few orbits and the separation of the RG core and the companion decreases much slower at the end of the simulation. At this point, the system evolved for over 80 orbits and the separation is about $4.3R_\odot$, a factor of 10 smaller than in the beginning. The initially circular orbit becomes eccentric ($e \approx 0.5$), circularizes somewhat in the course of the spiral-in, and the eccentricity settles at a value of 0.18. Thus, the orbit is rather eccentric compared to the simulation by Ricker & Taam (2012) with $e = 0.08$ which may be due to different initial conditions. At the end of the simulation, the time scale of orbital decay ($-a/\dot{a}$, a: semi-major axis) grows to ~ 1.5 yr.

The energy budget during the simulation is shown in Fig. 5.2 for the gas cells, the RG core and its companion, and the sum of both. In our simulation, the core cells interact only gravitationally,

---

[2]The density to which we resolve the initial RG model is 0.002 g cm^{-3}.
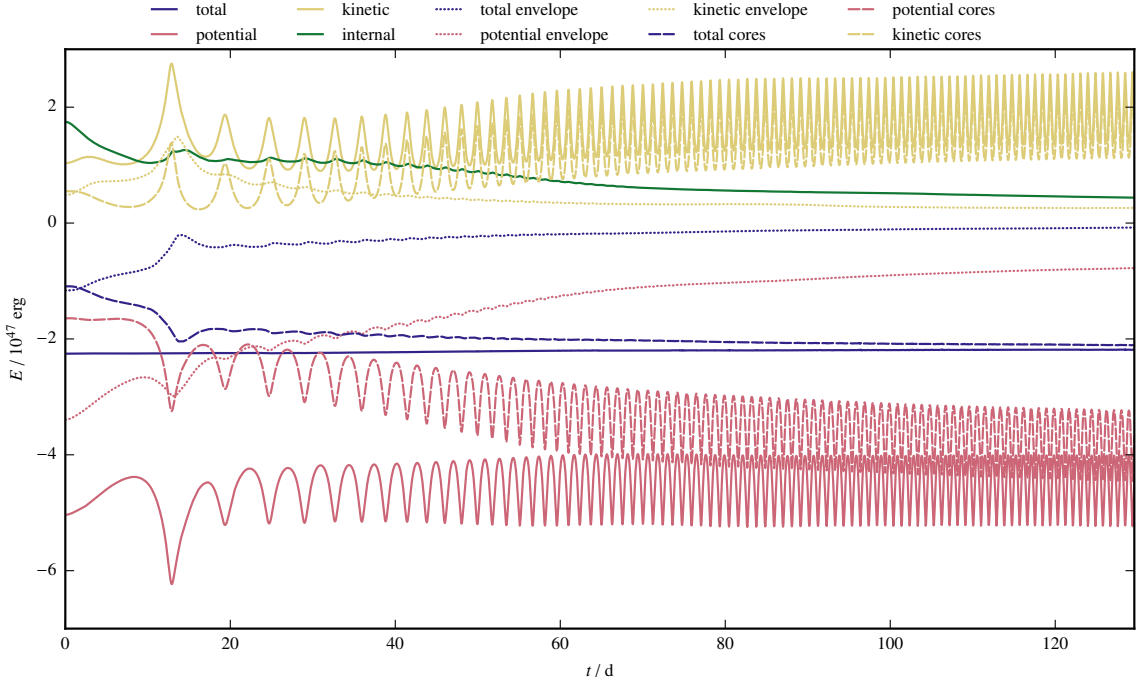
Figure 5.2 | Energy budget during inspiral. Shown are the total (blue), potential (red), kinetic (yellow), and internal energy (green) for the gas of the envelope (dotted), the RG core and the companion (dashed), and summed values (full lines). The summed value of the internal energy is the same as for the gas since the RG core and the companion are gravitation-only particles. The conservation of the total energy is better than 3% during the simulation.

hence, they do not possess internal energy; thus the total internal energy is given by the gas of the RG envelope only. Although large amounts of potential and kinetic energy are converted into one another (up to 1.5×10^{47} erg in one orbit, i.e. 65% of the total energy), the total energy is conserved to better than 3% during the whole run. This means that our resolution is sufficient to accurately represent the regions where gravity is coupled strongly to the hydrodynamics and where the conversion between potential and kinetic energies takes place[3].

During the simulation, energy is transferred from the binary system of the RG core and the companion to the envelope: its binding energy is raised from -1.2×10^{47} erg in the beginning to -7.7×10^{45} erg in the end of the simulation. This energy is mainly taken from the potential energy of the binary system of the RG core and the companion due to the shrinking orbit. The internal energy of the envelope decreases by 1.3×10^{47} erg because of its expansion. Although the total energy of the envelope is negative at the end of the simulation, $0.1 M_\odot$ of the envelope gets unbound, about 8% of its mass. Most of this material is expelled during the first 40 d. After this, the mass loss rate settles to about $0.015 M_\odot \, \text{yr}^{-1}$. If this mass loss rate is sustained, the envelope may be ejected in roughly 100 yr. Similar to the simulations by Passy et al. (2012) and Ricker & Taam (2008, 2012), only a small fraction of the envelope is unbound during the fast spiral-in, although more mass is lost in their simulations at a higher rate.

---

[3]This is not trivial: due to the different discretization of gravity and hydrodynamics, problems with large conversions of potential energy into kinetic or internal energy can lead to substantial errors in the total energy, when the resolution is too low (see the Evrard collapse example in Springel, 2010a). Convergence with resolution around the point masses is studied in Sec. 6.2.
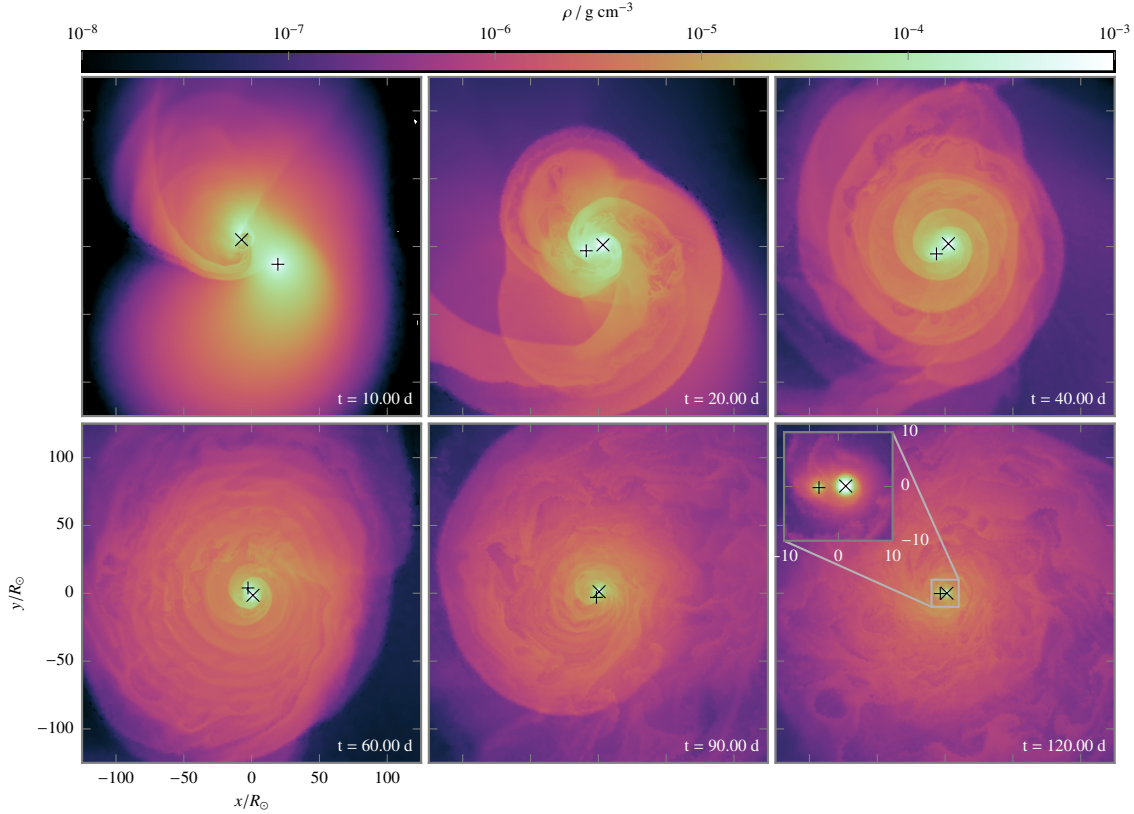
Figure 5.3 | Time series of density snapshots in the x-y plane during spiral-in at six different times. The $\times$ marks the position of the companion, the $+$ marks the position of the RG core. All plots are centered on the center of mass of the RG core and the companion. The inset in the last panel shows the central region of about $20 R_\odot$ with the color scale ranging from 10^{-6} to 10^{-3} g cm^{-3}.

Since systems similar to the final system of our simulation are observed (e.g., J0755+4800 from Gianninas et al., 2014; a $\sim 0.4 M_\odot + \sim 1 M_\odot$ system in a $\sim 3 R_\odot$ orbit), but in a shorter orbit and with the envelope ejected, additional mechanisms must contribute to the evolution that we do not capture in our simulation. This can either be processes acting on longer time scales (up to the thermal time scale) or additional microphysical effects, such as recombination (compare the SPH simulations by Nandez et al., 2015).

The dynamics of the spiral-in is illustrated in Fig. 5.3 as a series of density slices in the x-y plane. During the first orbit, the companion plunges into the envelope and an accretion stream onto it builds up. After 10 d (Fig. 5.3, upper left), an accretion shock is visible that results in a tidal arm moving outwards. Most of the material that is unbound at the end of the simulation stems from this first interaction. During the second orbit, the distance between the RG core and the companion has decreased by a factor of about 5 compared to their initial separation and the two compact components revolve in an eccentric orbit. The shock created by the companion reaches the inner part of the envelope while a second shock is caused by the motion of the RG core. After about 2 orbits (20 d, Fig. 5.3, upper center), the shock created by the RG core overtakes the first tidal arm caused by the companion. The density field in the regions between the shocks does not show

distinct features. After almost seven orbits (40 d, Fig. 5.3, upper right), a layered structure emerges that is created by spiral shocks continuously driven outwards by both the RG core and the compact companion. Shear flows between neighbouring shocks cause Kelvin–Helmholtz instabilities in the outer part of the spiral structure. The spiral structure of the shocks tightens and shear instabilities grow stronger at 60 d (Fig. 5.3, bottom left). At later times (90 d, Fig. 5.3, bottom center), shear instabilities of adjacent layers overlap and form a large-scale instability that connects several regions of the spiral structure. New shocks are still created in the inner part by the RG core and the companion. Near the end of the simulation (120 d, Fig. 5.3, bottom right), the spiral shock structure is not visible anymore. Instead, large-scale instabilities have emerged and dominate the flow pattern. The central part of the domain around the compact components is still well resolved (see inset of the bottom right panel of Fig. 5.3). The flow between the RG core and the companion remains smooth; shocks begin outside the innermost region. During the evolution, the flow shows some asymmetries caused by the first tidal arm which is ejected in the negative x and y directions, resulting in a relocation of the RG core and the companion in the opposite direction.

The structure of the envelope at the end of the simulation after 120 d is shown in Fig. 5.4. The density slice in the x-y plane (Fig. 5.4, upper left) shows that the layered shock structure is only retained in the innermost region. In the outer region, it is washed out and the flow is dominated by large-scale instabilities. In the x-z plane (see middle left in Fig. 5.4), the outflow is concentrated mostly around the equatorial plane in a toroidal structure. Shocks generated in the inner part are washed out by the shear instability in the outer region. To assess the convective stability of the envelope, we employ the Solberg–Høiland criterion (e.g., Kippenhahn et al., 2012) that predicts convective stability for

$$-\frac{\boldsymbol{g} \cdot \nabla s}{c_p} + \frac{1}{\varpi^3}\frac{\partial j^2}{\partial \varpi} > 0, \tag{5.1}$$

where $\boldsymbol{g}$ denotes gravitational acceleration, s entropy, c_p specific heat capacity at constant pressure, j specific angular momentum, and ϖ distance from rotational axis. This quantity is shown in Fig. 5.4 for the x-y plane (upper center) and the x-z plane (middle center). The flow is stabilized by the increase of specific angular momentum (second term) in a sphere of $\sim 7R_\odot$ around the center of mass that is located to the lower left compared to the cores in Fig. 5.4 (upper center). Farther away from the center of mass, the specific angular momentum is nearly constant, and the impact of the second term in the Solberg–Høiland criterion decreases rapidly. Apart from a small region of stability ($\sim 3R_\odot$) around the RG core and the companion, regions of stability and instability alternate over the envelope because of the hydrodynamical flows. The situation is similar perpendicular to the orbital plane, where unstable regions can be found throughout the toroidal structure. The growth time scale associated to the unstable regions is $\lesssim 100$ d; thus, we conclude that large parts of the envelope should be convectively unstable. The radial velocity in the orbital plane (Fig. 5.4, upper right) displays some regions with inflows in the left hemisphere but outflows in the rest of the envelope. The inflow is probably caused by the initial plunge-in of the companion. The layered structure of the shocks is visible in the inner part as jumps, but it is overlaid by the instability farther out. In the x-z plane the radial velocity (Fig. 5.4, middle right) shows mostly inflows in the upper and left hemispheres and outflows in the lower and right hemispheres. This pattern is also seen in the vector plot of the velocity in this plane (Fig. 5.4, lower right) that additionally shows a complex flow structure with whirls corresponding to the instabilities in the flow. This complex structure makes it difficult to predict the further evolution of energy transport in this plane. In the region of the developing instability, the flow is mostly
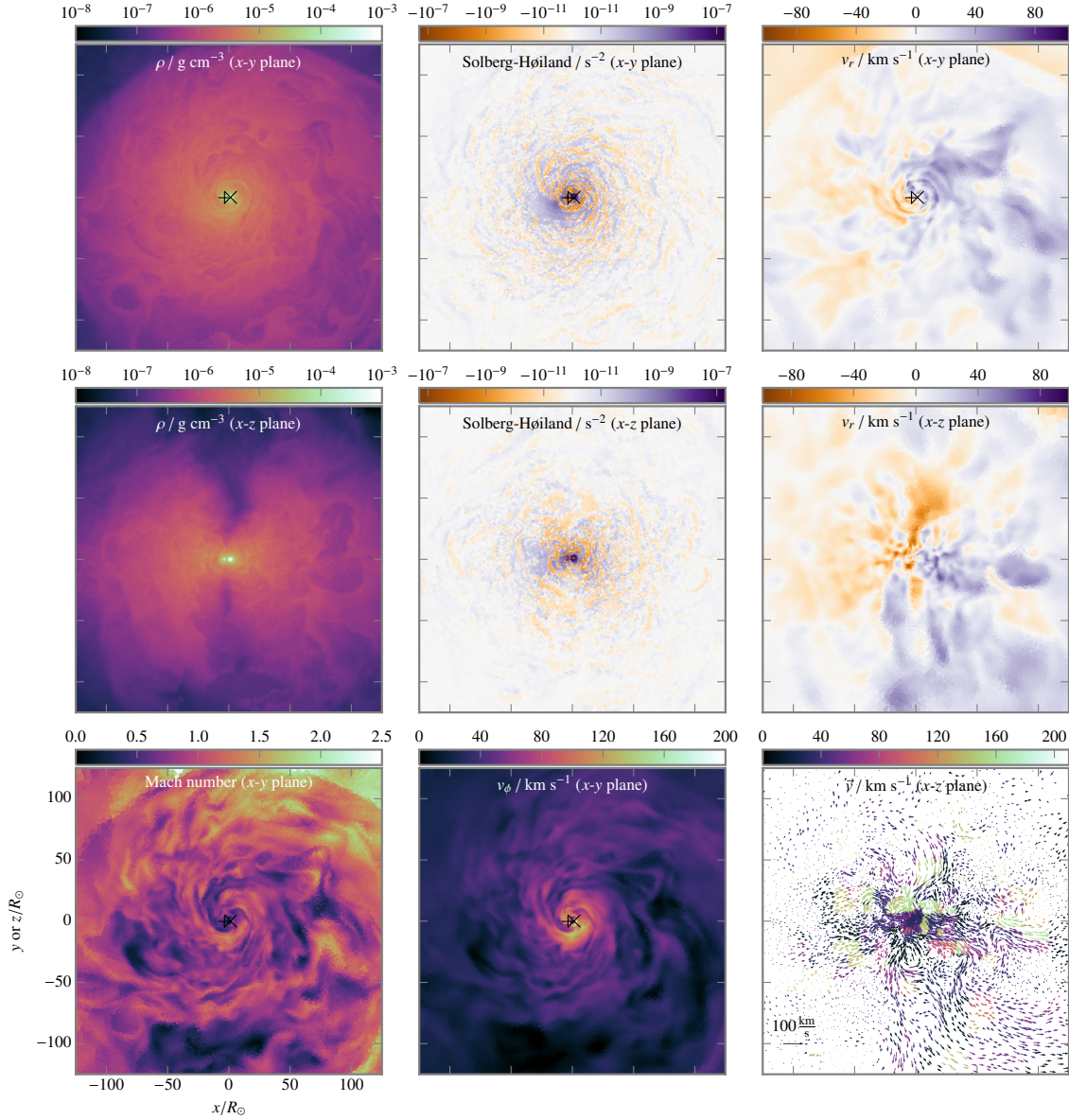
Figure 5.4 | Late snapshot at 120 d. Shown are the density ρ in the x-y (upper left) and x-z plane (middle left), the Solberg–Høiland criterion from Eq. (5.1) using a symmetric logarithmic color coding (blue: stable; orange: unstable) in the x-y (upper center) and x-z plane (middle center), the radial component of the velocity $v_r = \boldsymbol{v} \cdot \boldsymbol{e}_r$ in the x-y (upper right) and x-z plane (middle right), the Mach number (lower left), the angular component of the velocity $v_\phi = \boldsymbol{v} \cdot \boldsymbol{e}_\phi$ (lower center), and a vector plot of the velocity in the x-z plane (lower right), with the color coding indicating the magnitude of the velocity in km s^{-1}. The $\times$ marks the position of the companion, the $+$ marks the position of the RG core. All plots are centered on the center of mass of the RG core and the companion.

subsonic (Fig. 5.4, lower left), whereas it is transsonic in most other parts of the envelope and supersonic behind shocks in the outer regions. The envelope is still mostly co-rotating, as can be seen in the angular component of the velocity (Fig. 5.4, lower center), although the velocity is rather small in the region of the instability. Especially in the inner part, adjacent layers can be found with differing velocities, resulting in shear flows.

The development of large-scale flow instabilities and an inverse entropy gradient indicate the onset of turbulent convection in the differentially rotating envelope. This supports the assumptions of Meyer & Meyer-Hofmeister (1979) of a co-rotating interior and a differentially rotating envelope with angular momentum transport mediated by convection in the envelope.

Large-scale flow instabilities have not been observed in hydrodynamics simulations before. Passy et al. (2012) show a density distribution for their 256^3 grid run after about 5 orbits, where only spiral shocks with smooth regions in between are visible (see their Figure 6). The density slice of the AMR simulations by Ricker & Taam (2012) after roughly 5 orbits displays features that may be caused by shear flows between adjacent spiral shocks. Their simulation was stopped at this instant and it is unclear if large-scale instabilities would have emerged in the further evolution of the model. We suspect, however, that the development of shear instabilities is not seen due to large numerical diffusion in the SPH simulations and due to the background velocity field in the grid simulations. The violation of Galilean invariance in conventional grid-based hydrodynamics codes (when altering the background velocity at the same resolution) suppresses Kelvin-Helmholtz instabilities on a static mesh; this is illustrated in Figure 33 of Springel (2010a). The numerical scheme of AREPO is Galilean invariant, thus, shear instabilities may also develop on top of background velocities.

5.3 Conclusions

With this simulation, we explore the hydrodynamics of the rapid spiral-in during a CE event using the moving-mesh code AREPO. The combination of the nearly Lagrangian mesh motion and the Galilean-invariant scheme enables us to resolve the hydrodynamical structure in unprecedented detail, and complements recent hydrodynamics simulations (Passy et al., 2012; Ricker & Taam, 2012). In particular, we observe, for the first time, the emergence of large-scale flow instabilities. These are caused by shear between adjacent layers of the shock spiral that is created by the in-fall of the companion. These instabilities indicate the onset of turbulent convection, with important consequences for the further evolution of the system by, e.g., altering the energy transport on thermal time scales.

In terms of global quantities, we confirm earlier simulations (Ricker & Taam, 2008, 2012; Passy et al., 2012): only a small fraction of the envelope mass is ejected on a dynamical timescale and the final separation is larger than observed. This may be due to the envelope ejection proceeding on a much longer time scale than that followed in our simulation. It is also possible that we miss other processes driving the loss of the envelope, such as recombination (see Sec. 9).

As a next step, we will improve the modeling of additional microphysical effects, including recombination (see Sec. 9), magnetic fields (see Sec. 7), and examine different parameters (orbital parameters, masses; see Sec. 6) to link the final system characteristics to them in a systematic way. This opens up the exciting prospect to directly connect the hydrodynamics simulations to binary stellar evolution.

Chapter 6

Exploring Different Initial Conditions

The simulation method as established in Sec. 5 (cf. Ohlmann et al., 2016) for a system of a $2M_\odot$ RG star with a $1M_\odot$ companion is applied to different parameters in this section. First, we show that our simulations display convergence at the 5% level already using 1.3×10^6 cells with respect to global quantities such as final separation or mass loss. The crucial point here is to ensure a high enough resolution in the region around the point masses of at least ten cells per softening length. Next, we present results of simulations for different mass ratios, different initial rotational states, and different initial separations. For smaller mass ratios, the final separation is smaller, but still only a small fraction of the envelope is unbound. The initial rotational state of the envelope does not influence the outcome significantly. Starting the simulation at an initial separation 20% larger than in the standard case yields a different evolution but ends at nearly the same final separation.

6.1 Setup

The binary system uses the same initial model as the simulation presented in Sec. 5, a $2M_\odot$ RG star that was relaxed in a separate step to reach hydrostatic equilibrium using the methods described in Sec. 4.1. The computational grid is rebuild in every time step in a periodic box with a side length of 3.3×10^{14} cm $= 4700R_\odot = 22$ AU. On this grid, the relaxed $2M_\odot$ RG model is placed where the core was replaced by a point mass that interacts only gravitationally. The core has a mass of $0.38M_\odot$, the envelope a mass of $1.6M_\odot$; in total the model has $1.98M_\odot$. The companion is then placed in a specific distance as a point mass as well. For the point masses, the gravitational force is softened as given by Eq. (4.8) on a softening length of $h = 7.3 \times 10^{10}$ cm $\approx 1.0R_\odot$. The two stars are surrounded by a background grid with a low density of 10^{-14}g cm^{-3} and a specific internal energy of 10^{12}erg g^{-1}.

During the simulation, the grid was refined primarily to yield a certain target mass: if a cell has a mass larger than twice the target mass, it is refined; if its mass is smaller than half the target mass, it is de-refined. Moreover, in the vicinity of the point masses, an additional criterion is employed: if the distance to a point mass is less than five softening lengths of that point mass, a cell is refined if its radius is larger than a tenth of the softening length and de-refined if its radius is smaller than a 21th of the softening length. For lower resolution around the point masses, the energy conservation is worse and the spiral-in stops at larger separations (see analysis in the next section).

In addition to this refinement, the softening length of the point masses was required to be always smaller than $d/5$ where d is the distance between the RG core and its companion. In this way, the gravitational interaction between the point masses is never softened since the distance between them is large enough such that the acceleration in Eq. (4.8) is always proportional to $1/r^2$. This measure is necessary to ensure that the final orbit can be smaller than two softening lengths, which is important especially for the smaller mass ratios (cf. Tab. 6.3).

Table 6.1 | Properties of simulation runs with different resolution near the point masses. Given are the upper bound for the number of cells per softening length n_c, the maximum cell radius around the point masses r_{max}, the final semi-major axis a_f, the final period P_f, the final eccentricity e_f, the relative error of the total energy $(E_0 - E)/E_0$ (E_0: initial value of the total energy, E: final value of the total energy), the ejected mass M_{ej}, and the number of cells N. All values are given at 100 d. The mass ratio is $q = 0.5$ and the initial separation is $49R_\odot$ for all runs. The target number of cells is 5×10^5.

| n_c	$r_{max}/R_\odot$	$a_f/R_\odot$	P_f / d	e_f	$(E_0 - E)/E_0$	$M_{ej}/M_\odot$	$N/10^6$
1.5	1.0	7.64	2.10	0.18	37%	0.10	0.74
3	0.36	5.35	1.23	0.18	16%	0.10	0.74
5	0.19	4.81	1.05	0.16	7.2%	0.093	0.80
10	0.093	4.64	1.00	0.13	2.2%	0.095	1.3

6.2 Resolution Study

For the same setup as described in Sec. 5 and Ohlmann et al. (2016), i.e., a $2M_\odot$ RG with a companion with mass ratio $q = 0.5$, the refinement criterion around the point masses was varied to study the convergence behaviour with respect to the resolution around the point masses. Four runs were conducted enforcing a minimum resolution around the point masses of 1.5, 3, 5, and 10 cells per softening length. The main properties of these simulations are summarized in Tab. 6.1.

For higher resolutions around the point masses, the error of the total energy[1] decreases approximately to an order of 1.5 in the number of cells per softening length (or, equivalently, in the spatial resolution around the point masses). At the highest resolution of at least ten cells per softening lengths, the error in the total energy is only 2.2%. For the least-resolved run with only 1.5 cells per softening length, the error in the energy conservation is quite large at 37% since the gravitational interaction of the point masses is not resolved well enough. The additional refinement criterion around the point masses leads to a larger number of cells than only refining on the mass of the cells for all criteria. For the highest resolution, the number of cells is 1.3×10^6, a factor of two more than 5×10^5 which is the number of cells that would result from refining on mass only. This shows that for these quite low mass resolutions a significant additional refinement takes place around the point masses.

Only for higher resolutions around the point masses, the conversion of gravitational energy of the system of the point masses to thermal and kinetic energy of the envelope is well enough resolved to conserve the energy on a per cent level. Moreover, resolving the conversion processes with higher resolution results in smaller separations (Fig. 6.1) and smaller eccentricities since more energy can be extracted from the system of the point masses. The conversion of gravitational energy of the point masses to thermal and kinetic energy of the gas is strongest in the direct vicinity of the point masses, even within the softening length (see the detailed analysis in Chapter 8). Thus, the key to achieve convergence in these simulations is to resolve the flow around the point masses with sufficient resolution. The amount of unbound mass is similar in all simulations, varying only by 5% to 7%; the small variation can be explained by the fact that this material is ejected during the first orbit where the evolution is still quite similar for the different resolutions. Comparing the highest resolutions shows that the semi-major axis changes only by 4% and the period only by 5%

---

[1]It is an advantage of the AREPO code that the computational domain can be chosen to be so large to contain all the ejecta. Thus, the conservation of energy can be checked over the whole domain since no mass is leaving the grid.
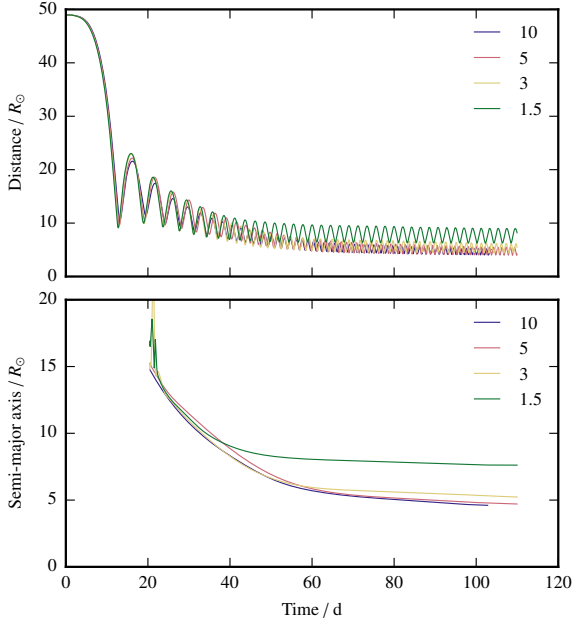
Figure 6.1 | Evolution of distance for different resolutions around the point masses. The upper panel shows the instantaneous distance between the RG core and its companion over time. In the bottom panel, the semi-major axis that was fit to the orbit is plotted. Both panels display four simulation runs with resolutions of 1.5, 3, 5, and 10 cells per softening length around the point masses.

Table 6.2 | Properties of simulation runs with different mass resolution. Given are the number of cells N, the mean cell mass $M_{\text{cell,mean}}$, the target mass of the cells $M_{\text{cell,target}}$ as endorsed by the refinement criterion, and the target number of cells N_{target} that follows from this. The total mass of the gas in the simulations is $1.6 M_\odot$. The two runs had the same initial conditions with $q = 0.5$. For other properties of the simulations, see Tab. 6.3.

$N/10^6$	$M_{\text{cell,mean}}/10^{-6} M_\odot$	$M_{\text{cell,target}}/10^{-6} M_\odot$	$N_{\text{target}}/10^6$
1.3	1.3	3.4	0.47
7.8	0.21	0.21	7.6

when going from 5 to 10 cells per softening lengths. Since this change is only small and the error in the total energy only a few per cent, we conclude that imposing a cell size of at least ten cells per softening length allows us to resolve the energy conversion processes while still being feasible in terms of computational effort.

For the highest resolution around the cores (min. 10 cells per softening length), two simulations with different mass resolutions were conducted to study the convergence behaviour. The number of cells and cell masses are given in Tab. 6.2; other properties, such as final separation and mass loss, are given in Tab. 6.3, along with other simulations.

The number of cells in both runs were 1.3×10^6 and 7.8×10^6 cells, respectively. The target mass of the low resolution run was set to $3.4 \times 10^{-6} M_\odot$, but the additional refinement around the point masses results in a mean cell mass of $1.6 \times 10^{-6} M_\odot$, a factor of 2.6 lower. This is equivalent to a larger number of cells by the same factor compared to the target resolution. Since the additional refinement around the point masses is necessary to ensure energy conservation, this resolution can be regarded as the minimum resolution that is necessary to ensure energy conservation by resolving the processes of converting gravitational energy to kinetic and thermal energy. Nonetheless, not only the number of cells is important, but mainly that the spatial resolution around the point masses is reached, as shown above. For the high resolution run, the actual mean mass of the cells

Table 6.3 | Properties of simulation runs with different initial conditions. Given are the mass ratio q, the factor of co-rotation χ (cf. Eq. (4.29)), the initial separation a_i, the final semi-major axis a_f, the final period P_f, the final eccentricity e_f, the relative error of the total energy $(E_0 - E)/E_0$ (E_0: initial value of the total energy, E: final value of the total energy), the ejected mass M_{ej}, and the number of cells N. All values are given at 95 d except for $q = 0.01$, where the values are given at 200 d.

q	χ	$a_i/R_\odot$	$a_f/R_\odot$	P_f / d	e_f	$(E_0 - E)/E_0$	$M_{ej}/M_\odot$	$N/10^6$
0.5	0.95	49	4.57	0.97	0.11	1.3%	0.094	7.8
0.5	0.95	49	4.72	1.02	0.13	2.4%	0.094	1.3
0.25	0.95	49	2.38	0.46	0.12	7.2%	0.19	2.7
0.25	0	49	2.46	0.48	0.11	7.1%	0.15	2.7
0.25	0.95	59	2.51	0.49	0.06	5.4%	0.17	2.7
0.1	0.95	49	1.42	0.26	0.04	7.1%	0.04	2.7
0.01	0.95	49	3.50	1.22	0.05	0.5%	0.0008	2.6

is equal to the target mass. This shows that the number of cells is not dominated by resolving the region around the cores in this run.

In the evolution of the energy there are only minor differences and the result is similar already at the low resolution. The error in the total energy decreases from 2.4% for the low resolution by a factor of 1.8 to 1.3% for the high resolution. The number of cells increases by a factor of 6, hence the spatial dimensions of the cells decrease roughly by a factor of $6^{1/3} = 1.8$ on average. This means that the energy error decreases roughly in first order with the average linear cell size.

The evolution of the separation of the RG core and the companion is very similar for both resolutions (Fig. 6.2). The upper panel shows the distance between the RG core and its companion, the lower panel the semi-major axis of the corresponding ellipse that was computed as described in Appendix C. Whereas the evolution of the semi-major axis is very similar, the distance between the RG core and the companion show oscillations due to the eccentricity of the orbit. They are slightly shifted during some time of the evolution because of slightly different periods. After 95 d, the difference in semi-major axis is 3%, the difference in period is 5% with the higher resolution run resulting in slightly smaller values for semi-major axis and period. The difference in the separation starts getting larger at ~ 40 d and the separation stays smaller for the higher resolution run. The eccentricities (see Tab. 6.3) are similar with values of 0.11 (high resolution) and 0.13 (low resolution). The relative difference is larger here with $\sim 18\%$, but this can also be due to the computation of the eccentricity from the fit to the ellipse that can show some scatter and uncertainty (cf. Appendix C).

The ejected mass is plotted against time in Fig. 6.3 for both resolutions. It is computed as the mass of all cells where the sum of gravitational, kinetic, and internal energy is larger than zero. Whether the internal energy is included or not proved to be of negligible impact (but compare Sec. 9.3 for simulations including recombination energy). The evolution of the ejected mass is very similar for both resolutions; after 95 d, the relative difference in ejected mass is less than 10^{-3}; in both simulations, about 6% of mass are unbound at this time. For both runs, similar to the simulation in Sec. 5 and Ohlmann et al. (2016), this mass is located in a tidal arm that is formed during the first orbit of the spiral-in. The details of the angular momentum and energy transport are studied in Sec. 8.

The convergence in the density distribution is examined in Fig. 6.4 in the orbital plane (left column) as well as perpendicular to it (right column). The global flow properties can be seen for
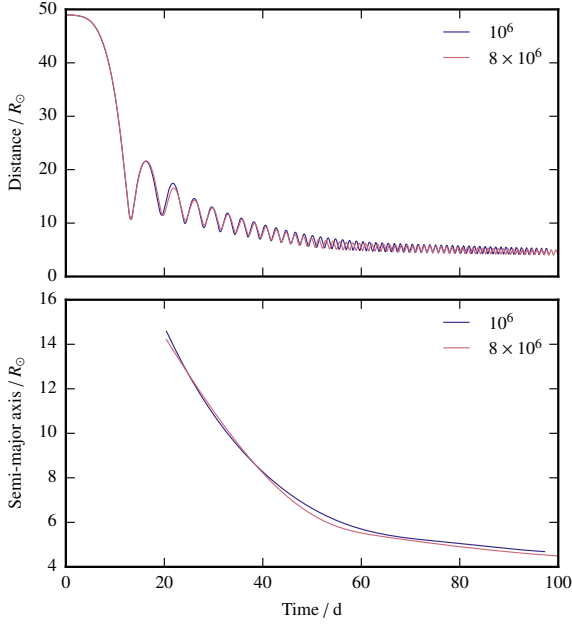
Figure 6.2 | Evolution of distance for different resolutions. The upper panel shows the instantaneous distance between the RG core and its companion over time. In the bottom panel, the semi-major axis that was fit to the orbit is plotted. Both panels display two simulation runs with $\sim 10^6$ and $\sim 8 \times 10^6$ cells.
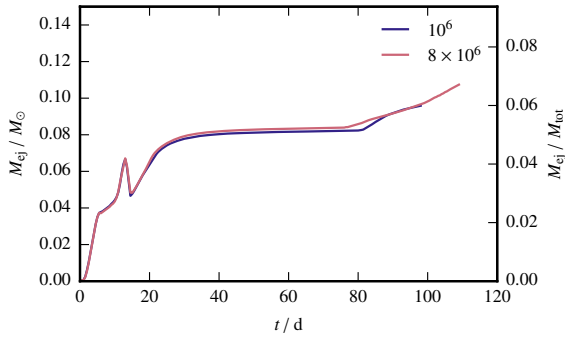
Figure 6.3 | Mass loss for different resolutions. Plotted is the mass unbound from the system as determined by a local energy criterion for two simulation runs with $\sim 10^6$ and $\sim 8 \times 10^6$ cells.

both the low and the high resolution run: strong shocks in the outer parts are located at the same positions; in the innermost part, the spiral shock wave pattern can be seen; in between, instabilities dominate the flow structure. Although the global flow structure is similar, the high resolution run reveals much more detail of the flow, especially in the outer part. A higher density stream in the lower right part of the envelope in the orbital plane, e.g., seems to be smooth in the low resolution case (Fig. 6.4, upper left panel), but is subject to instabilities and shows an irregular shape in the high resolution case (Fig. 6.4, lower left panel).

Thus, the global properties of the simulations are converged at a $\sim 5\%$ level already for a resolution of 1.3×10^6 cells using the refinement criterion around the point masses. Higher resolutions allow us to better resolve the structure of the flow in the outer part and to reveal more details of flow instabilities. Since most of the computation time is spent on the evolution of the small cells near the point masses, a higher resolution in the envelope does not increase the computational effort linearly with the number of cells and can thus be used without too much computational costs.
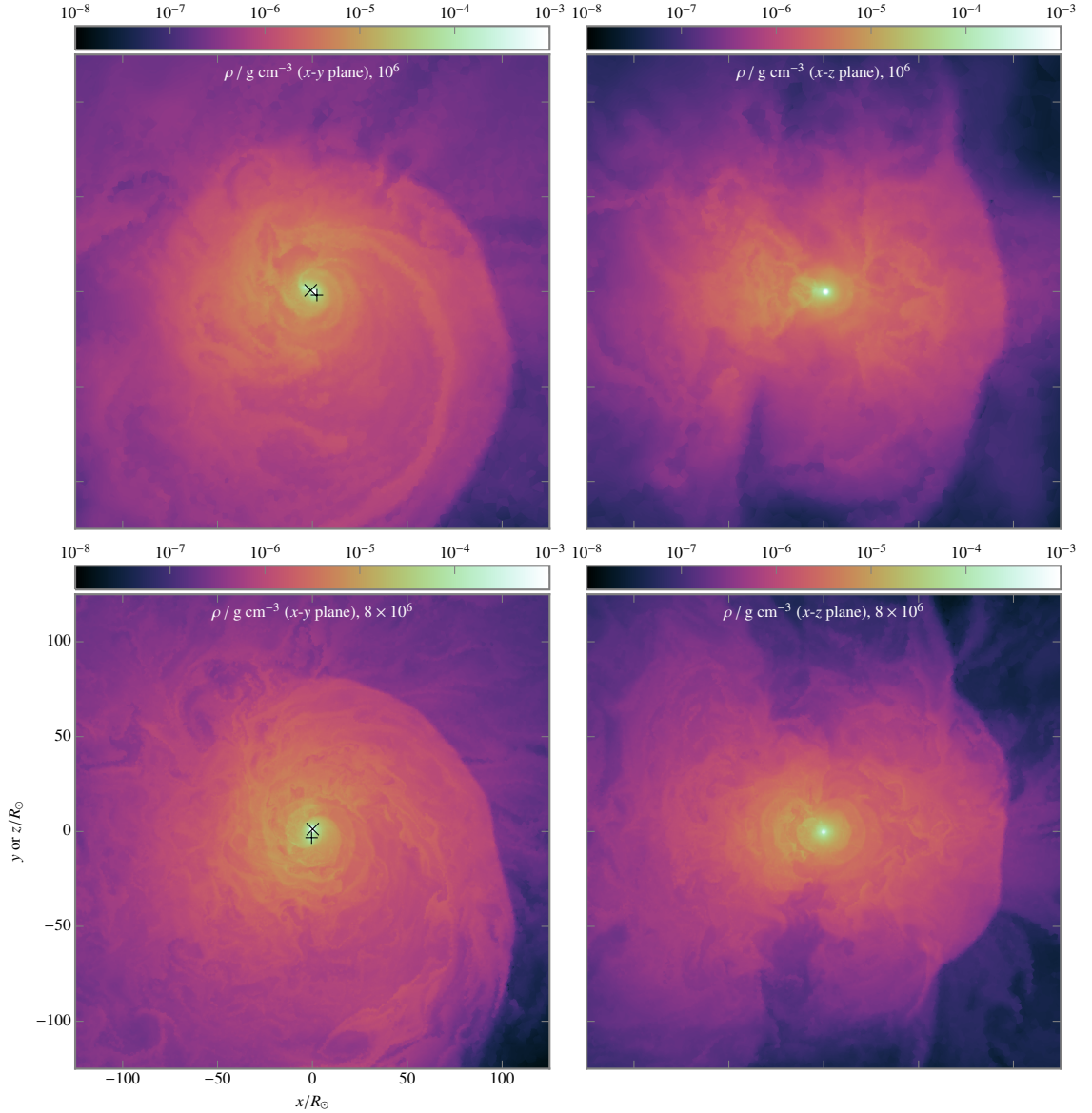
Figure 6.4 | Comparison of density structure for different resolutions. The panels show the density distribution in the *x-y* plane (left column) and *x-z* plane after 95 d for the run with $\sim 10^6$ cells (upper row) and $\sim 8 \times 10^6$ cells (lower row).

6.3 Mass Ratio

To compare the outcome of the CE phase for different mass ratios, simulations with $q = 0.25$, $q = 0.1$, and $q = 0.01$ have been conducted in addition to the $q = 0.5$ run. For each simulation, the same $2M_\odot$ RG model was used in combination with different companion masses. The resolution for these runs was $\sim 2.7 \times 10^6$ cells (see Tab. 6.3). The evolution of the separation of the RG core and the companion is shown in Fig. 6.5, the evolution of the ejected mass in Fig. 6.6.
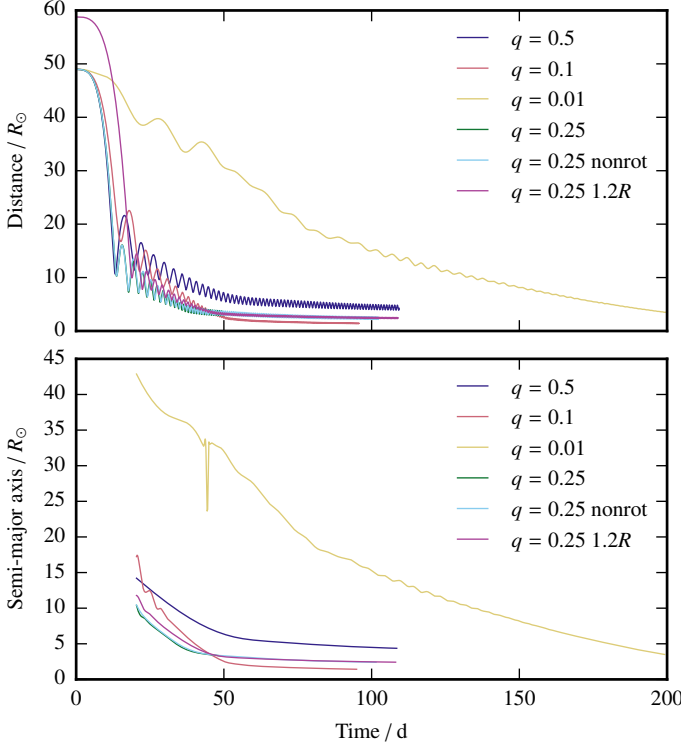
Figure 6.5 | Evolution of distance for different initial conditions. The upper panel shows the instantaneous distance between the RG core and its companion over time. In the bottom panel, the semi-major axis that was fit to the orbit is plotted. Both panels display simulations for different mass ratios and initial setups. The dip in the semi-major axis for $q = 0.01$ is due to an error in the fitting routine of the ellipse parameters.
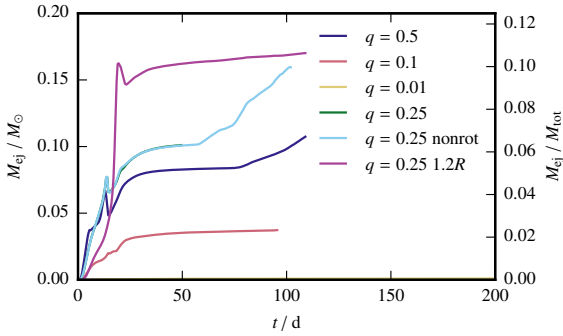
Figure 6.6 | Mass loss for different initial conditions. Plotted is the mass unbound from the system as determined by a local energy criterion for simulation runs with different mass ratios and initial setups. The line for $q = 0.01$ is located near the bottom edge since almost no mass is unbound.

The spiral-in of the $0.2 M_\odot$ companion ($q = 0.1$) is qualitatively similar to the $q = 0.5$ case, although the separation decreases more slowly first but ends at a smaller separation of $1.42 R_\odot$.[2] Moreover, the orbit is less eccentric at the end ($e = 0.04$). Substantially less mass than for $q = 0.5$ is ejected during the run, only 2.5% of the envelope mass is unbound (cf. Fig. 6.6). But also in this case, a spiral shock pattern is formed during the spiral-in. After ~ 50 d, similar to the $q = 0.5$ case (cf. Fig. 5.3), instabilities form and dominate the flow structure. This development is visualized in Fig. 6.7, where one can see slices in the orbital plane of the density, the Solberg–Høiland criterion from Eq. (5.1), and the Richardson number

$$R = \frac{N^2}{(\partial v_\phi / \partial r)^2} \tag{6.1}$$

---

[2]The fact that this final separation is smaller than twice the initial softening length of the point masses shows that the reduction of the softening length during the spiral-in allows us to reach also these small final separations.

Table 6.4 | Comparison of angular momentum and kinetic energy for models with varying initial rotation state and varying initial separation for $q = 0.25$. Given are the mass ratio q, the factor of co-rotation χ (cf. Eq. (4.29)), the initial separation a_i, the total angular momentum L_{tot}, the initial kinetic energy $E_{\text{kin,i}}$, and the number of cells N.

q	χ	$a_i/R_\odot$	$L_{\text{tot}}/10^{52}$ g cm^2 s^{-1}	$E_{\text{kin,i}}/10^{46}$ erg	$N/10^6$
0.25	0.95	49	4.3	6.2	2.7
0.25	0	49	4.3	6.2	2.7
0.25	0.95	59	4.1	4.6	2.7

($N^2 = \boldsymbol{g} \cdot \nabla s/c_p$: Brunt–Väisälä frequency, cf. Eq. (5.1), v_ϕ: tangential velcocity) for three different times. If $R < 0.25$ in a layer, this layer is unstable against shear motions (cf. Kippenhahn et al., 2012, Sec. 45.2). The Richardson number as computed here is an approximation since the derivative should be taken in direction of the gravitational field which is not exactly radial in this simulation. Fig. 6.7 shows that after ~ 50 d, the tightening of the shock spiral leads to a layer at a radius of $\sim 20 R_\odot$ that is highly unstable against shear instabilities as indicated by negative Richardson numbers. In the following, this layer forms typical shear wave patterns (cf. Fig. 6.7, lower right panel). At 54.5 d, the Brunt–Väisälä frequency as computed by the Solberg–Høiland criterion becomes more negative in the same layer, indicating a smaller time scale of the convective instability. This sets in a few days later and then dominates the flow structure completely.

As expected, the run with a mass ratio of $q = 0.25$ lies in between the runs with $q = 0.5$ and $q = 0.1$: the final semi-major axis is $2.38 R_\odot$. The error in the total energy is 7%, similar to the $q = 0.1$ case and larger than for the $q = 0.5$ simulation. Interestingly, the unbound mass is larger after 95 d and seems to increase faster than for $q = 0.5$ (cf. Fig. 6.6).

In the $q = 0.01$ case, the companion has a mass of $0.02 M_\odot$ (~ 20 Jupiter masses) and is thus more similar to a planet than to a star. In this case, the companion disturbs the envelope of the primary only slightly and the spiral-in takes much longer than in the other cases since the gravitational drag is much smaller. After 200 d, the separation still decreases. The final fate can be a disruption due to tidal forces or a merger with the He core of the RG. The variations in the separation during the first 60 d can be attributed to pulsations of the RG envelope due to the rotation that was imposed as initial conditions. They do not appear in the higher mass cases since the spiral-in timescale is smaller than the timescale of the pulsations. For this simulation, where the spiral-in takes longer, better initial conditions with relaxation in the binary frame (cf. Sec. 4.3.2) are necessary to reduce this kind of error. Almost no mass is unbound during this interaction from the system, the RG envelope is only puffed up slightly. The planet also does not produce enough shear to trigger instabilities in the envelope as seen in the higher mass cases; the envelope stays stable. This simulation is similar to the work by Staff et al. (2016b), where they simulated the interaction of a planet with ten Jupiter masses with giant envelopes of a star with a ZAMS of $3.5 M_\odot$. Our simulation shows similar results compared to their simulations: the spiral-in of the planet causes only a small disturbance of the envelope that is probably hard to observe.

6.4 Rotational State and Initial Distance

The impact of the rotational state of the envelope on the evolution of the CE phase is studied by conducting two simulations with different initial rotation profile for $q = 0.25$: the standard case
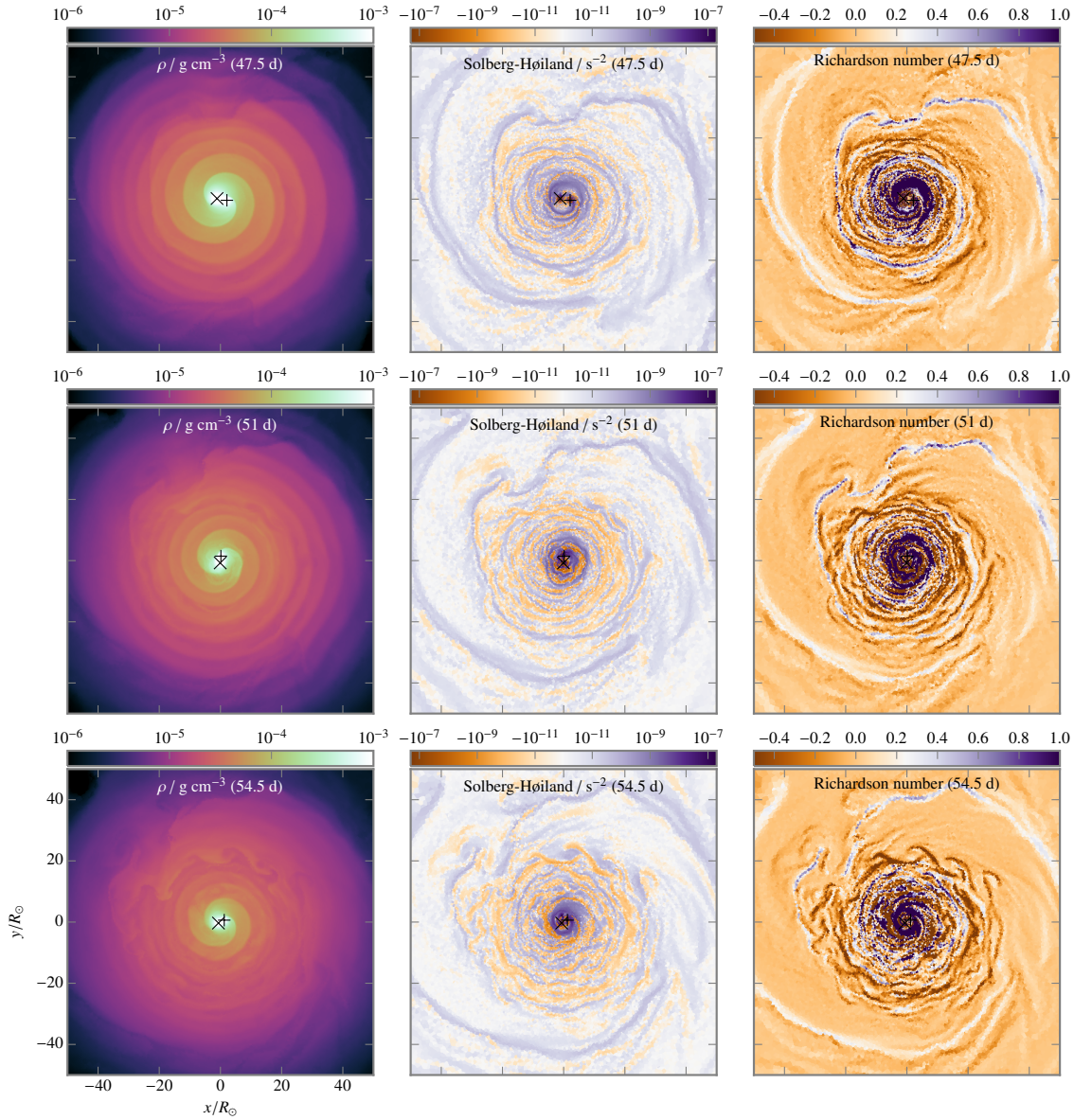
Figure 6.7 | Development of shear instabilities. The plots show quantities in the orbital plane of the simulation with $q = 0.1$ at 47.5 d (upper row), 51 d (middle row), and 54.5 d (lower row). The left column plots the density distribution, the middle column the Solberg–Høiland criterion (cf. Eq. (5.1), blue: stable regions, orange: unstable regions), and the right column shows the Richardson number (cf. Eq. (6.1), blue: stable regions, orange: unstable regions).
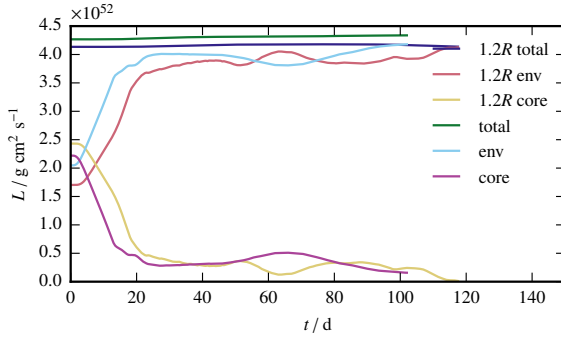
Figure 6.8 | Evolution of angular momentum. Plotted is the angular momentum of the whole system, the gas, and the system of the point masses for two simulations with $q = 0.25$: one with the point mass initially placed at the surface of the RG and one with the point mass placed at 1.2 times the stellar radius.

with $\chi = 0.95$ (cf. Eq. (4.29), i.e., 95% co-rotation, similar to the simulation by Ricker & Taam (2008, 2012); and a non-rotating case with $\chi = 0$, similar to the simulations by Passy et al. (2012). Tab 6.4 shows initial kinetic energy and angular momentum for both simulations. Since the moment of inertia of the RG is so small and since the rotation velocity of the giant envelope is small compared to the orbital velocity, the values of initial kinetic energy and angular momentum are the same for the nearly co-rotating ($\chi = 0.95$) and the non-rotating case ($\chi = 0$).[3] Thus, the evolution in both cases is expected to be very similar. This is confirmed in the simulations: the evolution of the distance (Fig. 6.5) and the ejected mass (Fig. 6.6) are not distinguishable. Moreover, the angular momentum transfer from the system of the point masses to the envelope is the same for both cases. Hence, we conclude that the initial rotational state is of minor importance for the dynamical evolution of the CE phase when placing the companion near the surface of the RG.

Instead of beginning the CE simulations with the companion located at the surface of the RG, more realistic initial conditions would start at the beginning of Roche lobe overflow. Since the timescale of orbital decay is still very long at this point, this is computationally not feasible. To test the impact of the choice of initial distance, a simulation was run with an initial separation that was 20% larger than in the standard simulation. The companion with a mass of $0.5M_\odot$ ($q = 0.25$) was placed at a distance of $1.2R_{RG} = 59R_\odot$ and the envelope was nearly co-rotating at $\chi = 0.95$. The angular momentum in this simulation is only 5% smaller than in the standard case, the initial kinetic energy is 26% smaller (see Tab 6.4). For a Keplerian system of point masses, one would expect a larger angular momentum for a larger separation. In the setup as employed here, the assumption of a Keplerian system of two orbiting point masses is very approximative since the center of mass is located far inside the envelope of the primary. Thus, the angular momentum decreases slightly for this increase in separation; at even larger separations, however, the angular momentum increases again, as expected. Most of the angular momentum that the system of the point masses loses to form a close binary system is transferred to the envelope during the first 20 d (see Fig. 6.8), similar to the simulation that starts with the companion at the surface. After this, the angular momentum of the binary stays nearly constant (for the details of angular momentum transport, see Sec. 8). During the evolution, the companion spirals in slower than for the run starting at the surface since it starts at an orbit with larger period. Despite the difference in initial separation, the final separation agrees very well, the difference is only 2% (Tab. 6.3). The ejected mass is also quite similar (roughly 15% of the envelope) and larger than in the $q = 0.5$ simulation. The eccentricity, however, is smaller for the simulation starting at a larger distance.

---

[3]This is also discussed in Passy et al. (2012), although they do not run simulations with different initial rotation states.

Thus, the initial distance of the companion seems to effect the global properties of the CE phase only to a small amount, although the detailed evolution may differ. This also shows that the final separation is probably determined by the initial envelope structure and the interaction of the point masses with the gas of the envelope. At even larger initial separations, however, the structure of the giant could change, especially in the outer layers, due to mass transfer in the binary and thus change the evolution of the dynamic plunge-in as well.

6.5 Conclusions

Exploring different initial conditions in this chapter highlights some numerical as well as physical aspects of hydrodynamics simulations of the CE phase. A convergence study reveals that the crucial process that needs to be resolved in this kind of simulation is the conversion of gravitational energy of the point masses to kinetic and thermal energy of the gas that takes place in the vicinity of the point masses. Only when resolving the region around the point masses with at least five to ten cells per softening length of the point masses, the error in the total energy is below 10% and the final separation changes only by 5% going from 5 to 10 cells per softening length. For lower resolutions, the energy conversion processes are not resolved well enough, resulting in larger errors of the total energy, and the spiral-in stops at larger separations. The analysis of energy and angular momentum transport in Chapter 8 confirms that this conversion is concentrated in the vicinity of the point masses, even within the softening length. For the highest resolution of at least ten cells per softening length, an increase in mass resolution by a factor of about 8 (spatial resolution: about a factor of 2) results in a decrease of the energy error by about a factor of 2 as well, but the final separation changes only by 5%. Hence, we conclude that we identified as key point for achieving convergence that the softened gravitational interaction of the point masses has to be resolved by at least five to ten cells per softening length.

Previous hydrodynamics simulations of the CE phase on grids (Sandquist et al., 1998, 2000; Ricker & Taam, 2012; Passy et al., 2012; Staff et al., 2016a,b; Iaconi et al., 2016) employed a resolution of 1.5 or 3 cells per softening length because it was difficult for their codes to accommodate for the range in spatial scales and because the importance of resolving the region around the point masses has not been recognized. The analysis of the spatial resolution around the point masses is more involved for simulations with SPH codes and has not been conducted so far. By using the refinement capabilities on arbitrary criteria of AREPO, we have shown that higher spatial resolutions around point masses are ensured in our simulations and that at least five to ten cells per softening length are needed to achieve convergence. Because the spiral-in stops too early for lower resolutions, we conclude that the grid simulations published so far probably overestimate the final separation of the system. This may also explain why the final separation in those simulations seem to be larger than found in post-CE systems (see Passy et al., 2012, Fig. 17; Iaconi et al., 2016, Fig. 4). Also our simulations show final separations that are larger than the bulk of post-CE systems for larger mass ratios, but they are significantly smaller than the separations reached with other methods so far (see Iaconi et al., 2016, Fig. 4).

Recent hydrodynamics simulations employed an initial giant envelope that is either nearly co-rotating (Ricker & Taam, 2012) or non-rotating (Passy et al., 2012; Iaconi et al., 2016). Comparing both initial rotation states for otherwise identical initial conditions results in nearly identical evolutions for the system studied here. Moreover, increasing the initial separation by 20% compared to the placement at the surface of the RG envelope leads to a similar final separation but slightly higher mass loss during the first orbit.

We also examined different mass ratios by changing the companion mass for the same $2M_\odot$ RG initial model. As expected from employing the energy formalism, Eq. (2.54), the companion spirals in further for lower mass ratios, since the gravitational binding energy of the binary system is smaller. Moreover, the final separation seems not to be affected by the fact that the softening length of the point masses is initially larger than half the final separation because we reduce the softening length to be at maximum a fifth of the separation of the point masses. A sub-stellar companion leads only to a minor disturbance and enlargement of the RG envelope without ejecting mass.

Chapter 7

Magnetic Fields

Magnetic fields play an important role in the evolution of stellar systems. Their origin is still unclear, and it is debated if they are remnants from fields in star-forming molecular clouds or if they are dynamically generated by dynamo processes. Wickramasinghe et al. (2014) suggest that magnetic MS stars and magnetic WDs (MWDs) result from mergers of stellar objects where the magnetic fields are generated in a dynamo process driven by the differential rotation during the merger process. For MWDs, the fossil field hypothesis might still hold, although in recent years, the generation of fields during CE phases gained more attention (see the review by Ferrario et al., 2015a), especially because this hypothesis can naturally explain the different populations in single MWDs and MWDs with a companion (Briggs et al., 2015).

Here, we present results of the first multi-dimensional MHD simulations of the CE phase: independent of the initial seed field present in the RG envelope, we find a strong amplification of the magnetic fields due to accretion on the companion, saturating in similar field strengths. The growth time-scale of a few days is compatible with the fastest-growing mode of the magneto-rotational instability (MRI) in the vicinity of the companion. The amplification of the field is much faster than would be expected for a dynamo process in the convective envelope that might nevertheless operate on longer timescales. After being saturated, the magnetic field is dispersed in the envelope, resulting in fields of tens to a hundred kG throughout the envelope. Although the magnetic fields do not significantly alter the dynamical evolution of the CE phase on the simulated time scales, they might be important for the evolution to a planetary nebula.

7.1 Overview

Magnetic fields have been studied in the context of CE evolution mainly in terms of dynamo models operating in the differentially rotating envelope (Regős & Tout, 1995; Tout & Regős, 2003; Nordhaus & Blackman, 2006; Nordhaus et al., 2007; Tout et al., 2008; Potter & Tout, 2010; Nordhaus et al., 2011; Wickramasinghe et al., 2014). This amplification mechanism has been used to explain the formation of high-field magnetic WDs (HFMWDs) as well as magnetic cataclysmic variables (MCVs[1]) in a unified picture (Regős & Tout, 1995; Tout & Regős, 2003; Liebert et al., 2005; Tout et al., 2008; Nordhaus et al., 2011; Briggs et al., 2015). Magnetic white dwarfs (MWDs) show surface fields between 10^3 G and 10^9 G with a complex, non-dipolar structure that do not decay significantly during their lifetime (Ferrario et al., 2015a). Moreover, MWDs are more massive ($0.78 M_\odot$ on average) than non-magnetic WDs ($0.66 M_\odot$ on average). Another field where magnetic fields that are amplified during the CE phase have been discussed to be important is the evolution of planetary nebulae (PNe, e.g., Nordhaus & Blackman, 2006; Nordhaus et al., 2007; Tocknell et al., 2014).

---

[1]Close binary systems of a MWD and a low mass MS companion that overflows its Roche lobe and transfers mass to the WD.

Investigations of magnetic fields during the CE phase started with the work by Regős & Tout (1995). In their model, the spiral-in leads to differential rotation in the envelope, thus activating an $\alpha-\Omega$ dynamo. The presence of strong magnetic fields may help reducing the orbit and ejecting the envelope through a magnetically driven wind. They compute the decay of magnetic fields due to magnetic buoyancy to proceed on much longer timescales than the envelope ejection, which takes 10 to 100 years in their models. The outcome of their simulations depends on the initial conditions: for small envelope masses, the envelope may be ejected with a small shrinkage in orbit; for large envelope masses, the core of the RG and the companion coalesce since the final separation is smaller than the Roche lobe radius of the companion. In between these two limiting cases, pre-MCVs are created where the magnetic field of the WD depends on the final separation: the smaller the final separation, the larger the magnetic field that can be extracted. Nevertheless, it is not clear how the magnetic field is transported and anchored to the surface of the WD. As a typical CV they use a $1M_\odot$ WD with a $0.6M_\odot$ MS companion in a semi-detached state at a separation of a few $R_\odot$. Thus, the initial model consists of an AGB star of varying mass, depending on the envelope, and a $0.6M_\odot$ companion. Regős & Tout (1995) state that their model is qualitative but can account for different field strengths by different final separations after the CE phase. These pre-CVs are then driven to the CV stage by angular momentum loss through magnetic braking.

The same dynamo model is also used by Tout & Regős (2003). They mention different energy sources that might alleviate the ejection of the envelope, such as nuclear energy from burning of H-rich material mixed into hotter zones, non-equilibrium burning, and ionization energy, but do not incorporate these into their model. One simulation ending as a potential pre-MCV consists of a $0.8M_\odot$ core surrounded by a $2M_\odot$ envelope with a $0.6M_\odot$ MS companion at an initial distance of $328R_\odot$ that ends up at a final separation of $3.9R_\odot$. They also compute a region of possible CV progenitors for different combinations of the envelope mass and the core mass.

The work by Liebert et al. (2005) analyzes a sample of WDs from the Sloan Digital Sky Survey (SDSS, York et al., 2000). They observe a strong disparity between MWDs in single systems and WDs in binaries with MS stars: in non-interacting binaries, they do not find a single MWD. Only in interacting binaries, they find about 25% of the WDs to be magnetic. This finding is difficult to explain if the same single-star process is responsible for the generation of magnetic fields, since this should not result in different populations in single systems and wide binaries. Although this may partly be due to a selection bias, they conclude that the most probable mechanism involves binary interactions: the dynamo model during CE evolution by Regős & Tout (1995) would be a plausible explanation. An updated analysis by Silvestri et al. (2007) uses SDSS data release five with a larger sample of MWDs and basically confirms the earlier results by Liebert et al. (2005).

This finding led to the proposal by Tout et al. (2008) that all HFMWDs originate from binary systems. Based on the dynamo model developed by Regős & Tout (1995), they propose that the generation of magnetic fields by a dynamo process during the CE phase leads to the formation of MCVs (i.e., HFMWDs in short-period binaries) if the outcome is a close binary and to the formation of single HFMWDs if the outcome is a merger of the core and the companion. This binary origin of HFMWDs can resolve the difference between single WDs and binary systems.

During the CE phase, it is, however, unclear how the magnetic field generated in the envelope can be anchored to the surface of the WD to create a surface field that may be detected later during the CV phase. This question was addressed by Potter & Tout (2010) by solving the induction equation for the magnetic field inside the giant core assuming some background field generated by a dynamo in the envelope. They find that a randomly oriented field cannot penetrate into the WD, stays confined to the surface layers and decays rapidly after the ejection of the envelope. This also

happens for rapidly varying fields. If the magnetic fields show a preferential direction, a field may be induced in the WD with surface field strengths of a few per cent of the external field, and this surface field decays only on long timescales (longer than the cooling time of the WD). To create a strong magnetic field of 10^7 G, however, this requires a CE lifetime of 36 000 yr which is quite long compared to the dynamical spiral-in timescales of months to years.

Also using a α–Ω dynamo model, Nordhaus et al. (2011) find that the generated fields are not strong enough to yield high surface fields on the core that may explain single HFMWDs, although this process might still explain MCVs. They propose that the tidal disruption of a low-mass companion leads to the formation of an accretion disk. In this accretion disk, a disk dynamo may provide fields of 10 to 1 000 MG that may be accreted to the core surface and thus explain HFMWDs.

As a different formation mechanism, García-Berro et al. (2012) conduct SPH simulations of mergers of two WDs in a double degenerate system. They do not include magnetic fields in their simulations, but they conclude that the resulting merger shows a hot, differentially rotating surface layer that may power a dynamo process being able to generate strong magnetic fields. They also estimate the diffusion times to be larger than the cooling time, thus the fields will not decay quickly. According to them, the statistics of double degenerate mergers roughly fits the number of HFMWDs in a local sample.

Magnetic fields were included in the simulation of a merger of a $0.625 M_\odot + 0.65 M_\odot$ CO WD binary by Zhu et al. (2015). Using the moving-mesh code AREPO, they find amplifications to strong magnetic fields $> 10^{10}$ G. During the post-merger evolution, a thermonuclear runaway may occur (depending on the temperature evolution), leading to the explosion of the remnant. If such an explosion does not occur, the merged remnant populates the high-mass end of the HFMWD range. These simulations show that single HFMWDs can result from mergers of two single WDs.

Double degenerate mergers, however, contribute only marginally to HFMWDs according to the population synthesis calculations by Briggs et al. (2015). They assume that HFMWDs are formed during CE as a merger of the degenerate core with the companion or by an accretion disk around the core, following the suggestion of Nordhaus et al. (2011), or as a merger of two WDs. Their population synthesis model can reproduce the number and mass distributions of HFMWDs for a range of values for the CE efficiency α (see Eq. 2.54) where the best fits are reached for $0.1 \leq \alpha \leq 0.3$. In their model, almost all HFMWDs are CO WDs (some ONe, some He WDs) resulting from a merger during a CE phase and only very few systems result from mergers of double degenerate systems. A major contribution comes from mergers of an AGB core with a MS companion where the resulting giant then ejects its envelope and evolves to a HFMWD.

In a more general context, Wickramasinghe et al. (2014) propose that magnetic A, B, and O stars as well as magnetic white dwarfs have a binary origin, where magnetic MS stars result from the merger of two stellar objects and where MWDs result from magnetic field generation during CE evolution. Braithwaite & Spruit (2004), however, found that stable magnetic field configurations can result from random initial fields as remnants from star formation; they propose these fossil fields as explanation of the observed magnetic A stars, MWDs, and some magnetic neutron stars. Braithwaite & Spruit (2015) consider the merger of two stellar cores as a possible source of the fossil fields that emerge as stable configurations in magnetic stars. There is, however, some observational evidence against the merging theory, e.g., the observation of two wide binaries with a HFMWD by Dobbie et al. (2013). Thus, Ferrario et al. (2015a) conclude in their review that the question about the origin of magnetic fields in WDs is still not settled. Both the fossil field hypothesis and the dynamo generated field hypothesis are still discussed, although the binary origin of the magnetic fields may explain the different distributions of HFMWDs in single and binary systems better.

Apart from HFMWDs, magnetic fields generated during CE evolution may have an impact on the shape and evolution of planetary nebulae. Nordhaus & Blackman (2006) study potential dynamo operation in systems consisting of a $3M_\odot$ primary in different stages (RGB, AGB, interpulse AGB) and a low-mass companion ($< 0.3M_\odot$) that undergo a CE phase. They find that no ejection is possible for RGB stars whereas partial or complete ejection is possible for AGB stars. This ejection can be caused by different processes: massive brown dwarfs lead to a equatorial ejection, as would be expected without magnetic fields. For lower mass companions, a dynamo process may create magnetic fields ejecting material poloidally. Moreover, if the companion is tidally disrupted, an accretion disc may form around the core leading to disc-driven outflow. These models are motivated by indications that magnetic fields and binarity may be important factors in the shaping of PNe. It was, e.g., found by Jordan et al. (2005) that four post-AGB stars as remnants of PNe show kG magnetic fields. A later re-evaluation of these results, however, led Jordan et al. (2012) to conclude that these detections were spurious and that no kG fields could be detected in a sample of ten central stars of PNe. Fields of 100 to 300 G are still possible within the uncertainties.

Using a more detailed dynamo model, Nordhaus et al. (2007) compare single star models to CE models as origins of magnetic fields in PNe. Their model includes the evolution of toroidal and poloidal magnetic fields as well as rotation and shear. They show that a dynamo in a single star can only operate when shear is resupplied, placing conditions on the convection in the envelope. For the CE evolution, they find a robust dynamo mechanism where the fast spiral-in can provide enough rotational energy and thus shear to power the dynamo. They conclude that two explosion types are possible: magnetically induced with collimated bipolar outflows, and thermally induced with quasi-spherical outflows. These different types would thus also indicate different shapes of the resulting PNe.

Using observational data on jets in four PNe, Tocknell et al. (2014) constrained the magnetic fields that could potentially launch the jets by the Blandford–Payne mechanism (Blandford & Payne, 1982). In three of those PNe, the jets pre-date the CE phase by a few thousand years and may be launched from an accretion disk around the companion due to Roche lobe overflow or wind accretion. These jets indicate field strengths of few to ten G. One other PN shows two jets that are about 3000 years younger than the CE evolution (as given by the expansion of the ionized shell) and may be due to accretion on the primary or due to accretion from fallback material. Here, the magnetic fields are estimated to be of the order of hundreds of G to a few kG, which fits to estimates made according to the dynamo models by Regős & Tout (1995) and Nordhaus et al. (2007). For the pre-CE jets, the velocities are roughly $100\,\mathrm{km\,s^{-1}}$, for the post-CE jets $270\,\mathrm{km\,s^{-1}}$ and $460\,\mathrm{km\,s^{-1}}$; the expansion velocity of the PN is about 25 to $50\,\mathrm{km\,s^{-1}}$. For one jet pair, the mass could be estimated to be $10^{-3}M_\odot$. Thus, these findings show that magnetic fields influence the evolution and shaping of PNe.

During CE evolution, magnetic fields may be generated that are important for explaining the properties of magnetic white dwarfs and planetary nebulae. The mechanisms examined so far include α–Ω dynamos in a differentially rotating envelope and accretion disks around the core (due to tidal disruption or fallback material) and around the companion (due to Roche lobe overflow before CE evolution). The most promising initial models seem to be AGB stars with low-mass companions. Up to now, no modeling approach of the CE phase included magnetic fields and hydrodynamics to study dynamic features during the spiral-in. The first MHD simulations of the CE phase are presented in this work.

7.2 Setup

In order to compare to the simulation as presented by Ohlmann et al. (2016, see also Sec. 5), the method and initial conditions were chosen to be similar. The initial conditions are based on the same RG model: a $2M_\odot$ RG with an $0.37M_\odot$ He core in the middle of the RG branch with a radius of $49R_\odot$. The model was relaxed to a hydrostatic equilibrium state that is stable in the hydrodynamics code in an additional step employing a damping term to get rid of spurious velocities (for more details on the relaxation procedure, see Sec. 4.1). As outlined in Secs. 4.1 and 5, the core of the RG and the companion are replaced by point masses with the gravitational acceleration being softened at a length $h \approx 1.0R_\odot$. Since the conversion of gravitational energy to kinetic and thermal energy is strongest in the region around the point masses (for a detailed analysis, see Sec. 8), we require the radius of the cells around the point masses to be at maximum a tenth of the softening length. The binary is set up in a Keplerian orbit with the RG envelope being in 95% co-rotation. To ensure proper gravitational interaction between the point masses, the softening lengths are always required to be smaller than a fifth of the separation.

In addition to the simulations presented so far, we include magnetic fields in our scheme: we solve the ideal MHD equations (see Sec. 2.1.3, Pakmor & Springel, 2013) using the HLLD solver (Miyoshi & Kusano, 2005) and the Powell scheme (Powell et al., 1999) to control the divergence constraint (for more details, see Sec. 3.2.2). For simplicity, we assume a dipolar magnetic field along the z axis (i.e., parallel to the rotation axis) as an initial configuration,

$$\boldsymbol{B}(\boldsymbol{r}) = \frac{B_\mathrm{s}}{2} \frac{3\boldsymbol{n}n_z - \boldsymbol{e}_z}{(r/R)^3}, \qquad (7.1)$$

where B_s is the surface field in z direction at the pole, R the stellar radius, and $\boldsymbol{n} = \boldsymbol{r}/r$ the normal vector. Magnetic fields at the surface of giant stars are supposed to be weak due to their large radius. In a recent study, Aurière et al. (2015) were able to detect weak surface magnetic fields of roughly 1 to 100 G for G-K giants at the base of the giant branch. Fuller et al. (2015) use *Kepler* data to infer from asteroseismological models that the magnetic fields in the core may well exceed 10^5 G. Magnetic fields exist in various types of stars for various masses (for reviews, see, e.g., Landstreet, 1992 and Ferrario et al., 2015b). For most stars, however, the magnetic field at the surface is too small to be measurable, i.e., usually below $\lesssim 1$ G. If we assume flux conservation[2], the magnetic field scales as $1/R^2$. Assuming surface fields at the ZAMS of about 10 G, 1 mG, and 0.1 µG yields for the $50R_\odot$ RG surface fields of roughly 10^{-2} G, 10^{-6} G, and 10^{-10} G. These values only serve as a reasonable estimate of a range in the parameter space of surface magnetic fields that we take as input for the CE simulations.

Here, we present results from four MHD simulations: three simulations where the envelope is nearly co-rotating ($\chi = 0.95$, see Sec. 4.3.1) with surface magnetic fields of 10^{-2} G, 10^{-6} G, and 10^{-10} G; and one simulation with a non-rotating envelope and a surface field of 10^{-6} G (marked as NR).

7.3 Temporal Evolution

The evolution of the distance and the semi-major axis of the orbit is shown in Fig. 7.1 for the four MHD simulations and the non-MHD simulation as presented in Sec. 5 and Ohlmann et al.

---

[2]This is the foundation of the fossil field hypothesis: since the flux is assumed to be conserved, the field strength scales as $1/R^2$. Thus, very large fields on compact objects can be explained (e.g. Landstreet, 1992).
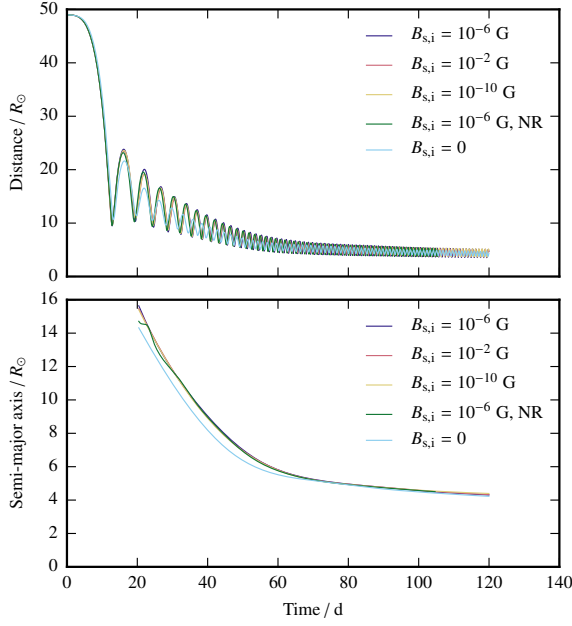
Figure 7.1 | Evolution of distance for MHD runs. Shown is the separation (upper panel) and semi-major axis (lower panel) for runs with different initial surface fields $B_{s,i}$. NR denotes the non-rotating model.
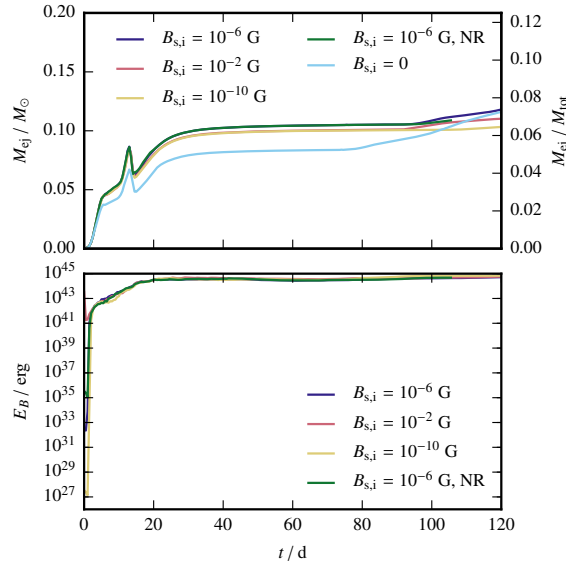
Figure 7.2 | Evolution of ejected mass and magnetic field energy for MHD runs. The upper panel shows the unbound mass over time, the lower panel shows the total magnetic energy for runs with different initial surface fields $B_{s,i}$. NR denotes the non-rotating model.

(2016). The evolution is very similar for all simulations, showing that the impact of the magnetic fields on the dynamics of the evolution is rather small. This is also supported by a more detailed analysis of the angular momentum and energy transport that shows that the contribution of the magnetic stress is negligible (see Sec. 8). During the first 50 d, the MHD simulations stay at slightly larger semi-major axes than the non-MHD simulations, but end up with a very similar value (2% difference in semi-major axis, 3% in period) compared to the non-MHD simulation. One can see, however, that the runs including MHD feature more eccentric orbits with eccentricities around 0.17 compared to 0.11 for the non-MHD run.

The evolution of the ejected mass is plotted in Fig. 7.2 (upper panel). The MHD simulations are all very similar and show an ejection of about 7% of the envelope mass in the first 100 d which is
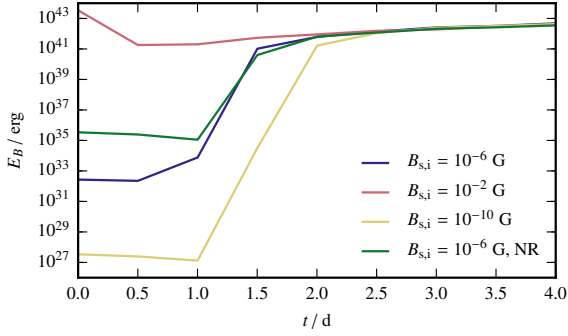
Figure 7.3 | Evolution of magnetic energy during the fast amplification phase. Shown is the total magnetic energy summed over the whole domain for runs with different initial surface fields $B_{\mathrm{s,i}}$. NR denotes the non-rotating model.

larger than for the non-MHD simulation where only about 5% of the envelope mass is ejected in the first 80 d. This ejected mass comes in both cases mainly from material that is ejected during the first orbit in a stream of material. Hence, magnetic fields increase the mass that is ejected during this first orbit slightly. After 80 d, the amount of ejected mass starts to rise in the non-MHD simulation; this is seen in the MHD simulations only after roughly 100 d. In order to continue the run for longer than the 120 d shown here, an additional grid has to be added around the simulation volume and the simulation has to be restarted from there to avoid that mass reaches the boundary. This is a goal for future simulations, although it is not clear how much further the simulation can be run in a reasonable amount of computational resources since the timestep restriction is quite stringent in the highly resolved region around the point masses.

The largest difference in the MHD simulations compared to the non-MHD simulation is of course the magnetic field itself. The total magnetic field energy in the simulation volume is shown in Fig. 7.2 (lower panel). A striking feature is that irrespective of the initial seed field strength, all simulations show a strong amplification of the magnetic fields during the first orbit. For all simulations, the field energy saturates at a value between 10^{44} erg and 10^{45} erg corresponding to roughly 1% of the internal energy at the end of the simulation (i.e., after 120 d) and to roughly 0.2% of the total energy. This magnetic field amplification does neither depend on the initial seed field strength nor on the rotational state of the envelope.

As can be seen in Fig. 7.2 (lower panel), the evolution of the magnetic field allows us to divide the CE phase into three phases that are examined in more detail in the following sections: the *fast amplification phase* during the first three days (Sec. 7.3.1), the *slow amplification phase* between three and 20 days (Sec. 7.3.2), and the *saturation phase* after 20 days (Sec. 7.3.3).

7.3.1 Fast Amplification Phase

The fast amplification phase takes place during the first three days of the simulation. During this phase, the field grows from the initial value beginning one day after the start of the simulation and ending at a value of about 10^{42} erg for the total magnetic field energy at three days (see Fig. 7.3). For the low initial field cases (initial surface fields of 10^{-6} G and 10^{-10} G), this corresponds to an increase in the magnetic field energy by 10 to 15 orders of magnitude. For the large initial surface field of 10^{-2} G, there is an initial decay in the magnetic field energy: this configuration seems to be unstable leading to a conversion of magnetic field energy to other energy forms. After 3 d, however, also this simulation shows a total field energy of about 10^{42} erg.

After the start of the simulation, gas from the envelope starts to form an accretion stream onto the companion. In this accretion stream around the companion, the magnetic field is amplified.
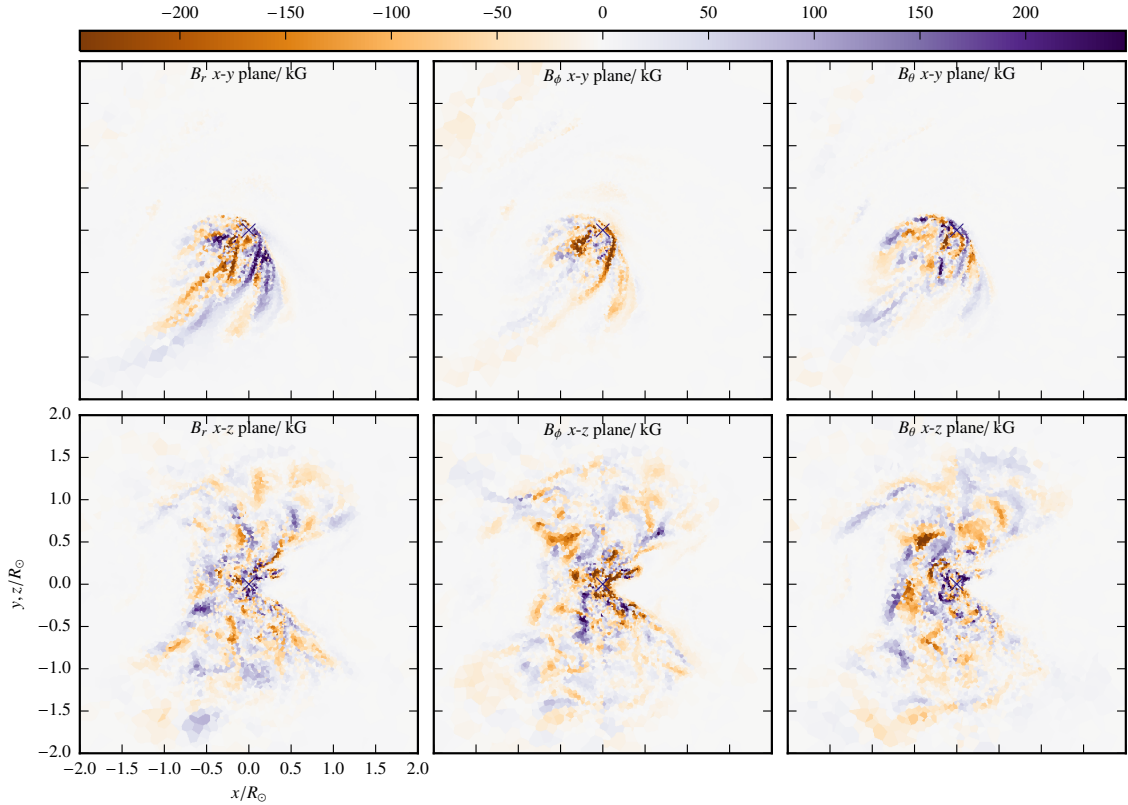
Figure 7.4 | Magnetic field components at 2 d. The panels show the spherical magnetic field components B_r (left column), B_ϕ (middle column), and B_θ (right column) in the orbital plane (upper row, rotated such that the point masses lie on the x axis) and in a plane perpendicular to this (lower row). The position of the RG core is marked by a +, the position of the companion by a ×. The plots show the simulation with an initial surface field of 10^{-6} G and are centered on the companion.

The magnetic field structure is shown for a small region of $4R_\odot$ around the companion in Fig. 7.4 after 2 d, in the middle of the fast amplification phase. Already at this time, the magnetic field strength reaches values over 200 kG, a huge increase compared to the initial value of 10^{-6} G at the surface and a few G near the center of the RG. The field structure in the orbital plane (Fig. 7.4, upper row) resembles the structure of the accretion stream of gas around the companion[3] with the polarity of the components changing throughout the plane. In the plane perpendicular to the orbital plane (Fig. 7.4, lower row), the fields are confined to a similar region as in the orbital plane and show a complex structure with large changes also in small regions.

Although the evolution is very dynamical here, the density structure around the companion resembles an accretion disk. This leads to the tentative suggestion that the magneto-rotational instability (MRI; Balbus & Hawley, 1991, for a review, see Balbus & Hawley, 1998) is the driving mechanism of the magnetic field amplification. In a differentially rotating fluid with magnetic fields, the Solberg–Høiland criterion (Eq. (5.1), see also Kippenhahn et al., 2012) has the same form

---

[3]Note that the orbital plane has been rotated in Fig. 7.4 (and also in the following Figs. 7.6 and 7.8) in such a way that the vector from the RG core to the companion points into the positive x direction.

as without magnetic fields, but all angular momentum gradients are replaced by angular velocity gradients (Balbus, 1995). Following the analysis of Rembiasz et al. (2016), this can be translated in a condition for the local rotational shear q,

$$q = -\frac{\mathrm{d}\ln\Omega}{\mathrm{d}\ln r}, \tag{7.2}$$

giving $0 < q < 2$ for a medium with a convectively stable (i.e., isentropic) stratification. Since the RG envelope is nearly adiabatic, we assume an isentropic stratification around the companion and use the criterion $0 < q < 2$. If this criterion is fulfilled, small perturbations of the form $\exp(ik_z z + \gamma t)$ are unstable for wavenumbers (Rembiasz et al., 2016, Eq. 14)

$$k_z < k_{\mathrm{crit}} = \sqrt{2q}\,\frac{\Omega}{v_{\mathrm{A}z}}, \tag{7.3}$$

where $v_{\mathrm{A}z} = b_z/\sqrt{\rho}$ is the Alfvén speed in z direction. These unstable solutions are called MRI channels. The fastest growing channel in ideal MHD has the wavenumber (Rembiasz et al., 2016, Eq. 24)

$$k_{\mathrm{mri}} = \sqrt{1 - \frac{(2-q^2)}{4}}\,\frac{\Omega}{v_{\mathrm{A}z}}, \tag{7.4}$$

and the growth rate (Rembiasz et al., 2016, Eq. 25)

$$\gamma_{\mathrm{mri}} = \frac{q}{2}\Omega. \tag{7.5}$$

We can now analyze the fluid flow near the companion to see if it is susceptible to the MRI instability. If the flow is unstable, we examine if the fastest growing mode can be resolved in our simulation and if the predicted growth rate fits the growth of the magnetic field seen in the simulation.

Computing the local rotational shear according to Eq. (7.2) in the vicinity of the companion for the simulation with an initial surface field of $10^{-6}\,\mathrm{G}$ yields $q \approx 1$ as an average. Thus, the differentially rotating flow around the companion should be unstable to MRI. In the beginning, the magnetic field around the companion is so low that the Alfvén velocity is too small for the fastest growing wavelength (cf. Eq. (7.4)) to be resolved on the grid. During the first day, the magnetic field present in the envelope is dragged into the vicinity of the companion and the Alfvén velocity increases until at 1.2 d, the wavelength of the fastest growing mode reaches about $0.02R_\odot$, which is marginally resolvable on the grid. Incidentally, the magnetic field energy starts to rise at this time. After 1.3 d, the wavelength of the fastest growing mode reaches $0.1R_\odot$ and is at this point resolved by roughly 1000 cells around the companion. The wavelength further grows to about $5R_\odot$ and stays at this value during the fast amplification phase. It is larger than the cell radius for roughly 200 000 cells around the companion. The value of $\gamma_{\mathrm{mri}}^{-1}$ during this phase is between 0.1 d and 0.6 d. These values as computed from the simulations can of course only be approximate since the real flow structure is more complicated than in an idealized MRI setting. Nevertheless, the growth rate can be compared to the growth rate of the total magnetic energy in the simulation since this quantity is dominated by the magnetic energy in the vicinity of the companion. Fitting the magnetic energy between 1 d and 3 d for the simulation with $B_{\mathrm{s,i}} = 10^{-6}\,\mathrm{G}$ yields 0.1 d as e-folding time[4] and is thus compatible with the theoretical MRI growth rate computed from the flow structure. Hence, we conclude that these agreements point to MRI as the mechanism responsible for magnetic field amplifications as seen in our simulations.

---

[4]We define this as the time in which the quantity increases by a factor of e.
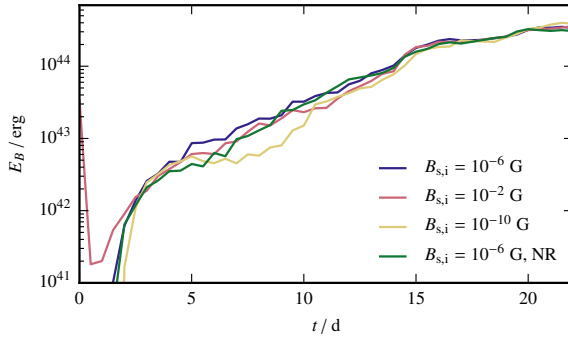
Figure 7.5 | Evolution of magnetic energy during the slow amplification phase. Shown is the total magnetic energy summed over the whole domain for runs with different initial surface fields $B_{\mathrm{s,i}}$. NR denotes the non-rotating model.

7.3.2 Slow Amplification Phase

After the initial fast amplification phase with an *e*-folding time of about 0.1 d, the amplification slows down beginning at 3 d to a timescale of roughly 3 d (see Fig. 7.5). This slow amplification phase ends at 20 d, and the magnetic field energy becomes nearly constant in time. As can be seen in Fig. 7.5, the magnetic field energy reaches a value of about 10^{42} erg at 3 d and is amplified to a few times 10^{44} erg at 20 d for all initial configurations.

The structure of the magnetic field is shown in Fig. 7.6, where the magnetic field components are plotted in a small region of $5R_\odot$ around the companion after 8 d in the orbital plane (upper row) and perpendicular to the orbital plane (lower row). In the orbital plane, the structure still resembles the accretion flow structure around the companion. In general, the field structure is complex with polarity changes on small scales, similar to the earlier phase (cf. Fig. 7.4), but extending to a slightly larger volume. Since the whole process is very dynamic with changes in the accretion flow compared to simulations of MRI in a shearing box (e.g., Rembiasz et al., 2016), it is difficult to compare the field structure in our simulation to the idealized situation of box simulations.

Similar to the fast amplification phase, parameters for the wavelength and growth rate of the fastest MRI channel can be estimated from the simulation data according to Eqs. (7.4) and (7.5). The flow around the companion can still be characterized by a mean value of the local rotational shear of $q \approx 1$. As the companion moves through the envelope and spirals in, the Alfvén velocity stays approximately constant, but the angular velocity Ω of the flow decreases. This leads to larger wavelengths of the fastest growing MRI channel and to smaller growth rates. This may the decrease of the growth rate comparing the initial fast amplification phase to the slow amplification phase after 3 d. Estimating the amplification timescale of the fastest growing mode from the flow around the companion yields roughly 1 d, which is smaller than the timescale of about 3 d found for the increase in the magnetic field energy but still of the same order of magnitude. The corresponding wavelengths of the channels increase with time and are larger ($> 10R_\odot$) than the structures seen in the magnetic field (cf. Fig. 7.6). Hence, the fastest growing mode might be suppressed. Reasons could be interactions with the background flow, the fact that MRI is usually derived in the incompressible limit, whereas the flow is compressible here, or the termination of some modes by secondary instabilities (see, e.g., Goodman & Xu, 1994 and Rembiasz et al., 2016).
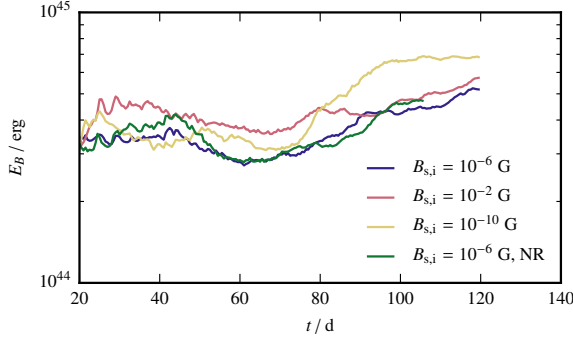
7.3.3 Saturation Phase

After about 20 d, the growth of the magnetic field energy stops and the magnetic field energy remains roughly constant between 3×10^{44} erg and 6×10^{44} erg during this saturation phase (Fig. 7.7).
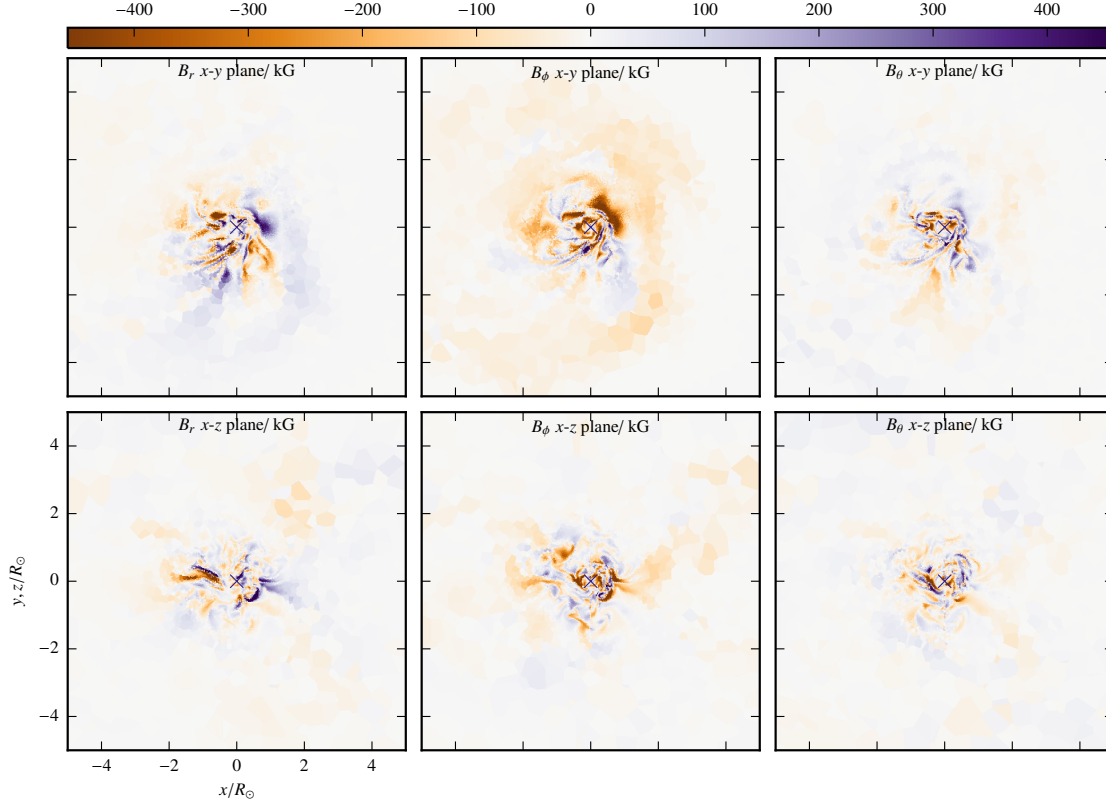
Figure 7.6 | Magnetic field components at 8 d. The panels show the spherical magnetic field components B_r (left column), B_ϕ (middle column), and B_θ (right column) in the orbital plane (upper row, rotated such that the point masses lie on the x axis) and in a plane perpendicular to this (lower row). The position of the RG core is marked by a +, the position of the companion by a ×. The plots show the simulation with an initial surface field of 10^{-6} G.

Differences may be due to the chaotic nature of the turbulent flow at later times. The magnetic field energy seems to rise again towards the end of the simulation, but whether or not this trend continues will have to be examined in simulations extending over longer times.

If indeed MRI is the driving mechanism of the field amplification, the saturation of the magnetic field energy is connected to the termination of the MRI. In the model of Goodman & Xu (1994), secondary instabilities can develop on top of the MRI channels. At some point, these secondary instabilities grow faster than the MRI, lead to a quenching of the MRI channels, and result in saturated turbulence. In our simulations, however, the structure of the flow around the companion is more important since it changes drastically during the evolution. During the first orbit (i.e., during the first 20 d) the flow around the companion resembles an accretion stream, with the magnetic field amplification taking place in a region up to $10R_\odot$ around the companion. This flow structure is disturbed near the end of the first orbit, where the separation at periastron is roughly $10R_\odot$; thus the presence of the RG core at this separation disturbs the flow structure around the companion. Thus, it seems plausible that the MRI is quenched by the change in the flow around the companion.

Figure 7.7 | Evolution of magnetic energy during the saturation phase. Shown is the total magnetic energy summed over the whole domain for runs with different initial surface fields $B_{s,i}$. NR denotes the non-rotating model.

This change is also observed in the magnetic field structure during the saturation phase (Fig. 7.8): at 20 d, the magnetic field in the orbital plane (upper left panel) is not confined to the vicinity of the companion anymore but is also present in trailing shocks. The field strength is larger in regions where it is compressed by shocks at 20 d and 70 d. Moreover, polarity changes occur on small scales, in the inner part mostly between adjacent layers of the spiral shock structure. After 120 d, the magnetic field structure seems complex and chaotic, probably due to turbulent flow induced by large-scale instabilities (cf. density structure in Fig. 5.3). In the plane perpendicular to the orbital plane, no obvious large scale structure can be seen (Fig. 7.8, lower row), only changes on small scales. During the evolution, the magnetic field is dispersed throughout the envelope, reaching strengths of roughly 10 kG in the envelope.

The orientation of the magnetic field to the fluid velocity is examined in Fig. 7.9 for the same times during the saturation phase as shown in Fig. 7.8. Fig. 7.9 shows the cosine of the pitch angle

$$\mu = \cos \vartheta = \frac{\boldsymbol{b} \cdot \boldsymbol{v}}{|\boldsymbol{b}||\boldsymbol{v}|}, \tag{7.6}$$

which is 1 for parallel configurations of magnetic field and velocity and -1 for anti-parallel configurations. After 20 d (left panel), the alignment is small and rather random in the regions with small magnetic fields. Near the shocks, however, the field is aligned to the velocity, but the direction (i.e., parallel or anti-parallel) changes in neighbouring layers perpendicular to the shocks. This can also be seen at 70 d (middle panel), where the shock spiral dominates the flow. The magnetic field is aligned to the velocity in most parts of the envelope with the direction (i.e., parallel or anti-parallel) changing in adjacent shock layers. After 120 d, (right panel), larger regions with parallel or anti-parallel directions of magnetic field and velocity form with some non-aligned regions with $\mu \approx 0$ in between. Nevertheless, during the whole evolution, no large-scale coherent magnetic field structure forms.

A measure for the impact of magnetic fields on the dynamical evolution is the ratio of the magnetic pressure,

$$p_b = \frac{1}{2}\boldsymbol{b}^2, \tag{7.7}$$

to the gas pressure. This ratio is shown for three different times in the orbital plane in Fig. 7.10 and perpendicular to the orbital plane in Fig. 7.11. During the first phases, the magnetic pressure is negligible almost everywhere. The evolution in the orbital plane (Fig. 7.10) shows that the ratio can be large in shocks (e.g., middle panel, bottom left structure) and can thus help to explain the larger ejection of mass during the first orbit compared to the non-MHD simulation (cf. Fig. 7.2). Apart from this, the ratio becomes larger during the simulation as the magnetic field is dispersed
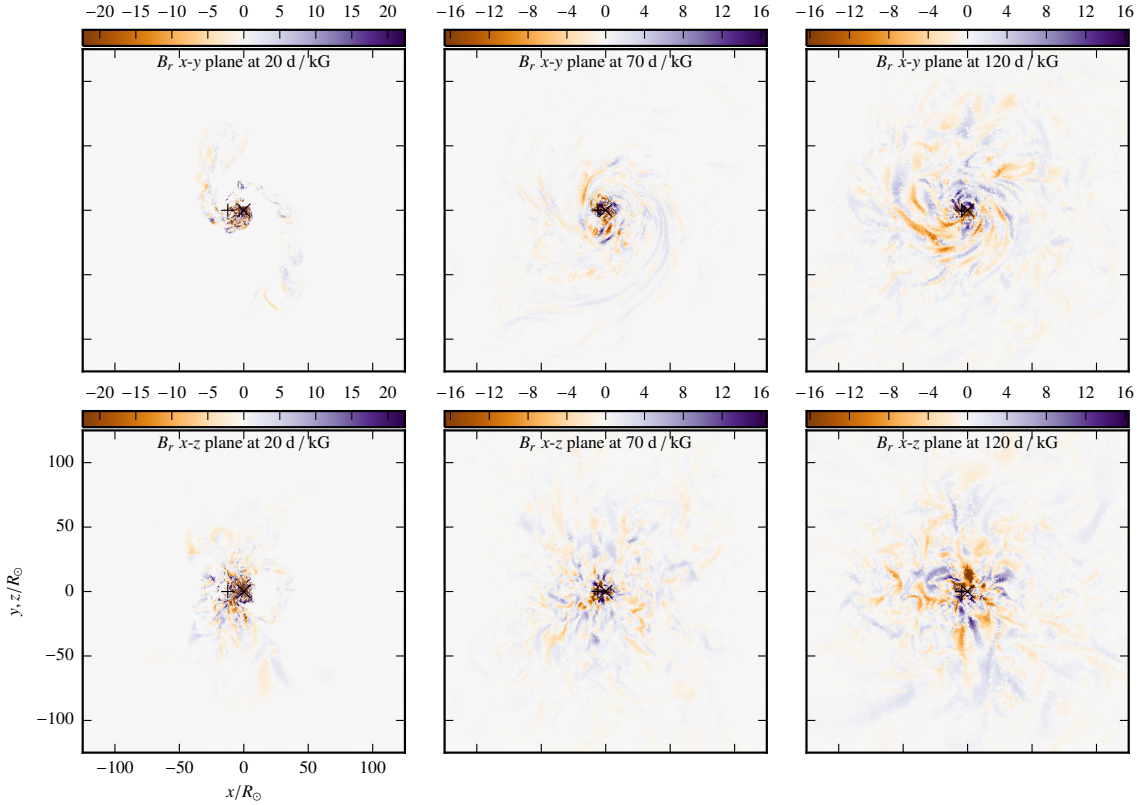
Figure 7.8 | Magnetic field during the saturation phase. The panels show the spherical magnetic field component B_r in the orbital plane (upper row, rotated such that the point masses lie on the x axis) and in a plane perpendicular to this (lower row) for three times: at 20 d (left column), at 70 d (middle column), and at 120 d (right column). The position of the RG core is marked by a +, the position of the companion by a ×. The plots show the simulation with an initial surface field of 10^{-6} G.

throughout the envelope and rises from nearly zero to a maximum of 10^{-3} in the orbital plane. Hence, the dynamical influence of the magnetic fields is small, as expected from the evolution of the distance (Fig. 7.1) that shows little difference between MHD and non-MHD simulations. Perpendicular to the orbital plane (Fig. 7.11), the situation is similar in the central regions with the same extents as in the orbital plane. Farther out, however, magnetic fields are transported to large distances from the orbital plane, where pressure and density of the gas are small, and ratios up to 10% are reached. Although this looks promising for driving large-scale motions, no enhanced outflows in the z directions are seen during the simulated time. Hence, the impact of magnetic fields on the dynamical evolution during CE phases seems mostly negligible, except from shocks where the magnetic pressure may contribute to slightly enhanced mass loss. This insignificant contribution is also supported by a more detailed analysis of the transport of angular momentum and energy that finds the contribution of Maxwell stress due to magnetic fields to be negligible (see Sec. 8).
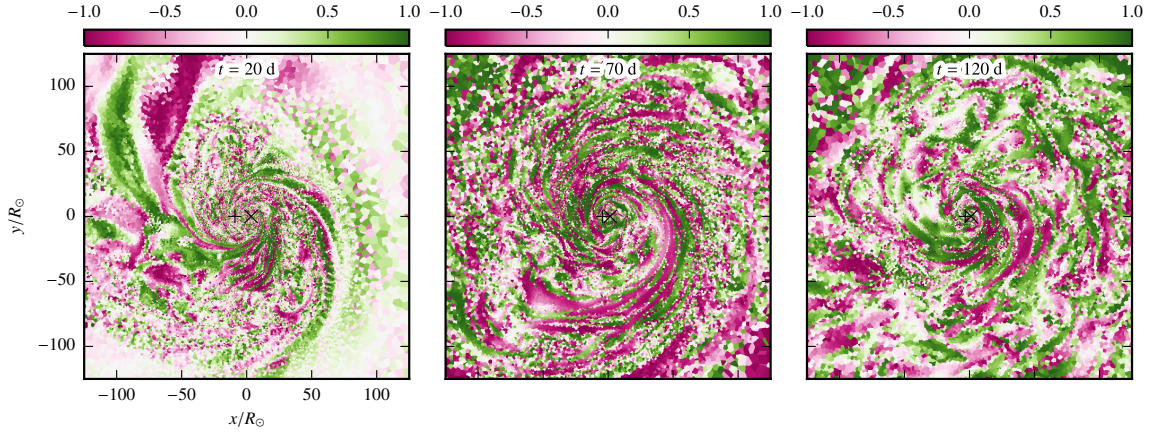
Figure 7.9 | Pitch angle during the saturation phase. The panels show the cosine of the pitch angle $\mu = \cos \vartheta = \boldsymbol{b} \cdot \boldsymbol{v}/(|\boldsymbol{b}||\boldsymbol{v}|)$ in the orbital plane for three times: at 20 d (left panel), at 70 d (middle panel), and at 120 d (right panel). The position of the RG core is marked by a +, the position of the companion by a ×. The plots show the simulation with an initial surface field of 10^{-6} G.
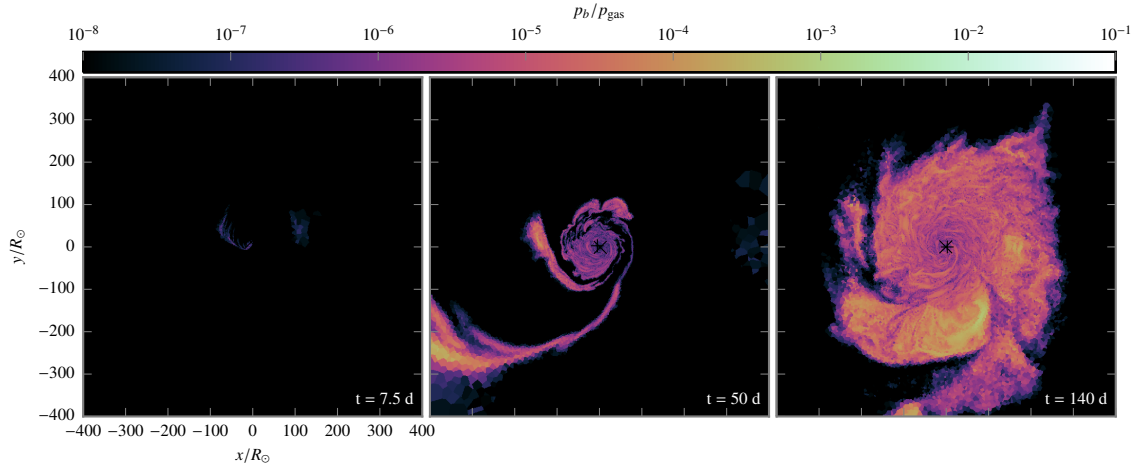
Figure 7.10 | Magnetic pressure over gas pressure in the orbital plane. Shown is the ratio of magnetic pressure $p_b = \boldsymbol{b}^2/2$ to gas pressure in the orbital plane for three times: at 7.5 d (left panel), at 50 d (middle panel), and at 140 d (right panel). The position of the RG core is marked by a +, the position of the companion by a ×. The plots show the simulation with an initial surface field of 10^{-6} G.

7.4 Conclusions

Here, we presented the first magnetohydrodynamic simulations of the CE phase, conducted using the moving-mesh code AREPO, solving the ideal MHD equations. The results show that magnetic fields can be amplified by orders of magnitude saturating after the first orbit of the in-spiral, independent of the initial seed field. We can distinguish three phases during the evolution: fast amplification, slow amplification, and saturation phase. A plausible mechanism for the amplification is the magneto-rotational instability operating in the accretion stream around the companion. In
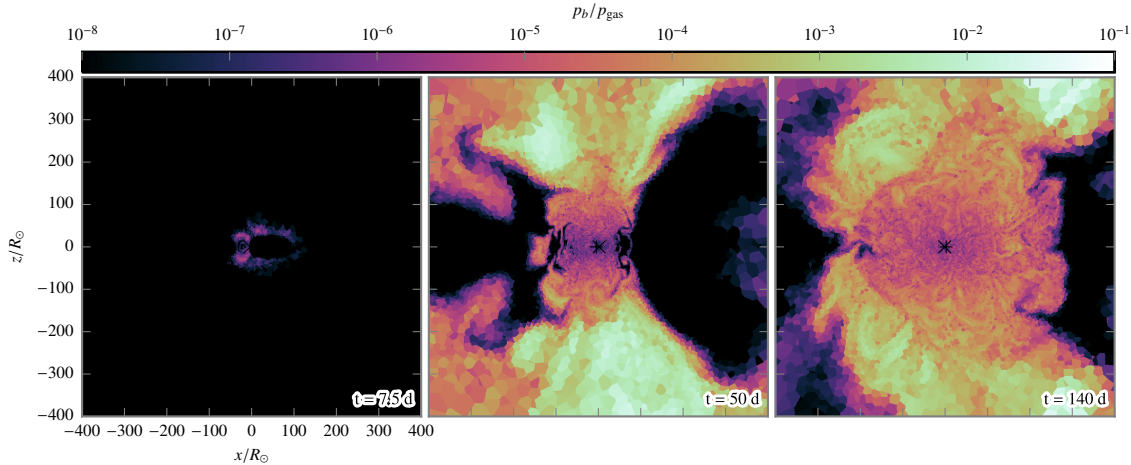
Figure 7.11 | Magnetic pressure over gas pressure perpendicular to the orbital plane. Shown is the ratio of magnetic pressure $p_b = \boldsymbol{b}^2/2$ to gas pressure perpendicular to the orbital plane for three times: at 7.5 d (left panel), at 50 d (middle panel), and at 140 d (right panel). The position of the RG core is marked by a +, the position of the companion by a ×. The plots show the simulation with an initial surface field of 10^{-6} G.

contrast to earlier studies that assume a dynamo process in the differentially rotating envelope (Regős & Tout, 1995; Tout & Regős, 2003; Nordhaus & Blackman, 2006; Nordhaus et al., 2007; Tout et al., 2008; Potter & Tout, 2010; Nordhaus et al., 2011; Wickramasinghe et al., 2014), this process shows that magnetic fields of 10 kG to 100 kG can be generated on timescales of a few days during the in-spiral. The magnetic fields are dynamically not relevant except in some shocks and lead to very similar final separations as simulations without magnetic fields. This is also supported by the analysis of the transport of angular momentum and energy in Sec. 8. Although we conducted simulations only for one mass ratio and one RG envelope, the mechanism seems to be quite universal since it operates in the accretion flow around the companion independent of the initial field.

On timescales longer than simulated here, it is still possible that dynamo processes operate in the differentially rotating envelope, producing even larger fields on longer timescales. The magnetic field strengths found in our simulations, roughly 10 kG to 100 kG throughout the envelope, are slightly larger but still of a similar order of magnitude compared to the field strength inferred by Tocknell et al. (2014) from analyzing jets in PNe. The dynamic generation of magnetic fields should be robust and universal in CE evolution and thus also an important factor for the evolution and shaping of PNe.

Since our simulations cover only a rather short time span during the whole CE evolution, it is difficult to foresee the consequences for the evolution of MWDs and MCVs. During our simulations, the magnetic field structure is highly variable such that it is very difficult to transport the magnetic field to the surface of the RG core on these short time scales (Potter & Tout, 2010). Moreover, the progenitor systems for MWDs and MCVs should mostly be AGB stars with low-mass companions (Briggs et al., 2015), having a more extended envelope structure than the RG model considered in our simulation.

The simulations presented here are just a first step to understanding the dynamical behaviour of magnetic fields during the dynamical spiral-in of a CE phase. Exploring simulations with different mass ratios, larger initial distances and also with AGB envelopes will enable us to better understand the role of magnetic fields during the CE phase with consequences for the evolution of PNe and MWDs.

Chapter 8

Transport of Angular Momentum and Energy

One important process during CE evolution is the transfer of angular momentum and energy from the binary system of the giant's core and the companion to the gas of the envelope since this is coupled to the decrease in orbital separation. Moreover, the ejection of the envelope may be related to the transport mechanisms of angular momentum and energy. In this section, the transport of angular momentum and energy is studied and the role of different factors, such as hydrodynamical fluxes, torques, and magnetic fields, is examined.

For circumbinary disks that are nearly static, the disk structure and angular momentum transport was examined, e.g., by Shi et al. (2012) and MacFadyen & Milosavljević (2008); for more references on circumbinary disks, see the introduction of Shi et al. (2012). Shi et al. (2012) conduct three-dimensional MHD simulations of a nearly Keplerian circumbinary disk around an equal-mass binary. Due to the binary nature of the stellar system, torques can be exchanged with the gas. The main contribution to the angular momentum transport, however, is thought to be MHD turbulence, where the magnetic fields are amplified by the magneto-rotational instability in the disk (cf. the accretion disk model by Shakura & Sunyaev, 1973). Shi et al. (2012) find in their simulation that the angular momentum transport is dominated by stress due to turbulent velocities (Reynolds stress), by magnetic stress (Maxwell stress), and by torques in different regions of the disk. Although circumbinary disks are already more dynamical than single accretion disks due to the binary torques, they show still steady features. Compared to this, a CE phase is highly dynamic with rapidly changing conditions over time. Nevertheless, we can gain insight into the nature of angular momentum transport by employing a similar analysis technique as in Shi et al. (2012). Moreover, we extend this analysis to the transport of energy.

8.1 Angular Momentum Balance

The evolution of the angular momentum density $\boldsymbol{l} = \rho \boldsymbol{r} \times \boldsymbol{v}$ can be obtained from the momentum balance of the MHD equations (2.7) when including magnetic fields,

$$
\begin{aligned}
\partial_t \boldsymbol{l} &= \boldsymbol{r} \times \partial_t (\rho \boldsymbol{v}) \\
&= -\boldsymbol{r} \times \nabla \left[\rho \boldsymbol{v} \otimes \boldsymbol{v} + \left(p + \frac{1}{2} \boldsymbol{b}^2 \right) \mathbf{I} - \boldsymbol{b} \otimes \boldsymbol{b} \right] + \rho \boldsymbol{r} \times \boldsymbol{f} + \boldsymbol{r} \times \nabla \boldsymbol{\sigma} \\
&= -\boldsymbol{r} \times \nabla (\rho \boldsymbol{v} \otimes \boldsymbol{v} - \boldsymbol{b} \otimes \boldsymbol{b} - \boldsymbol{\sigma}) - \boldsymbol{r} \times \nabla \left(p + \frac{1}{2} \boldsymbol{b}^2 \right) + \rho \boldsymbol{r} \times \boldsymbol{f}.
\end{aligned}
\tag{8.1}
$$

Since the outflow in our CE simulations is mostly concentrated around the orbital plane, angular momentum transport is studied best in cylindrical geometry. Neglecting the viscosity term and evaluating the derivatives in cylindrical coordinates (r, ϕ, z), the evolution of the z component can

be written as

$$\partial_t l_z = -\frac{1}{r}\partial_r \left[r^2 \left(\rho v_r v_\phi - b_r b_\phi \right) \right] - \partial_\phi \left(\rho v_\phi^2 - b_\phi^2 \right) - r\partial_z \left(\rho v_z v_\phi - b_z b_\phi \right)$$

$$- \partial_\phi \left(p + \frac{1}{2}\boldsymbol{b}^2 \right) + \rho r f_\phi, \quad (8.2)$$

where the vector components are obtained as usual by multiplying with the corresponding unit vectors. One can now see that the radial flux of angular momentum is given by the r-ϕ components of the hydrodynamical and magnetic stress tensors. Moreover, pressure gradients are only able to transport angular momentum in the azimuthal direction, but not in the radial direction. The last term in Eq. (8.2) corresponds to the torque due to the external force, which is gravity in our case.

The radial evolution of the angular momentum can be examined by integrating Eq. (8.2) over cylindrical shells, similar to the analysis by Shi et al. (2012, Sec. 2.4). This yields the integrated shell angular momentum $L(r)$,

$$L(r) = \int_{-Z}^{Z} \mathrm{d}z \int_{0}^{2\pi} \mathrm{d}\phi \int_{r-\Delta r}^{r+\Delta r} \mathrm{d}r\, r l_z(r, \phi, z), \quad (8.3)$$

where Z is the extent of the grid in z direction and $2\Delta r$ the width of the radial shell. Its evolution is given by

$$\partial_t L(r) = \int_{-Z}^{Z} \mathrm{d}z \int_{0}^{2\pi} \mathrm{d}\phi \left[-r^2 \left(\rho v_r v_\phi - b_r b_\phi \right) \right]_{r-\Delta r}^{r+\Delta r}$$

$$- \int_{-Z}^{Z} \mathrm{d}z \int_{r-\Delta r}^{r+\Delta r} \mathrm{d}r\, r \left[\rho v_\phi^2 + b_\phi^2 \right]_{0}^{2\pi}$$

$$- \int_{0}^{2\pi} \mathrm{d}\phi \int_{r-\Delta r}^{r+\Delta r} \mathrm{d}r\, r^2 \left[\rho v_z v_\phi - b_z b_\phi \right]_{-Z}^{Z} \quad (8.4)$$

$$- \int_{-Z}^{Z} \mathrm{d}z \int_{r-\Delta r}^{r+\Delta r} \mathrm{d}r\, r \left[p + \frac{1}{2}\boldsymbol{b}^2 \right]_{0}^{2\pi}$$

$$+ \int_{-Z}^{Z} \mathrm{d}z \int_{0}^{2\pi} \mathrm{d}\phi \int_{r-\Delta r}^{r+\Delta r} \mathrm{d}r\, r^2 \rho f_\phi \,.$$

Here, the terms in the second and fourth lines vanish since the quantities in the brackets are continuous. Morover, the term in the third line can be neglected, since the z integral extends to the boundaries of the domain, where the density and magnetic fields are small and can be neglected. The equation can be written in a simpler way by introducing the shell average of a quantity X as

$$\langle X \rangle(r) = \frac{1}{V} \int_{\mathrm{shell}} \mathrm{d}V X = \frac{1}{8\pi Z r \Delta r} \int_{-Z}^{Z} \mathrm{d}z \int_{0}^{2\pi} \mathrm{d}\phi \int_{r-\Delta r}^{r+\Delta r} \mathrm{d}r\, r X(r, \phi, z) \,. \quad (8.5)$$

For vanishing Δr, this yields an approximation of the surface average of the quantity X at radius r,

$$\lim_{\Delta r \to 0} \langle X \rangle(r) = \frac{1}{4\pi Z} \int_{-Z}^{Z} \mathrm{d}z \int_{0}^{2\pi} \mathrm{d}\phi\, X(r, \phi, z) \,. \quad (8.6)$$

With these definitions, we can rewrite Eq. (8.4) as

$$\partial_t L(r) \approx -4\pi Z \left[r^2 (\langle \rho v_r v_\phi \rangle(r) - \langle b_r b_\phi \rangle(r)) \right]_{r-\Delta r}^{r+\Delta r} + 8\pi Z r \Delta r \langle \rho r f_\phi \rangle(r) \quad (8.7)$$

Following Shi et al. (2012), we define the mean angular momentum flux as

$$F_{r\phi}(r) = \frac{\langle \rho v_r \rangle \langle \rho v_\phi \rangle}{\langle \rho \rangle}, \tag{8.8}$$

the r-ϕ component of the Reynolds stress tensor as

$$r_{r\phi}(r, \phi, z) = \rho \delta v_r \delta v_\phi = \rho \left(v_r - \frac{\langle \rho v_r \rangle}{\langle \rho \rangle} \right) \left(v_\phi - \frac{\langle \rho v_\phi \rangle}{\langle \rho \rangle} \right), \tag{8.9}$$

and its average as

$$R_{r\phi}(r) = \langle r_{r\phi} \rangle = \langle \rho v_r v_\phi \rangle - F_{r\phi}(r). \tag{8.10}$$

The Reynolds tensor gives the stress component due to velocity deviations from the mean velocity in a shell and can be interpreted as a turbulent stress. Also similar to Shi et al. (2012), we define the Maxwell stress tensor $m_{r\phi}$ and its average $M_{r\phi}$ as

$$\begin{aligned} m_{r\phi} &= -b_r b_\phi \\ M_{r\phi} &= -\langle b_r b_\phi \rangle. \end{aligned} \tag{8.11}$$

Moreover, the torque is denoted by $T(r) = 8\pi Z r \Delta r \langle \rho r f_\phi \rangle(r)$. Note that the notation adopted here differ slightly from the ones used by Shi et al. (2012): we only use cylindrical averages and denote averages over those by bracketed quantities.

Using these definitions, we can rewrite the transport equation (8.7) as (cf. Shi et al., 2012, Eq. 15)

$$\partial_t L(r) = -4\pi Z \left[r^2 \left(F_{r\phi}(r) + R_{r\phi}(r) + M_{r\phi}(r) \right) \right]_{r-\Delta r}^{r+\Delta r} + T(r). \tag{8.12}$$

From this equation, we can read off different transport mechanisms: the angular momentum in a shell changes either due to fluxes caused by mean hydrodynamic motions, by Reynolds stress, or by Maxwell stress or it changes due to torques.

To compute the terms in Eq. (8.12) from a simulation done with AREPO, the unstructured grid is binned in cylindrical radius around the center of mass of the point masses and the shell averages are split into a sum over the cell volumes.

8.2 Energy Balance

The evolution of the total energy density is governed by the last of the MHD equations Eq. (2.7). From this, the radial transport of the total energy can be examined in a similar way as the angular momentum (cf. Sec. 8.1).

Let the total energy in a cylindrical shell be $E(r)$. Integrating the last equation of Eq. (2.7) over a cylindrical shell and discarding the ϕ and z derivatives yields

$$\begin{aligned} \partial_t E(r) &= -4\pi Z \left[r \left(\langle v_r(\rho e_{\text{tot}} + p) \rangle(r) - \left\langle b_r \boldsymbol{v} \cdot \boldsymbol{b} - v_r \frac{\boldsymbol{b}^2}{2} \right\rangle(r) \right) \right]_{r-\Delta r}^{r+\Delta r} + 8\pi Z r \Delta r \langle \rho \boldsymbol{v} \cdot \boldsymbol{f} \rangle(r) \\ &= -4\pi Z \left[r \left(F_h(r) + F_b(r) \right) \right]_{r-\Delta r}^{r+\Delta r} + W(r). \end{aligned} \tag{8.13}$$

This defines the hydrodynamical energy flux F_h, the energy flux due to magnetic fields F_b and the gravitational work W. The averages are defined in Eq. (8.5).

Similar to the analysis of the angular momentum, these terms are computed by binning the grid in cylindrical shells and splitting the integrals into a sum of integrals over each cell.
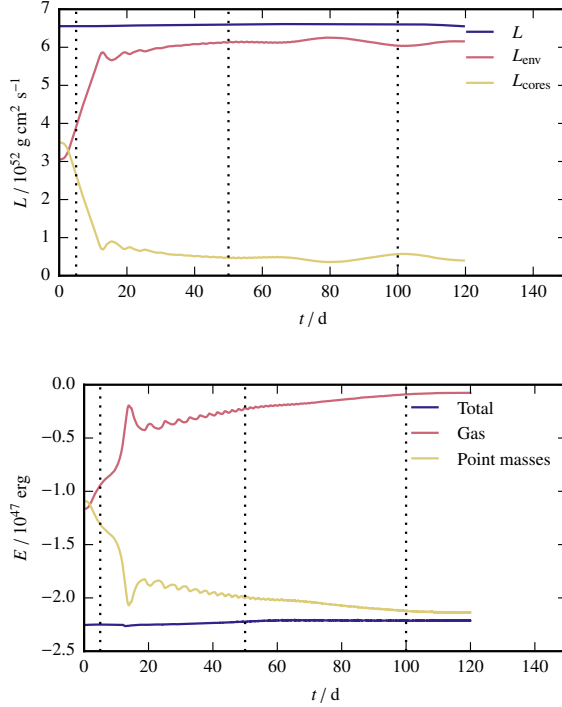
Figure 8.1 | Evolution of angular momentum. Plotted is the angular momentum of the whole system, the gas, and the system of the point masses for the MHD simulation with a mass ratio of $q = 0.5$ and an initial surface field of $B_{s,i} = 10^{-6}$ G. The black dotted vertical lines mark the times at which snapshots are analyzed in more detail.

Figure 8.2 | Evolution of energy. Plotted is the total energy of the whole system, the gas, and the system of the point masses for the MHD simulation with a mass ratio of $q = 0.5$ and an initial surface field of $B_{s,i} = 10^{-6}$ G. The black dotted vertical lines mark the times at which snapshots are analyzed in more detail.

8.3 Total Budget

The evolution of the angular momentum budget is shown in Fig. 8.1 for the MHD simulation with a mass ratio of $q = 0.5$ and an initial surface field of $B_{s,i} = 10^{-6}$ G. The total angular momentum is well conserved with an error less than 0.1%, much better than for Eulerian grid codes (cf. the error of about 5% during the first few orbits of the simulations by Iaconi et al., 2016). As Fig. 8.1 shows, the binary consisting of the RG core and the companion loses a large amount of the initial angular momentum in the first 20 d, i.e., during the first orbit. This angular momentum is transferred to the gas of the envelope. After the first orbit, no major exchange happens and the angular momentum of the envelope and the point masses stays nearly constant. After 120 d, the angular momentum of the binary system of the point masses is 4.0×10^{51} g cm^2 s^{-1}. This agrees very well with the angular momentum of a binary system with masses M_1 and M_2 with semi-major axis a and eccentricity e,

$$L = \sqrt{(1 - e^2) \frac{G M_1^2 M_2^2}{M_1 + M_2} a}. \tag{8.14}$$

For the semi-major axis $4.3 R_\odot$ at 120 d, this yields 4.0×10^{51} g cm^2 s^{-1} for $e = 0$.

For the same simulation, the evolution of the total energy budget is shown in Fig. 8.2. The binary system of the point masses transfers energy to the gas of the envelope over the course of the spiral-in. A large part is transferred in the first orbit, but the transfer continues and the energies do not become constant. After 120 d, the total energy of the gas is negative; hence, the envelope is still bound globally. A small amount of the envelope is unbound (roughly 8%, cf. Fig. 7.2), thus, the remaining envelope is bound even stronger than the binding energy of 7.6×10^{45} erg suggests. We cannot compute the efficiency of the ejection, since the envelope is not ejected during the first 120 d. The total energy of the binary of point masses is -2.1×10^{47} erg after 120 d. This includes

also potential energy from the self-gravity of the part of the envelope that is still bound. For a binary system consisting of the point masses only, without gas, the binding energy is given by

$$E = -\frac{GM_1M_2}{2a}. \tag{8.15}$$

The semi-major axis for an isolated binary consisting of the two point masses at an energy of -2.1×10^{47} erg (i.e., for a hypothetical system where the envelope would be ejected) is $3.3R_\odot$ according to Eq. (8.15). Hence, to eject the envelope, the binary system of the point masses has to decrease its separation from $4.3R_\odot$ after 120 d to at least $3.3R_\odot$. Supposing that the change of the separation stays constant at its value after 120 d, $\dot{a} = -10^{-2}R_\odot/\text{d}$, this decrease by $1R_\odot$ would take roughly another 100 d. If the orbital decay timescale increases further, however, this decrease in separation can also take substantially longer. For such a decrease in separation, the angular momentum of the binary would have to change from 4.0×10^{51} g cm^2 s^{-1} to 3.5×10^{51} g cm^2 s^{-1}, i.e., by 12.5%, according to Eq. (8.14).

One goal for further simulations is to extend the current simulations to a longer timescale to see if a further decrease in binary separation is possible on a dynamical timescale. This could, however, be computationally too expensive since the spatial resolution in the central part required to resolve the gravitational fields around the point masses is quite high. Moreover, the point masses orbit at a period of roughly 1 d, i.e., for a further 100 d, we would need to follow 100 orbits. Whether or not this is possible with currently available computational resources has to be explored in future simulations.

8.4 Angular Momentum Transport

The impact of different mechanisms of angular momentum transport are now examined using the analysis as described in Sec. 8.1. To this end, the distributions of the hydrodynamic stress and of the torque in the orbital plane as well as the radial distributions of the angular momentum and of the angular momentum fluxes in cylindrical shells are shown in Figs. 8.3, 8.4, and 8.5 for three different times during the simulation: after 5 d, during the first orbit of the spiral-in (Fig. 8.3); after 50 d, when a spiral shock wave pattern dominates the flow (Fig. 8.4); and after 100 d, with large-scale flow instabilities being present (Fig. 8.5).

At 5 d, one can see that the torque is quite strong around the point masses (Fig. 8.3, right panel) which leads to a transfer of angular momentum from the binary system of the point masses to the gas. This also shows up as a positive contribution to the angular momentum fluxes of the gas in the upper left panel of Fig. 8.3 (green line) with maxima near the positions of the point masses (marked by vertical black lines). This strong transfer of angular momentum from the point masses to the gas is expected, since most of this transfer happens during the first orbit (see Fig. 8.1). The distribution of the total hydrodynamical stress in the orbital plane (Fig. 8.3, middle panel) shows the largest contribution in the regions where mass is accreted onto the companion and thus also accelerated to larger radii. This transports angular momentum outwards: at the peak of the angular momentum distribution (Fig. 8.3, lower left panel), the mean hydrodynamic angular momentum flux is negative (Fig. 8.3, upper left panel; blue line). Thus, angular momentum is removed here and transported to larger radii, where the flux is positive. This corresponds to the outwards movement of a stream of material that is ejected during the first orbit and that transport angular momentum outwards with it.
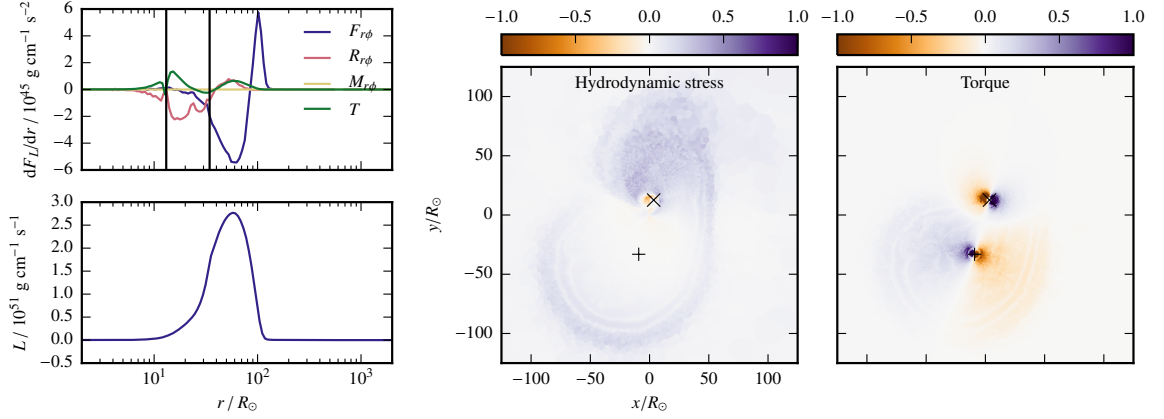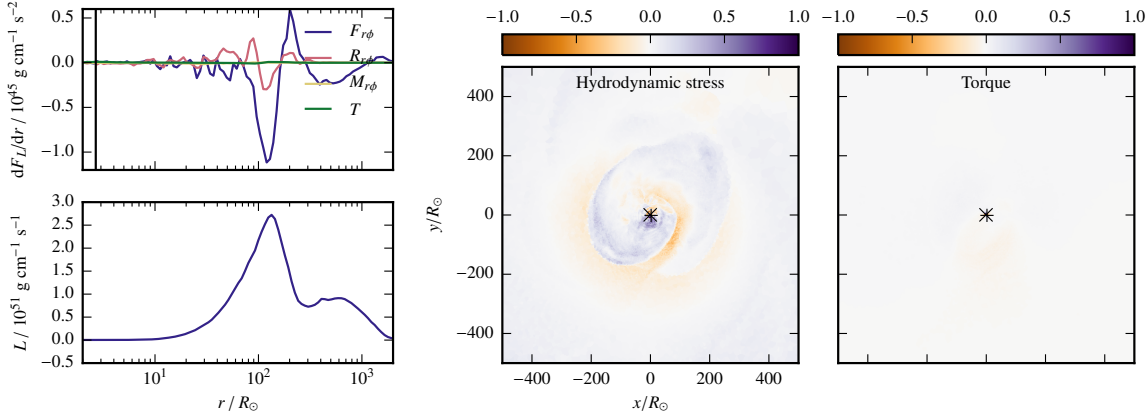
Figure 8.3 | Angular momentum transport after 5 d. The left column shows cylindrical integrals of the different contributions to the radial angular momentum flux in the top panel ($F_{r\phi}$: mean angular momentum flux, $R_{r\phi}$: Reynolds stress, $M_{r\phi}$: Maxwell stress, T: torque; compare Eqs. (8.8), (8.10), (8.11)) and the cylindrical integral of the angular momentum in the bottom panel. The black vertical lines denote the position of the point masses. The middle and right column show slices through the orbital plane of the hydrodynamic stress $mv_r v_\phi$ and the torque mrg_ϕ respectively. The hydrodynamic stress and the torque are divided by a factor 10^{42}. The position of the RG core is marked with a +, the position of the companion with a ×. All quantities were computed relative to the center of mass of the point masses.
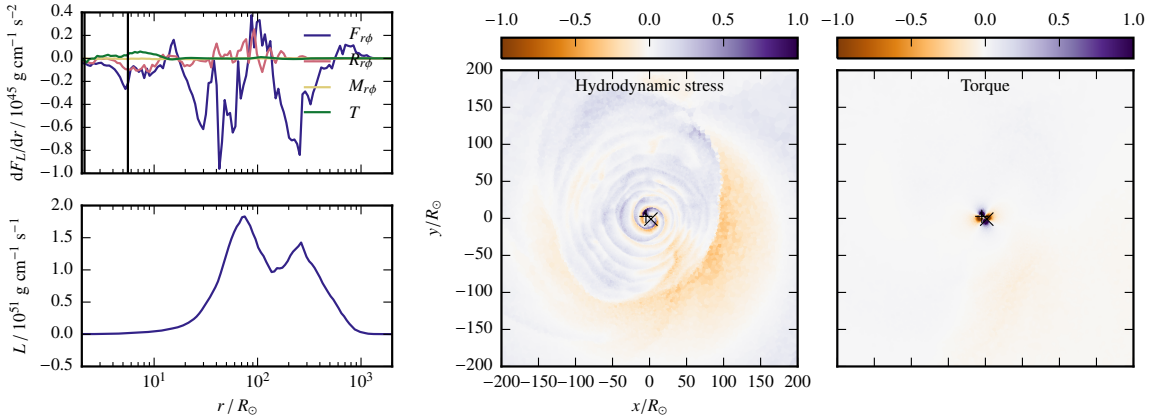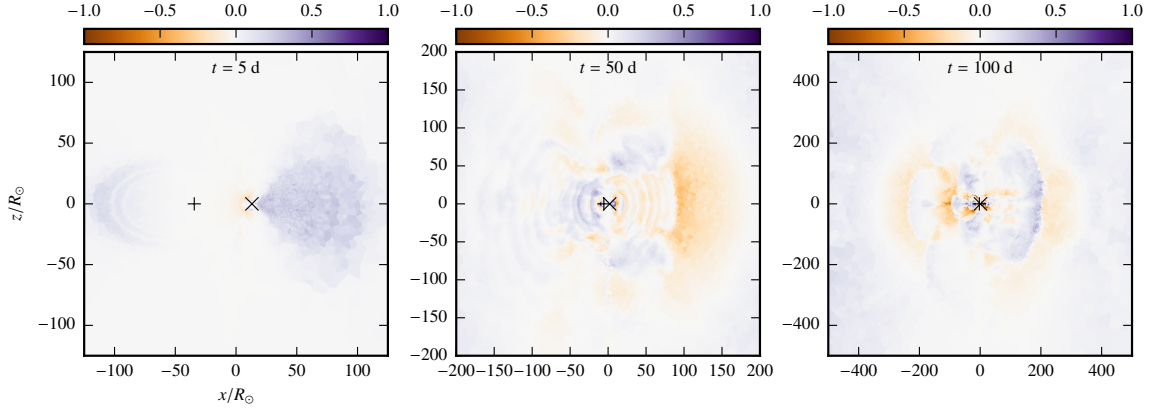

Figure 8.4 | Angular momentum transport after 50 d. The plots show the same quantities as in Fig. 8.3. The hydrodynamic stress and the torque are divided here by a factor 10^{41}.

After 50 d, this material can be identified with the second peak in the radial angular momentum distribution at larger radii (Fig. 8.4, lower left panel) that is still transported outwards. At this time, the torque exerted on the gas is concentrated to a small area (Fig. 8.4, right panel) and much smaller than during the first orbit.[1] This results in a smaller contribution to the angular momentum budget (Fig. 8.4, upper left panel) and consequently, less angular momentum is transferred from the system of the point masses to the gas, as expected at this time from the angular momentum budget (Fig. 8.1) that shows nearly constant values for the total angular momentum of the gas and the point masses, respectively. As the middle panel of Fig. 8.4 reveals, the main contribution to

---

[1]Note that the scale of the color bar is a factor of ten less in Figs. 8.4 and 8.5 compared to Fig. 8.3.

Figure 8.5 | Angular momentum transport after 100 d. The plots show the same quantities as in Fig. 8.3. The hydrodynamic stress and the torque are divided here by a factor 10^{41}.

the hydrodynamic angular momentum flux comes from shock waves that form a spiral pattern. These shock waves can be seen as peaks in the hydrodynamic angular momentum flux (Fig. 8.4, upper left panel) and lead to a transport of angular momentum to larger radii: they remove angular momentum at the peak of the angular momentum distribution and inject angular momentum at larger radii. The fluxes associated with this transport, however, are a factor of a few smaller than those seen after 5 d (cf. Fig. 8.3).

The torque on the gas further decreases and is not significant after 100 d (Fig. 8.5, right panel). At this time, the flow structure is dominated by large scale instabilities that washed out the spiral shock structure as seen before. The hydrodynamic stress is dominated at large scales by a one-armed spiral that is induced by the instabilities (Fig. 8.5, middle panel). The bulk of the angular momentum distribution (Fig. 8.5) is located at larger radii compared to earlier times and angular momentum is still transported outwards. The second peak at larger radii corresponds to the matter stream that was unbound during the first orbit and that is still moving outwards.

The hydrodynamical stress is shown in Fig. 8.6 in a plane perpendicular to the orbital plane that also contains the two point masses for three times corresponding to Figs. 8.3, 8.4, and 8.5. These distributions show that the cylindrical geometry used to describe the radial angular momentum transport corresponds well to the main flow features. At 5 d, the hydrodynamical stress is dominated by the accretion flow onto the companion (Fig. 8.6, left panel). Shock waves transporting angular momentum outwards at 50 d can be seen in Fig. 8.6 (middle panel). In Fig. 8.6 (right panel), the only large-scale structure is the one-armed spiral that is seen here as a cut.

At all times, the Maxwell stress due to magnetic fields is negligible compared to the hydrodynamical stress, hence we conclude that magnetic fields do not contribute significantly to the dynamics of the angular momentum transport in this simulation. Moreover, the mean angular momentum flux is larger than the flux due to Reynolds stress. This may be explained by the fact that at early times, no turbulent motions are present; and at late times (> 70 d) they may not be developed enough to contribute significantly.

Figure 8.6 | Angular momentum transport perpendicular to the orbital plane. The three panels shows the hydrodynamic stress in the plane perpendicular to the orbital plane that is rotated such that it includes the two point masses. The panels show the stress at 5 d, 50 d, and 100 d (left to right) and the hydrodynamic stress is divided by a factor 10^{42} (left panel), 10^{41} (middle panel), and 5×10^{40} (right panel). The times and spatial scales are the same as in Figs. 8.3, 8.4, and 8.5.

8.5 Energy Transport

A similar analysis as done in the previous section for the transport of angular momentum can be applied to the transport of energy, using the equations as described in Sec. 8.2. The distribution of the hydrodynamical flux term and the gravitational term in the orbital plane and the radial distribution of the total energy integrated over cylindrical shells as well as the fluxes in these shells are shown in Figs. 8.7, 8.8, and 8.9 at three different times: 5 d (Fig. 8.7), 50 d (Fig. 8.8), and 100 d (Fig. 8.9); at the same times as for the analysis of the angular momentum transport.

At 5 d, the radial energy fluxes are dominated by a conversion of gravitational energy (which is not included in the total energy) to total energy of the gas (i.e., internal, kinetic, and magnetic energy) around the position of the companion, which can be seen as large contributions of the hydrodynamical and the gravitational term that nearly cancel out (Fig. 8.7, upper left panel). This can also be seen in the distribution of the gravitational term in the orbital plane that is strongly concentrated around the companion, even inside the softening length (Fig. 8.7, right panel). This conversion of gravitational energy to total energy of the gas is expected from the evolution of the total energy budget (Fig. 8.2), it is strongest in the roughly the first 20 d. The hydrodynamic flux term shows contributions in the vicinity of the companion, but also due to the accretion stream onto the companion (Fig. 8.7, middle panel). The radial energy distribution (Fig. 8.7, lower left panel) peaks at the position of the RG core since this corresponds to the stellar structure of the initial RG profile that is still only slightly perturbed at this stage. Moreover, the potential energy is larger than the total energy (i.e., more negative than the total energy positive) over almost the whole profile, i.e., almost no material is unbound at this point.

After 50 d, gravitational energy is converted around both point masses (i.e., also around the core of the RG) into total energy of the gas: this can be seen from the radial distribution of the energy fluxes (Fig. 8.8, upper left panel). Near both point masses, the gravitational and hydrodynamical terms are large and nearly cancel out. This conversion is located in the direct vicinity of the point masses, also inside the softening lengths (Fig. 8.8, right panel). In contrast to the situation during
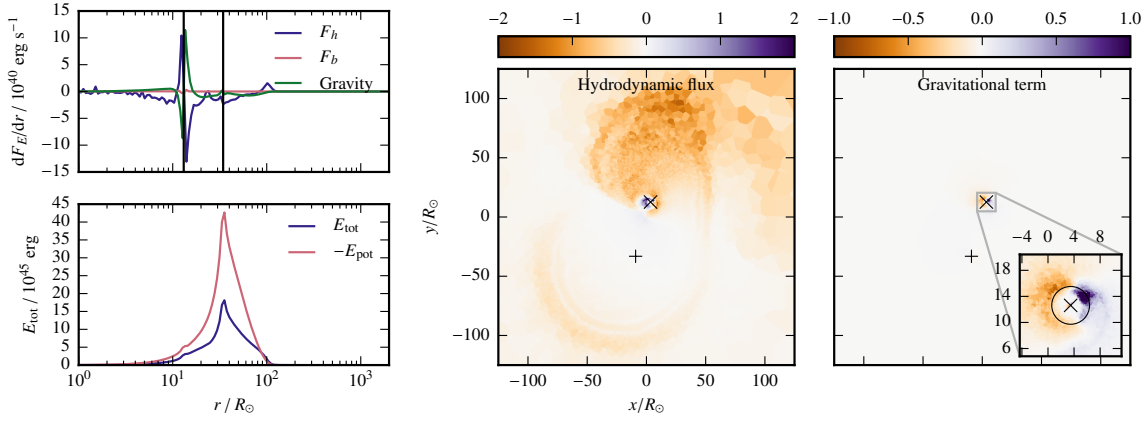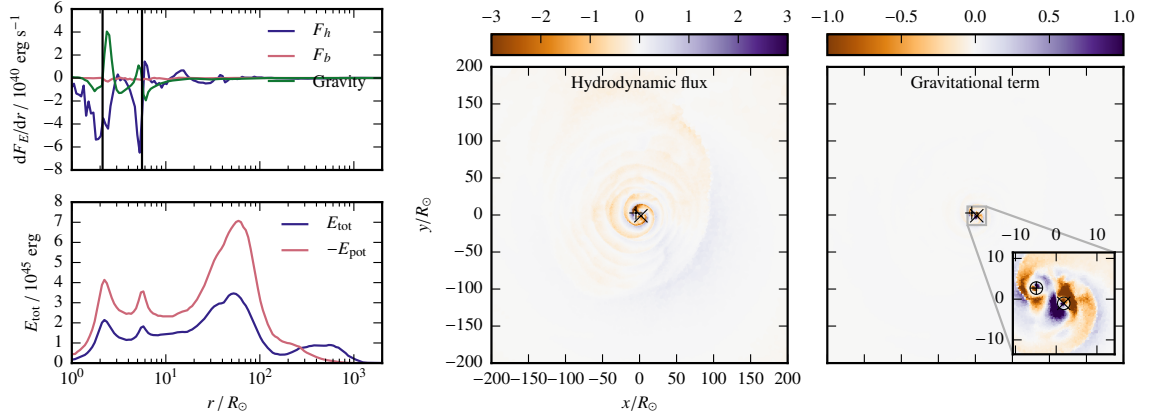
Figure 8.7 | Energy transport after 5 d. The left column shows cylindrical integrals of the different contributions to the radial energy flux in the top panel (F_h: hydrodynamic energy flux, F_b: energy flux due to magnetic fields, W: gravitational work term; cf. Eq. (8.13)) and the cylindrical integral of the total energy in the bottom panel. The total energy does not include gravitational energy but is defined as in the MHD equations (2.7). The black vertical lines denote the position of the point masses. The middle and right column show slices through the orbital plane of the hydrodynamic flux $v_r(\rho e_{\text{tot}} + p)$, multiplied by the volume of the cells, and the gravitational work $m\boldsymbol{v} \cdot \boldsymbol{g}$, respectively. The hydrodynamic term is divided by a factor of 10^{49}, and the gravitational term is divided by a factor 10^{38}. The position of the RG core is marked with a +, the position of the companion with a ×. All quantities were computed relative to the center of mass of the point masses. In the inset, a circle marks the softening length of the companion which is $2.9 R_\odot$.

the first orbit, the RG core and the companion orbit each other and move both through the gas of the envelope. Hence, gravitational energy is converted to total energy of the gas around both point masses. The magnitude of the fluxes, however, decreases by a factor of two to three compared to the snapshot at 5 d. The distribution of the hydrodynamical flux term in the orbital plane (Fig. 8.8, middle panel) shows the same shock pattern as the corresponding distribution for the angular momentum transport (Fig. 8.4, middle panel), although the contribution of these shocks to the energy transport seems to be smaller than to the angular momentum transport (cf. fluxes in the upper left panel of Fig. 8.8 and Fig. 8.4). The radial energy distribution shows several peaks (Fig. 8.8, lower left panel). The first two peaks correspond to the two point masses, the third peak to the bulk of the envelope mass, and the last peak to the stream of material that was ejected in the first orbit. This material is unbound since the sum of total energy of the gas and potential energy is larger than zero, as can be seen in Fig. 8.8 (lower left panel).

The conversion of gravitational energy to total energy of the gas stays localized around the point masses after 100 d (Fig. 8.9, right panel) and decreases further in magnitude (cf. the fluxes in Fig. 8.9, upper left panel). The large-scale distribution of the hydrodynamical flux in the orbital plane (Fig. 8.9, middle panel) does not show the spiral shock pattern since it has been washed out by large-scale flow instabilities. The only structure seen here is a one-armed spiral wave that is due to the large-scale instability. The radial distribution of the energy (Fig. 8.9, lower left panel) shows that most of the total energy of the gas around the point masses has been transported to larger radii. The bulk of the energy distribution is located at slightly larger radii than at 50 d, although the transport seems to be not as efficient as for the angular momentum. The last peak in the distribution still corresponds to the unbound material, where the total energy of the gas is larger than its potential energy.

Figure 8.8 | Energy transport after 50 d. The plots show the same quantities as in Fig. 8.7. The hydrodynamic term is divided by a factor of 10^{48}, and the gravitational term is divided by a factor 10^{37}. In the inset, circles mark the softening length around both point masses which is $1.5R_\odot$ at this time.
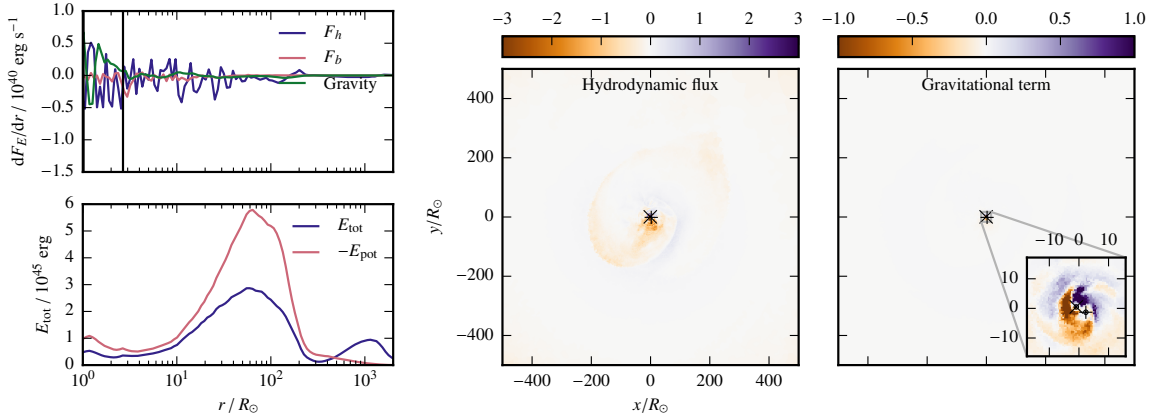
Figure 8.9 | Energy transport after 100 d. The plots show the same quantities as in Fig. 8.7. The hydrodynamic term is divided by a factor of 10^{48}, and the gravitational term is divided by a factor 10^{37}. In the inset, circles mark the softening length around both point masses which is $0.74R_\odot$ at this time.

The distribution of the hydrodynamical flux term in a plane perpendicular to the orbital plane that contains the two point masses is shown in Fig. 8.10 for the three times 5 d, 50 d, and 100 d. One can see that the cylindrical averages employed for the radial transport capture the geometry well. Moreover, the dominating flow structures can be seen here: the accretion on the companion at 5 d (Fig. 8.10, left panel), the shock wave pattern at 50 d (Fig. 8.10, middle panel), and the slice through the one-armed wave at 100 d (Fig. 8.10, right panel).

Similar to the transport of angular momentum, the transport of total energy due to magnetic fields is small at all times; only at 100 d, the other fluxes become so small that it is of similar magnitude around the RG core (Fig. 8.9, upper left panel). Thus, magnetic fields do not influence the transport of energy significantly during this CE simulation up to this time.
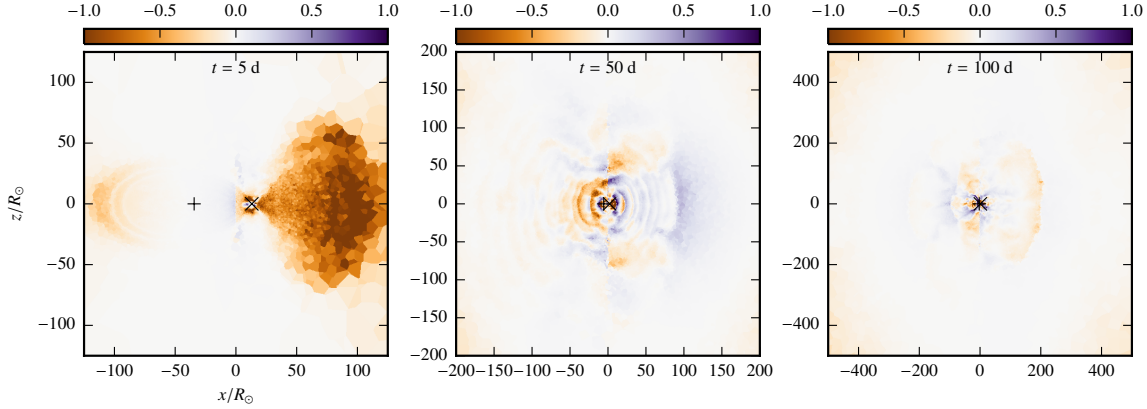
Figure 8.10 | Energy transport perpendicular to the orbital plane. The three panels shows the hydrodynamic term in the plane perpendicular to the orbital plane that is rotated such that it includes the two point masses. The panels show the term at 5 d, 50 d, and 100 d (left to right), which is divided by a factor 10^{49} (left panel) and 10^{48} (middle and right panel). The times and scales are the same as in Figs. 8.7, 8.8, and 8.9.

8.6 Conclusions

The analysis of the angular momentum and energy transport for an MHD simulation of an interaction between a $2M_\odot$ RG and a $1M_\odot$ companion yields the following picture: most of the angular momentum of the binary of the point masses is transferred to the gas during the first orbit whereas the transfer of energy takes place continuously. In the first phase of the spiral-in, during the first orbit, accretion onto the companion leads to the formation of a shock that creates gravitational drag. The corresponding torque acting on the gas leads to a transfer of angular momentum of the binary of point masses to the gas. Moreover, a stream of matter (about 8% of the envelope mass) is ejected that transports some angular momentum and energy outwards. In a second phase, the spiral-in of the companion leads to both point masses orbiting through the envelope. This creates a spiral pattern of shock waves that transport angular momentum and energy outwards. The gravitational energy of the binary of point masses is converted to total energy of the gas in the direct vicinity of both point masses. In the last phase, instabilities arise and wash out the spiral shock pattern; angular momentum and energy are transported outwards by a one-armed spiral wave that is formed by the instabilities. The radial fluxes of angular momentum and energy transport are strongest in the beginning and decrease over time. The impact of magnetic fields on the angular momentum and energy transport is small on the timescales of this simulation.

The conversion of gravitational energy to total energy of the gas is concentrated around the point masses also inside the softening length of the gravitational interaction of the point masses. Thus, high spatial resolution is needed here in order to resolve these processes properly. The chosen resolution of ten cell radii per softening length that is enforced around the point masses seems to be sufficient to ensure total energy conservation. For lower resolutions, however, the energy conservation is violated and the spiral-in ends at larger separations (Sec. 6.2).

The further evolution of the system cannot be predicted from the simulation and one goal for future work is the extension of the simulations to longer times. If the envelope is to be ejected, the orbit of the resulting binary has to shrink at least by a further 23% (from $4.3R_\odot$ to $3.3R_\odot$) in order to obtain the necessary energy from the binary orbit.

Chapter 9

Ionization State

Although the description of stellar matter as a fully ionized plasma is mostly a good approximation, the plasma is only partially ionized at lower densities and temperatures. The recombination of ions and electrons to atoms releases energy and, moreover, the opacity drops sharply at about 10^4 K. The ionization state of the gas depends on temperature and pressure and influences the equation of state (see Sec. 2.2.3). Partial ionization of H and He is especially important for the structure of large, dilute envelopes of giant stars (e.g., Kippenhahn et al., 2012). When ionized material expands and cools, recombination occurs due to decreasing temperature and densities and the corresponding recombination energy is released.

Including recombination energy when computing the structure of AGB stars leads to dynamically unstable envelopes; this has been discussed as a mechanism of planetary nebula (PN) ejection from single AGB stars (starting with, e.g., Roxburgh, 1967; Paczyński & Ziółkowski, 1968). Recombination energy may also be an additional energy source for ejecting the envelope during CE evolution as already discussed by Livio (1989).

In this chapter, we study the impact of including the ionization state of the plasma on the hydrodynamics of the CE phase by using an appropriate equation of state. After giving an overview of considering recombination energy in CE phases in the literature (Sec. 9.1), we discuss the setup and implementation in Sec. 9.2. We compare simulations with and without treating the ionization state and analyze the criterion for unbound mass in these simulations (Sec. 9.3). The spatial distribution of recombination energy release and the ionization structure is examined in Sec. 9.4. The optical display of CE events depends on the evolution of the photosphere. We discuss problems of accurately determining the photosphere by calculating opacities in Sec. 9.5. Finally, conclusions are drawn in Sec. 9.6.

9.1 Overview

The idea that recombination energy might help ejecting the envelopes of single stars, forming PNe, dates back to the end of the sixties (e.g., Roxburgh, 1967; Paczyński & Ziółkowski, 1968). In the context of CE evolution, Livio (1989) discusses different energy sources that potentially facilitate the ejection of the envelope, such as nuclear energy or recombination energy. In order to help ejecting the envelope, the corresponding process must be able to convert the recombination energy to mechanical energy of the gas; the simple presence of the energy reservoir is not enough. Thus, it is not clear if recombination energy helps ejecting the envelope.

Han et al. (1994) propose that the formation of a PN is connected to the time during the evolution at which the binding energy of the envelope of the progenitor AGB star becomes negative, including the recombination energy in the definition of the binding energy. During CE evolution, Han et al. (2002) include recombination energy in the energy budget for computing the final separation in

the context of formation of sdB stars. This treatment gives very efficient envelope ejection (i.e., high α values, cf. Eq. 2.54), resulting in larger final separations after a CE phase. In this way, the best fit to observed data could be obtained.

Using the recombination energy to determine the binding energy of the envelope in these studies was doubted by Harpaz (1998) and later by Soker & Harpaz (2003). They argue that the opacity drops above H recombination, thus the released energy is probably radiated away and cannot be trapped in the gas because there is no mechanism converting the recombination energy to mechanical energy. Hence, they argue, recombination energy should not drive the ejection of the envelope during PN formation or CE evolution.

In their review, Ivanova et al. (2013b) discuss the role of internal (i.e., thermal) and recombination energies during the CE phase but stay inconclusive if they should be included or not. In their study of stellar evolution models, Ivanova et al. (2015) present approximate structures that resemble a CE event after the companion has spiralled in deep into the envelope. They find that most solutions become dynamically unstable and energy especially from He recombination drives the expansion. In this way, it may help ejecting the envelope. This does, however, not show that the complete reservoir of recombination energy that is available in principle (i.e., including H recombination) can be used for ejection.

Hydrodynamics simulations of the CE phase published so far model the gas of the envelope using an ideal gas EOS, neglecting the ionization state of the gas – except the recent simulations by Nandez et al. (2015). In the simulations by Passy et al. (2012), the ionization state was not treated. The amount of energy that could be released from recombination in their simulations is estimated to be of the order of the binding energy at the end of their simulations. Hence, it may play an important role in unbinding the envelope. Nandez et al. (2015) present SPH simulations at rather low resolution (10^5 particles, one simulation with 2×10^5 particles) that employ the equation of state from the MESA stellar evolution code (Paxton et al., 2011, 2013, 2015). In the most important density and temperature regime in these simulations, this is equivalent to the OPAL EOS (Rogers et al., 1996; Rogers & Nayfonov, 2002), the same that is used in this work. As initial models, they take rather compact giants with radii between $16R_\odot$ and $30R_\odot$ although they do not show details of the radial structure, especially at which radius the profile is cropped to replace the core of the giant with a special SPH particle in their treatment. They find that for a simulation with an ideal EOS, 50% of the envelope mass is ejected, while for all simulations using the MESA EOS, 100% of the envelope is ejected. Moreover, they state that it is important where and when this energy is released, but they do not show information about that. Thus, the mechanism that leads to the ejection of the envelope in their simulations remains unclear.

9.2 Setup

For the simulation presented in this chapter, we use the same numerical methods as for the simulations presented so far: the AREPO code is employed (see Sec. 3.2, Springel, 2010a) with an additional refinement criterion around the point masses that represent the RG core and the companion. This refinement is crucial for resolving the energy conversion processes near the point masses and to achieve convergence (see Sec. 6.2 and Chapter 8). We do not include magnetic fields here. Instead, we include recombination energy in the internal energy by coupling the OPAL EOS (Rogers et al., 1996; Rogers & Nayfonov, 2002, see also Sec. 2.2.2) to the hydrodynamics scheme. This EOS is based on an expansion of the grand partition function and covers ionization effects. It

Table 9.1 | Properties of recombination runs with different initial conditions. Given are the mass ratio q, the factor of co-rotation χ (cf. Eq. (4.29)), the initial separation a_i, the final semi-major axis a_f, the final period P_f, the final eccentricity e_f, the relative error of the total energy $(E_0 - E)/E_0$ (E_0: initial value of the total energy, E: final value of the total energy), the ejected mass inluding only the kinetic energy, $M_{ej,kin}$, and including also internal energy, $M_{ej,tot}$. All values are given at 90 d except for $q = 0.1$, where the values are given at 60 d.

q	χ	$a_i/R_\odot$	$a_f/R_\odot$	P_f / d	e_f	$(E_0 - E)/E_0$	$M_{ej,kin}/M_\odot$	$M_{ej,tot}/M_\odot$
0.5	0.95	49	4.51	0.95	0.11	11%	0.14	0.30
0.5	0	49	4.45	0.93	0.092	11%	0.14	0.34
0.5	0.95	59	4.44	0.93	0.098	12%	0.21	0.35
0.1	0.95	49	1.77	0.37	0.067	21%	0.050	0.097

uses overlapping quadratic interpolation in the ρ-T plane to compute the thermodynamic quantities from pre-calculated tables. We implemented in addition an iterative solver for computing the EOS with density and internal energy as unknowns. Since the tables have a lower bound at 1.8×10^3 K, we impose this as a lower floor for the temperature in our simulations.

As initial model, we take relaxed RG models that were reconstructed with the OPAL EOS, as presented in Sec. 4.2. The advantage of using the same EOS as in the stellar evolution code is that the model shows the same convective behaviour (i.e., the envelope is convectively unstable) because all thermodynamic quantities are correctly reproduced from the stellar evolution code. Similar to the initial model presented in Sec. 5, the softening length of the RG core is 5% of the stellar radius in the beginning. During the simulation, the softening length is reduced such that it is always smaller than a fifth of the separation between the RG core and the companion. As we enforce a resolution of a maximum of a tenth of a softening length for the gas cells around the point masses, the radius of the smallest cells is 6×10^{-6} of the box size for $q = 0.5$, and 3×10^{-6} for $q = 0.1$ at the end of the simulation. The grid size is $9.8 \times 10^{14} = 14000 R_\odot = 65$ au. As a background grid, we add a low density gas with $\rho = 10^{-14}$ g cm^{-3} and $T = 10^4$ K to be approximately in pressure equilibrium with the surface of the star.

9.3 Temporal Evolution and Mass Loss

The impact of including the recombination energy was tested in four simulations exploring different initial conditions, similar to the simulations in Chapter 6. An overview of the simulations is given in Tab. 9.1. The evolution of the separation and of the semi-major axis for these models is shown in Fig. 9.1. One simulation was run for a non-rotating initial model, but the result is very similar (1.3% difference in orbital separation), as was also found in Chapter 6 for the simulations using an ideal EOS. Moreover, choosing the initial separation 20% larger than the radius of the star also has only a minor influence on the evolution (1.5% difference in orbital separation), similar to what was observed in Sec. 6 for the ideal EOS simulations. As expected, the simulation with $q = 0.1$ spirals in much farther. After 60 d, the computational cost is so large that the simulation was not continued because of the small cells near the point masses. The mesh refinement will have to be slightly less restrictive in order to continue the simulation in a reasonable amount of time.

The nearly co-rotating simulations ($\chi = 0.95$) are compared in Fig. 9.2 for both mass ratios and both equations of state in terms of the distance. One can see that the evolution is similar in both
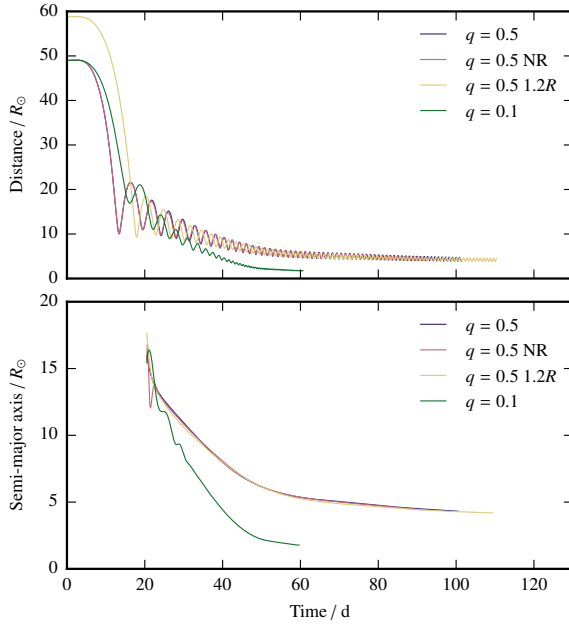
Figure 9.1 | Evolution of distance for different initial conditions. The upper panel shows the instantaneous distance between the RG core and its companion over time. In the bottom panel, the semi-major axis that was fit to the orbit is plotted.
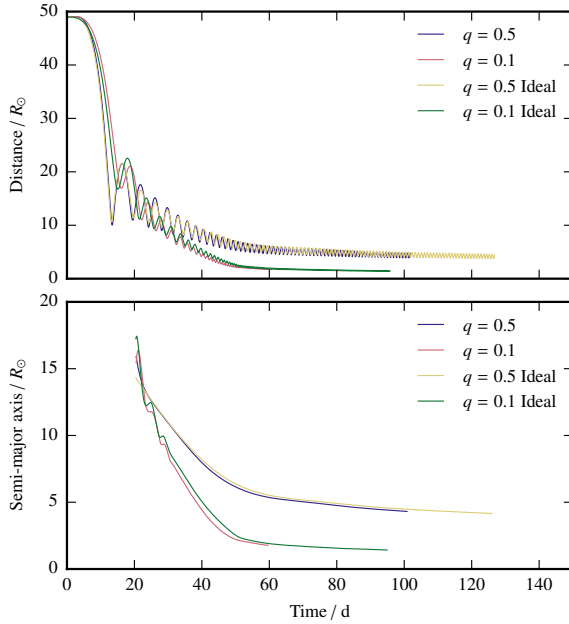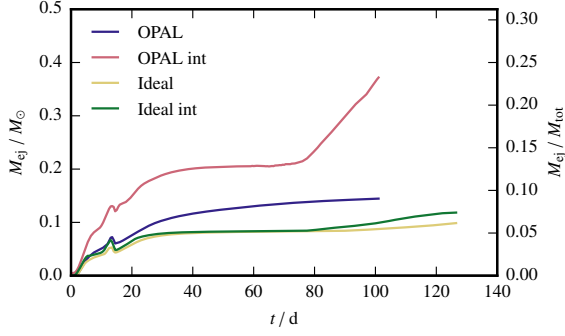

Figure 9.2 | Impact of the equation of state on the evolution of the distance. The upper panel shows the instantaneous distance between the RG core and its companion over time. In the bottom panel, the semi-major axis that was fit to the orbit is plotted. Compared are simulations using the OPAL EOS to models using an ideal EOS for two mass ratios $q = 0.5$ and $q = 0.1$.

cases, but the separation is smaller using the OPAL EOS: for the $q = 0.5$ simulation, the separation is 3.5% smaller after 90 d. The eccentricity is the same for $q = 0.5$ for both equations of state; for $q = 0.1$, the orbit is slightly more eccentric using the OPAL EOS. Thus, the impact of using the OPAL EOS on the orbital evolution is small on the timescales simulated so far, resulting in a similar final separation.

The mass that is ejected from the system differs between the different equations of state, however (Fig. 9.3). Since it is not clear, if all of the internal energy reservoir – that includes recombination energy here – can be tapped for ejecting material, we compare two methods of determining the

Figure 9.3 | Impact of the equation of state on the ejected mass. Compared are simulations using the OPAL EOS to models using an ideal EOS for the mass ratio $q = 0.5$. For both equations of state, we show the unbound mass according to the criterion including the internal energy (Eq. 9.1, marked with int) and excluding the internal energy (Eq. 9.2). The left-hand axis is in units of solar masses, the right-hand axis gives the fraction of the total envelope mass.

unbound mass. The first criterion counts all cells for which the total energy is larger zero, including the internal energy,

$$e_{\text{kin}} + e_{\text{pot}} + e_{\text{int}} > 0. \tag{9.1}$$

The second criterion takes only the kinetic energy into account,

$$e_{\text{kin}} + e_{\text{pot}} > 0. \tag{9.2}$$

The unbound mass according to both criteria is compared in Fig. 9.3 for the ideal EOS and the OPAL EOS. For the ideal EOS, the difference between the two criteria is negligible before 80 d. Afterwards, including the internal energy yields a slightly larger mass loss at the end of the simulation: $0.11 M_\odot$ of the envelope is ejected compared to $0.09 M_\odot$ excluding the internal energy (16% difference). The simulation with the OPAL EOS shows larger differences: the mass loss including the internal energy is twice as large compared to excluding the internal energy ($0.3 M_\odot$ vs. $0.14 M_\odot$). Both values are larger than for the simulation without recombination energy. Thus, the available recombination energy can be at least partly converted to kinetic energy leading to a larger mass loss. Although the ejected mass as computed including the internal energy is much larger and increases at the end up to 20% of the envelope, it is not clear that all of this can be converted to kinetic energy during the further expansion of the gas. One argument against this is that the opacity drops sharply at H ionization such that the energy may not be trapped but radiated away (cf. the arguments in Harpaz, 1998). Including the thermal energy only does not lead to a large difference as can be seen for the ideal EOS simulation that neglects the recombination energy. After 90 d, a recombination energy of 3.5×10^{46} erg has been released, 35% of the initially available 9.9×10^{47} erg. Most of this recombination energy (93%) comes from He recombination. At this point, computing the binding energy of the gas including recombination energy yields 2.9×10^{46} erg, i.e., the envelope is formally unbound. Without the potentially available recombination energy of 6.4×10^{46} erg, the binding energy is -3.5×10^{46} erg and thus still bound. This shows that the available recombination energy is in principle large enough to overcome the binding energy of the envelope. But whether the envelope is ejected depends on the release of this energy in the further evolution of the system.

The error in the total energy is larger for the runs including recombination with approximately 10% for $q = 0.5$ and 20% for $q = 0.1$ compared to the corresponding runs with the ideal EOS (2% to 7%, compare Tabs. 9.1 and 6.3). It is unclear what causes this error. A potential source might be the lower floor of the temperature that is imposed by the EOS, although this temperature is only seldomly reached during the simulation.

For all simulations, the mass lost during the first 80 d is concentrated in a spiral arm that is swung outwards by the in-spiraling companion during the first orbit, similar to what was noted in
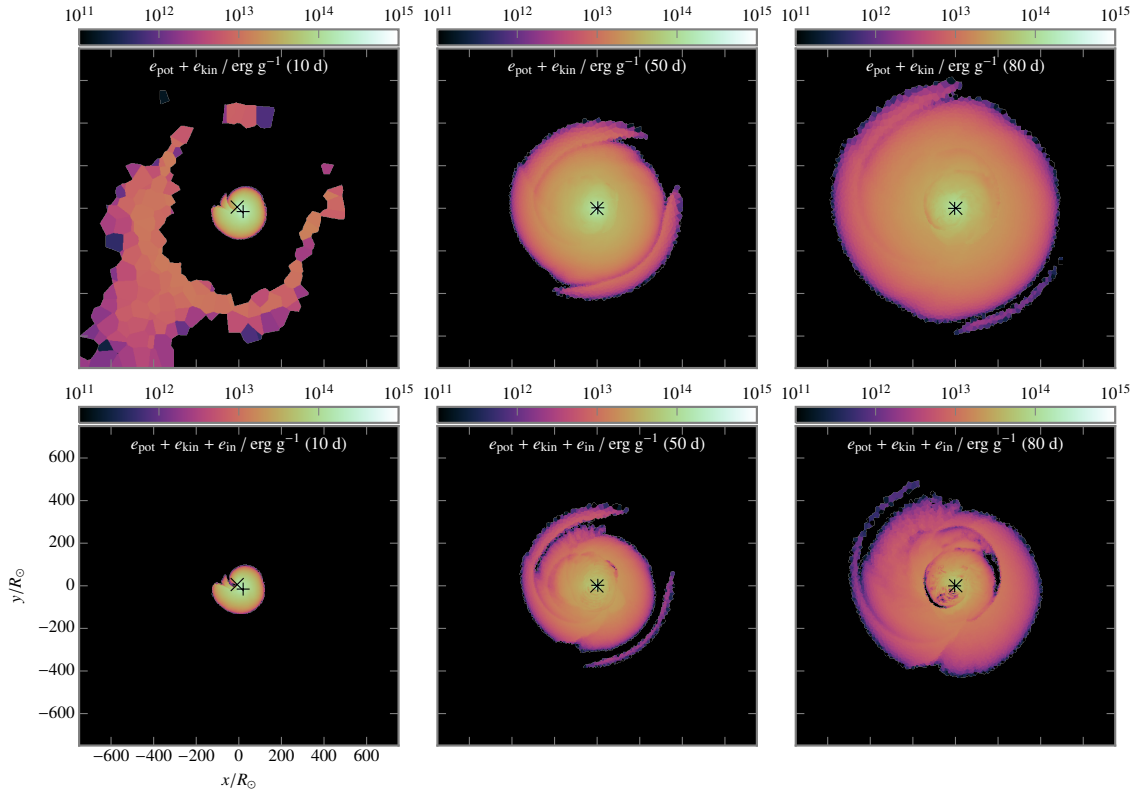
Figure 9.4 | Evolution of total specific energy in the orbital plane. Shown is the total specific energy excluding internal energy in the top row and including internal energy in the bottom row. These quantities are plotted at three times: at 10 d (left column), 50 d (middle column), and 80 d (right column). The core of the RG is marked by a +, the companion by a ×.

earlier simulations (e.g., Sandquist et al., 2000). As also described in the study of different initial conditions in Chapter 6, more mass is lost during the first orbit when the companion is placed at a larger distance (at 120% of the stellar radius) due to the larger amount of angular momentum that is dumped into the envelope during the first orbit. This effect, however, can only be seen if the recombination energy is not included for determining the unbound mass (cf. Tab. 9.1). This supports the view that including the recombination energy may overestimate the amount of unbound mass.

The different spatial distribution of the unbound mass as estimated by both criteria can be inferred from the distribution of the total specific energy of the gas (Fig. 9.4). The black regions in Fig. 9.4 correspond to the regions where the total energy is negative and thus, the unbound mass is located there. One can see a ring of bound low-density material at 15 d for the criterion without the internal energy (Fig. 9.4, upper left), but the mass of this material is negligible. In general, the region of bound mass becomes larger with time for both criteria, indicating that the envelope expands but does not eject all material above a certain radius. The shape is spherical with slight asymmetries indicating the positions of shocks. Employing the criterion without internal energy results in a region of bound material that is connected, i.e., the unbound mass is located outside of the bound mass (Fig. 9.4, upper row). The criterion including internal energy, however, predicts unbound material in high-temperature regions at shocks, resulting in pockets of unbound mass inside the

bound envelope (Fig. 9.4, lower row). It is not clear that this material will be indeed ejected since it will not simply expand but interact with the rest of the bound material. Thus, including the internal energy for determining unbound material overestimates the amount of ejected mass.

9.4 Ionization State

The ionization state of the gas during the simulation is computed by solving the Saha equation (2.25) in local thermodynamic equilibrium for H and He in a post-processing step for each snapshot of the simulation. This yields the ionization energy as well as the fractions of electrons and of H I, H II, He I, He II, and He III. Because we neglect the contribution of heavier elements that is important for supplying electrons, we should underestimate the electron fraction. Nevertheless, this still allows us to examine the approximate spatial distribution of neutral and ionized species.

The spatial distribution of the recombination energy release is shown in Fig. 9.5 at 10 d (upper row), 50 d (middle row), and 80 d (lower row). The figure shows density (left column), temperature (middle column) and the released recombination energy (right column) that was computed as the energy of a completely ionized gas minus the actual ionization energy. As one can see, the largest amount of recombination energy is released in the outer parts, where density and temperatures become small during expansion. In high-temperature regions the release of recombination energy is small, as for example in the inner part or near shocks, where the gas is heated by compression. In regions behind shocks, however, temperatures are smaller and recombination energy is dumped here, helping to expand the gas. This can be seen, e.g., between 50 d and 80 d: on the left side and on the right side of the central region, hot shocks are followed by expanding regions with increasing recombination energy release. In this way, the recombination energy can actually be converted to mechanical energy of the gas.

At 50 d, a shock in the upper left region (Fig. 9.5, middle row), shows filamentary structure which may be due to instabilities connected to the release of energy due to the recombination of H (cf. Fig. 9.6, middle left and lower left panels).

The spatial distribution of the species H I, He I, and He II is shown in Fig. 9.6 at 15 d (upper row), 50 d (middle row), and 80 d (lower row). In the beginning, the material in the outer part of the computational domain is ionized because the background temperature was chosen to be 10^4 K and this is above the ionization threshold of about 6×10^3 K at a density of 10^{-14} g cm^{-3}. This is unphysical because this material is expected to be at lower temperatures and thus forming neutral atoms or even molecules. Nevertheless, this temperature was chosen to stabilize the background medium at a pressure that is slightly larger than the outermost pressure in the star. Future simulations should, however, test if the outcome depends on the choice of background gas parameters. During the simulation, the material in outer parts becomes neutral after ejected material expands and cools down below the recombination threshold.

The spatial distribution shows a layered structure of the ionization zones, as expected: going from the center outwards, one encounters first a layer of singly ionized He II, then neutral He I, and finally neutral H I (columns from right to left in Fig. 9.6). Departures from this can be seen near shocks: the high temperature in the shock ionizes the gas, whereas recombination takes place behind the shock (see, e.g., the features in He II and He I at 50 d; Fig. 9.6, middle right and center panels). This behaviour is also reflected in a corresponding release in recombination energy (cf. Fig. 9.5, right column). Between 50 d and 80 d, these regions expand further and energy from He recombination is fully released there. During the evolution up to 80 d, however, this does not yet
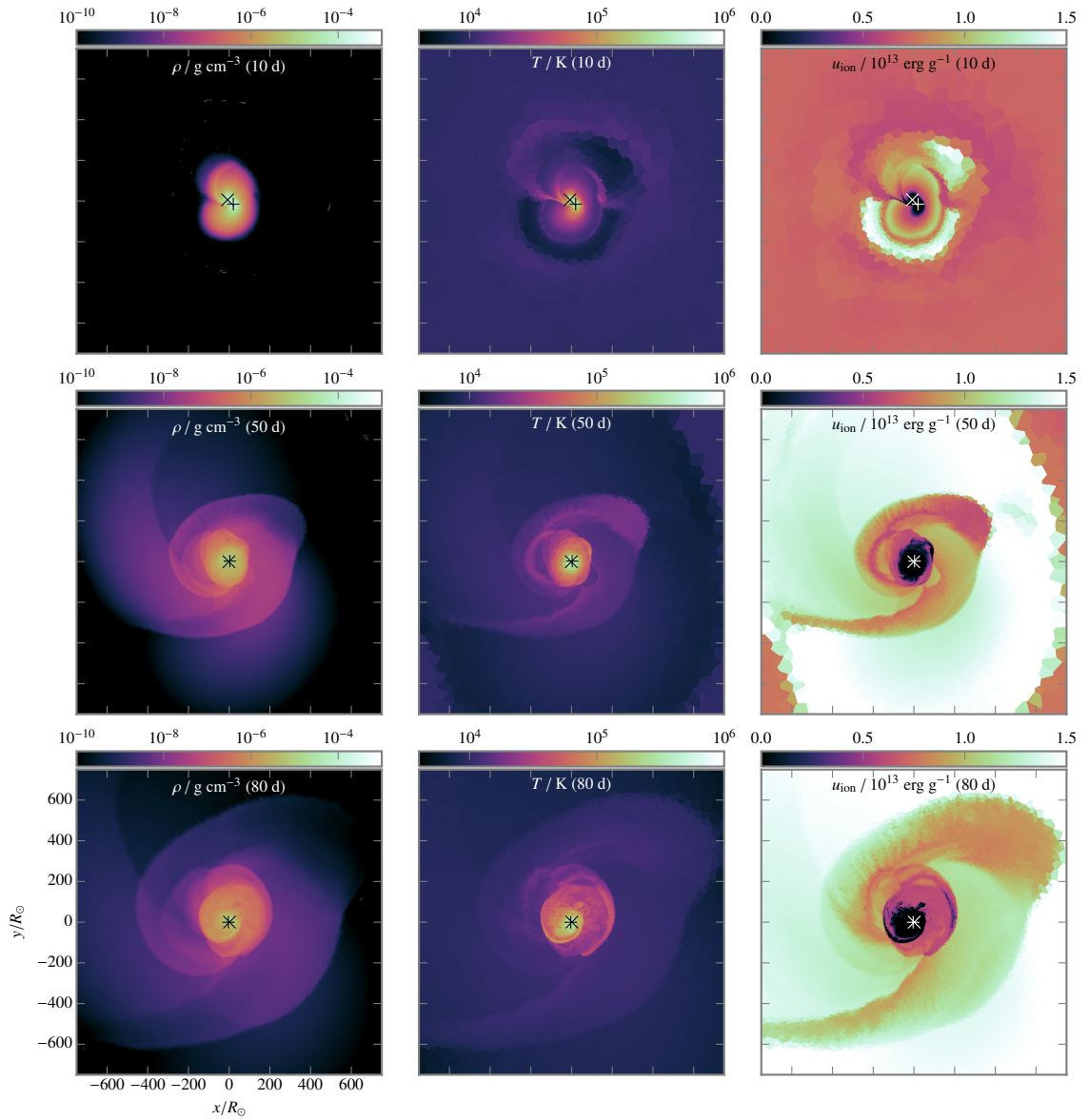
Figure 9.5 | Evolution of recombination energy release. Plotted is the density (left column), the temperature (middle column), and the released recombination energy, i.e., the ionization energy of a completely ionized gas minus the ionization energy in the cell (right column). These quantities are shown at three times: at 10 d (top row), 50 d (middle row), and 80 d (bottom row). The core of the RG is marked by a +, the companion by a ×.
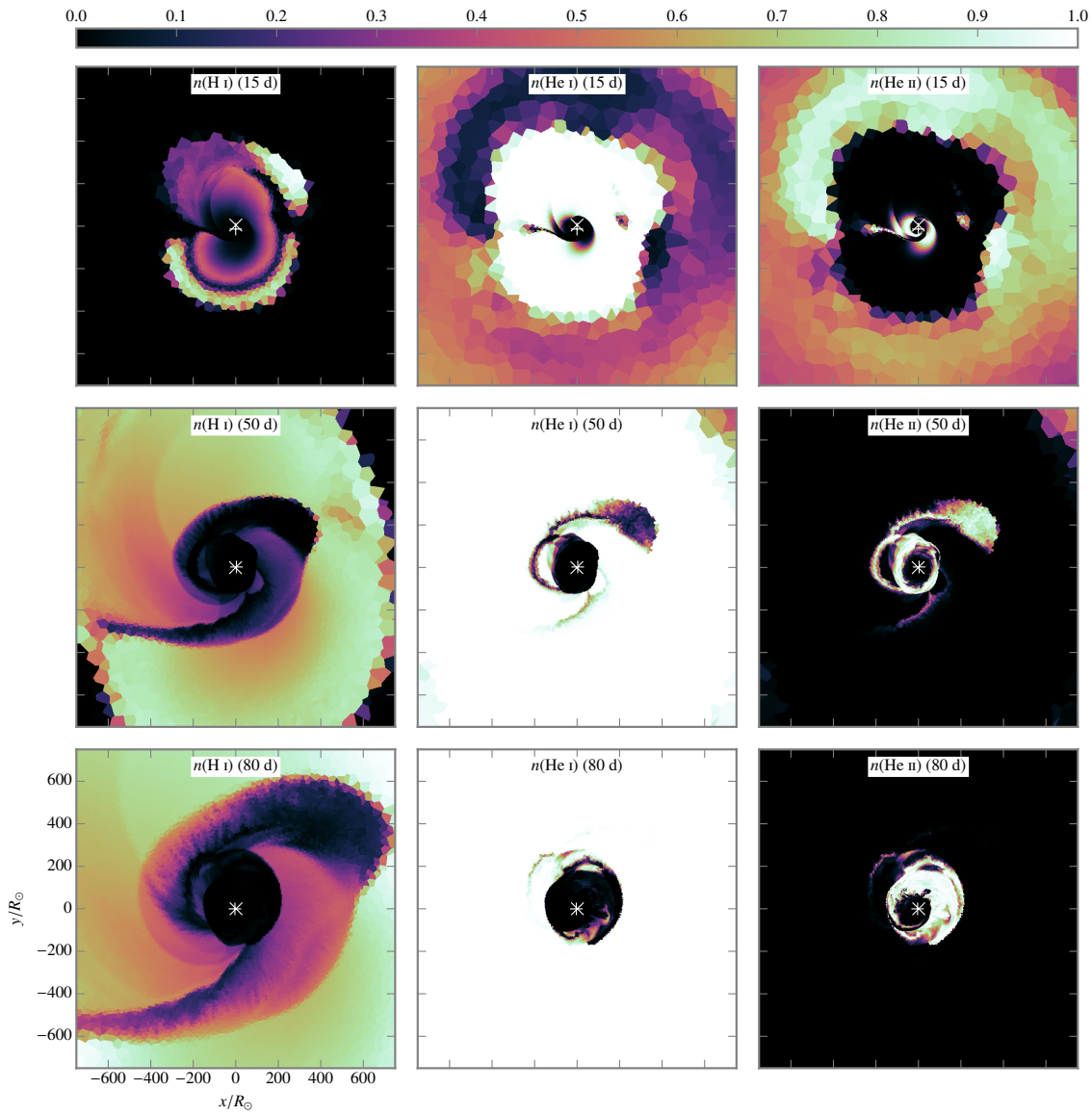
Figure 9.6 | Evolution of different ionization states. Plotted are the number fractions in terms of the corresponding element for H I (left column), He I (middle column), and He II (right column). These quantities are shown at three times: at 15 d (top row), 50 d (middle row), and 80 d (bottom row). The core of the RG is marked by a +, the companion by a ×.

lead to an increased amount of ejected mass. At 80 d, the radius of the region of bound material in the orbital plane is about $600R_\odot$ (Fig. 9.6, upper right panel), far outside the ionization fronts of He III (about $50R_\odot$ to $100R_\odot$) and He II (about $200R_\odot$), but near the ionization front of H II – which is quite asymmetric with the shape following shock fronts moving outwards. Although the mass ejection is not dramatically enhanced up to 80 d, the continuous release of recombination energy of He in the inner layers may boost the mass ejection during the further expansion of the envelope.

9.5 Opacities

The common envelope phase spans roughly a few thousand years, a short time compared to the lifetime of a star, even on the giant branch. Hence, the probability of observing such a binary system during this phase in a sample of stars is quite low. Recently, the first observation of a system that is probably captured just in a CE phase was reported by Chesneau et al. (2014) using VLTI, where the primary star is a massive yellow hypergiant. The expansion of the envelope during a CE event resembles Type IIP supernovae: their optical display during the plateau phase is probably dominated by a receding recombination front in the expanding envelope. This similarity led Ivanova et al. (2013a) to rescale estimates for luminosity and duration of the plateau phase to a CE event. They estimate values for CE events and find that these values together with a low photospheric temperature (about 5000 K) resemble a class of transient events called Luminous Red Novae. This class of events shows luminosities between novae and supernovae and was established only recently. In this model, the duration of the plateau is linked to the propagation of the recombination wavefront, and only the spectroscopic velocities obtained from Doppler shifts in absorption lines are coupled to the gas velocities at the photosphere.

In order to possibly link our simulations to an optical display, we compute opacities for the simulations and compare to the ionization state of the gas. In this way, we can examine if the model shows a recombination wavefront corresponding to a receding photosphere. This is, however, only a first step towards the development of more realistic simulations of the radiative output of CE events. Ultimately, multi-wavelength radiative transport in the envelope is needed.

The opacities are computed by combining opacities from the OPAL project (Iglesias & Rogers, 1996) with low-temperature opacities by Alexander & Ferguson (1994) and Ferguson et al. (2005) below 10^4 K. Both sources give opacity tables that are interpolated to yield the Rosseland mean opacity (cf. Eq. 2.38). Such a treatment, however, neglects the impact of line opacities of, e.g., neutral hydrogen, which may be important since the radiation emitted due to recombination is at these wavelengths. A full treatment is only possible with detailed radiative transfer calculation. Nevertheless, the Rosseland opacities allow us to approximately locate the photosphere.

The opacity χ, i.e., the inverse mean free path, is shown in Fig. 9.7 at 15 d (left panel), 50 d (middle panel), and 80 d (right panel). The opacity follows here the outer edge of the ejecta that move into the surrounding medium, increasing in radius along with the ejecta. This is contrary to what would be expected from the ionization state: as Fig. 9.6 (lower left panel) shows, the transition from neutral H I to ionized H II is located between $200R_\odot$ and $400R_\odot$, much further inward than the outer edge of the expanding ejecta at $1000R_\odot$ to $2000R_\odot$ (cf. Fig. 9.7, right panel). The explanation lies in the choice of temperature for the background grid: at 10^4 K, the background medium is ionized and thus still at large opacities. Hence, the expansion of the envelope into the hot background medium does not lead to enough cooling, thus overestimating the opacities.
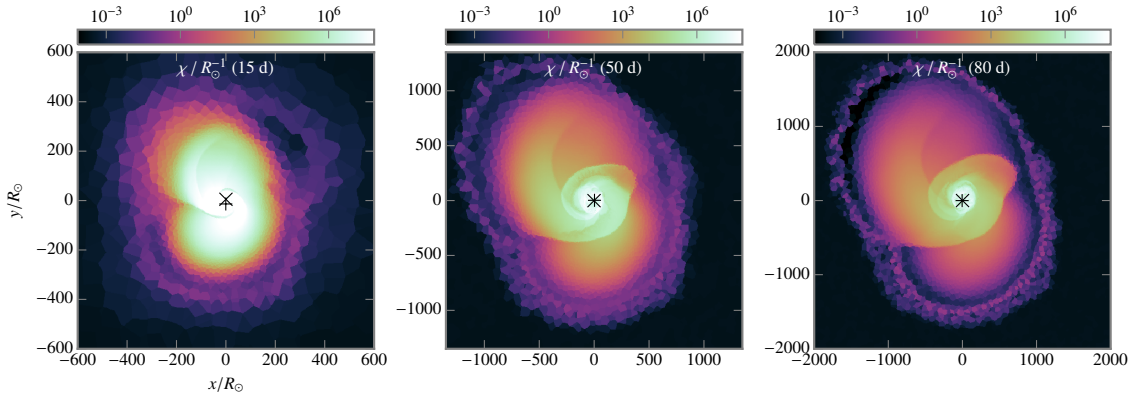
Figure 9.7 | Evolution of opacity. The opacity χ in inverse solar radii is shown at three times: at 15 d (left panel), 50 d (middle row), and 80 d (bottom row). The core of the RG is marked by a +, the companion by a ×.
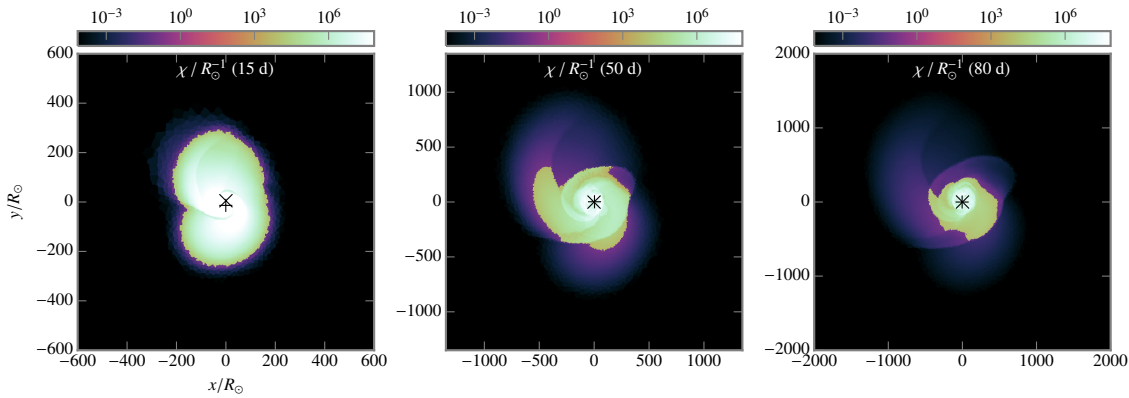
Figure 9.8 | Evolution of opacity for artificially reduced T. The opacity χ in inverse solar radii is shown at three times: at 15 d (left panel), 50 d (middle row), and 80 d (bottom row). For the computation of the opacity, the temperature was set to 4×10^3 K in all cells where $\rho < 3 \times 10^{-9}$ g cm^{-3}. The core of the RG is marked by a +, the companion by a ×.

In Fig. 9.8, we show opacities that were computed using an artificially reduced temperature for the outer regions: for $\rho < 3 \times 10^{-9}$ g cm^{-3}, the temperature was set to 4×10^3 K. The resulting opacity distribution shows a sharp boundary between high and low opacities, separating optically thick and optically thin regions and indicating the position of the photosphere. Despite the approximate method, the resulting photosphere expands between 15 d and 80 d from $300 R_\odot$ to about $500 R_\odot$, much less than the total ejecta. The shape of the optically thick region, however, is not symmetric, but dominated by shocks where a steep temperature increase leads to a jump in opacities. Nevertheless, the transition from high to low opacities corresponds well to the transition from ionized to neutral H (cf. Fig. 9.6, left column). Integrating the optical depth τ (cf. Eq. 2.36) along a ray from the outside shows that the layer with $\tau = 1$ is now located near this jump in opacity, whereas for the original simulation data, it is located near the outer edge of the ejecta.

In order to obtain better estimates for the location and shape of the photosphere in the simulations, the background temperature has to be lowered to allow sufficient cooling of the ejecta during the expansion. This will be tackled in future simulations.

9.6 Conclusions

In this chapter, we presented detailed simulations of the CE phase including recombination energy. The simulations show that the inclusion of recombination energy yields a similar orbital evolution. Furthermore, the ejected mass is increased, but the envelope is not completely ejected on the simulated timescale. The unbound mass can be estimated either including internal energy (and thus also recombination energy) or excluding it; including the internal energy probably overestimates the amount of unbound mass. Our findings are in contrast to the simulations by Nandez et al. (2015) that show a complete ejection of the envelope when including recombination energy. Possible reasons for this discrepancy are different initial models, differences in the numerical scheme, and the fact that they include recombination energy when computing the unbound mass. Moreover, the mass loss may increase when continuing our simulations to longer times that were captured in the simulations by Nandez et al. (2015).

An analysis of the ionization state shows that recombination energy can be released in cooler material behind shock fronts and thus help driving the expansion. Moreover, the spatial distribution of different ionization states of H and He show a layered structure of the ionization zones going from ionized material in the interior to neutral material in the outer part as would be expected for such a density and temperature stratification.

In order to link the simulations to observations, the opacities were computed as a first step. Unfortunately, their distribution depends sensitively on the temperature of the background grid. Artificially lowering the background temperature below a certain density threshold yields a sharp photosphere that expands only slowly and recedes compared to the expanding ejecta. This confirms the model of a receding recombination wavefront as proposed by Ivanova et al. (2013a) similar to models for Type IIP supernovae. For a quantitative determination of light curves and spectra, detailed radiative transfer calculations are necessary.

Thus, although the release of recombination energy increases the ejected mass in our simulations, the envelope is not fully ejected on the simulated timescales. The simulations have to be extended to longer times to see if further expansion and further recombination energy release may induce the ejection of the envelope. It is, however, interesting, that the orbital separation including the ionization state is very similar to the simulation using an ideal gas, and even slightly smaller. Therefore, the inclusion of recombination energy does not lead to larger final separations on the simulated timescales.

Chapter 10

A New Scheme for Gravitational Flows

In this chapter, a new scheme for gravitational flows and first steps towards its implementation are presented. The method combines the AREPO scheme introduced in Sec. 3.2 with the well-balanced Riemann solver by Desveaux et al. (2015). This Riemann solver uses the relaxation technique to include the gravitational force in the solution of the Riemann problem leading to a scheme that is able to preserve certain hydrostatic equilibria exactly. This property is very interesting for computations of processes near hydrostatic equilibrium, e.g., convection in stars. Moreover, the upwinding of the gravitational force may improve the modeling of gravitational flows in general, also far away from hydrostatic equilibrium. An additional modification in the Riemann solver improves the behaviour of the scheme for smaller Mach numbers, although tests show that the solver is probably unstable for small Mach numbers below 10^{-3}.

We will first shortly introduce the relaxation technique for constructing approximate Riemann solvers (Sec. 10.1), then we will present the Riemann solver as described by Desveaux et al. (2015) in Sec. 10.2. This solver is then extended to unstructured, multi-dimensional grids and a second-order scheme as used by the AREPO code (Sec. 10.3). Tests show the behaviour of the scheme for hydrostatic atmospheres as well as for flows near to and far from the hydrostatic equilibrium in one, two, and three space dimensions (Sec. 10.4). Finally, we propose a modification for the use in the low-Mach number regime (Sec. 10.5). Since the implementation has not been extended to the moving mesh up to now, this solver is not used for the CE simulations presented in this work.

10.1 Relaxation Schemes

The information on the relaxation approach and an earlier version of the Riemann solver is taken from Markus Zenk's master's thesis (Zenk, 2013); the Riemann solver itself follows Desveaux et al. (2015). More information on relaxation techniques can also be found in the book by Bouchut (2004).

The relaxation approach uses ideas from non-equilibrium thermodynamics: the Euler equations describing the equilibrium dynamics are extended with equations accounting for non-equilibrium dynamics that include terms for the tendency of relaxing to the equilibrium. In general, a relaxation system for a conservation law in one space dimension of the state vector u,

$$u_t + f(u)_x = 0, \tag{10.1}$$

(f: flux function) may be written as

$$U_t + F(U)_x = \frac{1}{\epsilon} R(U), \tag{10.2}$$

with the extended state vector U, the extended flux function F, and the relaxation source term R ($\epsilon > 0$ characterizes the departure from equilibrium). In equilibrium, R is assumed to vanish, and

the relaxation system (10.2) reduces to the system (10.1) that is in thermodynamic equilibrium. The advantage of this approach is that the larger relaxation scheme can be constructed in such a way that it yields a linear degenerate Riemann problem that may be solved easily.

The Suliciu relaxation (e.g., Suliciu, 1998a,b) employs a generalized equation of state for the non-equilibrium case that can be used to obtain a linear degenerate system. In the approach of Bouchut (2004), a linearized equation for the pressure is utilized. For this system, the Riemann problem can be computed explicitly as a solution of a linear system of equations and it can be shown that the Riemann solver for the relaxation scheme is an approximate Riemann solver for the original system, i.e., the Euler equations. Moreover, this approximate Riemann solver leads to a stable scheme, preserves positiveness of density and internal energy and satisfies an entropy condition. The solver depends on a parameter that has to fulfill an inequality for these properties to hold. For the Euler system (cf. Eq. (2.4), without external forces), the relaxation scheme can be formulated as (cf. Eq. (5.115), Zenk, 2013)

$$
\begin{aligned}
\rho_t + (\rho u)_x &= 0, \\
(\rho u)_t + (\rho u^2 + \pi)_x &= 0, \\
(\rho e_{\text{tot}})_t + (u(\rho e_{\text{tot}} + \pi))_x &= 0, \\
(\rho \pi)_t + (\rho u \pi)_x + c^2 u_x &= \frac{1}{\epsilon}(p - \pi).
\end{aligned}
\tag{10.3}
$$

Here, π is the relaxed pressure and $c \geq \rho^2(\partial p/\partial \rho)_s$ (derivative at constant entropy) is a constant. The Riemann solver for this system can be found in Zenk (2013). The solution of the system involves an operator splitting approach: first, the left-hand side is solved; then the right-hand side is solved (i.e., $\epsilon \to 0$, $\pi = p$). Thus the numerical scheme works as follows: the conserved quantities are evolved for a timestep using the approximate Riemann solver, then the pressure is computed using the equation of state $p(\rho, e_{\text{tot}})$ and the relaxed pressure is reset to the equilibrium pressure $\pi = p$.

10.2 A Well-balanced Scheme

A common source term for the Euler equations (2.4) is the gravitational force, e.g., when modeling the Earth's atmosphere or stellar fluid flows. Usual discretizations employ an operator splitting approach when dealing with the Euler equations including gravity: first, the hydrodynamical part is treated by using, e.g., a finite volume scheme with a Riemann solver for computing the numerical fluxes; second, the gravitational force is applied to the center of each cell.[1] For hydrostatic equilibria, this leads to discretization errors: although the partial differential equation should preserve these equilibria, the numerical scheme introduces spurious velocities and changes in the structure of the equilibrium.

An approach to overcome these limitations is *well balancing*. Here, the source terms – in our case gravity – are included into the numerical scheme in order to balance pressure gradients and gravity for hydrostatic equilibria. Different well-balanced methods are described in Zenk (2013). We will concentrate here on the relaxation scheme as described by Desveaux et al. (2015) that is extended here to resolve contact discontinuities and vacuum states. The scheme as described here assumes an ideal gas equation of state.

---

[1]Either the gravity is given and constant or it is computed using a Poisson solver.

The Euler equations with gravity (2.4) are extended to include an additional quantity, the relaxed potential Z,

$$
\begin{aligned}
\rho_t + (\rho u)_x &= 0, \\
(\rho u)_t + (\rho u^2 + \pi)_x &= -\rho \partial_x Z, \\
(\rho E)_t + (u(\rho E + \pi))_x &= -\rho u \partial_x Z, \\
(\rho \pi)_t + (\rho u \pi)_x + c^2 u_x &= \frac{\rho}{\epsilon}(p - \pi), \\
(\rho c)_t + (\rho u c)_x &= 0, \\
(\rho Z)_t + (\rho u Z)_x &= \frac{\rho}{\epsilon}(Z - \Phi),
\end{aligned}
\tag{10.4}
$$

in addition to the relaxed pressure π and the relaxation speed c. In the solution of the Riemann problem for this system of equations, there is one degree of freedom left, which is used to impose a discretization of the hydrostatic equilibrium,

$$
\pi_r^* - \pi_l^* = -\overline{\rho}\,(\rho_l, \rho_r)\left(Z_r^* - Z_l^*\right),
\tag{10.5}
$$

where the average $\overline{\rho}$ can be defined in a suitable way to preserve specific discrete equilibria and has to fulfill consistency and symmetry properties.

The system has three eigenvalues, u, and $u \pm c/\rho$, and correspondingly three waves that a linear. The solution in the four different regions (l, l^*, r^*, r from left to right) is given by

$$
\begin{aligned}
u^* = u_l^* = u_r^* &= \frac{c_l u_l + c_r u_r}{c_l + c_r} + \frac{1}{c_l + c_r}(\pi_l - \pi_r + \overline{\rho}(\rho_l, \rho_r)(Z_l - Z_r)), \\
\pi_l^* &= \pi_l + c_l(u_l - u^*), \\
\pi_r^* &= \pi_r + c_r(u^* - u_r), \\
\frac{1}{\rho_l^*} &= \frac{1}{\rho_l} + \frac{1}{c_l}(u^* - u_l), \\
\frac{1}{\rho_r^*} &= \frac{1}{\rho_r} + \frac{1}{c_r}(u_r - u^*), \\
e_l^* &= e_l + \frac{1}{2c_l^2}((\pi_l^*)^2 - \pi_l^2), \\
e_r^* &= e_r + \frac{1}{2c_r^2}((\pi_r^*)^2 - \pi_r^2).
\end{aligned}
\tag{10.6}
$$

The relaxation speeds can be computed by (Zenk, 2013)

$$
\begin{aligned}
p_r - p_l \geq -\overline{\rho}(Z_r - Z_l) &\begin{cases} c_l = \rho_l \left(c_{\mathrm{s},l} + \alpha \left(\frac{p_r - p_l + \overline{\rho}(Z_r - Z_l)}{\rho_l c_{\mathrm{s},l}} + u_l - u_r\right)_+\right) \\ c_r = \rho_r \left(c_{\mathrm{s},r} + \alpha \left(\frac{p_l - p_r - \overline{\rho}(Z_r - Z_l)}{c_l} + u_l - u_r\right)_+\right) \end{cases} \\
p_r - p_l < -\overline{\rho}(Z_r - Z_l) &\begin{cases} c_r = \rho_r \left(c_{\mathrm{s},r} + \alpha \left(\frac{p_l - p_r - \overline{\rho}(Z_r - Z_l)}{\rho_r c_{\mathrm{s},r}} + u_l - u_r\right)_+\right) \\ c_l = \rho_l \left(c_{\mathrm{s},l} + \alpha \left(\frac{p_r - p_l + \overline{\rho}(Z_r - Z_l)}{c_r} + u_l - u_r\right)_+\right) \end{cases}
\end{aligned}
\tag{10.7}
$$

where $(x)_+ = \max(x, 0)$ denotes the positive part, where $c_{\mathrm{s},l/r}$ denotes the sound speed in the left or right state, and where α is a constant depending on the equation of state which has to fulfill

$$
\alpha \geq 1 + \left.\frac{\partial \log c_{\mathrm{s}}}{\partial \log \rho}\right|_s,
\tag{10.8}
$$

(the derivative is taken at constant entropy). A value of two should work for most equations of state. For an ideal gas with $\gamma = \frac{5}{3}$, Eq. (10.8) yields $\alpha = \frac{4}{3}$.

The state at the interface depends on the wave speeds and is given by

$$
U_{\text{Riemann}} = \begin{cases}
U_l & , u_l - \frac{c_l}{\rho_l} > 0 \\
U_l^* & , u_l - \frac{c_l}{\rho_l} < 0 < u^* \\
U_r^* & , u^* < 0 < u_r + \frac{c_r}{\rho_r} \\
U_r & , 0 > u_r + \frac{c_r}{\rho_r}
\end{cases}, \tag{10.9}
$$

and the numerical flux is computed by evaluating the Euler flux at the corresponding state, i.e., the pressure is computed via the equation of state using the interface values for density and energy. As usual in relaxation schemes, the formulas above use $Z = \Phi$ and $\pi = p$ from the previous time step.

One can now prove that this relaxation solver is well-balanced for the Riemann problem (i.e., $u^* = 0$) in the following sense depending on the choice of the average $\overline{\rho}$ from Eq. (10.5) (Desveaux et al., 2015):

1. For initial conditions which fulfill

$$
p_r - p_l = -\overline{\rho}(\Phi_r - \Phi_l) \tag{10.10}
$$

   for arbitrary average functions $\overline{\rho}$ the state stays at rest, i.e. $u^* = 0$.

2. If the average is given by

$$
\overline{\rho}(\rho_l, \rho_r) = \begin{cases}
\rho_l & \rho_l = \rho_r \\
\frac{\rho_r - \rho_l}{\log \rho_r - \log \rho_l} & \text{else}
\end{cases}, \tag{10.11}
$$

   isothermal states are preserved that are given by

$$
\begin{aligned}
u &= 0, \\
\rho(x) &= \alpha \exp\left(-\beta \Phi(x)\right), \\
p(x) &= \frac{\rho(x)}{\beta},
\end{aligned} \tag{10.12}
$$

   where α and β are constants characterizing the specific hydrostatic equilibrium and $\Phi(x)$ the gravitational potential that is constant in time.

3. Polytropic equilibria are of the form

$$
\begin{aligned}
u(x) &= 0, \\
\rho(x) &= \left(\frac{\Gamma - 1}{\Gamma K}\left(C - \Phi(x)\right)\right)^{\frac{1}{\Gamma - 1}}, \\
p(x) &= K^{\frac{1}{1 - \Gamma}}\left(\frac{\Gamma - 1}{\Gamma}\left(C - \Phi(x)\right)\right)^{\frac{\Gamma}{\Gamma - 1}},
\end{aligned} \tag{10.13}
$$

   where $C, \Gamma > 1$, and $K = P/\rho^{\Gamma}$ are constants characterizing the equilibrium. These equilibria can be preserved exactly by choosing

$$
\overline{\rho}(\rho_l, \rho_r) = \begin{cases}
\rho_l & \rho_l = \rho_r \\
\frac{\Gamma - 1}{\Gamma} \frac{\rho_r^{\Gamma} - \rho_l^{\Gamma}}{\rho_r^{\Gamma - 1} - \rho_l^{\Gamma - 1}} & \text{else}
\end{cases}, \tag{10.14}
$$

where Γ can be computed for each interface as

$$\Gamma(U_l, U_r) = \frac{\ln(p_r) - \ln(p_l)}{\ln(\rho_r) - \ln(\rho_l)}. \tag{10.15}$$

Thus, the scheme is well balanced for *arbitrary* values of $\Gamma > 1$ and the value of Γ does not have to be an input for the numerical scheme.

For these choices, the solution of the Riemann problem fulfills $u^* = 0$. Moreover, the numerical flux cancels out exactly the following source term that has to be added to one of the two cells adjacent to the face, depending on the sign of u^*,

$$
\begin{aligned}
S_r &= \begin{cases} (0, s_{lr}, u^* s_{lr}) & u^* > 0 \\ (0, 0, 0) & \text{else} \end{cases}, \\
S_l &= \begin{cases} (0, s_{lr}, u^* s_{lr}) & u^* < 0 \\ (0, 0, 0) & \text{else} \end{cases},
\end{aligned}
\tag{10.16}
$$

where $s_{lr} = \overline{\rho}(\rho_l, \rho_r)(\Phi_r - \Phi_l)$ is a discretization of the source term.

Moreover, this relaxation solver is positivity preserving for ρ and e, satisfies an entropy inequality and handles vacuum states (also cf. Zenk, 2013). The entropy inequality can be used to show stability of the scheme.

A simple, first order finite volume scheme can be constructed for the state vector U as

$$U_i^{n+1} = U_i^n - \frac{\Delta t}{\Delta x}(F_{i+\frac{1}{2}} - F_{i-\frac{1}{2}}) + \frac{\Delta t}{\Delta x}(S_{i+\frac{1}{2}} - S_{i-\frac{1}{2}}), \tag{10.17}$$

where the timestep has to follow the condition (Desveaux et al., 2015)

$$\Delta t \leq \frac{\Delta x}{2 \max\left(\left|u - \frac{c}{\rho}\right|, \left|u + \frac{c}{\rho}\right|\right)}. \tag{10.18}$$

For this scheme, fluxes and source terms cancel exactly when the well-balanced property is fulfilled (i.e., for corresponding initial conditions and average $\overline{\rho}$).

10.3 Extensions for Use in AREPO

Since AREPO is a finite volume code that solves the multi-dimensional Euler equations on an unstructured Voronoi mesh using a second order scheme (see Sec. 3.2), the one-dimensional scheme from the previous section has to be extended in order to be used in AREPO.

In AREPO, the Riemann problem is solved in the rest frame of each face with the normal of the face pointing in x direction towards the right cell. After this, the numerical fluxes are turned back using the corresponding rotation matrix and added to the conserved quantities in each cell. This can be done in the same way for the relaxation solver, but two additional equations for the transverse velocities v and w have to be added. They are simply upwinded,

$$
\begin{aligned}
v_l^* &= v_l, & v_r^* &= v_r, \\
w_l^* &= w_l, & w_r^* &= w_r,
\end{aligned}
\tag{10.19}
$$

and inserted into the flux. Additionally, the source term is rotated back to the lab frame in the same way as the numerical flux and also added to the conserved quantities.

In AREPO, the integrals of the conserved quantities Q in the cells are evolved. For a simple forward Euler time discretization evolving the system from time t^n to time $t^{n+1} = t^n + \Delta t$, the scheme can be written as

$$Q_i^{n+1} = Q_i^n - \Delta t \sum_j A_{ij} F_{ij} + \Delta t \sum_j A_{ij} S_{ij}, \tag{10.20}$$

where the sum includes all neighbour cells j of cell i, A_{ij} denotes the area of the surface between cells i and j, and F_{ij} the numerical flux. The source term S_{ij} depends on the orientation of the face and the solution of the Riemann problem. The sum in Eq. (10.20) can also be interpreted as a convex combination of one-dimensional well-balanced problems for which one can show that all properties of the one-dimensional scheme also hold for the multi-dimensional case, especially that the scheme is also well-balanced.

Another improvement consists in considering all interfaces of a cell when their surface area is larger than 10^{-15} of the total surface area of the cell. In the standard version, AREPO neglects interfaces with an area $< 10^{-5}$ of the total surface area, since their contribution is usually negligible. But when preserving equilibria to machine precision, all interfaces must be considered.

The numerical scheme of AREPO has been recently improved and shown to be of second order for general meshes (Pakmor et al., 2016). It uses a linear reconstruction, and the gradients are computed using a least squares method. The relaxation scheme can be extended to linear reconstruction using the same method with one difference: the pressure gradient is computed on top of the hydrostatic atmosphere by subtracting for each face the source term when computing the gradient,

$$p_{j,\text{grad}} = p_j - \overline{\rho}(\rho_l, \rho_r)(\Phi_l - \Phi_r). \tag{10.21}$$

Here, the quadrature rule $\overline{\rho}$ is always evaluated with the cell center values. The reconstruction on the values in Eq. (10.21) leads to vanishing gradients in hydrostatic equilibrium when Eq. (10.5) is fulfilled. Thus the scheme stays well-balanced. Instead of a simple forward Euler integration as shown in Eq. (10.20), the same second order time integration as described by Pakmor et al. (2016) is employed, where the sum over the numerical fluxes is done as in Eq. (10.20).

The scheme as described up to now included gravity only as a fixed potential that is constant in time. For astrophysical applications, however, self-gravity is important. Thus, for self-gravitating flows, we use the standard tree solver that is implemented in AREPO to compute the gravitational potential. The relaxation scheme takes this potential then as input. The accuracy of the scheme is limited by the accuracy of the Poisson solver in this case. The scheme will still converge in second order, but hydrostatic self-gravitating equilibria cannot be preserved exactly.

The relaxation scheme works only on a fixed mesh up to now. For a moving mesh, the correct upwinding of the source terms and the Riemann solver is not yet clear. The implementation of the well-balanced relaxation scheme on a moving mesh is subject to future work.

10.4 Application to Test Problems

10.4.1 Hydrostatic atmospheres

The well-balanced scheme for AREPO as described in Sec. 10.3 is now applied to test problems. The first setup consists of hydrostatic atmospheres of the polytropic type (see Eq. (10.13)) in one, two, and three space dimensions.

For the one-dimensional setup, a polytropic atmosphere has been computed for a potential $\Phi(x) = x/0.5$ according to Eq. (10.13) using the parameters $K = 1$, $C = 5$, and $\Gamma = 4/3$. The one-dimensional grid consists of 100 randomly chosen points between 0 and 1. In this and the following simulations, cgs units are used for simplicity, but all results can be scaled to the desired length scales. The gravitational potential is fixed in time. The atmosphere has been evolved until $t = 1\,\mathrm{s}$. The difference in pressure as well as the Mach number are shown for different times in Figure 10.1. The pressure shows differences to the initial profile only in a few cells, and the differences are of the order 10^{-15}, i.e., machine accuracy for double precision. The Mach number grows with time, but also stays on the order of 10^{-15}. This shows that the relaxation scheme is able to preserve the hydrostatic equilibrium for polytropic atmospheres to machine accuracy in one dimension.
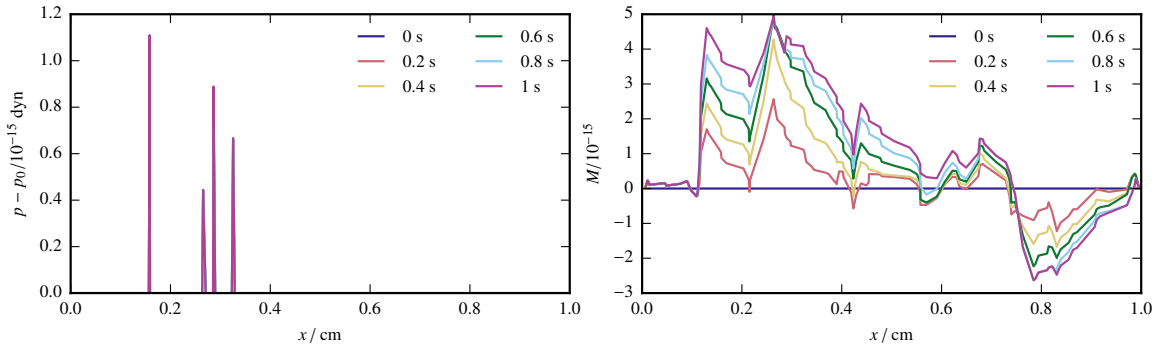
Figure 10.1 | 1D polytropic atmosphere: comparison of the pressure difference to the initial model (left panel) and Mach number (right panel) for different times in the simulation. The grid is a random grid in 1D.

Similarly, a polytropic atmosphere has been set up for a two-dimensional and three-dimensional test. The potential was chosen to be centered on the grid,

$$\Phi(\boldsymbol{x}) = \frac{|\boldsymbol{x} - 0.51_d|}{0.5}. \tag{10.22}$$

The parameters of the polytropic atmospheres according to Eq. 10.13 are $K = 1$, $C = 10$, and $\Gamma = 4/3$. The grid was chosen to consist of 50^2 and 24^3 randomly chosen points in the unit square and unit cube, respectively. The evolution of the mean of the relative error of the pressure to the initial distribution is shown in Fig. 10.2 (left panel). The error rises in the beginning and then stabilizes at a level between 10^{-14} to 10^{-13}. In Fig. 10.2 (right panel), the mean Mach number over the grid is plotted over time. Similar to the error of the pressure, it increases initially and then stays nearly constant. The error is larger in the two-dimensional simulation compared to the three-dimensional simulation which might be due to the fact that the randomly chosen grid leads to different discretization errors in the simulations. For both simulations, the errors are larger than in the one-dimensional test (cf. Fig. 10.1) and thus larger than expected for a conservation of the hydrostatic equilibrium to machine precision. The reason might be that the discretization of the source terms introduces an error that depends on the mesh geometry and may be larger for random meshes, where considerable deviations occur between the mesh-generating points and the center of mass of the cells. Nevertheless, the errors are very small compared to what is expected for a non-well-balanced scheme (cf. Fig. 10.4), thus the well-balanced relaxation scheme performs reasonably well in preserving hydrostatic equilibria of the polytropic type.
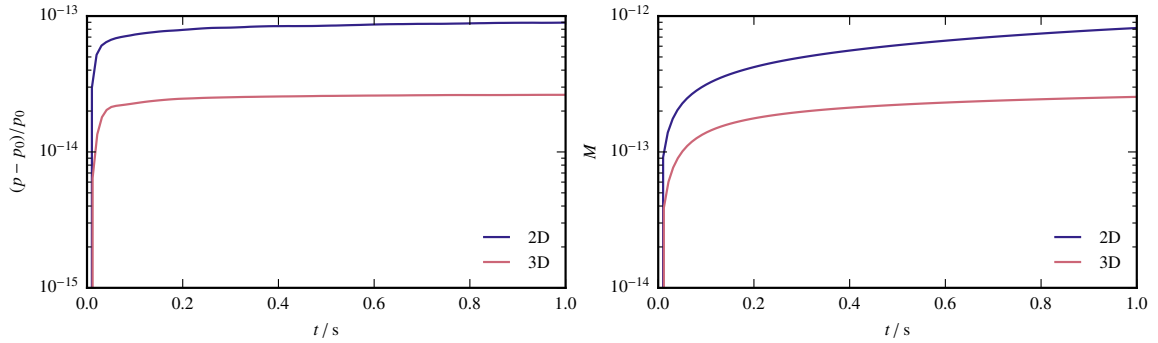
Figure 10.2 | Temporal evolution of the mean pressure difference to the initial atmosphere (left panel) and mean Mach number (right panel) for polytropic initial conditions in 2D and 3D on unstructured, randomly chosen grids.

The performance of the well-balanced scheme for general hydrostatic atmospheres in two dimensions also in comparison to the unmodified AREPO scheme is checked by setting up a specific temperature profile for a constant gravitational acceleration ($g = 1$) in negative y direction,

$$T = T_0 \left(1 + \Delta T \tanh(y/w)\right) \tag{10.23}$$

The parameters were chosen as $\Delta T = 0.1$, $w = 0.02$, and $T_0 = 10^{-8}$ K.[2] The temperature distribution is thus constant in the lower and upper part differing by 10%, and the narrow transition region has a width of 0.02, which is 2% of the box size. The initial profile of the internal energy is shown in Fig. 10.3. This atmosphere is not polytropic, so that it is not an equilibrium that is preserved exactly in the well balanced scheme. Nevertheless, it should be preserved to second order in the relaxation scheme as well as in the unmodified AREPO scheme.

The convergence was tested by conducting simulations for both schemes with resolutions of 50^2, 100^2, and 200^2 cells on a Cartesian mesh. In Fig. 10.4, the mean Mach number is plotted against the linear cell size for the different resolutions comparing both the unmodified and the well-balanced scheme. The order of convergence is ~ 2 for the unmodified scheme and ~ 1.7 for the well-balanced scheme. This is slightly lower than the expected value of 2, probably due to the multi-dimensional discretization of the source terms. The mean Mach number, however, is substantially smaller (roughly two orders of magnitude) when using the well-balanced scheme compared to the unmodified AREPO scheme.

The behaviour of the pressure is analyzed in Fig. 10.5 for both schemes. It shows the difference of the pressure at the end of the simulation (after 10 s) compared to the initial values. The unmodified scheme clearly shows a pressure difference with a systematic offset compared to the initial distribution (see Fig. 10.5, left panel): the pressure increases everywhere in the atmosphere, in the bottom part stronger than in the upper part. In contrast to this, the pressure difference is distributed around zero for the well balanced scheme (Fig. 10.5, right panel) with the largest error being in the region where the temperature changes strongly. Thus, the well-balanced scheme in general improves the stability of hydrostatic atmospheres, also if they are not of the isothermal or polytropic kind.

---

[2]The temperature is chosen so small to get an internal energy u of the order of 1.
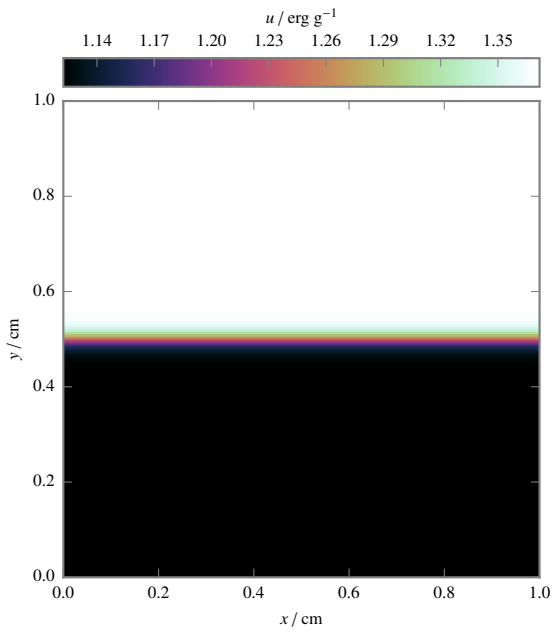
Figure 10.3 | Internal energy in the beginning for the general two-dimensional hydrostatic atmosphere with the temperature profile given in (Eq. 10.23).
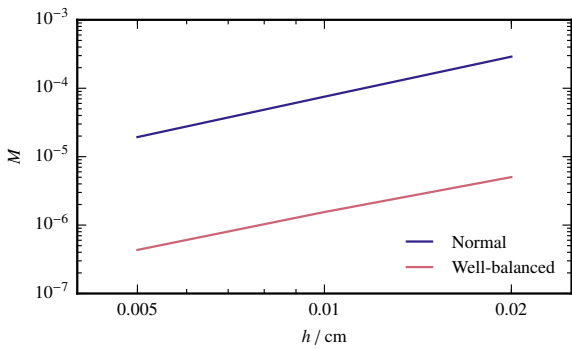
Figure 10.4 | Convergence for two-dimensional atmospheres. The plot shows the mean Mach number of the simulation over the cell size. The upper blue line for the unmodified scheme has a slope of ~ 2, whereas the lower red line for the well-balanced scheme has a slope of ~ 1.7.
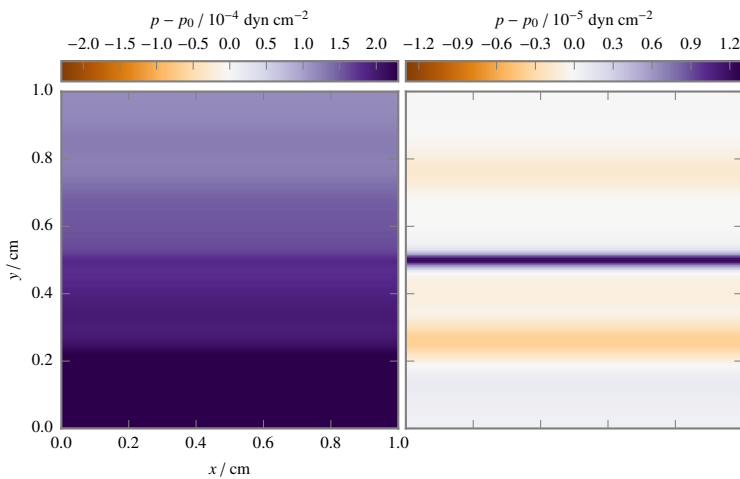

Figure 10.5 | Pressure difference to initial distribution for the standard scheme (left) and the well balanced scheme (right). The standard scheme shows a systematic offset, whereas the error is more symmetric around zero for the well balanced scheme.

10.4.2 Dynamical Test Problems

The dynamical behaviour of the well-balanced solver near the hydrostatic equilibrium is tested by setting up a small pressure distortion on top of a polytropic atmosphere in two dimensions. The polytropic atmosphere is given by Eq. 10.13 with the parameters $K = 1$, $C = 10$, and $\Gamma = 4/3$. The grid consists of 50^2 randomly chosen mesh-generating points. The pressure is disturbed by adding a small circular pressure excess

$$\delta p = 10^{-8} \exp\left(-\left(\frac{r - 0.2}{0.02}\right)^2\right), \tag{10.24}$$

where r is the radius from the center of the computational domain $(0.5, 0.5)$. This corresponds to a Gaussian shape at a distance of 0.2 from the center and a width of 0.02. The initial pressure profile is shown in Fig. 10.6, where the pressure excess can not be seen as it is too small to be visible in the colorscale. The temporal evolution of the distortion is shown in Fig. 10.7, where the difference of the pressure to the polytropic background pressure is shown. The bump splits in two waves which travel in- and outwards, as expected (cf. Zenk, 2013, Sec. 7). Although the relative strength of the pressure excess is 10^{-9} of the background pressure, the waves are not washed out, but captured with the scheme. Thus, the well-balanced scheme is suited to capture small-amplitude dynamics on top of hydrostatic atmospheres.
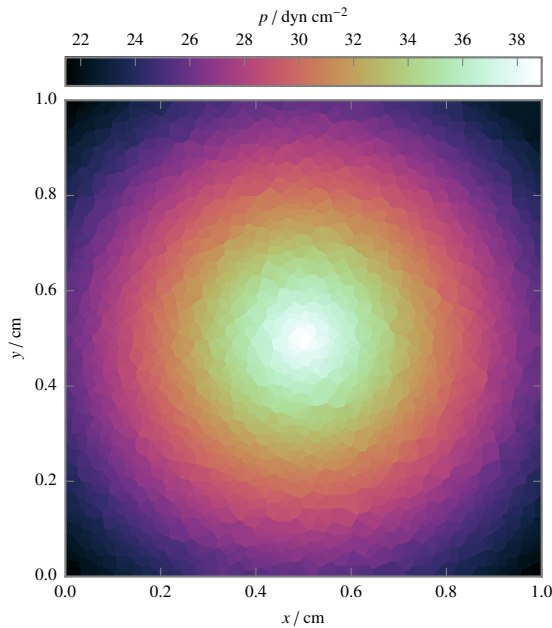
Figure 10.6 | Initial pressure distribution for the setup with a bump on a polytropic atmosphere.

10.4.3 Flows with self-gravitation

For many astrophysical applications, self-gravity is important, i.e., the gravitational potential is not fixed, but has to be computed from the density by solving the Poisson equation (2.5). A new idea is now to use the well-balanced solver not only near the hydrostatic equilibrium, but also far away from it since the inclusion of the gravitational potential into the Riemann solver may also be beneficial in this case. Specifically, the estimate for the intermediate velocity (Eq. (10.6,
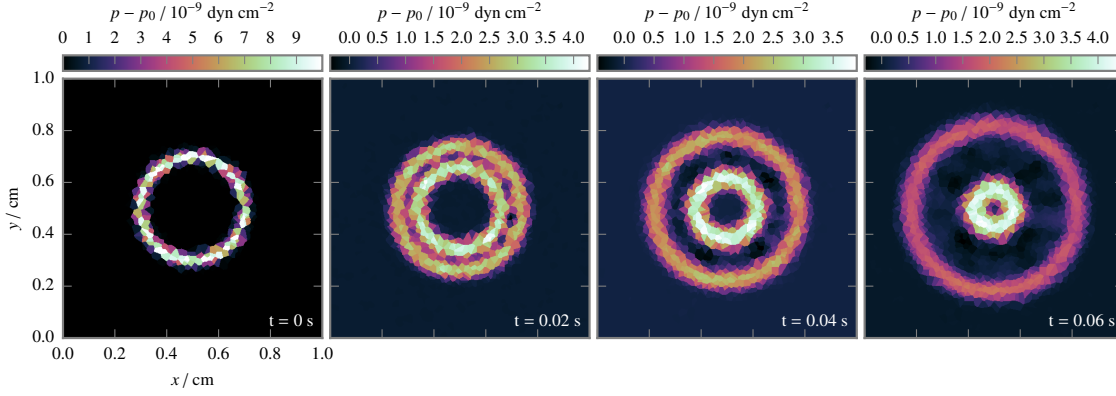
Figure 10.7 | Time series of the difference of the pressure to the polytropic background pressure (time advancing from left to right). The bump propagates although its height is only 10^{-8}.

first line) takes into account the pressure gradient as well as the gravitational force. Thus, the well-balanced Riemann solver should give a better estimate for the velocity – and hence also for the other quantities – than a normal Riemann solver, regardless of the directions of the pressure gradient and the gravitational force.

The well-balanced relaxation scheme as introduced in Sec. 10.3 is now tested for its performance in simulating self-gravitating flows away from equilibrium against the unmodified AREPO scheme for a gravitational collapse in 3D. The collapse problem was introduced by Evrard (1988) and is discussed for simulations with AREPO in Springel (2010a). During the collapse, a strong shock forms that moves outwards; thereby, gravitational energy is converted to kinetic and then thermal energy. Finally, the system tends towards a virialized equilibrium. This test problem is very sensitive to the conservation of total energy that can be easily violated if the conversion of gravitational energy to kinetic and thermal energy is not properly resolved. Thus, it also tests the coupling of gravity to the hydrodynamics.

The initial conditions for Evrard's collapse consist of a cold isothermal sphere of gas with an initial radial density profile of

$$\rho(r) = \begin{cases} \frac{M}{2\pi R^2 r} & \text{for } r \leq R \\ 0 & \text{for } r > R, \end{cases} \tag{10.25}$$

where R and M are radius and mass of the sphere, respectively. For the test simulations, $R = 1\,\text{cm}$ and $M = 1\,\text{g}$ is chosen, as well as $u = 0.05\,\text{erg\,g}^{-1}$ for the internal energy of the cells. The grid is constructed in spherical shells using a HEALPix distribution (Górski et al., 2005) on each shell for the mesh-generating points (see also Sec. 4.1 and App. A). This leads to a mass-adaptive grid with the highest resolution in the high-density regions, i.e., for this problem in the center. Simulations were run for the unmodified scheme and the well-balanced scheme in several resolutions, 10^5, 5×10^5, 2×10^6, and 10^7 cells.

The density profiles at 0.66 s for the different runs is shown in Fig. 10.8. One can see the strong shock at $r \sim 0.1\,\text{cm}$ that is moving outwards. The central density is in general larger for the well-balanced runs compared to the unmodified runs, and the position of the shock is farther inwards. The shock is steeper for higher resolutions, i.e., it is better resolved. Moreover, the

position of the shock does not change with increasing resolution for the well-balanced scheme whereas it moves inwards for the unmodified scheme, converging to the same position. Thus, the shock position can be resolved better for the well-balanced scheme already at lower resolutions.
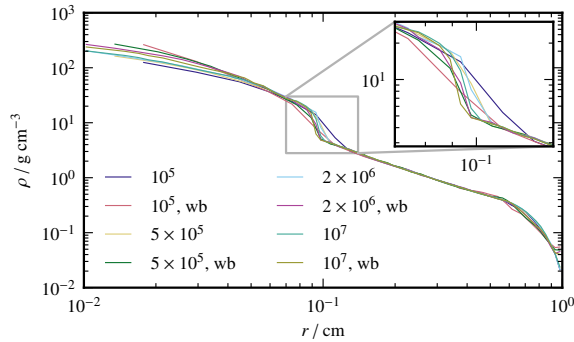
Figure 10.8 | Density profile for Evrard's collapse. Shown is the radial density distribution for Evrard's collapse problem after 0.66 s for different solvers and different resolutions. The inset shows a zoom on the shock region. The inset axes have the same units as the large axes.
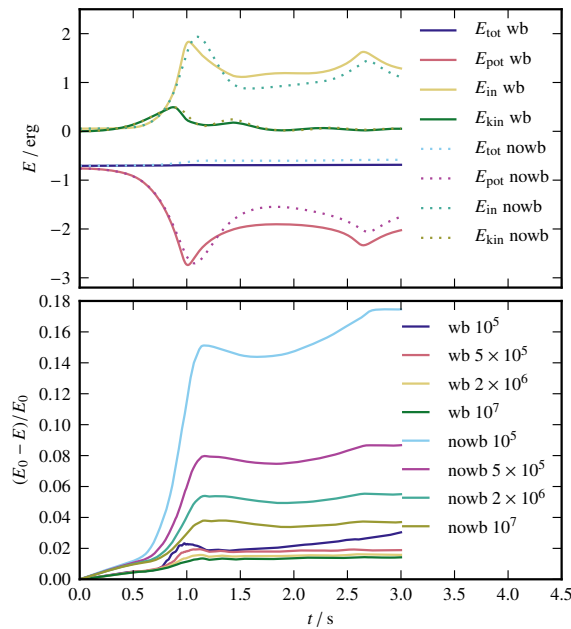
Figure 10.9 | Energy evolution for Evrard's collapse. The top panel shows the internal, kinetic, potential, and total energy for a simulation with well balanced solver and for one without at the lowest resolution of 10^5 cells. The bottom panel shows the relative energy error for simulations with and without well balanced solver and for different resolutions. The error is smaller for the simulations using the well balanced solver.

The evolution of the energies in the system is plotted in Fig. 10.9. During the collapse, the conversion from potential energy to kinetic and thermal energy happens faster for the well-balanced scheme than for the unmodified scheme (Fig. 10.9, upper panel). Thus, the coupling of gravity to hydrodynamics seems to be an advantage of the well-balanced scheme in this test. Moreover, the relative error in the energy decreases with larger resolution for both schemes (Fig. 10.9, lower panel). The error decreases for the unmodified scheme to an order of roughly 1 with $N^{1/3}$ (proxy for cell size, N: number of cells), for the well-balanced scheme to an order of roughly 0.6. However, the error for the well-balanced scheme is significantly smaller than for the unmodified scheme also still at the highest resolution.

Hence, the well-balanced relaxation solver may improve the numerical scheme of AREPO also far away from hydrostatic equilibria for self-gravitating flows in general. In order to use AREPO's most distinctive feature, the moving mesh, the solver still has to be adapted to the solution on the

moving mesh and may then improve the coupling of gravity to hydrodynamics. Since this is not implemented yet, the CE simulations presented in in this work use the unmodified AREPO scheme. Nevertheless, the scheme shows promising properties that CE simulations could benefit from: the improved modeling of hydrostatic equilibria should lead to more stable initial models, and the better coupling of gravity to hydrodynamics could improve the modeling of the gravitational interaction of the point masses with the envelope.

10.5 Modification for Low Mach Numbers

The problem of hydrodynamic flows near hydrostatic equilibria is connected to the problem of modeling flows at low Mach numbers since small departures from hydrostatic equilibrium result in flows with small velocities and hence small Mach numbers. Most finite volume schemes were designed for modeling hydrodynamics in the transonic regime and thus – not surprisingly – their treatment of low Mach number flows is prone to errors. One reason is that the numerical dissipation of theses schemes increase excessively for low Mach numbers, flow structures are simply smeared out (for a recent discussion and the introduction of a new Riemann solver, see Miczek et al., 2015). A better behaviour for different Mach numbers can be reached by modifying the numerical fluxes from the Riemann solver in such a way that the numerical dissipation scales correctly with the Mach number.

In a recent work, Oßwald et al. (2015) identify – similar to previous work – the jumps in the velocity as a source of excessive dissipation in the Roe solver and introduce the L^2Roe solver that scales these velocity jumps with the Mach number for low Mach numbers. The idea is to reduce the dissipation for low Mach numbers and reach a correct scaling of the numerical fluxes. But, as Oßwald et al. (2015) write, "modifying the numerical viscosity can influence stability". They do not show stability for their scheme and they do not notice any problems in their numerical tests. However, for certain problems it may be necessary to adapt the CFL criterion to a more stringent version (i.e., $\Delta t \propto 1/M^2$) in order to reach a stable numerical scheme.

Here, we propose a new Riemann solver, L^2Relaxation, that applies the same idea of scaling the velocity jumps to the relaxation solver as described in Sec. 10.2. To this end, we rewrite the expressions for π and ρ in the star regions. With $\Delta\pi = \pi_l - \pi_r + \overline{\rho}(\rho_l, \rho_r)(Z_l - Z_r)$, this yields

$$
\begin{aligned}
u^* = u_l^* = u_r^* &= \frac{c_l u_l + c_r u_r}{c_l + c_r} + \frac{\Delta\pi}{c_l + c_r} \\
\pi_l^* &= \pi_l - \frac{c_l \Delta\pi}{c_l + c_r} + \frac{c_l c_r}{c_l + c_r}\Delta u \\
\pi_r^* &= \pi_r + \frac{c_r \Delta\pi}{c_l + c_r} + \frac{c_l c_r}{c_l + c_r}\Delta u \\
\frac{1}{\rho_l^*} &= \frac{1}{\rho_l} + \frac{1}{c_l}\frac{\Delta\pi}{c_l + c_r} - \frac{c_r}{c_l(c_l + c_r)}\Delta u \\
\frac{1}{\rho_r^*} &= \frac{1}{\rho_r} - \frac{1}{c_r}\frac{\Delta\pi}{c_l + c_r} - \frac{c_l}{c_r(c_l + c_r)}\Delta u,
\end{aligned}
\tag{10.26}
$$

where $\Delta u = u_l - u_r$, and the expressions for the internal energy remain the same. These states are now modified by substituting Δu by $z\Delta u$, where $z = \min(1, \max(M_l, M_r))$ ($M_{l,r}$ are the Mach numbers in the l and r regions). This leads to a decreased dissipation for low Mach numbers. The tangential velocities are simply upwinded as in the normal relaxation solver (cf. Sec. 10.3).

The behaviour of the L^2Relaxation solver for small Mach numbers is tested by simulating the Gresho vortex that has been set up as described in Miczek et al. (2015). The Gresho vortex is a stationary circular flow reaching a certain maximum Mach number that can be scaled to the desired value. The simulation uses the second order scheme as described in Sec. 10.3 and either the normal relaxation solver or the L^2Relaxation solver is used as Riemann solver. In this problem, the kinetic energy should be conserved since the flow is stationary. If the solver shows some dissipation of kinetic energy, this dissipation should not depend on the Mach number as a correct behaviour for low Mach numbers.

The evolution of the kinetic energy for both solvers over one orbit of the Gresho vortex is shown in Fig. 10.10. The normal relaxation solver shows larger dissipation for lower Mach numbers (left panel) and thus is not well suited for simulating Mach number flows. The L^2Relaxation solver, however, shows the same dissipation of kinetic energy for $M = 0.1$ and $M = 0.01$. Thus, the L^2Relaxation solver shows the right scaling of the dissipation with the Mach number. For even lower Mach numbers, at $M = 0.001$, the scheme becomes unstable and the kinetic energy rises.
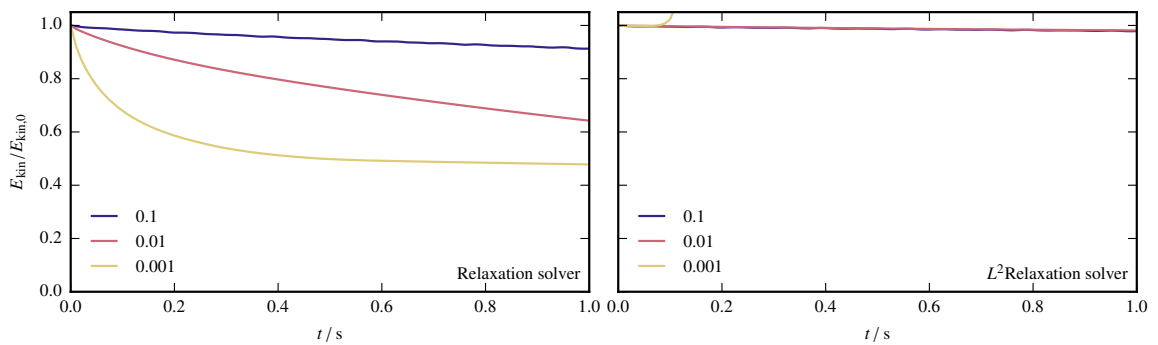
Figure 10.10 | Temporal evolution of kinetic energy for different solvers. The plots show the kinetic energy divided by initial kinetic energy over time for one orbit of the Gresho vortex for different Mach numbers. The left panel shows the unmodified relaxation solver whereas the right panel shows the L^2Relaxation solver.

The distribution of the Mach number and its difference to the initial value can be seen in Fig. 10.11. The overall structure of the vortex is still visible, but spurious oscillation appear, especially in the outer regions with very low Mach numbers. Thus, the scheme seems to be unstable using the usual CFL criterion. Maybe the timestep criterion is not stringent enough and has to be proportional to $1/M^2$ instead of $1/M$, as is the case for other low Mach solvers as well. Schemes with such a timestep restriction are not useful for explicit time integration due to the high computational costs. A more thorough stability analysis is postponed to future work. The prospect of this solver, however, is that it can combine an improved treatment of gravity by well-balancing with an improved modeling of low Mach number flows.
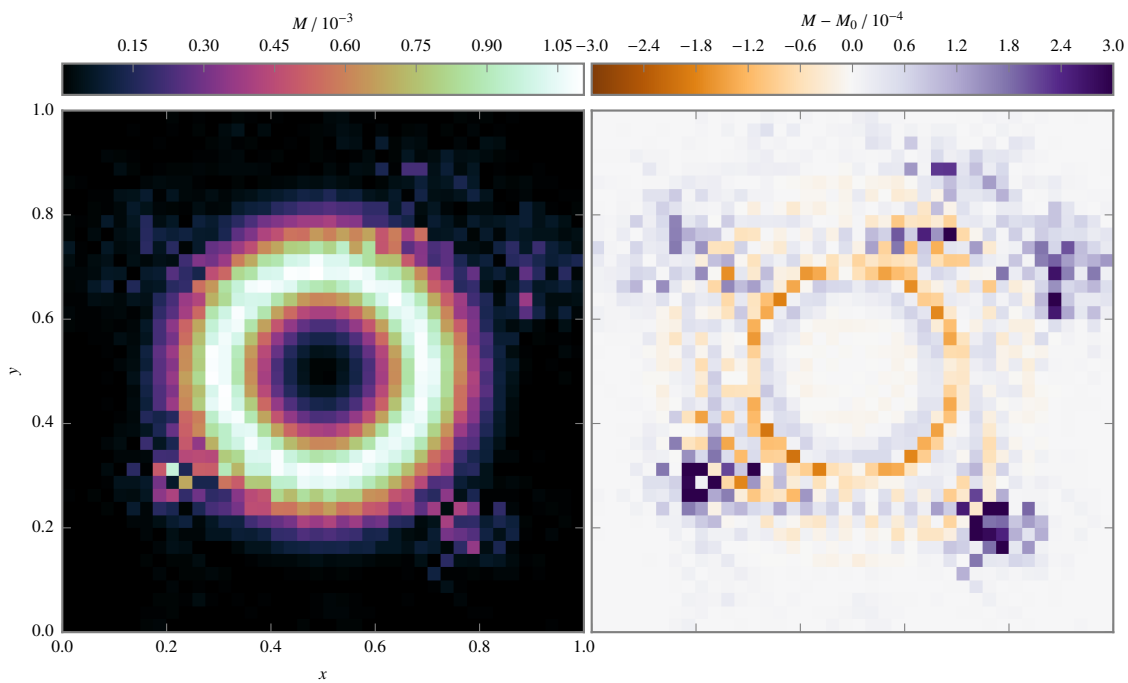
Figure 10.11 | Instability of the L^2Relaxation solver. The plots show the Mach number (left panel) and the difference of the Mach number to the initial distribution (right panel) for $M_{\max} = 0.001$ after 0.11 s. Spurious oscillations occur in the outer parts and hint to an unstable scheme.

Finale

The common envelope (CE) phase is important as a sink of energy and angular momentum for the formation of close binary stars that include at least one compact star. Astrophysically relevant examples for systems fundamentally dependent on CE phases are Type Ia supernovae, cataclysmic variables, X-ray binaries, and black hole binaries. Clarifying the underlying mechanism of the CE phase is a long-standing problem in binary stellar evolution. Numerical methods currently used to simulate this three-dimensional interaction are limited in their scope. In this work, a new approach of modeling the hydrodynamics of the CE phase is introduced to go beyond the state of the art: the moving-mesh hydrodynamics code AREPO, developed by Volker Springel (see Springel, 2010a) mainly for cosmological simulations, combines advantages of different modeling approaches and is utilized to model the dynamical spiral-in of a companion star into the envelope of a red giant.

After summarizing theoretical foundations (Chapter 2) and numerical methods (Chapter 3), the AREPO code is established as a new method for simulating the CE phase. First, stable giant envelopes are generated that can be used as initial conditions for CE simulations (Chapter 4). Then, the first CE simulation on a moving mesh demonstrates that AREPO is a powerful tool for modeling the CE phase that is able to resolve dynamical instabilities for the first time (Chapter 5). Different initial conditions are explored to test the robustness of the method: convergence can be achieved in these simulations only by resolving the region around the point masses representing the core of the giant and the companion (Chapter 6). Having introduced the method as a new state of the art, it is applied to different aspects of the CE phase. The first magnetohydrodynamic simulations of the CE phase show strong field amplifications possibly due to the magnetorotational instability (Chapter 7). Analyzing the transport of angular momentum and energy shows that magnetic fields do not contribute to the transport, but that gravitational torques and shocks are responsible for most of the transport (Chapter 8). Including the ionization state of the gas enhances the mass loss, but does not lead to a complete ejection of the envelope on the simulated timescales of a few months (Chapter 9). First steps towards a new scheme for gravitational flows are presented that improves conserving hydrostatic equilibria, but also modeling flows far away from hydrostatic equilibrium (Chapter 10).

11.1 Achievements

How did we advance in our knowledge of the common envelope phase in this dissertation? We summarize the results by answering the questions posed at the beginning (Sec. 1.4):

1. This work establishes the moving-mesh code AREPO (Springel, 2010a), originally developed for cosmological applications (e.g., Vogelsberger et al., 2014a), for simulating the CE phase, pushing limits of current simulation methods. To create initial models, special approximations for giant atmospheres are needed due to the wide range in temporal and spatial scales: the

core is replaced by a point mass and the stellar profile is continued in a suitable way to the center (Sec. 4.1). Using damping to remove spurious velocities, we can generate stable representations of giant envelopes recovering the convective or non-convective behaviour of the one-dimensional stellar model (Sec. 4.2). Moreover, the convective behaviour depends on the equation of state that is used for reconstructing the stellar model; only when using the same equation of state, convective regions are recovered correctly. These giant envelope models can be confidently used as initial conditions for simulating the CE phase (Sec. 4.3).

The moving-mesh technique of AREPO in combination with its refinement capabilities allows us to resolve the gas flow around the core of the RG and its companion with unprecedented resolution as demonstrated in a first CE simulation on a moving mesh (Chapter 5, published as Ohlmann et al., 2016). Here, a $1M_\odot$ companion spirals into the envelope of a $2M_\odot$ RG with a $0.4M_\odot$ He core and a radius of about $50R_\odot$. During the spiral-in, both the companion and the RG core drive shock waves into the envelope, forming a spiral structure. After some time, however, a hitherto unseen phenomenon is observed: shear instabilities lead to the formation of large-scale flow instabilities that mark the onset of convection starting on a dynamical timescale. Similar to previous simulations (Passy et al., 2012; Ricker & Taam, 2012; Iaconi et al., 2016), only a small part of the envelope mass is ejected on the simulated timescale; thus processes on longer timescales might be responsible for the ejection.

2. After having established the numerical method, a convergence study (Chapter 6) shows that the adaptive mesh refinement around the point masses is crucial for obtaining converged results. If the gravitational softening length of the point masses is resolved with less than five to ten cells, the spiral-in stops earlier and leaves a system with larger separation behind. Thus, current grid simulations that utilize a resolution of only 1.5 or 3 cells per softening length (Passy et al., 2012; Ricker & Taam, 2012; Iaconi et al., 2016) probably overestimate the final separation. Moreover, the error in the energy decreases to an order of about 1.5 with the spatial resolution around the cores. When the overall mass resolution is increased in addition to the refinement around the point masses, the spatial structure of the flow in the envelope is better resolved, and the energy error decreases, but the final separation changes only slightly.

For smaller mass ratios ($q = 0.25$, $q = 0.1$), the companion spirals in further to a smaller final separation, as expected. The final separation is nevertheless larger than needed as estimated from the energy criterion. The rotational state of the primary, i.e., non-rotating or nearly co-rotating, is insignificant for the evolution of the system for $q = 0.25$. When the simulation is started at a distance 20% larger than the radius, the evolution is similar, ending at the same separation; only slightly more mass is ejected during the first orbit.

A planet-like companion with $q = 0.01$ (i.e., $0.02M_\odot$) disturbs the envelope of the giant only marginally while spiralling in tightly. The envelope expands only slightly, and no significant amount of mass is ejected.

3. The hypothesis that strong magnetic fields in white dwarfs have a binary origin and are generated during the common envelope phase has gained support (Ferrario et al., 2015a; Briggs et al., 2015). Until now, the origin of the magnetic fields in CE phases was believed to be due to a dynamo process in the differentially rotating envelope (Tout et al., 2008) or in an accretion disk formed from a tidally disrupted companion (Nordhaus et al., 2011). In this work, the first three-dimensional MHD simulations of the CE phase show that strong

magnetic fields are generated during the dynamical spiral-in of the companion (Chapter 7). The spatial scales of the magnetic fields and the amplification time scales are compatible with the magneto-rotational instability (Balbus & Hawley, 1991) operating in the accretion stream around the companion. After an amplification by many orders of magnitude, the magnetic fields saturate at an energy less than a percent of the total energy, independent of the strength of the seed field. This results in magnetic fields between 10 kG and 100 kG throughout the envelope.

The dynamical impact of the magnetic fields is small: the mass ejected from the system is slightly larger than without magnetic fields, but the final separation is similar. This may change, however, on longer timescales. Magnetic fields can also be important for subsequently shaping the ejected material that will form a planetary nebula, as discussed by Nordhaus et al. (2007).

The magnitude of the magnetic fields is too small to explain the formation of magnetic CVs that show field strengths up to 3×10^8 G (Wickramasinghe & Ferrario, 2000) especially because it is hard to anchor highly variable fields in a short time in the WD (Potter & Tout, 2010). The long-term evolution, however, is unclear. A dynamo process may operate on longer times in the differentially rotating envelope. Moreover, the $2M_\odot$ RG used as initial model is not expected to be a magnetic CV progenitor because it has an $0.4M_\odot$ He core, whereas magnetic CVs possess more massive CO WDs. Thus, AGB stars seem more promising progenitors for future studies.

4. An analysis of the transport of angular momentum and energy during a dynamical spiral-in (Chapter 8, similar analysis as in Shi et al., 2012 for circumbinary disks) shows that most of the angular momentum of the binary system of the RG core and the companion is transferred to the gas during the first orbit. The transfer of energy, however, takes place continuously also at later times. During the first orbit, strong torques around the companion lead to the formation of a shock that induces gravitational drag. The torques remove angular momentum from the binary system of the point masses that is transferred to the gas. A small part of the envelope (about 8%) is ejected at this point, carrying along some angular momentum and energy. Later on, both point masses orbit through the envelope and create a spiral shock pattern. This transports angular momentum and energy to larger radii. After the instabilities emerge and wash out the spiral shock pattern, angular momentum and energy transport becomes weaker and is mediated by a one-armed spiral structure. The simulation includes magnetic fields, but their impact on the transport processes is unimportant, except that their inclusion slightly increases mass ejection during the first orbit.

Gravitational energy is converted to kinetic and thermal energy of the gas in the direct vicinity of the point masses, also inside the radius where the gravitational acceleration is softened. Although the shock forms at a larger distance, high resolution inside the softening radius of the point masses is needed in order to resolve the conversion processes. If this is violated, the spiral-in stops earlier and larger errors in energy conservation result (see also Sec. 6.2). Thus, hydrodynamics simulations of the CE phase can only yield upper limits of the final separation if the spatial scales around the point masses are not resolved by at least five to ten cells. Using the adaptive mesh refinement capabilities of AREPO, we ensure that our simulations always fulfill this constraint.

5. In the ionized stellar plasma, H and He can recombine below temperatures of about 10^4 K, releasing energy by forming bound atoms. This energy reservoir has long been discussed as a candidate for driving the envelope ejection during CE phases (e.g., Livio, 1989; see also the review by Ivanova et al., 2013b). Recently, Nandez et al. (2015) presented SPH simulations that include the ionization state of the gas by coupling the equation of state of the MESA stellar evolution code to the hydrodynamics scheme. They find a complete ejection of the envelope for different, rather compact giant progenitors when including the recombination energy – compared to 50% ejection using an ideal gas equation of state.

   In our simulations (Chapter 9), the OPAL equation of state (essentially the same in the important regime) is coupled to AREPO to account for the ionization state. We find, however, that the evolution of the orbit is very similar when including recombination energy, the final separation is only smaller by 1.5%. The release of recombination energy, especially from He recombination, behind shocks leads to an increased expansion and a larger mass loss of 10% of the envelope during the first orbit compared to 6% without including recombination energy. Including the internal energy for determining the unbound mass leads to pockets of formally unbound material at high-temperature shocks inside bound material of the envelope. Since this material will still interact, the inclusion of internal and thus also recombination energy overestimates the amount of unbound mass. At the end of the simulations, the amount of unbound mass increases and may continue to do so on longer timescales than simulated.

   The ionization state of the gas computed using the Saha equation in local thermodynamic equilibrium shows a layered stratification of the ionization zones of He II, He I, and H I going from the center to the outer part of the envelope. The spatial distribution follows the shock structures in the envelope. Until 90 d, 3.5×10^{46} erg of recombination energy are released, with He recombination being dominant up to this time.

   For an estimate of the optical display of the CE event, the opacities are calculated to infer the location of the photosphere. Since they depend sensitively on the background temperature (2×10^4 K), no firm prediction can be made. Assuming a lower background temperature yields a sharp photosphere that slightly expands to about $500 R_\odot$, but recedes compared to the expanding ejecta. This would confirm the model of a receding recombination wavefront similar to Type IIP supernovae, as proposed by Ivanova et al. (2013a).

6. First steps towards a new solver for gravitational flows that was implemented into AREPO are presented in Chapter 10. The solver extends the one-dimensional method by Desveaux et al. (2015) to the unstructured multi-dimensional grid of AREPO. This scheme preserves hydrostatic equilibria much better than using the normal coupling of gravity to hydrodynamics. The reason is that the gravitational acceleration is taken into account during the solution of the Riemann problem. Moreover, simulations of a gravitational collapse show that this scheme can prove valuable also for flows far from hydrostatic equilibrium. Although the method has been implemented only on a static mesh up to now, its capabilities seem promising for future simulations of CE phases: the initial hydrostatic equilibrium of the giant atmosphere could be stabilized more easily and the gravitational interaction could be captured better.

11.2 Outlook

The ultimate goal of hydrodynamics simulations of the CE phase as presented in this work is to improve the modeling of the CE phase in binary stellar evolution. This can be reached by connecting the initial state of the binary at the beginning of the CE phase to the final state after the envelope is ejected.

Pursuing this approach is currently limited by the difficulties of extending the hydrodynamics simulations to both the beginning and the end of the CE phase. Reaching the beginning of the mass transfer is important since the initial conditions determine the outcome of the simulations, but the timescales at the onset of mass transfer are too large to be resolved in a hydrodynamics simulations with current methods. Similarly, the final state, i.e., separation and masses of the components, can only be predicted by extending the simulations to longer times to finally reach an ejection of the envelope. But also here, the orbital decay timescale becomes very long rendering the continuation of the simulation computationally expensive. Nevertheless, one goal for future work is to develop approximations that allow to extend the hydrodynamics simulations further to the beginning and to the end of the CE phase.

The parameter space of possible progenitor systems for CE phases is huge: the evolutionary state and mass of the primary and of the secondary can vary. The primary can be a RG, an AGB star, or a supergiant with different core and envelope masses and the secondary can be a MS, WD or NS of varying mass. Exploring this variety of systems offers promising prospects for future work.

Up to now, constraints on the CE phase are indirect and mostly come from modeling binary systems or stellar populations that went through a CE phase (e.g., Davis et al., 2010; Zorotovic et al., 2010; De Marco et al., 2011; Davis et al., 2012; Toonen & Nelemans, 2013). Missions such as GAIA (Perryman et al., 2001) also target contact binaries and transients. Over its five year lifetime, it may also detect systems just undergoing a CE event. This paves the way to directly constrain CE events by observing their light curves. For this, theoretical modeling of the light curve is needed, extending simplified approaches (e.g., Ivanova et al., 2013a) by modeling the radiative transfer during the event.

Computational Grids

As AREPO works on an unstructured grid, we have the freedom to adapt the grid to the problem at hand. We implemented different types of initial grids (for examples, see Fig. A.1):

1. Regular cubic and face-centered cubic (fcc) grids, where the fcc grid can be obtained by adding shifted versions (by $(0.5, 0.5, 0)$, $(0.5, 0, 0.5)$, and $(0, 0.5, 0.5)$ times the grid spacing) of the cubic grid to itself. The advantage of the fcc grid is that it has more neighbours (12) compared to the cubic grid (8).

2. Nested cubic and fcc grids, where for each level of nesting the inner eighth of the grid of the corresponding level (i.e., half in each direction) is replaced by a grid with half the grid spacing.
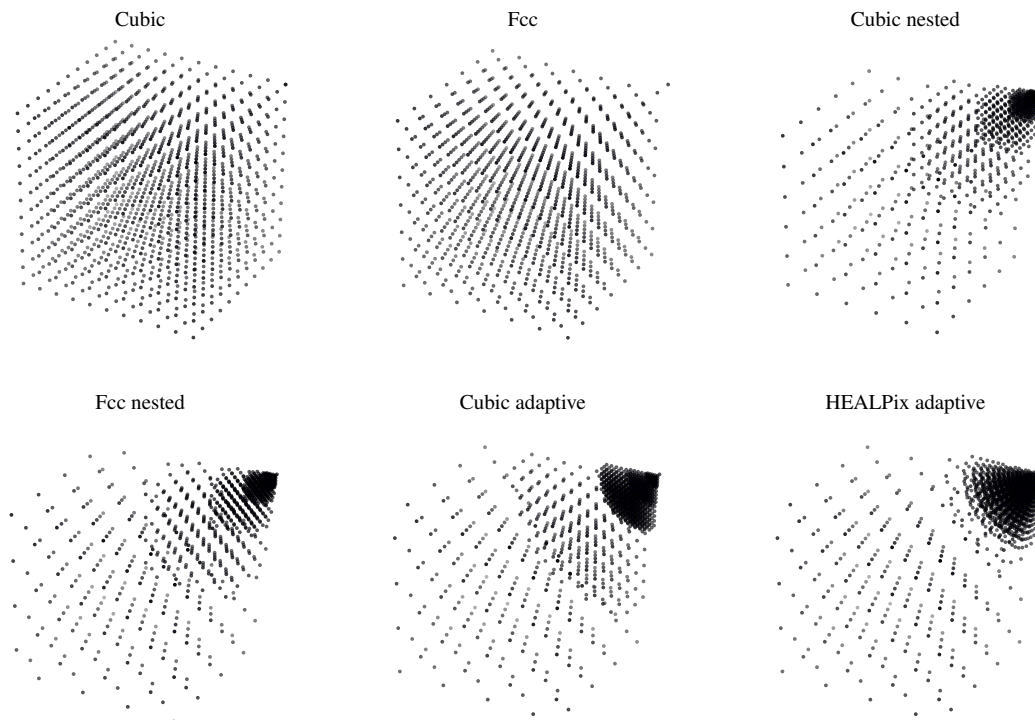
Figure A.1 | Examples of different grid types. Shown are the cell-generating points of all Voronoi cells in one octant. The center of the star lies at the upper right corner of each plot. The number of cells is about 10^4.

3. An adaptive cubic grid, where the grid is built in spherical shells tracking the mass distribution of the star to create approximately equal-mass cells. Given the mass profile $m(r)$ of the star and the mass of cells m_c, we searched for the outer radius r_2 (given the inner radius r_1) and the grid spacing a. The mass in the shell yields the condition

$$m(r_2) - m(r_1) = Nm_c, \tag{A.1}$$

the volume yields

$$\frac{4\pi}{3}\left(r_2^3 - r_1^3\right) = Na^3, \tag{A.2}$$

where N is the number of particles in the shell. As an additional constraint, we imposed that the width of the shell is a multiple of the grid spacing,

$$r_2 - r_1 = ka, \tag{A.3}$$

where we usually chose $k = 5$. These equations were solved for each shell to yield r_2, a, and N.

4. A HEALPix grid with spherical shells tracking the mass profile of the star, where the cells are distributed in each shell according to the HEALPix tesselation (Górski et al., 2005) similar to the distribution of SPH particles by Pakmor et al. (2012). We deviated slightly from their scheme as we are not bound to strictly equal-mass cells compared to particles in SPH simulations.

In each shell ranging from a given radius r_1 to r_2, we distributed $12N_{side}^2$ cells using the algorithm of Górski et al. (2005). Thereby, we ensured that the cells are symmetric and have approximately a mass of $m_{c,0}$. The cells have a radial diameter of $\Delta r_r = r_2 - r_1$, whereas the lateral diameter can be computed by multiplying the midpoint $(r_1 + r_2)/2$ by the angular resolution θ of the shell (Górski et al., 2005),

$$\Delta r_l = \frac{r_1 + r_2}{2}\theta = \frac{r_1 + r_2}{2}\sqrt{\frac{\pi}{3}}\frac{1}{N_{side}}. \tag{A.4}$$

We defined the symmetry factor as $S = \Delta r_r / \Delta r_l$, which is one for symmetric cells. By imposing $S = 1$, we can compute r_2 for different values of N_{side}. We then chose the radius for which the resulting cell mass,

$$m_c = \frac{m(r_2) - m(r_1)}{12N_{side}^2}, \tag{A.5}$$

is nearest to the given cell mass $m_{c,0}$. In order to avoid large jumps in the cell mass, we limited the cell mass by

$$\frac{1}{1.3} < \frac{m_c}{m_{c,0}} < 1.3. \tag{A.6}$$

If the mass limit was enforced for a shell (i.e., when condition (A.6) was violated), we computed the number N_{side} for which $\log(S)$ was nearest to zero (i.e., we looked for the most symmetric cells) and take the corresponding radius r_2.

To resolve the steep gradients near the surface of the star, we did not enforce the mass limit in the outermost 5% in radius of the star.

Grid orientation effects are minimized by randomly rotating the axes according to which the positions on the corresponding sphere are computed.

For each grid, we continued the density and pressure profiles outside the stellar surface to sufficiently low values to emulate the vacuum there in a numerically feasible way. For the adaptive cubic and HEALPix grids, we added in the outer part a regular grid (cubic/fcc) to sample the vacuum values in the rest of the box. Low-resolution examples of these grids are shown in Fig. A.1 for the $2M_\odot$ RG model as introduced in Sec. 4.1.3.

Appendix B

Derivation of Mach Number Fluctuations

The magnitude of the velocity fluctuations introduced by the spatial discretization can be computed for the AREPO scheme as follows. For an overview of numerical hydrodynamics and an in-depth explanation of Godunov schemes and Riemann solvers, see the book by Toro (2009).

The initial condition is an isothermal atmosphere given in z direction as $p(z) = p_0 \exp(-z/H)$ and $\rho(z) = \rho_0 \exp(-z/H)$, with H denoting the pressure scale height. We assume an ideal equation of state. The gravitational acceleration is constant and given by $g = \frac{p_0}{H\rho_0}$. The speed of sound is also constant and given by $c_\mathrm{s} = \sqrt{\gamma P/\rho}$. The grid is assumed to be equidistant with grid spacing δ. We use the HLLC solver (Toro et al., 1994) to compute the Riemann problems at the cell interfaces.

For this setup, the update of the conserved quantities $\boldsymbol{U}_i$ for cell i reads for a simple forward Euler time step (from time t^n to $t^{n+1} = t^n + \Delta t$):

$$\boldsymbol{U}_i^{(n+1)} = \boldsymbol{U}_i^{(n)} - \frac{\Delta t}{\delta} \left(\boldsymbol{F}_{i+\frac{1}{2}} - \boldsymbol{F}_{i-\frac{1}{2}} \right) + \Delta t \boldsymbol{S}_i, \tag{B.1}$$

where $\boldsymbol{F}_{i\pm\frac{1}{2}}$ denotes the flux over the left (right) cell boundary and $\boldsymbol{S}_i = (0, \rho_i g, \rho_i g v_i)^\top$ is the gravitational source term (ρ_i: density, v_i: velocity).

For the initial conditions given here, the velocity is zero and for each Riemann problem, $p_\mathrm{L} > p_\mathrm{R}$ (L: left interface, R: right interface). Thus, the fluxes are computed for the subsonic L^* region of the HLLC solver (Toro et al., 1994) as

$$\boldsymbol{F}_\mathrm{L}^* = \boldsymbol{F}_\mathrm{L} + S_\mathrm{L} \left(\boldsymbol{U}_\mathrm{L}^* - \boldsymbol{U}_\mathrm{L} \right), \tag{B.2}$$

where S_L is the left wave speed and $\boldsymbol{U}_\mathrm{L}^*$ the solution of the Riemann problem in the L^* region. $\boldsymbol{F}_\mathrm{L}$ is the Euler flux computed with the values at the left interface. Plugging in the solution of the Riemann problem as given in Toro et al. (1994) for zero velocities ($v_\mathrm{L} = v_\mathrm{R} = 0$) yields for the momentum flux

$$p_\mathrm{L} + \frac{S_\mathrm{L}^2 S_\mathrm{M}}{S_\mathrm{L} + S_\mathrm{M}} \rho_\mathrm{L}, \tag{B.3}$$

where S_M denotes the velocity of the contact discontinuity. This flux can now be combined with Eq. B.1 to compute the update of the momentum,

$$(\rho v)_i^{(n+1)} = -\frac{\Delta t}{\delta} \left(p_{i+\frac{1}{2}}^\mathrm{L} - p_{i-\frac{1}{2}}^\mathrm{L} + \left(\frac{S_\mathrm{L}^2 S_\mathrm{M}}{S_\mathrm{L} + S_\mathrm{M}} \rho_\mathrm{L} \right)_{i+\frac{1}{2}} - \left(\frac{S_\mathrm{L}^2 S_\mathrm{M}}{S_\mathrm{L} + S_\mathrm{M}} \rho_\mathrm{L} \right)_{i-\frac{1}{2}} \right) + \Delta t \rho_i g, \tag{B.4}$$

where $v^{(n)} = 0$ is assumed. To obtain the magnitude of velocity fluctuations caused by the spatial discretization, a reconstruction has to be chosen. For constant reconstruction, $p_{i+\frac{1}{2}}^\mathrm{L} = p_i$ holds,

whereas for linear reconstruction a central finite difference for the derivative is employed which yields

$$p^{\mathrm{L}}_{i+\frac{1}{2}} = p_i + \frac{p_{i+1} - p_{i-1}}{2\delta}\frac{\delta}{2} = p_i + \frac{1}{4}\left(p_{i+1} - p_{i-1}\right). \tag{B.5}$$

After inserting the reconstruction into Eq. (B.4), pressure and density are expanded into a Taylor series around cell i and only the highest order terms are retained. For this expansion, we assume that the value p_i represents the pressure at x_i and not the average over cell i, which is the usual interpretation, because we use the same procedure in the setup of our simulations[1]. For better comparison between different initial values, the resulting Mach number $M = v/c_{\mathrm{s}}$ is computed. The first order term in the expansion cancels out the gravitational source term, but for constant reconstruction, Mach number fluctuations are of the order of $(\delta/H)^2$. For linear reconstruction, this order vanishes as well and we obtain Eq. (4.24).

A similar derivation was done by Zingale et al. (2002, Sec. 3.1), but for a PPM scheme in the context of mapping hydrostatic atmospheres into the AMR code FLASH. For their scheme, they find a coefficient of 5/24 and the same order of the error, similar to our findings.

---

[1]If p_i is taken as the average over cell i, the result remains the same for constant reconstruction. For linear reconstruction, the constant in Eq. (4.24) changes from 1/12 to 7/72, i.e., by roughly 20%. The order of magnitude and the scaling with δ/H stays the same.

Appendix C

Fitting Ellipse Parameters

During the common envelope simulations, the core of the RG and the companion can be thought of evolving on elliptical orbits with changing parameters. In this appendix, a method of computing ellipse parameters from a few points of the orbit is summarized.

The general equation of an ellipse in the x-y plane can be written as

$$Ax^2 + Bxy + Cy^2 + Dx + Ey + F = 0, \tag{C.1}$$

where the parameters have to fulfill $B^2 - 4AC < 0$ to describe an ellipse. Eq. (C.1) contains five parameters, thus five points are needed at least to determine the parameters. A more intuitive parametrization of the ellipse is

$$\frac{((x - x_c)\cos\theta + (y - y_c)\sin\theta)^2}{a^2} + \frac{(-(x - x_c)\sin\theta + (y - y_c)\cos\theta)^2}{b^2} = 1, \tag{C.2}$$

where x_c and y_c denote the center of the ellipse, θ is the angle of the major axis to the x axis, and a and b denote the semi-major axis and semi-minor axis, respectively. These five parameters can be related to the parameters from Eq. (C.1),

$$\begin{aligned}
A &= a^2 \sin^2\theta + b^2 \cos^2\theta \\
B &= (b^2 - a^2)2\sin\theta\cos\theta \\
C &= a^2 \cos^2\theta + b^2 \sin^2\theta \\
D &= -2x_c A - y_c B \\
E &= -x_c B - 2y_c C \\
F &= x_c^2 A + y_c^2 C + x_c y_c B - a^2 b^2.
\end{aligned} \tag{C.3}$$

The inversion of this relation yields

$$\begin{aligned}
x_c &= \frac{BE - 2CD}{4AC - B^2} \\
y_c &= \frac{BD - 2AE}{4AC - B^2} \\
\theta &= 0.5 \operatorname{arccot}\left(\frac{A - C}{B}\right) = 0.5 \arctan\left(\frac{B}{A - C}\right) \\
a, b &= \sqrt{\frac{2(AE^2 + CD^2 + FB^2 - BDE - 4ACF)}{(B^2 - 4AC)\left[-(A + C) \pm \sqrt{(A - C)^2 + B^2}\right]}}.
\end{aligned} \tag{C.4}$$

Although the set of parameters (A, B, C, D, E, F) is not unique and may be rescaled by an arbitrary factor, the set of parameters (x_c, y_c, θ, a, b) is invariant under such a rescaling.

Now this set of five parameters may be determined if the x and y coordinates of five or more points are given. Plugging these values into Eq. (C.1) yields a linear system of equation,

$$
M\boldsymbol{x} = \begin{pmatrix} x_1^2 & x_1 y_1 & y_1^2 & x_1 & y_1 & 1 \\ x_2^2 & x_2 y_2 & y_2^2 & x_2 & y_2 & 1 \\ \vdots & & & & & \vdots \end{pmatrix} \begin{pmatrix} A \\ B \\ C \\ D \\ E \\ F \end{pmatrix} = 0, \tag{C.5}
$$

where the matrix $M \in \mathbb{R}^{(m,6)}$ when the coordinates of m points are given. For more than five points, the system is overdetermined and only an approximate solution can be found.

The system Eqs. (C.5) can now be solved using the singular value decomposition of M (see, e.g., Bronstein et al., 2008). The singular value decomposition for a general matrix $M \in \mathbb{R}^{(m,6)}$ is given by

$$
M = U\Sigma V^T, \quad U \in \mathbb{R}^{(m,m)}, \quad \Sigma \in \mathbb{R}^{(m,6)}, \quad V \in \mathbb{R}^{(6,6)}, \tag{C.6}
$$

where U and V are orthogonal matrices (i.e., $U^T U = 1$) and where Σ has the structure

$$
\Sigma = \begin{pmatrix} \mathrm{diag}(\sigma_1, \ldots, \sigma_n) & 0 \\ 0 & 0 \end{pmatrix}, \tag{C.7}
$$

with m rows and six columns. Here, $n \le \min(m, 6)$ is the number of singular values that are not equal to 0, and $\sigma_1, \ldots, \sigma_n$ denote these singular values. It is assumed in the following, that they are ordered by magnitude, $\sigma_1 > \sigma_2 > \ldots$.

The goal is now to solve the equation $A\boldsymbol{x} = 0$. If there are more than five equations, this equation should be solved approximately. For a least squares approach, the value of $\|A\boldsymbol{x}\|^2$ has to be minimized while keeping $\|\boldsymbol{x}\| = 1$. Since $\|A\boldsymbol{x}\|^2 = \boldsymbol{x}^T A^T A \boldsymbol{x}$, and we want to minimize this expression, we have to set its gradient to zero,

$$
\nabla(\boldsymbol{x}^T A^T A \boldsymbol{x}) = 2\boldsymbol{x}^T A^T A = 0 \iff A^T A \boldsymbol{x} = 0. \tag{C.8}
$$

Using the orthogonality of U, the matrix $A^T A$ can written as

$$
A^T A = V\Sigma^T U^T U\Sigma V^T = V\Sigma^T \Sigma V^T \equiv V\Xi V^T, \tag{C.9}
$$

where the matrix $\Xi \in \mathbb{R}^{(6,6)}$ has the structure

$$
\Xi = \begin{pmatrix} \mathrm{diag}(\sigma_1^2, \ldots, \sigma_n^2) & 0 \\ 0 & 0 \end{pmatrix} = \begin{pmatrix} D & 0 \\ 0 & 0 \end{pmatrix}, \tag{C.10}
$$

with the squared singular values on the diagonal ($D \in \mathbb{R}^{(n,n)}$). If $n = m$, i.e., if there are no non-zero singular values, the singular values fill the complete diagonal. This structure can be used to rewrite the equation

$$
V^T A^T A V = \Sigma^T \Sigma = \Xi = \begin{pmatrix} D & 0 \\ 0 & 0 \end{pmatrix} \tag{C.11}
$$

by splitting the matrix V into a matrix V_1 containing the first five columns and a vector $\boldsymbol{v}_2$ containing the last column as

$$
\begin{bmatrix} V_1^T \\ \boldsymbol{v}_2^t \end{bmatrix} A^T A \, [V_1 \boldsymbol{v}_2] = \begin{pmatrix} D & 0 \\ 0 & 0 \end{pmatrix}. \tag{C.12}
$$

If the last singular value, σ_6, is zero, the last blocks of Eq. (C.12) containing $\boldsymbol{v}_2$ can be written as

$$\boldsymbol{v}_2^T A^T A \boldsymbol{v}_2 = 0 \iff A \boldsymbol{v}_2 = 0. \tag{C.13}$$

Thus the vector $\boldsymbol{v}_2$, i.e., the last column of the matrix V of the singular value decomposition, is a solution of Eq. (C.5).

If, however, the last singular value, σ_6, is larger than zero, the last blocks of Eq. (C.12) can be written as

$$\boldsymbol{v}_2^T A^T A \boldsymbol{v}_2 = \sigma_6^2 \iff \|A \boldsymbol{v}_2\|^2 = \sigma_6^2 \iff \|A \boldsymbol{v}_2\| = \sigma_6. \tag{C.14}$$

In this case, the vector $\boldsymbol{v}_2$ is only an approximate solution of Eq. (C.5) in the least squares sense that corresponds to the smallest singular value σ_6.

Hence, the solution strategy is as follows: for a given number of coordinates m, the matrix A is computed according to Eq. (C.5). Then the singular value decomposition is computed with ordered singular values. The least squares solution finally consists of the last column of the matrix V. From this, the parameters a, b, θ, x_c, y_c can be computed using Eq. (C.4). Using these parameters, one can also compute the eccentricity

$$e = \sqrt{1 - \frac{b^2}{a^2}}, \tag{C.15}$$

and the period

$$P = \sqrt{\frac{4\pi^2 a^3}{G(m_1 + m_2)}}. \tag{C.16}$$

For computing the ellipse parameters in the CE simulations, usually eight neighbouring points are used. Since there is still some noise in these values, they are post-processed first using a low band filter and second using a spline fit of order three in a small error band. This yields reasonably smooth values for the ellipse parameters.

Appendix D

Gravitational Waves from Common Envelope Events

Recently, the first gravitational wave signal ever was reported by Abbott et al. (2016). The signal was detected at the advanced Laser Interferometer Gravitational-Wave Observatory (aLIGO). It was shown to match a merger of two black holes of about $30 M_\odot$. This detection thus confirms the existence of gravitational waves and of binary black hole mergers.

An overview of sensitivities and background sources is given by Moore et al. (2015). Current detectors like aLIGO and VIRGO are sensitive only to frequencies in the range between 10 Hz and 1 kHz. Future space-based missions like LISA, DECIGO, or BBO will be sensitive in frequency ranges roughly between 10^{-4} Hz to 10 Hz. Using pulsar timing arrays, very low frequencies between 1×10^{-9} Hz and 1×10^{-6} Hz can be reached. In different frequency ranges, different sources contribute to the potential signal. The merger of binaries in our Galaxy contributes to the medium to lower frequency range (compare Fig. D.3).

For a CE simulation as presented in Sec. 5, we computed the gravitational wave signal. Since our simulations are run in the Newtonian approximations, only the approximate quadrupole radiation is computed. To this end, we proceed as described in Seitenzahl et al. (2015) following the computations of Blanchet et al. (1990) and Müller & Janka (1997). The strain tensor of the gravitational waves, $\mathbf{h}$, can be expressed in terms of the linear polarization tensors $\mathbf{e}_+$ and $\mathbf{e}_\times$ as

$$\mathbf{h} = \frac{1}{D} \left(A_+ \mathbf{e}_+ + A_\times \mathbf{e}_\times \right), \tag{D.1}$$

where the amplitudes A_+ and $A_\times$ depend on the propagation direction of the gravitational waves and the fluid quantities, and D denotes the distance to the source. The amplitude tensor can be computed as

$$A_{ij} = \frac{G}{c^4} \int \mathrm{d}^3 x \rho \left(2 v_i v_j - x_i g_j - x_j g_i \right), \tag{D.2}$$

where g_i is the gravitational acceleration. The amplitudes in Eq. (D.1) can be computed in the z direction as

$$\begin{aligned} A_+^z &= A_{xx} - A_{yy} \\ A_\times^z &= 2 A_{xy}, \end{aligned} \tag{D.3}$$

and in x direction as

$$\begin{aligned} A_+^x &= A_{zz} - A_{yy} \\ A_\times^x &= -2 A_{yz}. \end{aligned} \tag{D.4}$$

The product hD is shown in Fig. D.1 in the course of a CE simulation of a $2 M_\odot$ RG with a $1 M_\odot$ companion (compare Sec. 5). The beat frequencies at later times after 60 d are due to the orbital
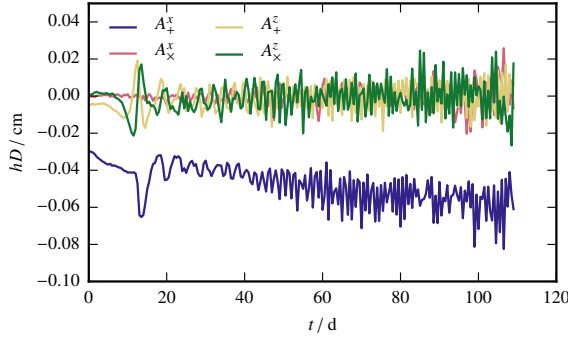
Figure D.1 | Gravitational wave amplitudes hD (strain times distance) during a common envelope event. Shown are the two polarisation modes + and × for two viewing angles, along the x axis and along the z axis. The resolution of the simulation was 8×10^6 cells.
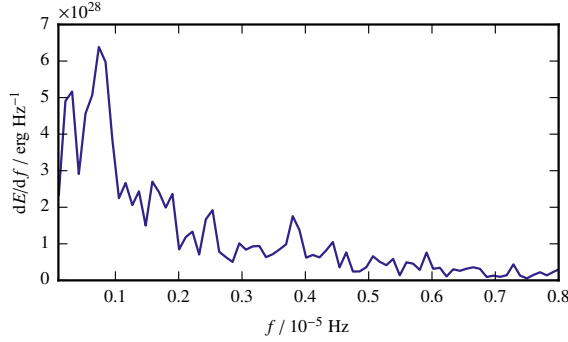
Figure D.2 | Gravitational wave energy spectrum dE/df for the amplitudes shown in Fig. D.1 as computed according to Eq. (D.6). The maximum of the spectrum is at 7.4×10^4 Hz.

period being similar to the time span where snapshots are written out during the simulations (0.5 d). The maximum strain is reached for a propagation in x direction in the + polarization. The mean strain for a distance of 1 kpc is -1.5×10^{-23}.

The energy spectrum of the gravitational waves can now be computed using the Fourier transforms $\tilde{A}_{ij}$,

$$\tilde{A}_{ij}(f) = \int dt A_{ij}(t) \exp(2\pi i f t), \tag{D.5}$$

according to Seitenzahl et al. (2015, Eq. 20) as

$$\frac{\partial E_{\mathrm{gw}}}{\partial f} = \frac{2c^3 (2\pi f)^2}{15G} \left(\left| \tilde{A}_{xx} - \tilde{A}_{yy} \right|^2 + \left| \tilde{A}_{xx} - \tilde{A}_{zz} \right|^2 + \left| \tilde{A}_{yy} - \tilde{A}_{zz} \right|^2 + \right.$$
$$\left. 6 \left(\left| \tilde{A}_{xy} \right|^2 + \left| \tilde{A}_{xz} \right|^2 + \left| \tilde{A}_{yz} \right|^2 \right) \right). \tag{D.6}$$

This spectrum is shown for the CE simulation in Fig. D.2. The maximum of the spectrum is at 7.4×10^{-7} Hz, i.e., at very low frequencies compared to current gravitational wave detectors. This corresponds to a period of 16 d which is roughly the in-spiral timescale in this simulation (cf. Fig. 5.1).

This event is plotted in Fig. D.3 in the frequency-strain plane. At these low frequencies, the sensitivity of pulsar timing arrays is several orders of magnitude larger than the amplitude of the expected signal; thus such a CE event will not be detected in the near future. For CE phases where the core of the RG and the companion merge, the signal should move to higher frequencies because of the smaller timescales during merger. Moreover, the amplitudes might be larger due to the larger velocities in a merger. Thus, in this case the point should move into the direction of galactic binaries.
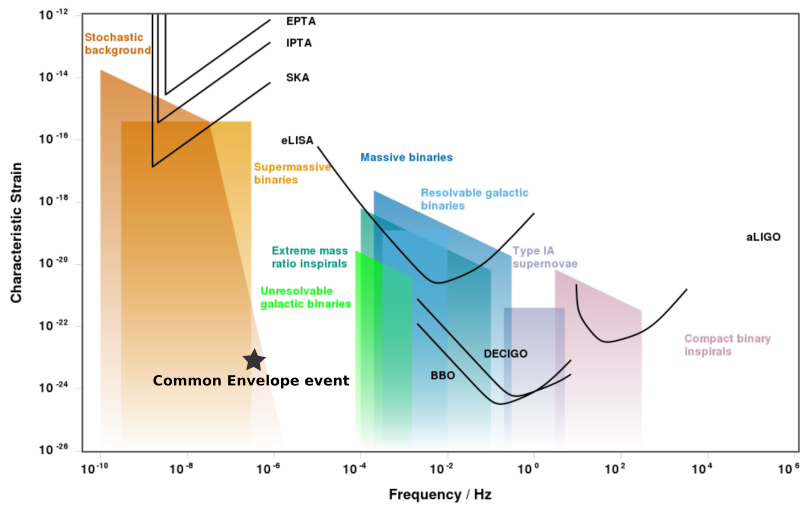
Figure D.3 | Gravitational wave detector sensitivities. Shown are characteristic strains for different types of events as well as sensitivity curves for different instruments. Included are pulsar timing arrays at the lowest frequencies, second and third generation detectors like advanced LIGO, eLISA, and DECIGO/BBO at higher frequencies. The star marks the common envelope event as shown in Figs. D.1 and D.2. The figure was created using the gravitational wave sensitivity plotter at `http://rhcole.com/apps/GWplotter/` as described in (Moore et al., 2015).

Bibliography

Abbott, B. P., Abbott, R., Abbott, T. D., et al. 2016, Phys. Rev. Lett., 116, 061102

Alexander, D. R., & Ferguson, J. W. 1994, ApJ, 437, 879

Aurière, M., Konstantinova-Antova, R., Charbonnel, C., et al. 2015, A&A, 574, A90

Balbus, S. A. 1995, ApJ, 453, 380

Balbus, S. A., & Hawley, J. F. 1991, ApJ, 376, 214

—. 1998, Reviews of Modern Physics, 70, 1

Batchelor, G. K. 2000, An introduction to fluid dynamics (Cambridge: Cambridge University Press)

Batten, A. H. 1989, Space Sci. Rev., 50, 1

Belczynski, K., Bulik, T., & Ruiter, A. J. 2005, ApJ, 629, 915

Belczynski, K., Kalogera, V., Rasio, F. A., et al. 2008, ApJS, 174, 223

Blanchet, L., Damour, T., & Schaefer, G. 1990, MNRAS, 242, 289

Blandford, R. D., & Payne, D. G. 1982, MNRAS, 199, 883

Blöecker, T. 1995, A&A, 297, 727

Bode, J. E. 1795, Claudius Ptolemäus Astronom zu Alexandrien, im zweyten Jahrhundert Beobachtung und Beschreibung der Gestirne und der Bewegung der himmlischen Sphäre (Berlin und Stettin: Nicolai), das Werk des Ptolemäus ist auch unter dem Einheitssachtitel "Almagest" bekannt. Aus dem Griech. übers.

Bodenheimer, P., & Taam, R. E. 1984, ApJ, 280, 771

Bondi, H., & Hoyle, F. 1944, MNRAS, 104, 273

Bopp, B. W., & Stencel, R. E. 1981, ApJ, 247, L131

Bouchut, F. 2004, Nonlinear Stability of Finite Volume Methods for Hyperbolic Conservation Laws (Basel: Birkhäuser), doi:10.1007/b93802

Brahe, T. 1573, De nova et nullius ævi memoria prius visa Stella, iam pridem anno á nato CHRISTO 1572, mense Novembri primum Conspecta, contemplatio mathematica (Kopenhagen: Laurentius Benedictus)

Brahe, T. 1610, Astronomiae Instauratae Progymnasmata (Francofurti: Tampachius)

Braithwaite, J., & Spruit, H. C. 2004, Nature, 431, 819

—. 2015, ArXiv e-prints, arXiv:1510.03198

Briggs, G. P., Ferrario, L., Tout, C. A., Wickramasinghe, D. T., & Hurley, J. R. 2015, MNRAS, 447, 1713

Bronstein, I. N., Semendjajew, K. A., Musiol, G., & Mühlig, H. 2008, Taschenbuch der Mathematik, 7th edn. (Frankfurt am Main: Verlag Harri Deutsch)

Chesneau, O., Meilland, A., Chapellier, E., et al. 2014, A&A, 563, A71

Courant, R., Friedrichs, K. O., & Lewy, H. 1928, Math. Ann., 100, 32

Dan, M., Rosswog, S., Guillochon, J., & Ramirez-Ruiz, E. 2011, ApJ, 737, 89

Davis, P. J., Kolb, U., & Knigge, C. 2012, MNRAS, 419, 287

Davis, P. J., Kolb, U., & Willems, B. 2010, MNRAS, 403, 179

de Kool, M. 1987, PhD thesis, University of Amsterdam

—. 1990, ApJ, 358, 189

Bibliography

De Marco, O. 2009, PASP, 121, 316

De Marco, O., Passy, J.-C., Moe, M., et al. 2011, MNRAS, 411, 2277

De Marco, O., Sandquist, E. L., Mac Low, M.-M., Herwig, F., & Taam, R. E. 2003a, in Revista Mexicana de Astronomia y Astrofisica Conference Series, Vol. 15, Revista Mexicana de Astronomia y Astrofisica Conference Series, ed. J. Arthur & W. J. Henney, 34–37

De Marco, O., Sandquist, E. L., Mac Low, M.-M., Herwig, F., & Taam, R. E. 2003b, in Revista Mexicana de Astronomia y Astrofisica Conference Series, Vol. 18, Revista Mexicana de Astronomia y Astrofisica Conference Series, ed. M. Reyes-Ruiz & E. Vázquez-Semadeni, 24–30

Dedner, A., Kemm, F., Kröner, D., et al. 2002, Journal of Computational Physics, 175, 645

Delgado, A. J. 1980, A&A, 87, 343

Desveaux, V., Zenk, M., Berthon, C., & Klingenberg, C. 2015, International Journal for Numerical Methods in Fluids, doi:10.1002/fld.4177, fld.4177

Dewey, R. J., & Cordes, J. M. 1987, ApJ, 321, 780

Dewi, J. D. M., & Tauris, T. M. 2000, A&A, 360, 1043

Dobbie, P. D., Külebi, B., Casewell, S. L., et al. 2013, MNRAS, 428, L16

Duquennoy, A., & Mayor, M. 1991, A&A, 248, 485

Eggleton, P. 2011, Evolutionary Processes in Binary and Multiple Stars (Cambridge: Cambridge University Press)

Eggleton, P. P. 1983, ApJ, 268, 368

Evrard, A. E. 1988, MNRAS, 235, 911

Ferguson, J. W., Alexander, D. R., Allard, F., et al. 2005, ApJ, 623, 585

Ferrario, L., de Martino, D., & Gänsicke, B. T. 2015a, Space Sci. Rev., 191, 111

Ferrario, L., Melatos, A., & Zrake, J. 2015b, Space Sci. Rev., 191, 77

Freytag, B., & Höfner, S. 2008, A&A, 483, 571

Freytag, B., Steffen, M., Ludwig, H.-G., et al. 2012, Journal of Computational Physics, 231, 919

Fryer, C., Burrows, A., & Benz, W. 1998, ApJ, 496, 333

Fuller, J., Cantiello, M., Stello, D., Garcia, R. A., & Bildsten, L. 2015, Science, 350, 423

García-Berro, E., Lorén-Aguilar, P., Aznar-Siguán, G., et al. 2012, ApJ, 749, 25

Gianninas, A., Dufour, P., Kilic, M., et al. 2014, ApJ, 794, 35

Goodman, J., & Xu, G. 1994, ApJ, 432, 213

Górski, K. M., Hivon, E., Banday, A. J., et al. 2005, ApJ, 622, 759

Han, Z., Podsiadlowski, P., & Eggleton, P. P. 1994, MNRAS, 270, 121

—. 1995, MNRAS, 272, 800

Han, Z., Podsiadlowski, P., Maxted, P. F. L., & Marsh, T. R. 2003, MNRAS, 341, 669

Han, Z., Podsiadlowski, P., Maxted, P. F. L., Marsh, T. R., & Ivanova, N. 2002, MNRAS, 336, 449

Harpaz, A. 1998, ApJ, 498, 293

Harten, A., Lax, P. D., & Van Leer, B. 1983, SIAM Review, 25, 35

Heber, U. 2009, ARA&A, 47, 211

Herschel, W. 1782, On the parallax of the fixed stars (London: J. Nichols)

—. 1785, Catalogue of double stars (London: J. Nichols)

Hunter, J. D. 2007, Computing in Science & Engineering, 9, 90

Hurley, J. R., Tout, C. A., & Pols, O. R. 2002, MNRAS, 329, 897

Iaconi, R., Reichardt, T., Staff, J., et al. 2016, ArXiv e-prints, arXiv:1603.01953

Iben, Jr., I., & Livio, M. 1993, PASP, 105, 1373

Iben, Jr., I., & Tutukov, A. V. 1984, ApJS, 54, 335

—. 1985, ApJS, 58, 661

Iglesias, C. A., & Rogers, F. J. 1996, ApJ, 464, 943

Ivanova, N., Justham, S., Nandez, J. L. A., & Lombardi, J. C. 2013a, Science, 339, 433

Ivanova, N., Justham, S., & Podsiadlowski, P. 2015, MNRAS, 447, 2181

Ivanova, N., Justham, S., Chen, X., et al. 2013b, A&A Rev., 21, 59

Joos, G. 1945, Lehrbuch der theoretischen Physik, 6th edn. (Leipzig: Akademische Verlagsgesellschaft Becker & Erler Kom.-Ges.)

Jordan, S., Bagnulo, S., Werner, K., & O'Toole, S. J. 2012, A&A, 542, A64

Jordan, S., Werner, K., & O'Toole, S. J. 2005, A&A, 432, 273

King, A. R. 1988, QJRAS, 29, 1

Kippenhahn, R., & Weigert, A. 1967, ZAp, 65, 251

Kippenhahn, R., Weigert, A., & Weiss, A. 2012, Stellar Structure and Evolution (Berlin Heidelberg: Springer-Verlag), doi:10.1007/978-3-642-30304-3

Kolb, U. 1993, A&A, 271, 149

Kornilov, V. G., & Lipunov, V. M. 1983, Soviet Ast., 27, 334

Landau, L. D., & Lifshitz, E. M. 1987, Fluid Mechanics (Course of Theoretical Physics: Volume 6), 2nd edn. (Oxford: Butterworth-Heinemann)

Landstreet, J. D. 1992, A&A Rev., 4, 35

LeVeque, R. J. 1992, Numerical Methods for Conservation Laws, 2nd edn. (Basel: Birkhäuser), doi:10.1007/978-3-0348-8629-1

LeVeque, R. J. 1998, in Computational Methods for Astrophysical Flows, ed. O. Steiner & A. Gautschy, Saas-Fee Advanced Course 27 (Berlin Heidelberg New York: Springer), 1–159

Lewin, W. H. G., van Paradijs, J., & van den Heuvel, E. P. J. 1997, X-ray Binaries (Cambridge: Cambridge University Press)

Liebert, J., Wickramasinghe, D. T., Schmidt, G. D., et al. 2005, AJ, 129, 2376

Lipunov, V. M., & Postnov, K. A. 1988, Ap&SS, 145, 1

Livio, M. 1989, Space Sci. Rev., 50, 299

Livio, M., Shankar, A., Burkert, A., & Truran, J. W. 1990, ApJ, 356, 250

Livio, M., & Soker, N. 1984a, MNRAS, 208, 783

—. 1984b, MNRAS, 208, 763

—. 1988, ApJ, 329, 764

MacFadyen, A. I., & Milosavljević, M. 2008, ApJ, 672, 83

Marinacci, F., Pakmor, R., & Springel, V. 2014, MNRAS, 437, 1750

Mayer, C. 1778, Gründliche Vertheidigung neuer Beobachtungen von Fixsterntrabanten, welche zu Mannheim auf der kurfürstlichen Sternwarte entdecket worden sind (Mannheim: Hof- und Akademie-Buchdruckerei)

—. 1779, De Novis In Coelo Sidereo Phaenomenis (Mannhemii: Typographia Elector. Aulica & Academica)

Meyer, F., & Meyer-Hofmeister, E. 1979, A&A, 78, 167

Michell, J. 1767, Philosophical Transactions (1683-1775), 57, 234

Miczek, F., Röpke, F. K., & Edelmann, P. V. F. 2015, A&A, 576, A50

Mihalas, D., & Mihalas, B. W. 1984, Foundations of radiation hydrodynamics (New York: Oxford University Press)

Bibliography

Miyoshi, T., & Kusano, K. 2005, Journal of Computational Physics, 208, 315

Moore, C. J., Cole, R. H., & Berry, C. P. L. 2015, Classical and Quantum Gravity, 32, 015014

Müller, E. 1998, in Computational Methods for Astrophysical Flows, ed. O. Steiner & A. Gautschy, Saas-Fee Advanced Course 27 (Berlin Heidelberg New York: Springer), 343–494

Müller, E., & Janka, H.-T. 1997, A&A, 317, 140

Nandez, J. L. A., Ivanova, N., & Lombardi, J. C. 2015, MNRAS, 450, L39

Nandez, J. L. A., Ivanova, N., & Lombardi, Jr., J. C. 2014, ApJ, 786, 39

Nelemans, G. 2010, Ap&SS, 329, 25

Nelemans, G., Portegies Zwart, S. F., Verbunt, F., & Yungelson, L. R. 2001a, A&A, 368, 939

Nelemans, G., & Tout, C. A. 2005, MNRAS, 356, 753

Nelemans, G., Verbunt, F., Yungelson, L. R., & Portegies Zwart, S. F. 2000, A&A, 360, 1011

Nelemans, G., Yungelson, L. R., Portegies Zwart, S. F., & Verbunt, F. 2001b, A&A, 365, 491

Nordhaus, J., & Blackman, E. G. 2006, MNRAS, 370, 2004

Nordhaus, J., Blackman, E. G., & Frank, A. 2007, MNRAS, 376, 599

Nordhaus, J., Wellons, S., Spiegel, D. S., Metzger, B. D., & Blackman, E. G. 2011, Proceedings of the National Academy of Science, 108, 3135

Ohlmann, S. T., Röpke, F. K., Pakmor, R., & Springel, V. 2016, ApJ, 816, L9

Oliphant, T. E. 2007, Computing in Science & Engineering, 9, 10

Oßwald, K., Siegmund, A., Birken, P., Hannemann, V., & Meister, A. 2015, International Journal for Numerical Methods in Fluids, doi:10.1002/fld.4175, fld.4175

Ostriker, E. C. 1999, ApJ, 513, 252

Paczynski, B. 1976, in IAU Symposium, Vol. 73, Structure and Evolution of Close Binary Systems, ed. P. Eggleton, S. Mitton, & J. Whelan, 75

Paczyński, B., & Ziółkowski, J. 1968, Acta Astronomica, 18, 255

Pakmor, R., Bauer, A., & Springel, V. 2011, MNRAS, 418, 1392

Pakmor, R., Edelmann, P., Röpke, F. K., & Hillebrandt, W. 2012, MNRAS, 424, 2222

Pakmor, R., & Springel, V. 2013, MNRAS, 432, 176

Pakmor, R., Springel, V., Bauer, A., et al. 2016, MNRAS, 455, 1134

Passy, J.-C., De Marco, O., Fryer, C. L., et al. 2012, ApJ, 744, 52

Paxton, B., Bildsten, L., Dotter, A., et al. 2011, ApJS, 192, 3

Paxton, B., Cantiello, M., Arras, P., et al. 2013, ApJS, 208, 4

Paxton, B., Marchant, P., Schwab, J., et al. 2015, ApJS, 220, 15

Pérez, F., & Granger, B. E. 2007, Computing in Science & Engineering, 9, 21

Perryman, M. A. C., de Boer, K. S., Gilmore, G., et al. 2001, A&A, 369, 339

Pickering, E. C. 1880, Proceedings of the American Academy of Arts and Sciences, 16, 1

Pols, O. R., & Marinus, M. 1994, A&A, 288

Portegies Zwart, S. F., & Verbunt, F. 1996, A&A, 309, 179

Potter, A. T., & Tout, C. A. 2010, MNRAS, 402, 1072

Powell, K. G., Roe, P. L., Linde, T. J., Gombosi, T. I., & de Zeeuw, D. L. 1999, Journal of Computational Physics, 154, 284

Pustylnik, I. 1998, Astronomical and Astrophysical Transactions, 15, 357

Rasio, F. A., & Livio, M. 1996, ApJ, 471, 366

Regős, E., & Tout, C. A. 1995, MNRAS, 273, 146

Reichl, L. E. 2009, A Modern Course in Statistical Physics, 3rd edn. (Weinheim: WILEY-VCH Verlag)

Reimers, D. 1975, Memoires of the Societe Royale des Sciences de Liege, 8, 369

Rembiasz, T., Obergaulinger, M., Cerdá-Durán, P., Müller, E., & Aloy, M. A. 2016, MNRAS, 456, 3782

Ricker, P. M., & Taam, R. E. 2008, ApJ, 672, L41

—. 2012, ApJ, 746, 74

Ritter, H. 1986, A&A, 169, 139

—. 2012, Mem. Soc. Astron. Italiana, 83, 505

Ritter, H., & Kolb, U. 2003, A&A, 404, 301, update RKcat7.23, 2015

Roe, P. L. 1981, Journal of Computational Physics, 43, 357

Rogers, F. J., & Nayfonov, A. 2002, ApJ, 576, 1064

Rogers, F. J., Swenson, F. J., & Iglesias, C. A. 1996, ApJ, 456, 902

Rosswog, S., Speith, R., & Wynn, G. A. 2004, MNRAS, 351, 1121

Roxburgh, I. W. 1967, Nature, 215, 838

Ruiter, A. J., Belczynski, K., Sim, S. A., et al. 2011, MNRAS, 417, 408

Rusanov, V. V. 1961, J. Comput. Math. Phys. USSR, 1, 267

Sandquist, E. L., Taam, R. E., & Burkert, A. 2000, ApJ, 533, 984

Sandquist, E. L., Taam, R. E., Chen, X., Bodenheimer, P., & Burkert, A. 1998, ApJ, 500, 909

Schreiber, M. R., & Gänsicke, B. T. 2003, A&A, 406, 305

Seitenzahl, I. R., Herzog, M., Ruiter, A. J., et al. 2015, Phys. Rev. D, 92, 124013

Shakura, N. I., & Sunyaev, R. A. 1973, A&A, 24, 337

Shi, J.-M., Krolik, J. H., Lubow, S. H., & Hawley, J. F. 2012, ApJ, 749, 118

Shore, S. N. 2007, Astrophysical hydrodynamics: an introduction, 2nd edn. (Weinheim: WILEY-VCH Verlag)

Silvestri, N. M., Lemagie, M. P., Hawley, S. L., et al. 2007, AJ, 134, 741

Soker, N., & Harpaz, A. 2003, MNRAS, 343, 456

Soker, N., Livio, M., & Harpaz, A. 1984, MNRAS, 210, 189

Sparks, W. M., & Stecher, T. P. 1974, ApJ, 188, 149

Springel, V. 2005, MNRAS, 364, 1105

—. 2010a, MNRAS, 401, 791

—. 2010b, ARA&A, 48, 391

Staff, J. E., De Marco, O., Macdonald, D., et al. 2016a, MNRAS, 455, 3511

Staff, J. E., De Marco, O., Wood, P., Galaviz, P., & Passy, J.-C. 2016b, MNRAS, 458, 832

Suliciu, I. 1998a, International Journal of Engineering Science, 36, 921

—. 1998b, International Journal of Engineering Science, 36, 949

Taam, R. E., & Bodenheimer, P. 1989, ApJ, 337, 849

—. 1991, ApJ, 373, 246

Taam, R. E., Bodenheimer, P., & Ostriker, J. P. 1978, ApJ, 222, 269

Taam, R. E., Bodenheimer, P., & Rozyczka, M. 1994, ApJ, 431, 247

Taam, R. E., & Sandquist, E. L. 2000, ARA&A, 38, 113

Terman, J. L., & Taam, R. E. 1996, ApJ, 458, 692

Terman, J. L., Taam, R. E., & Hernquist, L. 1994, ApJ, 422, 729

—. 1995, ApJ, 445, 367

Thorne, K. S., & Żytkow, A. N. 1977, ApJ, 212, 832

Timmes, F. X., & Swesty, F. D. 2000, ApJS, 126, 501

Tocknell, J., De Marco, O., & Wardle, M. 2014, MNRAS, 439, 2014

Toonen, S., Claeys, J. S. W., Mennekens, N., & Ruiter, A. J. 2014, A&A, 562, A14

Toonen, S., & Nelemans, G. 2013, A&A, 557, A87

Toro, E. F. 2009, Riemann Solvers and Numerical Methods for Fluid Dynamics: A Practical Introduction (Berlin Heidelberg: Springer)

Toro, E. F., Spruce, M., & Speares, W. 1994, Shock waves, 4, 25

Tout, C. A., & Regős, E. 2003, in Astronomical Society of the Pacific Conference Series, Vol. 293, 3D Stellar Evolution, ed. S. Turcotte, S. C. Keller, & R. M. Cavallo, 100

Tout, C. A., Wickramasinghe, D. T., Liebert, J., Ferrario, L., & Pringle, J. E. 2008, MNRAS, 387, 897

Vanbeveren, D., van Bever, J., & De Donder, E. 1997, A&A, 317, 487

Vogelsberger, M., Genel, S., Springel, V., et al. 2014a, MNRAS, 444, 1518

—. 2014b, Nature, 509, 177

Webbink, R. F. 1984, ApJ, 277, 355

Webbink, R. F. 2008, in Astrophysics and Space Science Library, Vol. 352, Astrophysics and Space Science Library, ed. E. F. Milone, D. A. Leahy, & D. W. Hobill, 233

Weiss, A., Hillebrandt, W., Thomas, H.-C., & Ritter, H. 2004, Cox & Giuli's Principles of Stellar Structure (Cambridge: Cambridge Scientific Publishers)

Wickramasinghe, D. T., & Ferrario, L. 2000, PASP, 112, 873

Wickramasinghe, D. T., Tout, C. A., & Ferrario, L. 2014, MNRAS, 437, 675

York, D. G., Adelman, J., Anderson, Jr., J. E., et al. 2000, AJ, 120, 1579

Yorke, H. W., Bodenheimer, P., & Taam, R. E. 1995, ApJ, 451, 308

Yungelson, L. R., & Tutukov, A. V. 1991, in IAU Symposium, Vol. 143, Wolf-Rayet Stars and Interrelations with Other Massive Stars in Galaxies, ed. K. A. van der Hucht & B. Hidayat, 459

Zenk, M. 2013, Master's thesis, Julius-Maximilians-Universität Würzburg

Zhu, C., Pakmor, R., van Kerkwijk, M. H., & Chang, P. 2015, ApJ, 806, L1

Zingale, M., Dursi, L. J., ZuHone, J., et al. 2002, ApJS, 143, 539

Zorotovic, M., Schreiber, M. R., Gänsicke, B. T., & Nebot Gómez-Morán, A. 2010, A&A, 520, A86

Zorotovic, M., Schreiber, M. R., Gänsicke, B. T., et al. 2011, A&A, 536, L3

Danksagung

Eigenständigkeitserklärung

Hiermit versichere ich, die vorliegende Arbeit selbstständig verfasst zu haben und keine Quellen oder Hilfsmittel außer den angegebenen verwendet zu haben.

Heidelberg, den 13. April 2016, _____

Sebastian Ohlmann